PROPULSION MATERIALS

VEHICLE TECHNOLOGIES PROGRAM

Less dependence on foreign oil today, and transition to a petroleum-free, emissions-free vehicle tomorrow.

2007

annual progress report

U.S. Department of Energy
Energy Efficiency and Renewable Energy
Bringing you a prosperous future where energy is clean, abundant, reliable, and affordable

U.S. Department of Energy
Office of Vehicle Technologies
1000 Independence Avenue S.W.
Washington, DC 20585-0121

FY 2007

Progress Report for Propulsion Materials

Energy Efficiency and Renewable Energy
Office of Vehicle Technologies
Advanced Materials Technologies

Edward J. Wall **Program Manager, OVT**
Rogelio A. Sullivan **Advanced Materials Technologies Team Leader**
Jerry L. Gibbs **Technology Manager**

January 2008

CONTENTS

INTRODUCTION

Propulsion Materials R&D: Enabling Technologies to Meet Vehicle Technologies Program Goals

The Department of Energy's (DOE's) Office of Vehicle Technologies (OVT) is pleased to introduce the *FY 2007 Annual Progress Report for the Propulsion Materials Research and Development Program*. Together with DOE national laboratories and in partnership with private industry and universities across the United States, the program continues to engage in research and development (R&D) that provides enabling materials technology for fuel-efficient and environmentally friendly commercial and passenger vehicles.

This introduction summarizes the objectives, progress, and highlights of the program in FY 2007. The Propulsion Materials R&D Program has supported the Vehicle Technologies Program since its inception. In research areas where industry views the risks as too high and uncertain, the Vehicle Technologies Program conducts long-term research, development, and demonstration activities that bring the technology to a stage of maturity such that industry can undertake the final commercialization stages. In order to provide more effective support to the program's stakeholders and participants, the former Automotive Propulsion Materials and Heavy-Vehicle Propulsion Materials R&D programs were combined in FY 2007 into a single Propulsion Materials R&D program.

The Propulsion Materials program is a partner and supporter of the (OVT) Hybrid and Vehicle Systems, Energy Storage, Power Electronics and Electrical Machines, Advanced Combustion Engines, and Fuels and Lubricants R&D programs. Projects within the Propulsion Materials Program address materials concerns that directly impact the critical technical barriers in each of these programs—barriers such as fuel efficiency, thermal management, emissions reduction, and reduced manufacturing costs. The program engages only the barriers that involve fundamental, high-risk materials issues.

Enabling Technologies

The Propulsion Materials program focuses on enabling and innovative materials technologies that are critical in improving the efficiency of advanced engines. The program provides enabling materials support for combustion, hybrid, and power electronics development, including the following:

- Materials for low-temperature combustion, for example, homogenous-charge compression-ignition
- Materials for hydrogen engine fuel systems
- Materials for 55% thermal efficiency heavy-duty diesel engines
- Materials for waste-heat recovery via thermoelectric modules, with potential 10% increase in fuel efficiency

The program supports these core technology areas by providing materials expertise, testing capabilities, and technical solutions for materials problems. The component development, materials processing, and characterization that the program provides are enablers of the successful development of efficient and emissions-compliant engines.

Program Organization

The Propulsion Materials Program consists of five R&D projects which support the OVT propulsion technologies. Each project consists of several related R&D agreements.

- Materials for Electric and Hybrid Drive Systems
  - Develop materials appropriate for power electronics and other hybrid system applications

- Combustion System Materials
  - Develop materials for HCCI engines and fuel injection systems

- Materials for High Efficiency Engines
  - Develop materials for efficient engine components, such as valve-train components, fuel injectors, and turbochargers

- Materials for Exhaust and Energy Recovery
  - Develop materials for exhaust aftertreatment and thermoelectric exhaust heat recovery applications
- Materials by Design
  - Adopt a computational materials – atomic-scale characterization protocol to develop advanced materials for NOx catalysts, lithium-ion batteries, thermoelectric generators

R&D Projects and Agreements are evaluated annually using strategic objectives. Agreements are evaluated on relevance to OVT objectives and supported team's priorities, strength of industrial support for the activity, and perceived value of the R&D activity to the OVT Program. In order to keep the program fresh and up-to-date, over 10% of agreements are retired annually. New projects are selected in accordance with identified Office of Vehicle Technologies needs, for example:

- Advanced Combustion Team
  - Internal combustion engine materials
  - Thermoelectric materials
  - Catalysts and aftertreatment materials
  - Materials for engine sensors

- Hybrid Electric Systems Team
  - Power electronics materials
  - Materials for energy storage

- Fuels Team
  - Alternative fuels materials compatibility

Selected Highlights:

Materials for Electric and Hybrid Drive Systems

The goal of the Automotive Power Electronic and Electric Machines Program is to reduce the size, weight, and volume of the power electronics without increasing the cost or reducing the reliability. Many, if not most, technical barriers are directly linked to the contemporary material limitations of subcomponents found within devices that comprise inverters, converters, and motors. The material limitations include:

- Insufficient temperature capability
- Excessive thermal insulations
- Excessive electrical insulation
- Insufficient power density in permanent magnets
- Insufficient bandgap

Many of these issues are already being addressed in the Vehicle APEEM Program, but there is interest in exploring additional means to overcome some of those materials limitations through the application of advanced materials science and engineering that are not currently being considered. An assessment of the materials needs for power electronics was completed in FY07 by researchers at ORNL. The conclusions of this assessment will be used to initiate several new projects in this area.

Combustion System Materials

Based on discussions with automotive companies, improvement in high temperature operating capability of exhaust valves has been identified as an area that would be essential for the development of homogeneous charge compression ignition (HCCI) engines. Automotive valves in use today are designed to operate at temperatures up to 1400°F. It is anticipated that with advances in HCCI engines, the operating temperature requirements will increase to 1600°F. Researchers at Oak Ridge National Laboratory researchers are using computational design concepts to develop advanced materials for such applications. Ni-based alloy compositions currently used for this application may not have the required properties for higher temperature operation due to dissolution and/or rapid coarsening of the strengthening precipitates. With input from a leading automotive valve manufacturer, high temperature fatigue strength at 1600°F was identified as a critical property of interest in valve materials. With input from a materials supplier, eight commercial Ni-based alloys have been identified for the development of an initial database linking alloy composition with microstructure and high temperature fatigue properties. Computational thermodynamic modeling was used to calculate the types and amount of the strengthening phases present in these alloys (Figure 1). High temperature fatigue tests at 1600°F are being carried out on these alloys (Figure 2). Results clearly show the effect of strengthening precipitate contents on fatigue properties and will be used to identify alloy compositions with requisite properties.

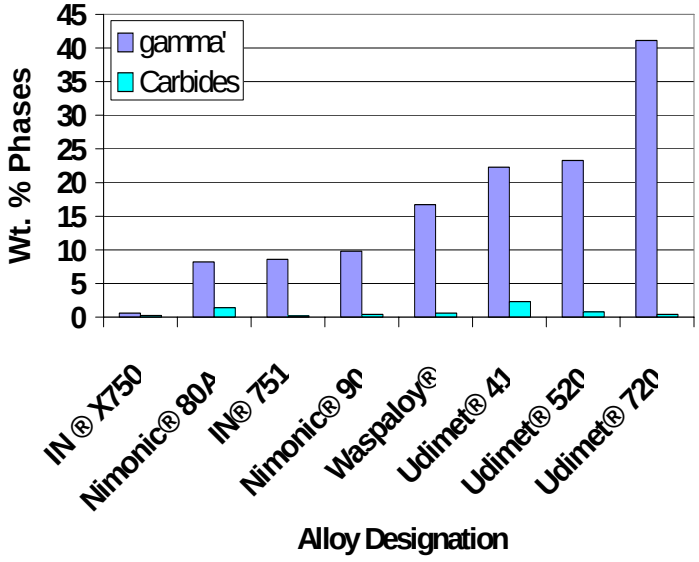

Fig. 1. Calculated amounts of strengthening phases in selected alloys

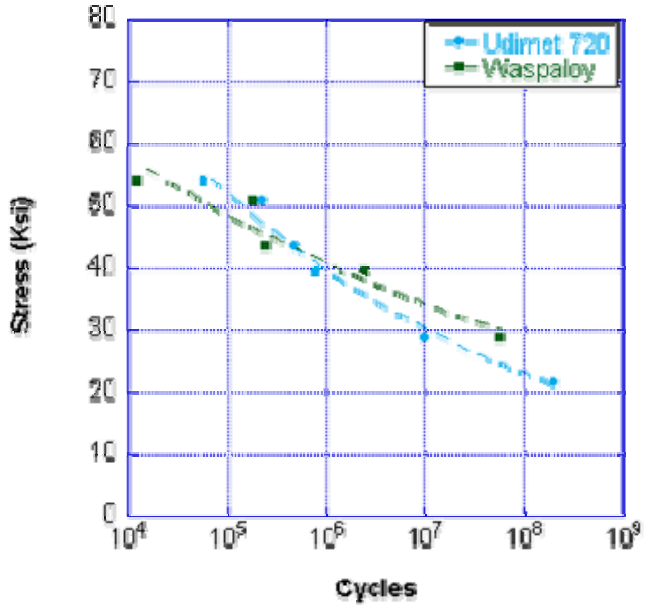

Fig. 2. Fatigue properties of Udimet 720 and Waspaloy

In order to comply with stringent Environmental Protection Agency (EPA) regulations, diesel engines are being redesigned to increase efficiency and reduce emissions and in-cylinder soot production. One of the design changes is an increase in the pressure at which fuel is injected. The high pressure makes it necessary to reduce the diameter of fuel injectors to improve fuel atomization, which will increase efficiency and reduce emissions. Researchers at Argonne National Laboratory (ANL) have successfully developed a process to reduce the diameter of fuel injectors from 150 to 50 µm through an electroless nickel plating process that deposits nickel/phosphorus or nickel/boron alloys on the internal diameters of injector orifices. This process is necessary to effectively produce small, uniform orifice diameters from inlet to outlet because conventional fabrication processes result in unacceptable variation or error rates. Figure 3 illustrates a commercial nozzle with multiple orifices that has been coated to reduce the diameter of the holes from 150 to ~50 µm. The spray characteristics (Figure 4) of the electroless nickel-coated nozzle was characterized in collaboration with the EPA.

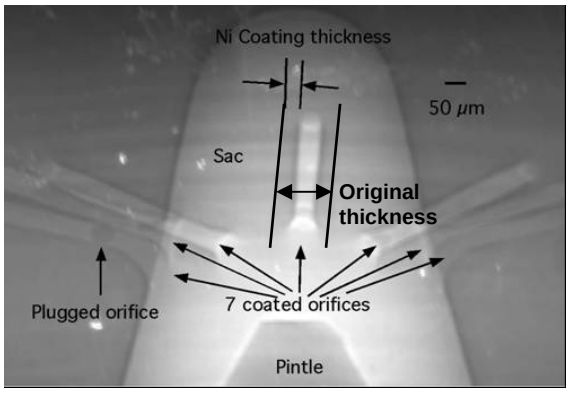

Fig. 3. Phase contrast X-ray image of commercial nozzle plated with electroless nickel

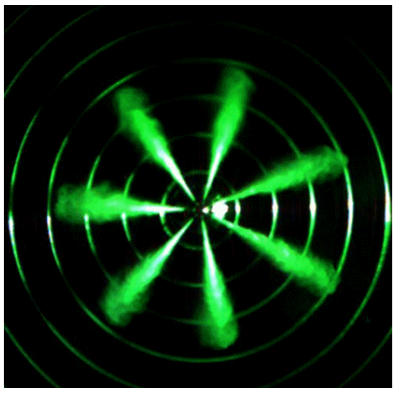

Fig. 4. Laser image of fuel spray from 50 µm orifice.

Materials for High Efficiency Engines

The feasibility of using lightweight, corrosion-resistant silicon nitride and titanium aluminide high-temperature valves in a heavy-duty diesel engine was evaluated by Caterpillar, assisted by Argonne National Laboratory (ANL) and Oak Ridge National Laboratory. A 500-hour endurance test of prototype valves in a stationary engine at ORNL was successfully completed. Figure 5 shows post-test nondestructive wear data from tests conducted by ANL which show significant differences in the two valve materials.

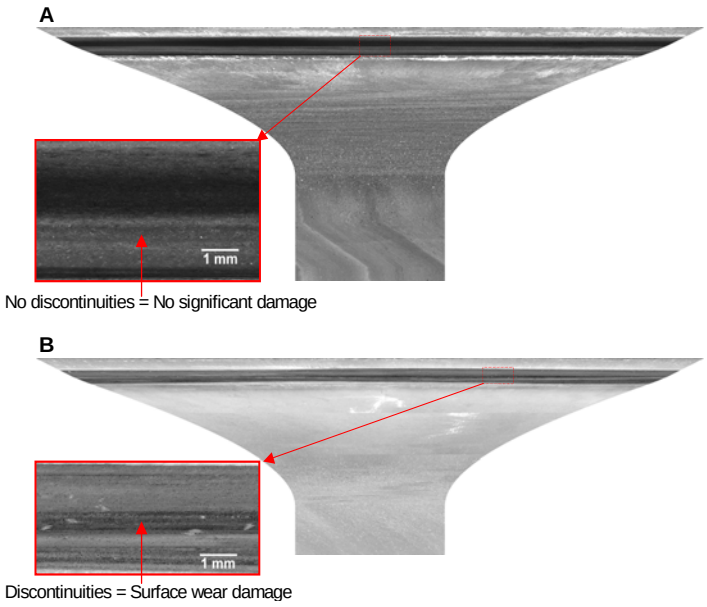

Figure 5. Laser-based NDE scans after 100 hours of engine exposure time of (A) Si3N4E-32 and (B) TiAl-5, indicating that the Si_3N_4 valve has not sustained major wear damage, but the TiAl valve is showing signs of significant valve/seat wear.

PNNL is developing Friction Stir Processing (FSP) for engine materials (cast iron, alloy steels, and aluminum alloys), with the goal of increasing their high temperature performance, durability, and thermal properties Figure 6 shows initial trials designed to show the feasibility of stirring ceramic surface coatings into the substrate to modify the thermal conductivity of the base material. To-date the addition of up to 20% ceramic to aluminum has been demonstrated**,** and approximately 10% addition to steel has been achieved. These trials demonstrated the feasibility, but it is clear that more work is needed to bring the ceramic loading up to the point where it will strongly affect the thermal conductivity.

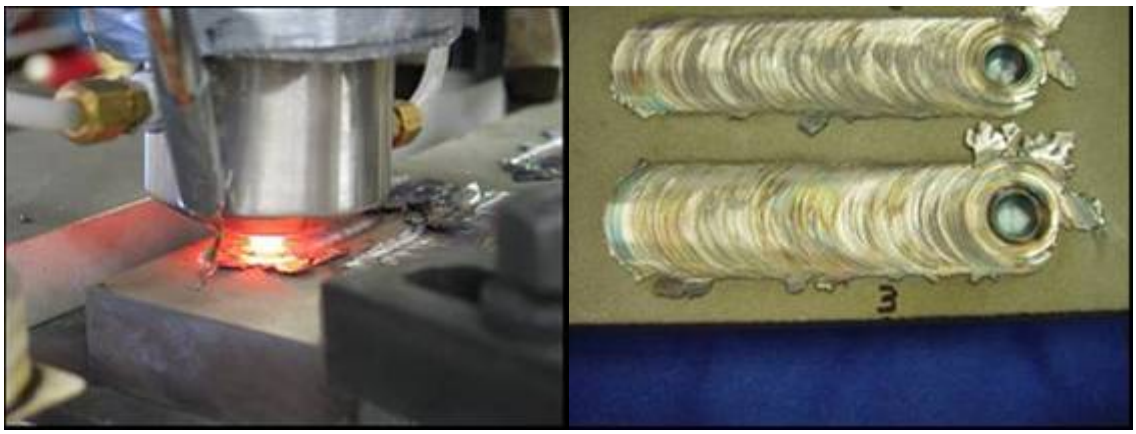

Figure 6. FSP test in progress (left) and initial results showing that ceramic coatings can be stirred into the substrate (right).

Materials for Exhaust and Energy Recovery

The Oak Ridge National Laboratory and Caterpillar engaged in a cooperative research and development agreement (CRADA) for development of a new, cast austenitic stainless steel (CF8C-Plus) as an upgrade alternative to SiMo cast iron. CF8C-Plus steel, invented and patented in the course of the effort, was found to have outstanding mechanical properties and excellent castability and weldability. Caterpillar chose CF8C-Plus stainless steel for the Caterpillar Regeneration System (CRS) housing shown in Figure 7, which became standard equipment on all Caterpillar heavy-duty highway truck diesel engines in 2007.

Figure 7. The first commercial application of CF8C-Plus is the Caterpillar Regeneration System (CRS) housing, which was included on all on-highway truck diesel engines after January 2007. This combustor ignites exhaust gas and injected diesel fuel to clean diesel particulate filters, and must withstand high temperatures and rapid thermal cycling.

In 2007 Cummins very successfully introduced their entire on-road product range, all of which meet the very demanding 2007 EPA Emissions Regulations. Cummins credits DOE Vehicle Technologies Propulsion Materials program CRADAs with a significant role in the EPA-compliant, fuel-efficient engines. Figure 8 illustrates one of the tests conducted on diesel particulate filters.

Figure 8: Sample furnace at 1000°C for the resonant ultrasound spectroscopy of diesel particulate filters.

Materials by Design

ANL has developed a process for strong, pore-free joints which have been demonstrated with various ceramics, cermets, intermetallics, composites, and more recently, biomaterials. The ANL process contributed to an

R&D 100 award for an oxygen sensor and will be used in future work for joining metals and intermetallics to ceramics for solid-oxide fuel cell applications. Figure 9 illustrates the integrity of the joints produced by the process.

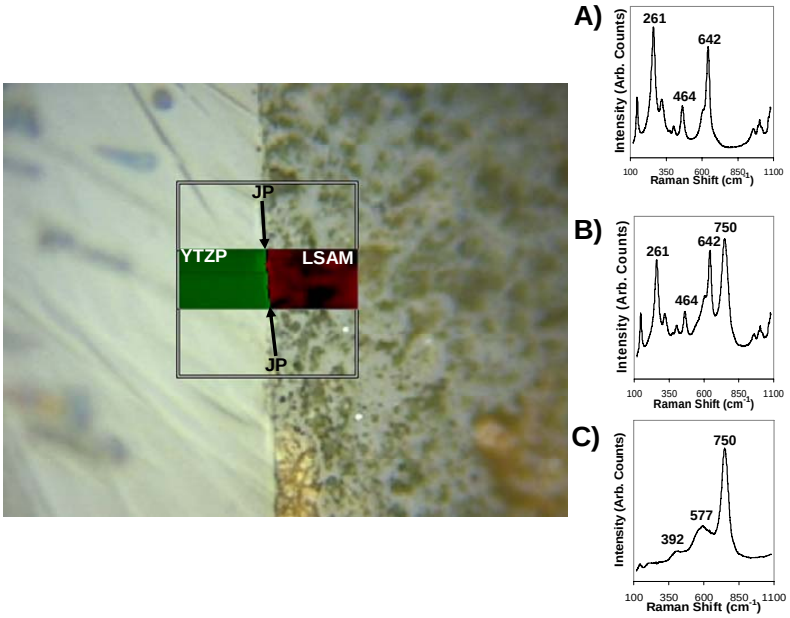

Figure 9. Raman map of interface in sample joined at 1250°C. The joining plane is the narrow region denoted as JP that lies between the bulk of YTZP and LSAM. A) Representative spectrum of the YTZP region marked in green. B) Representative spectrum of the joining plane denoted by arrows. C) Representative spectrum of the LSAM region marked in red.

The remainder of this report communicates the progress achieved during FY 2007 under the Propulsion Materials Program. It consists of annual progress contributions from the several R&D Agreements that make up each of the five overarching R&D Projects that are highlighted above. The R&D contributions provide an overview of the critical work being conducted to develop enabling materials technologies for high-efficiency passenger and commercial vehicles, including goals, barriers, progress to date, and future plans.

Rogelio A. Sullivan
Team Leader, Advanced Materials Technologies
Office of Vehicle Technologies
Energy Efficiency and Renewable Energy

Jerry L. Gibbs
Technology Manager
Office of Vehicle Technologies
Energy Efficiency and Renewable Energy

Project 18518 - Materials for High Efficiency Engines

Agreement 13329 - Mechanical Reliability of Piezoelectric Multilayer Actuators for Fuel Injectors

Andrew A. Wereszczak, Hong Wang, and H. -T. Lin
Ceramic Science and Technology Group (CerSaT)
Oak Ridge National Laboratory
P.O. Box 2008, MS 6068
Oak Ridge, TN 37831-6068
(865) 576-1169; fax: (865) 574-6098; e-mail: wereszczakaa@ornl.gov

DOE Technology Manager: Jerry L. Gibbs
(202) 586-1182; fax: (202) 586-1600; e-mail: jerry.gibbs@ee.doe.gov
ORNL Technical Advisor: D. Ray Johnson
(865) 576-6832; fax: (865) 574-6098; e-mail: johnsondr@ornl.gov

Contractor: Oak Ridge National Laboratory, Oak Ridge, Tennessee
Contract No.: DE-AC05-00OR22725

Objectives

- Apply established structural ceramic probabilistic design and reliability analysis to piezoelectric multilayer actuators (PMLAs).
- Generate required micromechanical property data on lead zirconate titanate (PZT) piezoceramics and macromechanical property data on PMLAs for input into the design and reliability analysis of the latter.
- Identify minimum mechanical performance requirements for fuel injector PMLAs.
- Adapt these strategies to improve reliability of PMLAs under candidacy for use in diesel engine fuel injectors.

Approach

- Evaluate PMLA reliability under representative service conditions.
- Link constituent piezoceramic micro-mechanical and PMLA macro-mechanical responses.

Accomplishments

- Mechanical test facilities established to enable evaluation of PZT piezoceramics and PMLAs.
- Identified that strength of poled PZT is side dependent with negative side weakest in tension and that surface-located flaws were strength-limiters.
- Identified ~5% strain reduction in a PMLA after about 500 million cycles with no significant loss of polarization.

Future Direction

- Develop accelerated tests for both piezoceramics and PMLAs.
- Fabricate additional PMLA fatigue test frames.
- Compare performances of competing piezoceramics and competing PMLAs.

Introduction

The use of piezoelectric multilayer actuators (PLMAs) as diesel fuel injectors has the potential to reduce injector response time, provide greater precision and control of the fuel injection event, and lessen energy consumption. Compared to conventional solenoid operation of an injector, the alternative use of a PMLA can enable precise rate shaping of the entire injection cycle that accurately controls injection timing and fuel quantity. An example of a fuel injector containing a piezo-actuator is shown in Fig. 1. Piezoelectric multilayer actuators (or piezo-stacks) fuel injectors contain a solid-state ceramic actuator (or "piezostack") that converts electric energy into linear motion precisely controlling the needle's opening and closing. This capability results in an engine with outstanding performance, improved fuel economy, low noise, and low emissions. Their development for the automotive market has progressed and now strong interest exists to adapt their use to heavy vehicle diesel engines.

Figure 1. *Piezo-actuated fuel injector used in Ford 6.4L Power Stroke® diesel engine.*

Though their use is very attractive for the reasons mentioned above, uncertainty continues to exist over how reliable piezo-actuated fuel injectors will be in the challenging environment of a heavy vehicle diesel engine. Though piezoelectric function is the obvious primary function of lead zirconate titanate (PZT) ceramic PMLAs for fuel injectors, their mechanical reliability can be a performance and life limiter because the PZT ceramic within them is brittle, lacks high strength, and may exhibit fatigue (e.g., electromechanical, slow crack growth) susceptibility. That brittleness and relatively low strength can be overcome with proper design though.

This project undertakes the reliability characterization of candidate PMLAs used in these fuel injectors and the piezoceramics used in the PMLAs. Two parallel efforts comprised this project's work in FY07. In one, test facilities were developed to mechanically evaluate piezoceramics as a function of electric field. In the other, test facilities were also established to enable the study of long-term fatigue performance of PMLAs.

Results

This project's progress in FY07 is broken up into two subsections: piezoceramic characterization (micromechanical) and PMLA characterization (macromechanical).

Piezoceramic Characterization

A micromechanical test facility was constructed that enables the measurement of mechanical strength of piezoceramics while an electric field is concurrently superimposed. It is shown in Fig. 2.

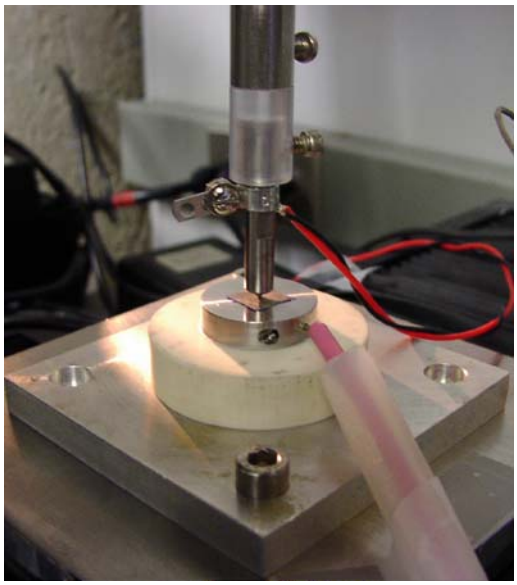

Figure 2. *Setup of the ball-on-ring biaxial flexure strength test with capability to apply concurrent electric field.*

The test setup applies a biaxial stress field on a piezoceramic specimen (typically manufactured by the tape-casting process) using ball-on-ring (BoR) loading. Applied load is increased until the specimen fails and the maximum sustained force is used to calculate the biaxial flexure strength. Both the ball and support ring are made from steel, and an electrical leads is connected to both thusly enabling the application of a voltage bias. That applied voltage is insulated from the test frame and applies an electric field across the electroded piezoceramic test coupon. An electric field is applied and then the mechanical loading is commenced until failure is produced, and biaxial flexure strength is measured in the presence of an electrical field.

Biaxial flexure strengths of four combinations of applied field and poled direction were examined. A schematic of cross-section of the specimen loading configuration is shown in Fig. 3. The electroded PZT were already poled. Two orientations were then available; namely, applying a tensile stress on the positive or negative side. And two electric fields were considered: no field (or "open circuit") and one whose magnitude was equivalent to coercive electrical field of the PZT (1.2 kV/mm). The strength study of these four possible combinations obviously enabled the study of the "side-effect" on poled PZT strength.

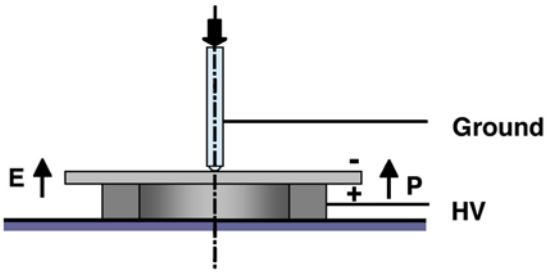

Figure 3. *Cross-section of ball-on-ring test configuration for the condition when an electric field was applied across the PZT specimen with its positive poled side positioned to be loaded in tension during flexure. Four combinations were examined: positive poled side in tension or compression with or without an applied concurrent electric field.*

The resulting strength distributions for the four combinations are shown in Fig. 4. In the absence of an applied electric field, there was no observable side dependence on strength of the poled PZT so their data were pooled. It is shown in Fig. 4 that the strength of the poled PZT was highest in the presence of an electric field when its positive side was tested in tension and lowest when the (opposite) negative side was tested or about 15% higher or lower, respectively, than the no-field cases. These differences were statistically significant. These results suggest that if crack initiation were occur that it would be more apt to occur on the negatively poled side than the positive side.

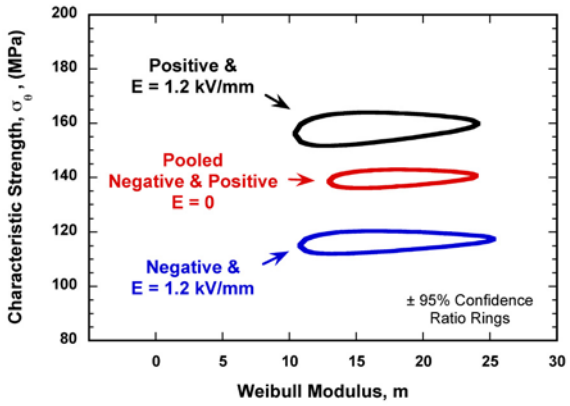

Figure 4. *Confidence ratio rings of characteristic strength and Weibull modulus of the four test conditions. Specimens had nominal dimensions of 10 x 10 x 0.273 mm, and the diameters of the loading ball and support ring were 2.0 and 7.4 mm, respectively.*

Fractography revealed that surface-located flaws limited the strength of all PZT test specimens. Three distinct flaw-types were found: agglomerates, pores, and porous regions. An example of a pore flaw type is shown in Fig. 5. Flaw types such as these can be reduced in size with appropriate alterations of processing.

Flaw sizes were measured and were used with the measured strengths to estimate fracture toughness. The scatter plot of this analysis is shown in Fig. 6. Like the trend of strength in Fig. 4, the apparent fracture toughness of the poled PZT was highest when its positive side was loaded in tension and lowest when its negative side was tested (both in the presence of an electric field).

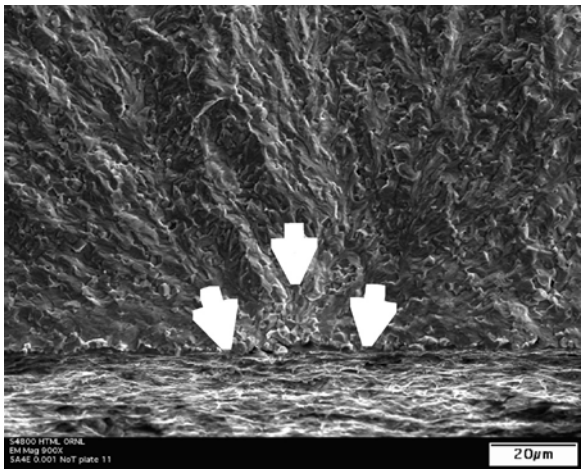

Figure 5. *Example of a strength-limiting flaw.*

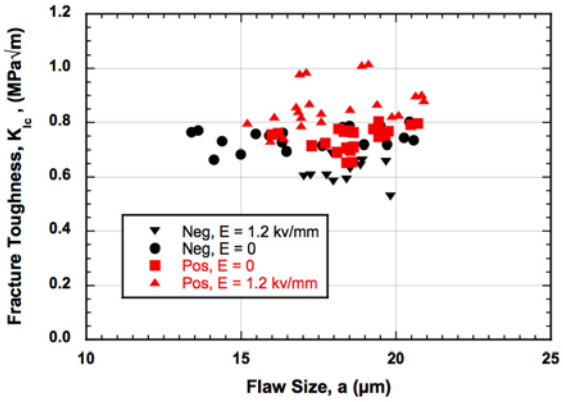

Figure 6. *Fracture toughness as a function of poled direction and electric field.*

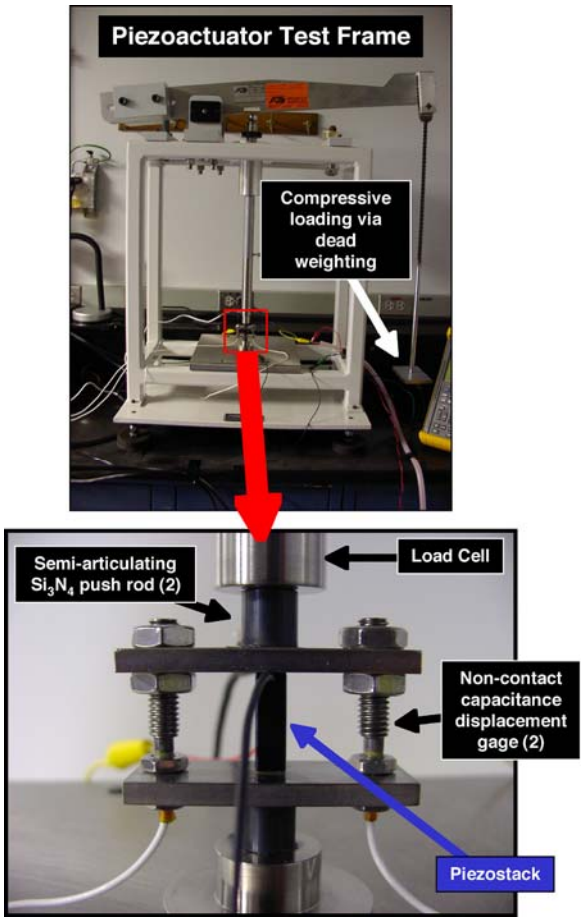

Figure 7. *Test setup that enables PMLA fatigue characterization.*

PMLA Characterization

A macromechanical test facility was constructed that enables fatigue testing of PMLAs. It is shown in Fig. 7. Independent parameters are (externally) applied compressive force, and produced voltage amplitude and waveform frequency within the PMLA. Dependent parameters are measured displacement and electrical charge, with engineering parameters strain and polarization, respectively, being calculatable. Though compressive force is applied with dead-weight loading, a load cell within the load train measures and verifies that. Two capacitance gages are used to measure axial displacement (i.e., elongation or contraction) of the PMLA.

The effect of applied compressive force or stress on piezoelectric response was first examined. Axial displacement, strain, charge, and polarization hysteresis loops for several compressive stresses are shown in Figs. 8-11, respectively. As anticipated, the applied compressive stress affects the response of all those parameters.

For future work involving the dependent parameters, new accelerated test methods will be sought where monotonically increasing compressive force (or stress) or continuously increasing magnitude of voltage or both are employed to more efficiently understand the effect of stress on PMLA response.

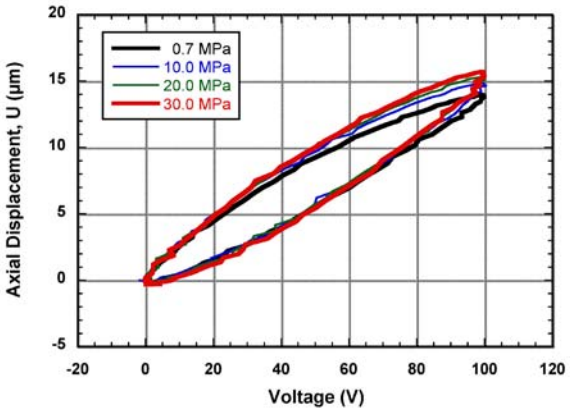

Figure 8. *Axial displacement in a PMLA as a function of applied voltage.*

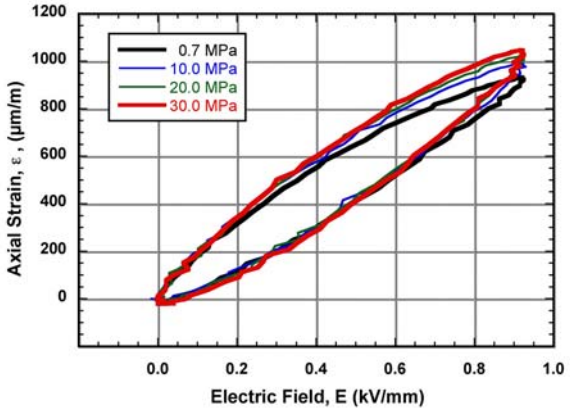

Figure 9. *Calculated axial strain in a PMLA as a function of calculated electric field.*

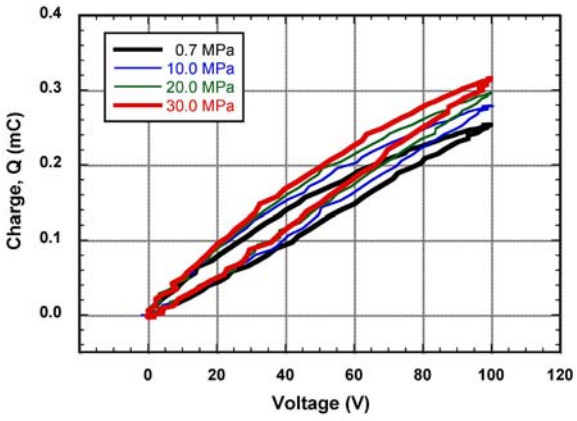

Figure 10. *Charge in a PMLA as a function of applied voltage.*

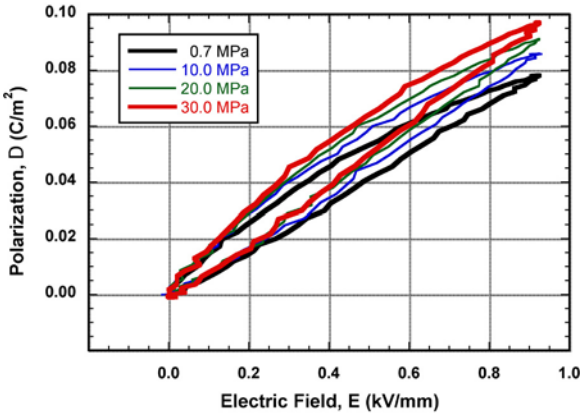

Figure 11. *Calculated polarization in a PMLA as a function of calculated electric field.*

Because the sought-after lifetime of a PMLA is 10^9 cycles, a long-term test was initiated to generate that many cycles and to identify any changes in response over that long duration. At 50 Hz, generating one-billion cycles will take ~ 5556h or ~ 8 months. The cyclic waveform is unipolar, and oscillates between 0.7 and 30 MPa of compressive stress.

Axial displacement and polarization of the PMLA are shown in Figs. 12-13, respectively. The displacement has decreased by ~5% during that time with the majority of that accruing after ~ 50 million cycles. Polarization during that same time has arguably gone unchanged. Because of that, the initial explanation for that strain decrease is believed to be due to domain wall pinning.

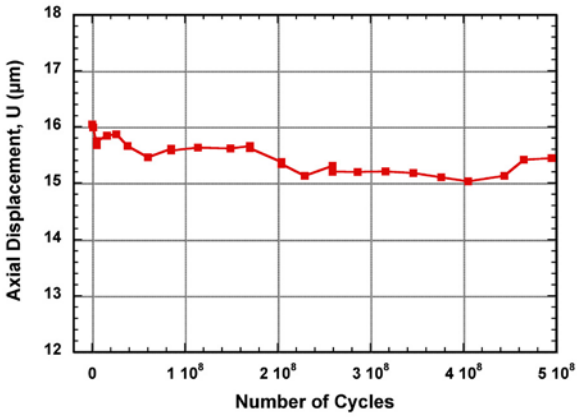

Figure 12. *Examples of piezo-stack actuators. Left is a top view, middle is a side view, and right is a stack removed from the protective.*

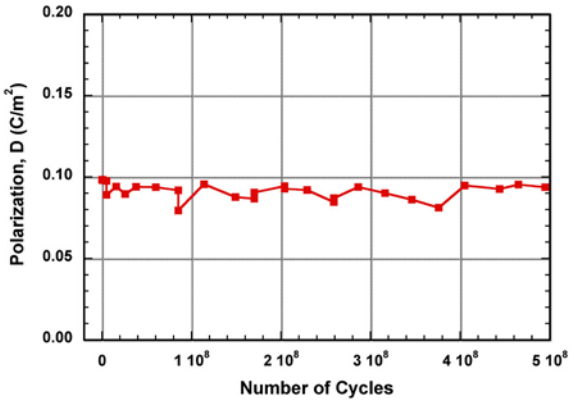

Figure 13. *Examples of piezo-stack actuators. Left is a top view, middle is a side view, and right is a stack removed from the protective.*

Primarily because of the very lengthy test durations for PMLA's, new methods of accelerated testing will be sought in FY08 that will enable fatigue characterization but at shorter times. New and additional capabilities in the test facility are planned to facilitate that.

Conclusions

Mechanical test facilities were established in FY07 to enable evaluation of PZT piezoceramics and PMLAs. Effects of electric field on mechanical strength and long-term cyclic performance were studied.

Strength of poled PZT is side dependent with negative side weakest in tension, so crack initiation is more apt to occur on the negatively poled side than on the positive side. Surface-located flaws were strength-limiters, and their size could be reduced with processing alterations.

There was ~5% strain reduction in a PMLA after about 500 million cycles with no significant loss of polarization. Because of that, the reduction may be due to pinned domain motion.

Agreement 9010 - Joining of Advanced Materials by Plastic Deformation

Principal Investigator: J. L. Routbort (co-workers: D. Singh, Cinta Lorenzo-Martin, G. Chen, and U. Leinert)
Argonne National Laboratory
9700 S. Cass Avenue
Argonne, IL 60439-4838
(630) 252-5065; fax: (630) 252-5568; e-mail: routbort@anl.gov

DOE Technology Manager: Jerry L. Gibbs
(202) 586-1182; fax: (202) 586-1600; e-mail: jerry.gibbs@ee.doe.gov

Contractor: UChicago Argonne LLC
Contract No.: DE AC03 06CH11357

Objective

- Join advanced materials such as ceramics, cermets, intermetallics, composites, biomaterials, etc. by plastic deformation, collaborate with industry and universities to produce sensors
- Investigate grain rotation that is assumed to occur during grain–boundary sliding resulting in deformation bonding

Approach

- Apply a modest compressive load to two pieces of similar or dissimilar materials that have had little surface preparation in the temperature region where the materials are known to deform by grain-boundary sliding
- Measure strength of the interface by 4-point bend tests and compare to theory
- Use electron back-scattered diffraction to measure grain rotation as a function of strain
- Perform Advanced Photon Source experiment to measure grain rotation as a function of strain
- Use technique to produce gas sensors with sealed internal references

Accomplishments

- Strong, pore-free joints have been made with various ceramics, cermets, intermetallics, composites, and more recently, biomaterials, with and without various interlayers, fracture occurs away from interface
- Published 21 journal papers, patent issued for plastic joining process, patent applications filed for oxygen sensor and joining of advanced materials
- R&D 100 Award for oxygen sensor
- Received one patent, three patent applications filed
- Completed APS experiments on $SrTiO_3$

Future Direction

- Joining metals and intermetallics to ceramics for solid-oxide fuel cell applications
- Program will be transitioned from deformation joining to application of deformation joining to produce sensors, initially concentrating on NO_x sensors.

Introduction

It has been suggested that the joining of materials by plastic deformation is the result of the grain rotation and interpenetration of the grains [1] that may result from the grain-boundary sliding (GBS) process. It is expected that if there is no cavitation and no change in grain shape, then the grains must rotate to accommodate the deformation strains [2]. However, the rotation of grains during deformation has never been investigated. Most, if not all, fine-grain ceramics deform by GBS [3,4]. Understanding grain rotation phenomenon during high-temperature deformation has implications in processing of ceramic materials with enhanced mechanical properties as well as in joining of ceramics. In the FY06 annual report we presented results on grain rotation during sequential deformation of $SrTiO_3$ using electron-backscattered diffraction. Grains rotated as much as 7° after a strain of 6%, as shown in Fig. 1. Diffraction patterns or Kikuchi bands were recorded from ≈7 specific grains [5]. However, these grains were all on the surface and certainly could not be construed to represent the behavior of an ensemble of grain in the bulk. Therefore, we have used the Advanced Photon Source at ANL to measure grain rotation in the bulk of a $SrTiO_3$ polycrystalline sample.

As a second topic in this annual report, we present results obtained by a cooperative effort by the Chemistry Department of Ohio State University and ANL on joining of aluminum-doped lanthanum strontium manganese oxide (LSAM) to YTZP. The LSAM, commonly used as a cathode in fuel cells, has been proposed as a replacement for $La_xSr_{1-x}MnO_3$ as it has been demonstrated that the Al-doping reduces the creation of interlayers formed via reaction of LSM with YTZP. Furthermore, the LSAM could be used as an interconnect in the oxygen sensor with an internal reference that was produced by plastic deformation [6]. The original interconnect was a Pt wire that was difficult to seal. Joining of the LSAM directly to YTZP would solve that problem. This work has been submitted for publication and formed part of the Ph.D. thesis of John Spirig, Chemistry Department, Ohio State University.

Grain Rotation Experiment at APS

The preparation of the polycrystalline sample has been adequately described [5]. Briefly, the $SrTiO_3$ sample has dimensions of 5x5x9 mm and an equiaxed grain size of about 6 μm. It was not possible to make diffraction measurements while undergoing compression because of equipment limitations. Hence, the sample was strained ex-situ at a rate of 10^{-5}/s at a temperature of 1250°C using laboratory equipment [5]. After an small strain increment (up to a total maximum of 2.4%) the sample was brought to the APS, and mounted as shown in Fig. 2.

The sample is mounted on a holder with three translational and one rotational degree of freedom. A Pt line was deposited and used with fluorescence so that the x-ray beam would be in the same location after each straining. The conical slit restricts the diffracted (2Θ) angle and hence the volume of the sample illuminated. The gauge is 30x30x300 μm^3 that translates to diffraction from about 1200 grains. The energy of the incident x-rays was 80.725 keV.

Measurements

At each strain a series of oscillation images was recorded. The total sample rotation range was ±60° in steps of 0.2 deg. Within this range a grain that is situated sufficiently close to the rotation axis so that it always stays within the beam (defined by the conical slit) should produce about 32 diffraction spots on the images using hkl's of 211, 220, 222, and 400. By means of the multigrain indexing software GRAINDEX, spots originating from the same grain were identified. The set of spots defines the

orientation of the grain. About 70 grains were identified at each load step.

Finding correlated grains

While the grain orientation is determined to high accuracy, no information is obtained about the spatial location of the grain (except of course that it must be in the illuminated gauge volume). Grains can be followed upon loading if the rotation is smaller than the average misorientation between the illuminated grains. Thus it is critical that (i) the loading steps and thus the grain rotations are small and (ii) the number of illuminated grains must be kept small. If the sample could be deformed in-situ in the x-ray beam then many more measurements could be taken and thus following individual grains would be significantly easier.

However, Fig. 3a demonstrates that correlated grains can be distinguished from the random misorientations of uncorrelated grains. At 0.05% strain 218 grains were identified and 231 grains after straining to 0.45%. The resulting 218*231=50358 misorientations are histogrammed in Fig. 3b. The ordinate plots the number of grain pairs with misorientations in bins of 0.1 degree. Because the orientations of the grains in the sintered sample are nearly random, the misorientation distribution for random cubic grains is observed. The maximum misorientation is 62.8 deg due to cubic symmetry. Important to the present study is the fact that the probability to find grains with small misorientation tends to zero. Zooming into small misorientations (Fig. 3a) a distinct peak is observed around 0.8°. These 64 grains do not follow the random cubic misorientation distribution and are therefore identified as identical grains. Thus, the grains identified at the individual strains can be paired. This seems realistic due to the uncertainty in repositioning the sample upon loading which results in a slight mismatch of the illuminated gauge volumes.

Evaluating grain rotations

In order to extract grain rotations the fact that the sample may be slightly tilted when repositioned in the holder after loading must be considered. The rotation of an individual grain is assumed to have two components: (i) a contribution due to sample tilt identical for all grains, and (ii) Individual grain rotations. Based on the random orientation and presumably random shape of the grains (verified by SEM) it is assumed that the individual grain rotations will have positive or negative sign with equal probability. Therefore, the average rotation of all grains is considered to be a good approximation of the contribution from sample tilt. Thus, the average rotation is calculated and subtracted from the individual grain rotations. The individual grain rotations are plotted in Fig. 3 as Rodrigues vectors. The Rodrigues vector of a rotation is given by the rotation axis unit vector times the tangent of half the rotation angle. The rotations are centered randomly around the origin from which the average rotation was subtracted. It is seen that the individual grains typically rotate only by ± 0.002 rad = 0.1 deg for a strain increment of 0.4%. This is a small rotation and includes the experimental uncertainty. Therefore, an upper limit of the grain rotations of about 0.25 deg per 1% deformation can be made. The rotation axes seem randomly distributed but further analysis is required. That analysis will include more strain steps.

However, these results are in full accord with those reported by the electron-back scattered diffraction experiments [5] and for the first time prove that grain boundary sliding is accompanied by grain rotation. This fully supports the idea that grain rotation and interpenetration is responsible for the excellent joints that are formed by plastic deformation in the grain-boundary sliding regime.

Joining of Aluminum-doped Lanthanum Strontium Manganese Oxide with Tetragonal Zirconia

Experimental

LSAM powder was synthesized via the solid-state method. Nitrates of La, Sr, and Al (Alfa Aesar) were mixed with the chloride of Mn (Alfa Aesar) in the stoichiometric ratio of La:Sr:Al:Mn, 0.8:0.2:0.9:0.1. The powder mixture was milled (SPEX 5100) at high speed for five minutes and transferred to a covered platinum crucible. The powder mixture was reacted at 1000°C in air for four hours and ground in an agate mortar and pestle upon cooling. Following grinding, the powders were calcined at 1200°C for fifty hours to ensure complete reaction. Thereafter, the powder was pressed at 3000 kg into 1.1 cm^2 pellets and fired in a covered platinum crucible at 1500°C for fifty hours to densify the powders into a pellet suitable for joining. Densified pellets were briefly ground to planarize the mating surfaces.

The YTZP wafers were cut from preformed and densified rods/tubes of 3 mol % yttria-stabilized tetragonal zirconia polycrystals (YTZP, average particle size ~0.4 μm). A pellet of LSAM was deformed at a strain rate of 4.5 x 10^{-5} s^{-1} to determine the yield stress of the perovskite at 1250°C. After the yield stress of the LSAM was determined, YTZP/LSAM sandwiches were compressed in a static argon atmosphere at either 1250 or 1350°C at crosshead speeds ranging from 0.01 mm/min to 0.02 mm/min resulting in strain rates of 4.5 x 10^{-5} s^{-1}. Results are shown in Fig. 5.

Results

Microstructure of Joining Planes

SEM micrographs of the joint produced at and 1350°C at two different magnifications are presented in Fig. 6. As there are two distinct materials, the joining planes are clearly distinguishable from the bulk ceramics (indicated by arrows in each image). The samples exhibited some native porosity. A high-resolution SEM image of the joint produced at 1250°C is presented in Fig. 7. Some cracks were observed, but because they were away from the joining plane, they are believed to be introduced after joining by the sectioning process.

Raman Microscopy

Raman maps along the joining plane between YTZP and LSAM are presented in Fig. 8. The scanned regions are presented within the view from the 50x objective so the joining plane is clearly visible. In this manner, it is possible to determine the extent to which the LSAM phase reacted with the YTZP. The laser was line-focused to a 1 x 32 μm^2 illumination area and moved across the joining plane in 0.5 μm increments in the x-direction and 1.056 μm increments in the y-direction. In the samples joined at 1250 and 1350°C, the sizes of the scanned areas were 67 x 32 μm and 37 x 62 μm, respectively. The large area marked in green in Fig. 8 is a ≥90% match to the YTZP control. The representative spectrum of the green region is shown in Fig. 8a. The large region on the right marked in red is a ≥90% match to the LSAM control. The representative spectrum of the red region is shown in Fig. 8c. Within the bulk of the red region, dark spots represent islands of poor comparisons. These result from the mismatch with the control LSAM sample. The joining plane is the narrow region sandwiched between the green-labeled YTZP bulk and red-labeled LSAM bulk. This region is marked as JP and designated as the thin black area between the arrows in Fig. 8. Raman spectra from the joining plane exhibit features of YTZP and LSAM. The representative spectra from this region are shown in Fig. 8b. No new Raman peaks were observed that indicate absence of any new phases in the joining plane.

Conclusion

$La_{0.77}Sr_{0.20}Al_{0.9}Mn_{0.1}O_3$ exhibits plasticity in the same temperature and stress regime as YTZP, allowing for the creation

of pore-free joints via a lower-temperature alternative to diffusion bonding. Electron microscopy of the joining planes indicate that even though residual porosity of the LSAM persists through the joining process, the grains at the mating points of each surface have intermingled, likely as a result of simultaneous grain-boundary sliding. The high aluminum content of LSAM inhibits reaction with YTZP and therefore the production of interlayers that would serve to diminish the quality of the joint. This is confirmed by the absence of new bands in the Raman spectral maps of the bulk material and joining planes. By choosing a composition of LSAM that does not react with YTZP, it is possible to create joints between these two dissimilar materials without an intermediate bonding agent or compositionally graded interlayer.

Future Directions

Back-scattered electron diffraction and microdiffraction using high-intensity x-rays from the APS have conclusively demonstrated that grains rotate while undergoing grain-boundary sliding in $SrTiO_3$. These results, combined with SEM observations, have substantiated the assumption that deformation joining is the result of the grain rotation and interpenetration of grains. This highly successful program has resulted in 21 papers in peer-reviewed journals, one patent, three patent applications filed, an R&D 100 award, one Ph.D. (Ohio State), and negotiations for licensing the technology are in progress. We have demonstrated that one can create pore-free, gas-tight, strong joints in a wide variety of materials that deform by grain-boundary sliding. This project will be transitioned at the end of FY08. Future work will concentrate on the construction of miniature gas sensors (particularly NO_x) using the deformation joining technique to produce gas-tight seals for the internal reference metal/metal-oxide.

References

1. F. Gutierrez-Mora, A. Dominguez-Rodriguez, J. L. Routbort, R. Chaim, and F. Guiberteau, "Joining of Yttria-tetragonal Stabilized Zirconia Polycrystals using Nanocrystals," Scripta Mater. **41** 455-60 (1999).
2. M. F. Ashby and R. A. Verrall, "Diffusion-Accommodated Flow and Superplasticity," Acta Metall. **21** 149-163 (1973).
3. W. R. Cannon and T. G. Langdon, "Creep of Ceramics – 1. Mechanical Characteristics," J. Mater. Sci., **18** [1] 1-50 (1983).
4. F. Gutierrez-Mora, K. C. Goretta, S. Majumdar, J. L. Routbort, M. Grimdisch, and A. Domínguez-Rodriguez, "Influence of Internal Residual Stresses in Superplastic Joining of Zirconia Toughened Alumina," Acta Mater. **50** 3475-3486 (2002).
5. D. Singh, M. Lorenzo-Martin, F. Gutierrez-Mora, and J. L. Routbort, "High-temperature Deformation Behavior in $SrTiO_3$ Ceramics, J. European Ceramic Soc. **27**, 3377-3384 (2007).
6. J. V. Spirig, R. Ramamoorthy, S. Akbar, J. L. Routbort, D. Singh, and P. K. Dutta, "High-temperature Zirconia Oxygen Sensor with Sealed Metal/Metal Oxide Internal Reference", Sensors and Actuators B **124**, 192-201 (2007).

ACRONYMS

APS: Advanced Photon Source
GBS: Grain–boundary sliding
EBSD: Electron back–scattered diffraction

Figures for FY07 Annual report on Joining

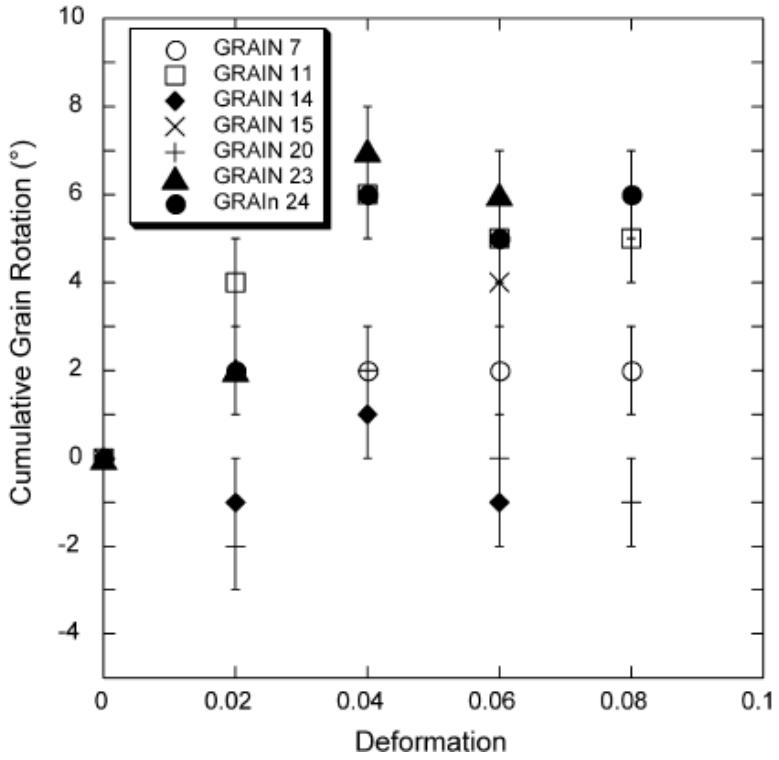

Figure 1. Cummulative grain rotation of seven surface grains as a function of strain in $SrTiO_3$ deformed at 1280°C and 5 x 10^{-6}/s.

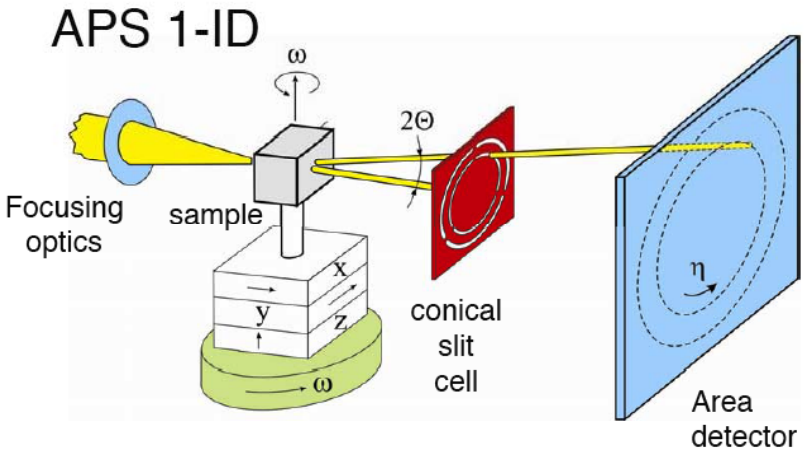

Figure 2. Experimental setup for measuring grain rotation as a function of strain.

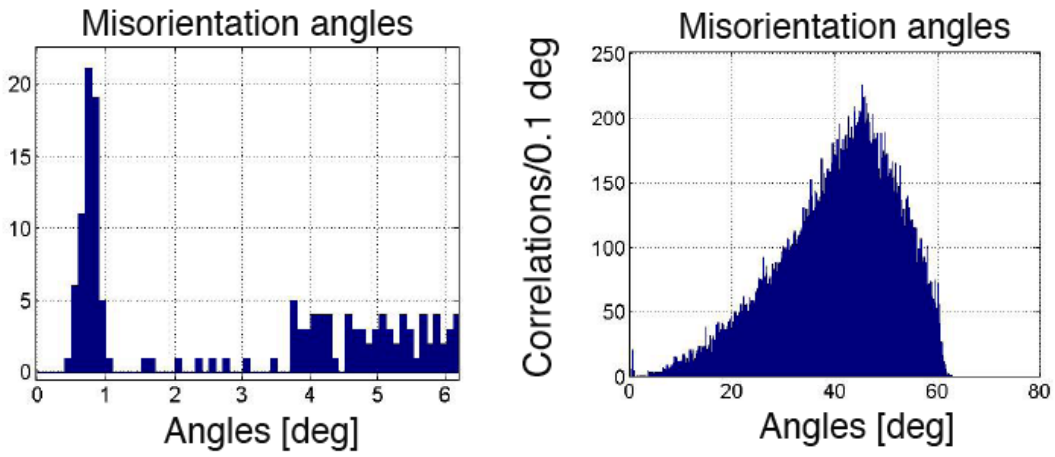

Fig.3. Misorientation angles after straining from 0.05% to 0.45%. Sixty-four grains have been correlated and tracked.

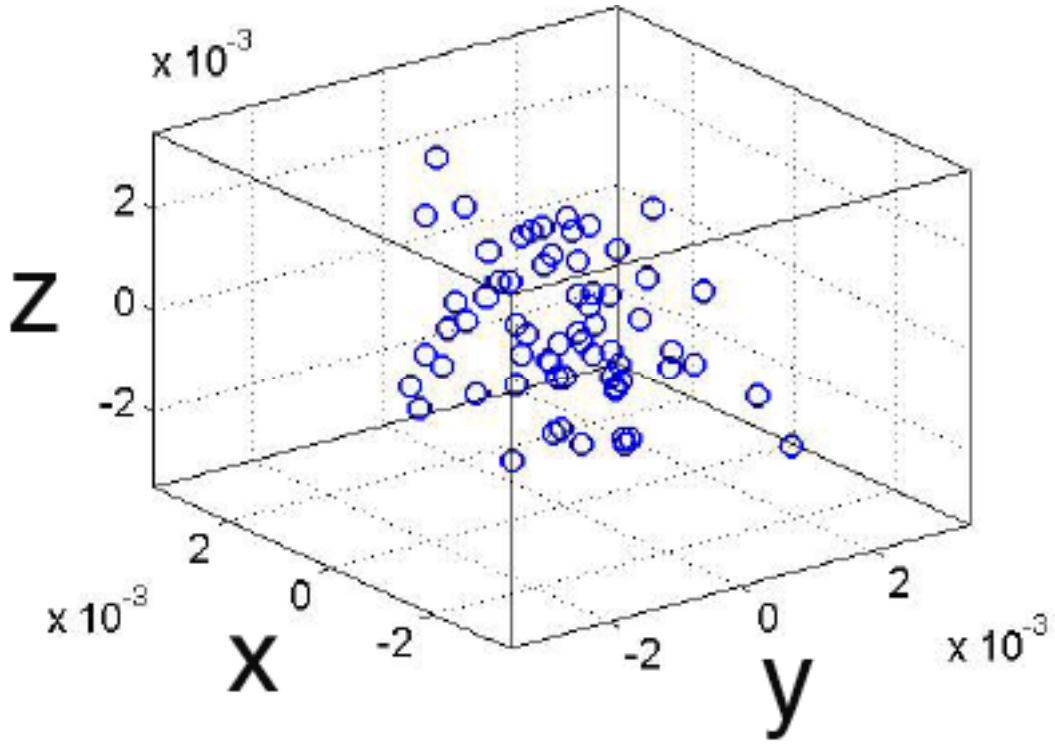

Figure 4. Misorientations in Rodriguez space.

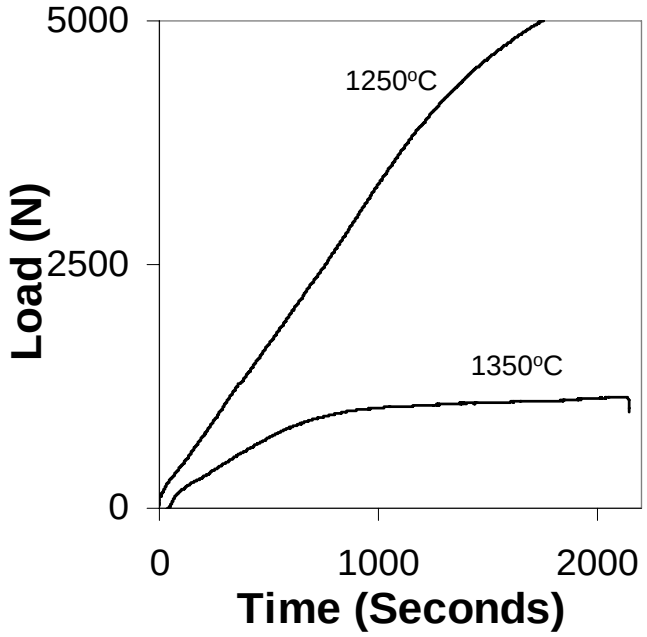

Figure 5. Load versus time curve for $La_{0.77}Sr_{0.20}Al_{0.9}Mn_{0.1}O_3$ sandwiched between wafers of YTZP at 1250 and 1350°C.

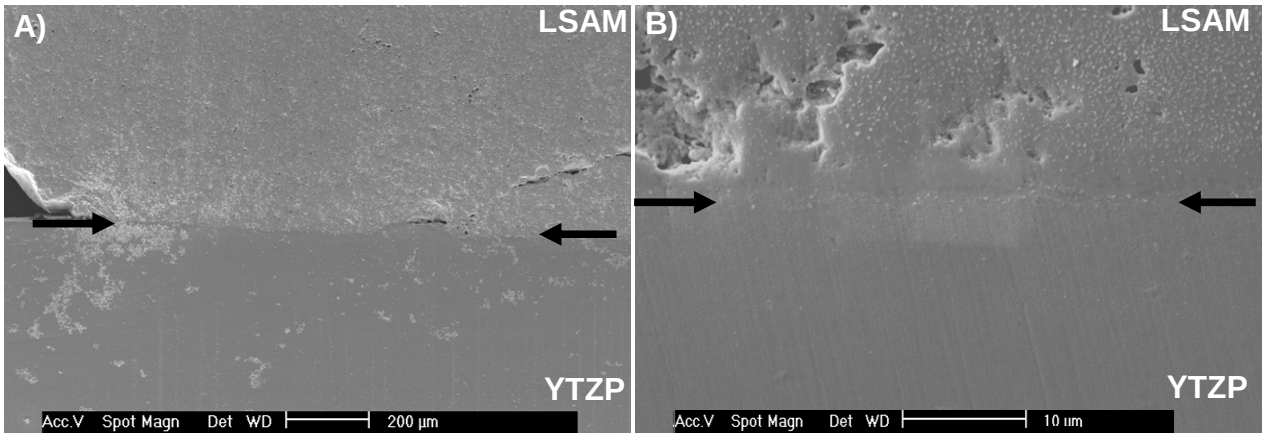

Figure 6. Joining plane of $La_{0.77}Sr_{0.20}Al_{0.9}Mn_{0.1}O_3$ joined to YTZP at 1350°C. Arrows denote the joining plane. A) Wide view of joint. B) The same joint viewed at higher magnification exhibits that a joint was created even though the material is not fully dense.

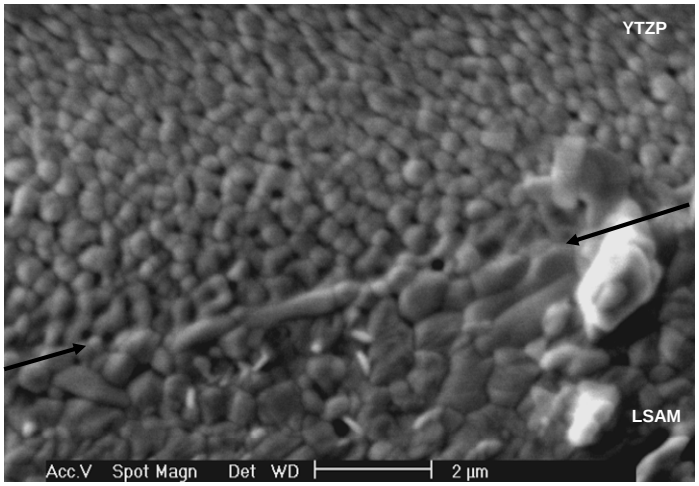

Figure 7. High-resolution SEM of the joining plane in YTZP/LSAM/YTZP joined at 1250^{o}C.

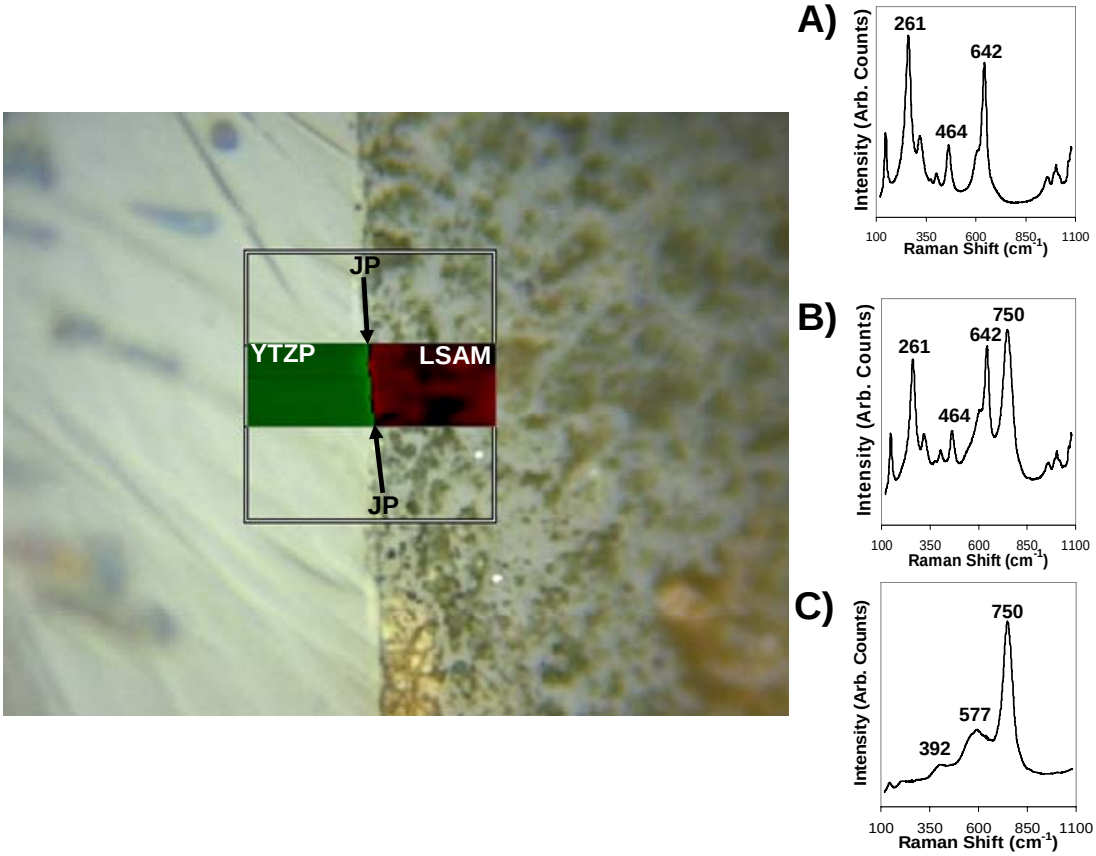

Figure 8. Raman map of YTZP/$La_{0.77}Sr_{0.20}Al_{0.9}Mn_{0.1}O_3$/YTZP interface in sample joined at 1250^{o}C. The joining plane is the narrow region denoted as JP that lies between the bulk of YTZP and LSAM. A) Representative spectrum of the YTZP region marked in green. B) Representative spectrum of the joining plane denoted by arrows. C) Representative spectrum of the LSAM region marked in red.

Agreement 13332 – Friction and Wear Reduction in Diesel Engine Valve Trains

Peter J. Blau
Oak Ridge National Laboratory, P. O. Box 2008, Mail Stop 6063
Oak Ridge, TN 37831-6063
(865) 574-5377; fax (865) 574-6918; e-mail: blaupj@ornl.gov

DOE Technology Manager: Jerry L. Gibbs
(202) 586-1182; fax: (202) 586-1600; e-mail: jerry.gibbs@ee.doe.gov
ORNL Technical Advisor: D. Ray Johnson
(865) 576-6832; fax: (865) 574-6098; e-mail: johnsondr@ornl.gov

---

Contractor: Oak Ridge National Laboratory, Oak Ridge, TN
Prime DOE Contract Number DE-AC05-00OR22725

Objectives

- To enable the application of next-generation diesel engine materials by developing test methods which simulate the mechanical, thermal, and chemical environments of wear-prone engine parts, like exhaust valves and exhaust gas recirculation (EGR) systems.

- To characterize the friction and wear of promising new engine component materials, surface treatments, composites, and coatings with the goal of understanding the scientific basis for their performance in severe environments, and providing guidance for the selection of new, more durable engine materials.

Approach

- Working with U.S. diesel engine manufacturers, identify components that require durability and low friction in order to improve propulsion system energy-efficiency and reduce emissions. Such components include piston rings and cylinder materials, wastegate bushings for exhaust gas recirculation (EGR) components, fuel injector plungers, and valve and valve seat materials.

- Develop test methods, data analysis methodology, and models to evaluate and quantify the performance of candidate materials under simulated use conditions.

- Investigate and understand the characteristics of friction and wear transitions that affect the lifetimes of materials in wear-critical applications like valve trains.

Accomplishments

- In prior years, we designed a high-temperature oscillatory scuffing test system that operates at EGR wastegate bushing temperatures (~ 600 – 700^{o}C). This apparatus was used to evaluate a range of metallic alloys, ceramics, and hard-facings to determine which had the best durability under high-temperature conditions. It is now part of the Tribology User

Center in the High Temperature Materials Laboratory at ORNL and has been used to support user projects with both an engine company and a valve material supplier.

- Developed a novel, 'pin-on-twin' scuffing test to evaluate fuel injector materials in diesel fuel and low sulfur fuel environments, and used the method to develop scuffing transition diagrams and a general model for scuffing of engine components.

- Presented a general review of engine component scuffing and modeling at the 13th Diesel Engine-Efficiency and Emissions Research Conference in August 2007.

- Designed a high-temperature exhaust valve wear testing system to investigate the combined influences of repetitive impacts, elevated temperatures, and gaseous environments on the durability of candidate valve and seat materials. Conducted initial experiments to verify its operating characteristics and to prepare for studies of advanced valve materials in FY 2008.

Future Directions

- Employ the new high-temperature valve wear tester to support the development of more durable exhaust valve materials for advanced, energy-efficient diesel engines.

- Participate in and lead the development of an ASTM standard test method for evaluating the wear performance of piston ring and liner materials. A previous standard, ASTM G181 for friction of piston rings and liners, was developed with support from the Department of Energy. This new companion standard for wear can be used to study the effects of both conventional and alternative fuels on diesel engine component durability.

Introduction

The diesel engine industry faces the important challenge of improving fuel efficiency while meeting increasingly strict emissions regulations. These challenges are being addressed by modifying engine designs, introducing homogeneous combustion, designing advanced control systems, and using exhaust gas after-treatments. Such modifications affect the mechanical, thermal and chemical environments in which the engine materials must operate, and currently-used materials may fall short of meeting these needs. New materials or engineered surfaces are needed to enable new technological goals.

The objective of this effort is to enable the selection and use of durable, lower-friction moving parts in diesel engines for heavy vehicle propulsion systems through the systematic evaluation of promising new materials, surface treatments, composites, and coating technologies. The underlying approach involves developing simulative test methods, analyzing microstructures of candidate materials, developing design maps with variables like surface finish and frictional behavior, and modeling the damage process itself.

In prior years, the focus of this effort was on wastegate bushings for exhaust gas recirculation (EGR) systems and fuel injector plungers that must operate in low sulfur fuels. A variety of materials was evaluated using specially-designed tests to simulate the operating environment of the components, and data that compared traditional materials with potential replacement materials was analyzed and shared with industry. For example, computer-based techniques for measuring the onset of scuffing damage were developed, as was a model to describe the progression of surface damage under

boundary-lubricated sliding. This work resulted in seven publications.

In FY 2006 the focus of this effort was redirected to address the selection and use of materials for the demanding environment of diesel engine exhaust valves, where temperatures can reach over 850°C. In order to address this challenge, a new apparatus was designed to investigate candidate valve materials, surface treatments, and coatings under conditions that reasonably simulate their performance in engines. Construction of the apparatus was completed in the first quarter of FY 2007 and preliminary tests were run.

Also during 2007, studies and analysis of engine durability issues like scuffing and piston ring wear continued. The former resulted in a presentation at the DOE Diesel Engine Efficiency and Emissions Reduction Conference, and the later work is leading to a new ASTM test method.

Approach

Valve material durability. The approach to addressing exhaust valve durability has involved: (a) defining the operating environment and modes of surface damage experienced by diesel engine exhaust valves, (b) designing and building an exhaust valve testing system, (c) conducting tests to compare current valve materials with candidate alternative materials and surface treatments, and (d) providing an assessment of the candidate materials' response to engine manufacturers and designers.

During FY 2006-7 a high-temperature, repetitive impact (HTRI) testing system, was constructed based on a consideration of the damage modes that exhaust valves and valve seats experience. In designing the HTRI, it was desirable to be able to test not only simple test coupons, but also actual diesel engine valves. A schematic diagram of the apparatus is shown in Figure 1. Certain details, like the loading system and controls, have been omitted for clarity. Symbol "A" shows the location of the test specimen holder inside an environmental chamber "B", which in turn is surrounded by a custom-built tube furnace "C." The lower specimen is actuated by a cam drive "D" and a variable-speed motor "E." Gas feed-throughs, labeled "F" and "G," control the environment in the test chamber. Water cooling is supplied to critical components at the top and bottom of the furnace chamber

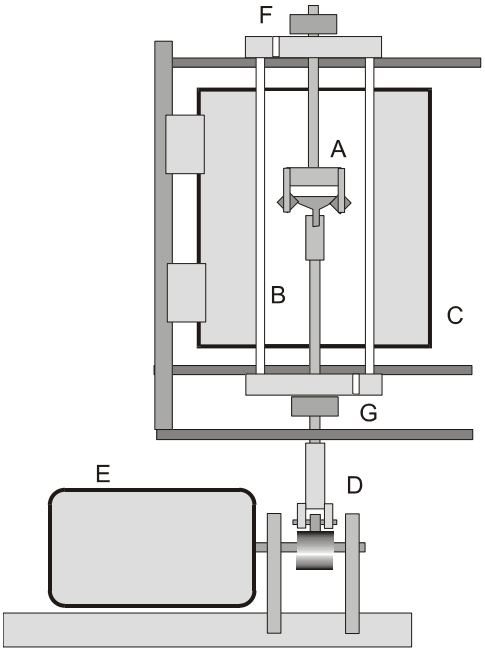

Figure 1. *Schematic representation showing the major parts of the HTRI.*

Several production-grade diesel engine exhaust valves were provided by Caterpillar Corporation to aid in the design of the holders so they would fit commercially-sized exhaust valves. The clearances in the specimen holders were made large enough to accommodate a range of valve diameters and bevel sizes. Previous room temperature tests with repetitive impacts on ceramics indicated the most severe wear occurred when the impact angle was 45 degrees. Therefore, the initial HTRI experiments were performed with a holder inclined at that angle.

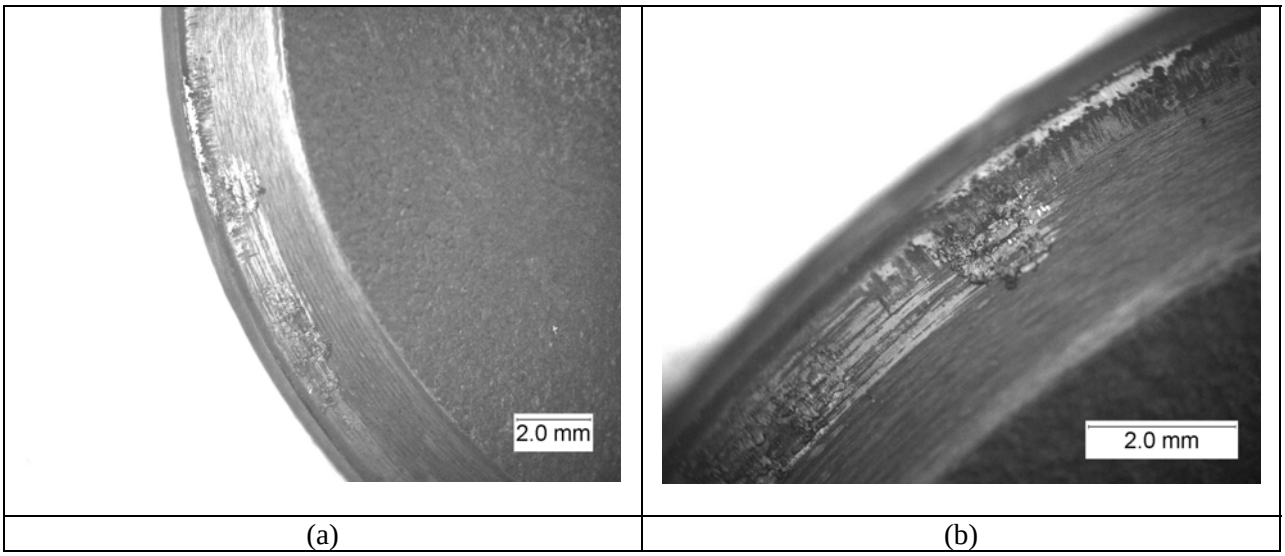

Figure 2. *Close-up views of a commercial diesel exhaust valve subjected to 20,000 impacts at 800°C in the HTRI. Significant micro-welding, plastic deformation, and material transfer are indicated.*

Figure 2 shows the wear damage produced on a commercial exhaust valve material subjected to 20,000 repetitive impacts at 800°C. In FY 2008, more experiments of this kind will be conducted and the results compared with worn valves from engines to establish the ability of the HTRI to simulate service failures.

Following the baseline tests, newly proposed valve and insert materials will be selected, evaluated, and ranked in order of their potential to improve durability. The mechanisms by which the surfaces of those materials degrade will be studied and used to develop a better rationale for the design and selection of engine materials for extreme environments.

Progress on Wear Test Methods and Standardization. Participation continues with ASTM Committee G2 on Wear and Erosion to advance the development of standards for wear testing of engine materials. In the past this work has led to the approval of ASTM G 181, a method for measuring the friction of piston ring and cylinder liner materials in used oil environments. Work will continue in FY 2008 to extend that activity to wear. That will involve coordinating a series of inter-laboratory wear tests with industrial participants. Such studies are necessary to establish the repeatability of the new test.

Summary and Conclusions

- A repetitive-impact diesel engine valve material testing system that operates at temperatures in excess of 800°C has been designed and constructed. Initial tests have been run, but additional baseline tests are needed.

- Once baseline tests are completed in FY 2008, it will be possible to test a wide variety of candidate exhaust valve materials, including novel coatings and surface treatments. These tests will be initiated in conjunction with industry partners such as Caterpillar Inc.

- Work is continuing toward providing the diesel engine industry with a new ASTM standard for measuring the wear of new materials for piston rings and cylinder liners.

Publications/Presentations

1) P. J. Blau* (2006) "The Origins of Subsurface Layers below Tribological Contacts: A Historical Perspective on Research and Understanding" Invited presentation, ASM International Materials Science and Technology Week, Cincinnati, October 15-19, 2006.

2) P. J. Blau served as co-chairman and co-editor, with S. J. Shaffer of Battelle Memorial Institute, of the ASTM "Symposium on Friction and Wear Test Methods for Coatings and Surface Treatments," held on June 21, 2007, in Miami Beach, FL Proceedings are being published in Journal of ASTM International.

3) P. J. Blau (2007) "Scuffing: From basic understanding to engine materials testing," Diesel Engine Efficiency and Emissions Research (DEER) Conference paper, Detroit, August 12-16, 2007.

Agreement 9089 - NDE of Diesel Engine Components

Jiangang Sun
Argonne National Laboratory
9700 South Cass Avenue
Argonne, IL 60439
630-252-5169; fax: 630-252-2785; e-mail: sun@anl.gov

DOE Technology Manager: Jerry L. Gibbs
(202) 586-1182; fax: (202) 586-1600; e-mail: Jerry.gibbs@ee.doe.gov
ORNL Technical Advisor: D. Ray Johnson
(865) 576-6832; fax: (865) 574-6098; e-mail: johnsondr@ornl.gov

Contractor: Oak Ridge National Laboratory, Oak Ridge, Tennessee
Contract No.: DE-AC05-00OR22725
Subcontractor: Argonne National Laboratory, Argonne, Illinois

Objectives

- Develop laser-scattering and other nondestructive evaluation (NDE) technologies for detection and characterization of defect and damage in diesel-engine valve-train components made from advanced materials such as ceramics and intermetallics.
- Develop quantitative NDE analysis methods to identify strength-limiting flaws, evaluate damage evolution/growth, and predict mechanical properties for advanced materials.

Approach

- Develop fast and reliable automated laser-scattering NDE systems for surface/subsurface inspection of Si_3N_4 ceramic and TiAl intermetallic engine valves.
- Analyze NDE image data to determine the level of machining damage and accumulated damages in engine valves from bench and engine tests.
- Correlate NDE data with microstructure and strength of advanced materials to establish NDE capability for predicting failure initiation defects and mechanical properties.

Accomplishments

- Completed NDE inspection of 10 Si_3N_4 and 4 TiAl natural-gas engine valves after 500-h engine test.
- Inspected stem surface of 10 ceramic engine valves after engine-test failure due to a failed valve-groove keeper. Considerable scratch/impact damage was detected in the subsurface of the valve stems.
- Established sensitivity for 3D subsurface imaging of optically translucent ceramics using high-resolution cross-polarization confocal microscopy and optical coherence tomography (OCT).

Future Direction

- Complete NDE evaluation for subsurface damage in engine-tested ceramic and TiAl valves.
- In collaboration with Caterpillar and ORNL, correlate NDE data with mechanical properties derived from destructive analyses of the engine-tested valves.
- Develop/evaluate advanced NDE technologies including optical confocal and OCT, thermography, ultrasonics and x-ray imaging for evaluation of advanced materials for diesel engine components.

Introduction

Advanced ceramics and intermetallics are leading candidates for high-temperature engine applications that offer improved fuel efficiency and reduced emissions. Among them, silicon nitrides (Si_3N_4) and titanium aluminide (TiAl) are being evaluated as valve-train materials for diesel and natural gas engines because of their lighter weight, high strength and corrosion resistance at elevated temperatures. However, these brittle materials are susceptible to microscopic defect/damage within a thin subsurface, which may significantly degrade their mechanical properties. Material damage in the subsurface may be induced by machining or from service due to impact, wear, and corrosion. For silicon nitrides, material strength may also be limited by inherent defects such as voids and porosities within subsurface. To detect and characterize these defects, Argonne National Laboratory (ANL) has developed several laser-based NDE methods for these materials. The objective of this research is to demonstrate that these methods can be used to assess/evaluate the cost-effectiveness and reliability of valve-train components manufactured from advanced ceramic and intermetallic materials for diesel engines. The primary effort in FY 2007 was to utilize a fast NDE valve-scan system to evaluate SN235P Si_3N_4 and TiAl valves after 500-hour and at end of an engine duration test. Another effort was directed on continued development of cross-polarization confocal microscopy and on evaluation of optical coherence tomography (OCT) for high-spatial-resolution 3D subsurface imaging of translucent materials such as ceramics. This research is collaborated with Caterpillar, Inc.

Approach

The critical region for brittle ceramic and intermetallic components in structural applications is near surface. The common types of defects in this region are mechanical, such as cracks, spalls, inclusions, and voids. The size of the defects that limits the component strength is generally small, say <100 µm. To detect these defects, ANL developed an optical NDE method based on cross-polarization detection of optical scattering originated from surface and subsurface discontinuities (i.e., defects). Because ceramics are partially translucent to light, optical penetration can reach the subsurface to directly interact with the subsurface defects. For metallic or intermetallic materials, optical penetration is not possible. However, cross-polarization detection eliminates optical reflection from smooth surface and extracts only optical scattering from rough or cracked surface features. By scanning the entire surface (flat or curved) of a component and constructing a two-dimensional (2D) scatter image, surface/subsurface defects can be readily identified as they exhibit excessive scattering over the background, and their type and severity may be analyzed. To apply this technology for NDE of engine valves, ANL has developed an automated laser-scatter system for scanning the entire valve surface with high spatial resolutions (10 or 5 µm). The resulting 2D scattering image data are used to identify the location, size, and relative severity of subsurface defects/damages.

NDE development may also lead to quantitative prediction of mechanical properties for advanced materials and components. For advanced ceramics, although many parameters (e.g., residual stress[1]) are known to affect material strength, the most important parameters are likely the characteristics of individual flaws that cause the initial failure. These characteristics, such as flaw size and depth, can be determined from 3D NDE imaging methods such as confocal microscopy and OCT. For metallic materials, other NDE methods such as thermography and ultrasonic and x-ray imaging may be used to determine these characteristics. By combining NDE data with life-prediction analysis tools, quantitative prediction of the strength and lifetime of diesel engine components may become more realistic.

Results

NDE Characterization of Si_3N_4 and TiAl Valves after 500-h Engine Test

Ten Si_3N_4 and four TiAl valves were run successfully for 500 hours in a Caterpillar natural-gas G3406 generator set at the National Transportation Research Center (NTRC). Of the 10 Si_3N_4 valves, 6 were intake valves (identified by I) and 4 were exhaust valves (identified by E); while all TiAl valves were exhaust valves. Figure 1 shows a photograph of these valves, including two standard steel valves I14 and I16. For these valves, the combustion coating deposited on the valve surface during the engine test has been mostly cleaned

before the NDE examination. The impact area is not entirely within the conical contact surface; it lies around the edge between the contact surface and the fillet surface, as illustrated in Fig. 2.

Figure 1. Photograph of 500-h engine-tested Si_3N_4 and TiAl valves.

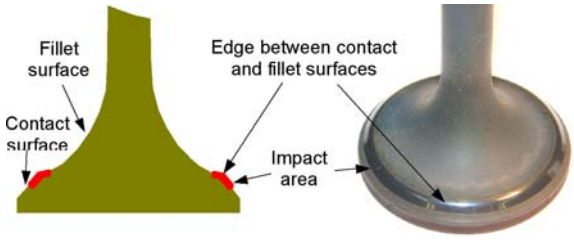

Figure 2. Location of impact area on valve surface.

Laser-scatter NDE scans of the valve-head surface for all valves were conducted. Typical results for Si_3N_4 intake, Si_3N_4 exhaust, and TiAl exhaust valves are presented and discussed below. Figure 3 shows the laser-scatter image of the Si_3N_4 intake valve I2 after the 500-h engine test. The scatter intensity in the impact area is slightly lower than that in the fillet and stem surface. Because subsurface damage always exhibits higher laser-scatter intensity, low scatter intensity in the impact surface is an indication of surface contamination. Within the impact area, shown in the enlarged NDE image in Fig. 3, no apparent subsurface damage was detected. The stripe pattern in the stem surface is due to the surface coloration variation.

Figure 4 shows the laser-scatter image of the Si_3N_4 exhaust valve E1 after the 500-h engine test. Within the impact area, shown in the enlarged NDE image, many horizontal narrow bands of lower scatter intensity are detected. In addition, three wider bands of lower intensity are also observed, which were present in the NDE data from the 100-h engine test[2]. Because a lower laser-scatter intensity does not indicate subsurface damage, the complex NDE indications detected within the impact area should represent severe surface wear, not subsurface damage such as cracks or spalls.

Figure 5 shows the laser-scatter image of the valve-head surface of TiAl exhaust valve E9 after the 500-h engine test. The scatter intensity in this image is scaled logarithmically in order to suppress the strong scatter from the coating on the fillet and stem surfaces. Two types of damage indications were observed from the NDE data. First, the impact region exhibits considerable wear damage represented by distributed bands of high and low scatter intensities over the entire impact region. Second, many low scatter-intensity spots with sizes up to ~0.5 mm were detected within the impact region (see enlarged image in Fig. 5). Low scatter intensity from TiAl surface is usually an indication of a much rougher surface. These results suggested that the impact damages in TiAl valves were more severe than those observed in the Si_3N_4 valves.

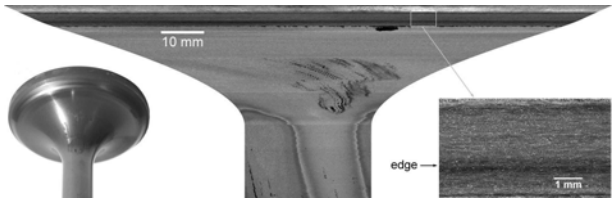

Figure 3. Laser-scatter scan image of Si_3N_4 intake valve I2 after 500-h engine test.

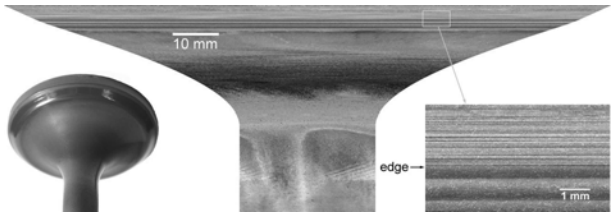

Figure 4. Laser-scatter scan image of Si_3N_4 exhaust valve E1 after 500-h engine test.

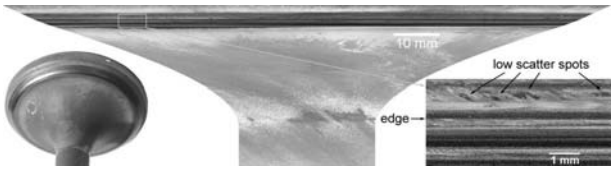

Figure 5. Laser-scatter scan image of TiAl exhaust valve E9 after 500-h engine test.

Figure 6 shows photomicrographs of impact surfaces of the Si_3N_4 intake valve I2, Si_3N_4 exhaust valve E1, and TiAl exhaust valve E9 after the 500-h engine test. For intake valve I2, the machining surface mark has been worn off due to a "polishing" wear effect. The worn surface appears to be rough, making it susceptible for surface contamination as indicated from the NDE data (see Fig. 3). For exhaust valve E1, the impact surface displays considerable polishing wear and nonuniform wear

damage represented by narrow ridges and grooves that were detected in the NDE data (Fig. 4). It is unclear how these ridges/grooves were generated. For TiAl exhaust valve E9, however, several small "indents" and a large (~0.5 mm) "pit" (from a spalled chip?) are observed. The pit surface appears rough, which accounts for the lower scattering intensity from the spots detected in the NDE data (see Fig. 5). In addition, several wear grooves are observed in the impact surface of the TiAl valve. In general, the micrographic observations of these valves are consistent with those detected by the laser scatter NDE.

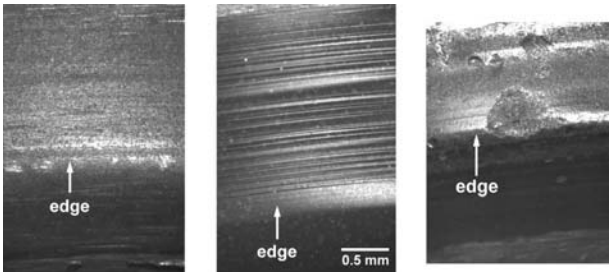

Si_3N_4 intake I2 Si_3N_4 exhaust E1 TiAl exhaust E9

Figure 6. Photomicrographs of impact surfaces of Si_3N_4 and TiAl valves after 500-h engine test.

NDE Characterization of Ceramic Valve Stem Surfaces at End of Engine Duration Test

After NDE examinations of the 500-h engine-tested ceramic and TiAl valves, 10 ceramic and 4 TiAl valves were reinstalled inside the G3406 generator set at NTRC for the final phase of 500-h engine test. However, on June 20, 2007, after 55 hours at full load operation, an intake valve located in Cylinder 6 (#22) failed, causing the rest of the valves in that cylinder being destroyed[3]. The ceramic pieces were also sucked into other cylinders and damaged other ceramic and TiAl valves. The failure was later identified to be due to a worn valve-groove keeper that allowed the ceramic valve to be dropped inside the cylinder and crashed with the piston. As a result, the engine test was ended. The Si_3N_4 and TiAl valves were removed from the engine for NDE analyses at ANL and destructive analyses at ORNL. Figure 7 shows a photograph of the Si_3N_4 valves; note that the damaged valve head for all valves in Cylinder 6 has been removed before the NDE examination.

Figure 7. Photograph of Si_3N_4 engine valves at end of engine duration test.

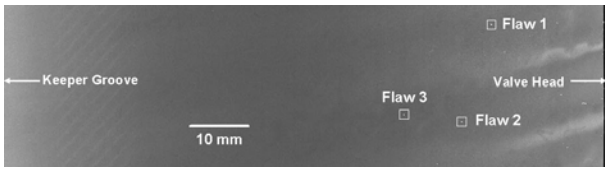

Figure 8. Laser-scatter scan image of stem surface of Si_3N_4 intake valve Cyl6-I#22.

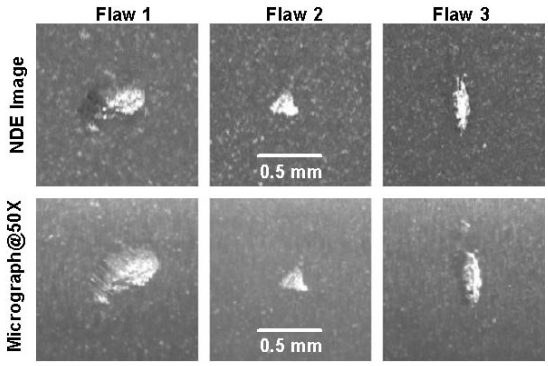

Figure 9. Detailed laser-scatter NDE images and photo-micrographs of 3 flaws marked in Fig. 8.

Laser-scatter NDE scans were performed on the stem surface of all Si_3N_4 valves. Figure 8 shows the scan image of an 11 cm-long stem surface of the Si_3N_4 intake valve I#22, which was the initially failed valve. The NDE data did not indicate any large-scale damage such as large cracks on the stem surface of this and all other valves. However, many smaller surface/subsurface damages were detected within a distance of more than 7 cm from the base of the fillet surface. Three such damages were marked in Fig. 8. Figure 9 shows the detailed NDE images and photomicrographs of these damages. It is apparent that Flaws #1 and #3 were scratch damages and Flaw #2 was an impact-chipping damage. These damages have penetrated substantially into the subsurface and could have significantly degraded the component strength.

Cross-Polarization Confocal Microscopy of 3D Subsurface Microstructure in Silicon Nitrides

Three-dimensional imaging of detailed subsurface microstructure can directly determine the characteristics of subsurface flaws (e.g., size, depth and orientation of cracks) in advanced ceramics. Because mechanical properties of brittle ceramics are sensitive to subsurface microstructure, measured flaw characteristics may be used to predict material's mechanical properties such as strength. To achieve 3D subsurface imaging with high spatial resolutions, ANL developed a cross-polarization confocal microscopy technology in FY 2006[2], which was further improved in FY 2007.

Previous tests demonstrated that, with a moderate 40X objective lens at an optical wavelength of 633 nm, the ANL confocal system has an axial (depth) resolution of ~2 μm and a lateral resolution of ~0.6 μm[2]. These spatial resolutions are directly related to the size of the focused light spot by the objective lens. For a diffraction-limited lens, the focused spot has a diameter of $D = 1.22\lambda/NA$ in the focal plane and an axial length of $Z = 4\lambda/(NA)^2$, where λ is light wavelength and *NA* is the numerical aperture of the lens. Therefore, high spatial resolutions can be achieved by using high-magnification lenses that have high *NA* values.

Two high-magnification objective lenses, a 63X with *NA*=0.75 and a 100X with *NA*=0.9, were utilized for spatial resolution investigation. The axial resolution, which is lower than the lateral resolution for confocal systems, is normally determined by scanning a mirror surface. Figure 10 shows axial intensity profiles from the scanned images of a mirror surface for all lenses, where the intensity is normalized to be 1 at the mirror surface. From these profiles, an axial resolution parameter, commonly defined as the full width at half maximum (FWHM), can be determined. The FWHM is 1.3 μm for the 63X lens and 0.8 μm for the 100X lens; these values are consistent with the theoretical formulation based on the *NA* change between these lenses.

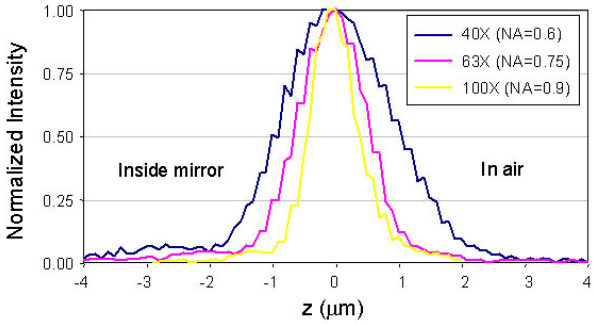

Figure 10. Axial intensity profiles obtained from mirror scan images using various objectives.

A NT551 silicon nitride specimen with known subsurface C cracks was tested using the confocal setup with the 63X objective lens. Figure 11 shows a lateral (plane) scan image of a damaged region with two C cracks. Higher scatter intensity is observed from both C cracks as well as from many individual material defects (pores). To examine the crack angle and depth within the subsurface, five cross-sectional scans, spaced at 40-μm distances from each other and marked as Slices 1-5 in Fig. 11, were performed. The 5 cross-sectional scan images are shown in Fig. 12, with the inside of the material on the top and the specimen surface at the bottom in each image of 1 mm x 0.04 mm size. The subsurface extension of the C cracks is clearly seen in these cross-sectional images. However, as shown in the enlarge image in Fig. 13, which is taken from the marked region in Fig. 12, the horizontal scan lines were not well aligned in the vertical direction. This was due to the poor accuracy of the scan stage. This problem was resolved later by modifying the data acquisition program and using a lower scan speed. Figure 14 shows a comparison of two cross-sectional scan images of a micro-ruler with 10μm-spaced marks. The alignment of the marks in the lateral direction is much better after the modification (Fig. 14b) than before (Fig. 14a). The lateral alignment error between the scan lines is now typically <1μm.

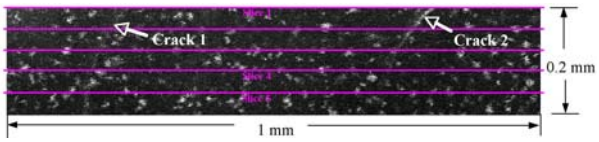

Figure 11. Plane confocal-scan image of a NT551 silicon nitride specimen with two C cracks.

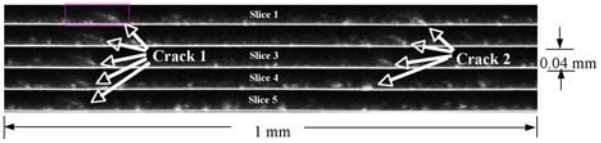

Figure 12. Five cross-sectional confocal-scan images along slice lines 1-5 as indicated in Fig. 11.

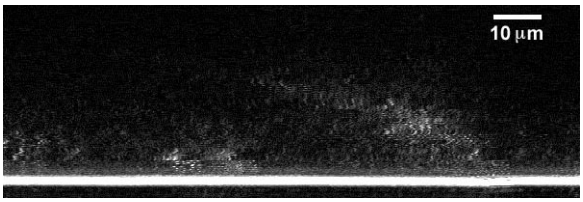

Figure 13. An enlarged region from a cross-sectional confocal-scan image as marked in Fig. 12.

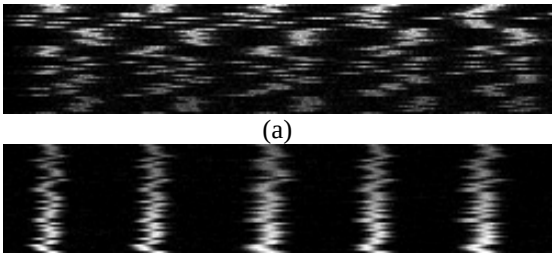

(a)

(b)

Figure 14. Scan images of a micro-ruler surface at (a) before and (b) after data-acquisition program modification. Size of images is 50 μm x 5μm.

Optical Coherence Tomography (OCT) for 3D Imaging of Ceramic Subsurface

Another technology for 3D subsurface imaging is OCT which was originally developed for imaging biological materials. It utilizes a Michelson interferometer to differentiate optical reflections from different depths of a translucent material. The block diagram of ANL's OCT system is shown in Fig. 15. In this system, light from an optical source is split into two paths, a sample path and a reference path. Light in the reference path is reflected from a fixed-plane mirror, whereas light in the sample path is reflected from surface and subsurface features of a ceramic sample. The reflected light from the sample path will only be detected if it travels a distance that closely matches the distance traveled by the light in the reference path. Thus, by scanning the sample, data can be obtained in a plane perpendicular or parallel to the sample surface. The typical spatial resolutions of OCT systems are in the range of 5–15 μm when a low-coherence diode laser is used. Although OCT has lower resolution than the confocal method, OCT systems normally use optical sources of longer wavelengths (the ANL system uses a 1310-nm diode laser) that are capable of deeper optical penetration for ceramics than visible wavelengths typically used by confocal systems.

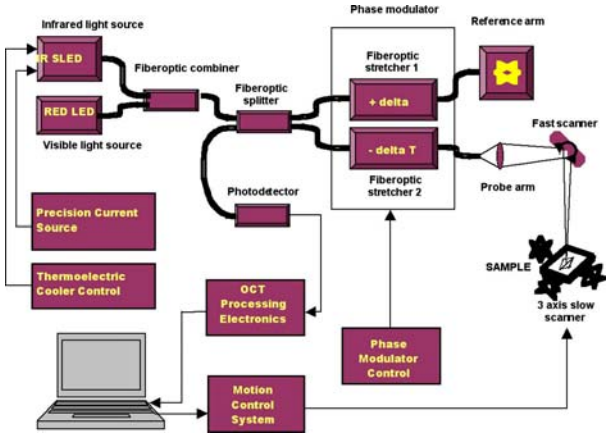

Figure 15. Block diagram of ANL's OCT system.

The imaging depth of ANL's OCT system was evaluated by scanning the cross sections of a NT551 and a SN235P step wedge. Figure 16 shows the micrographs of the step-wedge edges, with the average thickness of each step being listed. The corresponding OCT (composite) scan images are shown in Fig. 17. For the NT551 step wedge, the bottom surface of the first three steps (34, 84, and 184-μm thick) was visible; while bottom surface of only first two steps (35 and 84μm thick) was detected for the SN235P wedge because of its shallow penetration depth. A third surface below the wedges came from a mirror surface that supported the wedges during the scan. The thickness of the wedge steps determined from the images is the optical thickness. Because optical penetration depth for OCT equals the physical depth multiplied by the refraction index of the material, direct comparison of optical and physical depths allows for the determination of the refraction index of silicon nitrides, for which conflicting data exist in the literature. The measured refection index for both NT551 and SN235P was determined to be 2.0, which is consistent with most reported values for deposited silicon-nitride films. In addition, the OCT images in Fig. 17 also revealed many scattering sites within the NT551 and SN235P subsurface. Higher scattering is usually an indication of porosity or defects; this method therefore may be used for NDE of these ceramics.

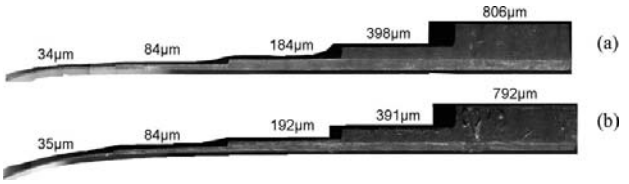

Figure 16. Micrographs and average thickness at edges of (a) NT551 (b) SN235P step wedges.

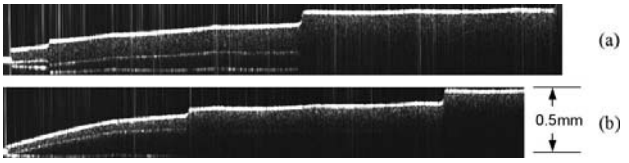

Figure 17. Scanned cross-sectional OCT images for (a) NT551 and (b) SN235P step wedges.

Conclusions

Ten Si_3N_4 (6 inlet and 4 exhaust) and four TiAl exhaust valves that were successfully tested for 500 hours in a Caterpillar natural-gas G3406 generator set at NTRC were examined using ANL's laser-scatter NDE system. The NDE data were analyzed and compared with surface photomicrographs. In general, a "polishing" wear effect was observed in all Si_3N_4 ceramic valves. The polishing wear was minor for intake valves but more intensive in the exhaust valves, likely due to the difference in temperatures at the valve face/seat insert contact region. In addition, a significant amount of surface damage, represented by narrow ridges/grooves, was detected within the impact surface of all Si_3N_4 exhaust valves. This surface damage pattern was not observed on the matching surfaces of the seat inserts, indicating it was not induced by the contact or "polishing" during the valve-seat insert impacts. Nevertheless, the NDE examinations did not detect subsurface damage such as cracks within and around the impact area for all Si_3N_4 valves. For TiAl exhaust valves, the NDE test detected many small "indents" and large (~0.5 mm) "pits" as well as wear grooves within the impact surface. These results suggested that the impact damages in TiAl valves were more severe than those observed in the Si_3N_4 valves.

3D imaging technologies were investigated for detecting subsurface flaw characteristics that may be used for quantitative prediction of material's mechanical properties. The cross-polarization confocal microscopy developed at ANL was further improved for high-resolution imaging of subsurface C cracks; an axial (depth) resolution of 0.8 μm was achieved. In addition, an OCT system was evaluated for increased 3D imaging depths for ceramics. It was identified that OCT can image depths >184 μm for NT551 and >84 μm for SN235P, the two primary Si_3N_4 ceramics evaluated as engine-valve materials.

References

1. N. S. L. Phillips, "Lightweight Valve Train Materials," *Quarterly Report for Jan.-Mar. 2007, Heavy Vehicle Propulsion Materials Program.*

2. J. G. Sun, "NDE of Diesel Engine Components," *Annual Report for FY 2006, Heavy Vehicle Propulsion Materials Program.*

3. M. D. Kass, et al., "Report on the G3406 Engine Failure Investigation: Heavy-Duty Natural Gas Lightweight Valve Project," *ORNL Report,* August 7, 2007.

Presentations and Publications

J. G. Sun, J. S. Trethewey, N. Phillips, N. N. Vanderspiegel, and J. A. Jensen, "Nondestructive Evaluation of Silicon-Nitride Ceramic Valves from Engine Duration Test," paper to be published in the Proceedings of the 31st Int. Cocoa Beach Conf. & Exposition on Advanced Ceramics and Composites held in January 21-26, 2007, in Daytona Beach, FL.

J. G. Sun, J. M. Zhang, J. S. Trethewey, N. S. L Phillips, and J. A. Jensen, "Evaluation of Silicon-Nitride Ceramic Valves," *International Journal of Applied Ceramic Technology*, in press.

N. S. L. Phillips, J. A. Jensen, M. J. Andrews, J. S. Tretheway, D. M. Longanbach, H. T. Lin, and J. G. Sun, "Effect of Machining Procedures on the Strength of Ceramics for Diesel Engine Valves," presented at the 13th Diesel Engine-Efficiency and Emissions Research (DEER) Conference, Detroit, Michigan, August 13-16, 2007.

Agreement 9128 - High-Temperature Advanced Materials for Lightweight Valve Train Components

Nathaniel S. L. Phillips, Principal Investigator
Jeff Jensen, Eric Kelsey, Natalie Vanderspiegel, and Mike Vogler
Caterpillar Inc.
Tech Center 854-22 TC-E
14009 Old Galena Rd.
Mossville IL, 61552
(309) 578- 5788 (voice)
(309) 578-2953 (fax)
E-mail: Phillips_Nate@cat.com

DOE Technology Manager: Jerry L. Gibbs
(202) 586-1182; fax: (202) 586-1600; e-mail: jerry.gibbs@ee.doe.gov
ORNL Technical Advisor: D. Ray Johnson
(865) 576-6832; fax: (865) 574-6098; e-mail: johnsondr@ornl.gov

Contractor: Oak Ridge National Laboratory, Oak Ridge, Tennessee
Contract Number: DE-AC05-00OR22725
Subcontractor: Caterpillar Inc., Peoria, Illinois

Objective

- Evaluate prospective lightweight valve materials and determine feasibility of implementation in heavy-duty diesel and natural gas applications.

Approach

- Design, procure, and evaluate γ-phase titanium aluminide (TiAl) and silicon nitride (Si_3N_4) heavy-duty engine valves.
- Demonstrate performance and durability advantages by performing 1000-hour durability test on valves in a Caterpillar G3406 natural gas engine.
- Develop finite-element analysis (FEA)-based life prediction model (NASA CARES/Life) that will generate life prediction curves for advanced valve materials.
- Evaluate the thermal, chemical and mechanical properties of TiAl and Si_3N_4 that are critical to on-engine valve performance and durability.
- Investigate manufacturing considerations (i.e., machinability and quality inspection technique) of these novel materials.

Accomplishments

- Analysis of 500-hour post test non-destructive evaluation results
- Started 2nd 500 hours of testing, but was stopped prematurely due to engine failure
- Analysis of the remaining strength of Si_3N_4 and TiAl valves following engine failure
- Trip made to ORNL/HTML to complete residual stress measurements of machined Si_3N_4 test bars

Future Direction

- Destructive and non-destructive tests of valves that were taken from the engine after 500 hours and valves that survived the engine failure
- Quantify performance gains and establish useful life estimates of Si_3N_4 and TiAl valves in a heavy-duty engine environment with a full project report for the Lightweight Valve Study
- Project end date is December 31, 2007

Introduction

Valve train components in heavy-duty engines operate under high stresses, at elevated temperatures, and in severely corrosive environments. Structural ceramics and emerging intermetallic materials are highly corrosion and oxidation resistant and possess high strength and hardness at elevated temperatures. These properties are expected to allow higher engine operating temperatures, lower wear, and enhanced reliability. In addition, the lighter weight of these materials (~50% of production alloys) will lead to lower reciprocating valve train mass that could improve fuel efficiency.

Over the past decade, the automotive engine industry has demonstrated moderate success with TiAl as a valve material. Eylon et al.[1] demonstrated a 2% fuel savings on a Chevrolet Corvette that ran for 25,000km with TiAl valves. This fuel efficiency increase was attributed to the decrease in valve train parasitic frictional losses. In another study with TiAl valves, Maki et al.[2] demonstrated a 1000-rpm increase in over-speed performance on a Nissan VRT35 engine. This capability would allow more efficient engines to operate in more demanding regimes. The current research and development program at Caterpillar, Inc. has extended this body of knowledge from the automotive community and will examine TiAl and Si_3N_4 in the context of heavy-duty diesel and natural gas engine environments.

The valve train material development effort will provide the materials, design, manufacturing, and economic information necessary to bring these new materials and technologies to commercial realization. With this information, component designs will be optimized using probabilistic lifetime prediction models, and validated in rig bench tests and short- and long-term engine tests. After establishing proof-of-concept with valves, this design approach will be applied to other components made from high-temperature materials.

Approach

Many perspectives must be considered when evaluating TiAl and Si_3N_4 materials for use in valve applications. As such, there are several facets to this project. Validation of these components begins with the fabrication of TiAl and Si_3N_4 valves and testing them on a Caterpillar G3406 (in-line 6 cylinder) natural gas engine. Previous annual reports documented the design process used to modify the current baseline metallic valve to accommodate the limited ductility of ceramic and intermetallic materials.[3] For example, the head dimensions were changed to reduce the stress concentration

experienced in the fillet radius. Silicon nitride and TiAl valve blanks were formed, rough machined, friction welded to a Ti-6Al-4V shaft (TiAl only), and finish machined.

A parallel effort to develop a design tool for high-strength, brittle materials is also being pursued. A FEA-based life prediction code (NASA CARES/Life) is used to evaluate component design and generate life prediction curves. This approach uses material properties and thermo-mechanical boundary conditions as the primary inputs. A probability-based code then calculates the accumulated damage through the life of the valve and creates a life prediction curve.

A variety of other studies contribute to the understanding of the behavior of TiAl and Si_3N_4 and how they may perform in an engine environment. Several studies examine the fundamental properties of the materials: tensile strength, creep strength, thermo-physical properties, friction coefficient, wear resistance, oxidation resistance, and corrosion resistance. Two other studies examine the manufacturability of the materials: the effect of machining damage on fatigue resistance and a NDE technique to evaluate surface quality.[4]

Results and Discussion

Engine testing of Titanium Aluminide, Silicon Nitride and production valves

One of the primary goals of this study is to evaluate the performance of ceramic (Si_3N_4) and intermetallic (TiAl) valves in an engine environment. As outlined in previous quarterly reports (see Oct-Dec 2004), arrangements have been made to perform parallel 1000-hour endurance tests on three valve materials: γ-TiAl, Si_3N_4 and the austenitic steel production valve. These tests were performed at the National Transportation Research Center (NTRC) on a natural gas G3406 genset.

Table 1 outlines the progress of this engine durability test.

Engine operating conditions

The valves were installed, as shown in Table 2, to ensure that the performance of the Si_3N_4 and TiAl valves could be isolated during post-test analysis. The first 500 hours of engine testing was performed at half-rated conditions (125kW) due to a "knocking" phenomenon as described in the previous annual reports (see 2006 Annual Report).

To avoid "knocking" issues for the second 500 hours, the Si_3N_4 valves were removed from Cylinder 1 and new production steel valves were inserted. New Si_3N_4 replaced the production steel valves in Cylinder 6 for the second 500 hours of testing. This was done because the combustion temperatures in Cylinder 6 were thought to be lower than in Cylinder 1, thus eliminating pre-ignition, "knocking", caused by hot spots on the ceramic exhaust valves. The Si_3N_4 valves that were removed after Phase #2 were destructively tested for remaining strength. A TiAl exhaust valve from Cylinder #4 was also removed for destructive evaluation and replaced with a new TiAl valve. A diagram presenting the differences in arrangement of valves between the Phase #2 and #3 is presented in Table 2.

It was determined that switching the Si_3N_4 valves to the cool side of the engine eliminated the "knocking" problem; therefore, the 2nd 500 hours was run at rated conditions (235 kW).

Post Phase #2 valve analysis Non-Destructive Evaluation

In a heavy-duty engine, the first 100 hours of operation time is considered the "break-in" period. During this initial phase the valve seat and seat insert typically conform to each other, resulting in scuffing of the valve seat.

Valve/guide contact may also cause break-in wear on the stem and valve/bridge contact may cause stem tip wear. After the initial 100 hours, the wear will continue to increase, although at a slower rate, before eventually reaching a steady state where minimal wear is observed. The TiAl and Si_3N_4 valves showed minimal stem tip wear, acceptable valve/guide wear but significant seat/insert wear after the first 100 hours (for more details see Annual Report 2006).

Similar results were seen after 500 hours, except the seat/insert wear was slightly worse. Figures 1a shows a representative Si_3N_4 exhaust valve (Si3N4E-32) after 100 hours as it was positioned in the cylinder, while Figure 1b shows the valve after 500 hours of test engine time. As expected, there was an even coating of combustion byproduct on the head face, fillet and lower valve stem region. The stem wear was evident in the discoloration that ends halfway up the valve. Figures 2a-d shows the seat area from which profilometry scans were taken, along with the 2D wear patterns after 100 and 500 hours of test engine exposure. Figures 3a and b and Figures 4a-d show the same results for a representative TiAl valve (TiAl-5).

Surface roughness, Ra, was measured in certain areas, as well. Table 3 illustrates the surface roughness of each Si_3N_4 and TiAl valve prior to engine aging and after the first 100 and 500 hours. Measurements were not available for the valve seat and TiAl valve guide after 500 hours.

Table 1. Engine durability test progress

Phase	Action	Status
Initial Installation	Valve Installation	Completed in March 2006
Phase #1 (0 h – 100 h)	Engine Exposure	Completed in May 2006
	Post-test Analysis	Completed in June 2006
Phase #2 (100 h – 500 h)	Engine Exposure	Completed in July 2006
	Post-test Analysis	Completed in November 2006
Phase #3 (500 h – 1000 h)	Engine Exposure	Completed in June 2007
	Post-test Analysis	Started in August 2007

Table 2. Valve installation arrangement

	0 – 500 hours		500 – 1000 hours	
Cylinder	Intake	Exhaust	Intake	Exhaust
1	Si_3N_4	Si_3N_4	Production Steel	Production Steel
2	Si_3N_4	Si_3N_4	Si_3N_4	Si_3N_4
3	Si_3N_4	TiAl	Si_3N_4	TiAl
4	Production Steel	TiAl	Production Steel	TiAl (1 new)
5	Production Steel	Production Steel	Production Steel	Production Steel
6	Production Steel	Production Steel	Si_3N_4 (new)	Si_3N_4 (new)

Table 3. Surface roughness measurement of valves at 0, 100, and 500 hrs

	Valve ID #	Valve Location	Time (hrs)	Ra (Valve Guide)		Ra (Valve Seat)
Si3N4 Intake	Si3N4I-20	I2-SI3N4	0	0.067		0.152
			100	0.095		0.226
			500	0.058		NA
	Si3N4I-21	I4-SI3N4	0	0.061		0.15
			100	0.079		0.779
			500	0.05		NA
	Si3N4I-25	I6-SI3N4	0	0.069		0.143
			100	0.069		0.199
			500	0.046		NA
	Si3N4I-28	I8-SI3N4	0	0.063		0.178
			100	0.093		0.435
			500	0.057		NA
	Si3N4I-33	I10-SI3N4	0	0.067		0.174
			100	0.089		0.185
			500	0.059		NA
	Si3N4I-41	I12-SI3N4	0	0.069		0.174
			100	0.096		0.394
			500	0.053		NA
Si3N4 Exhaust	Si3N4E-11	E1-SI3N4	0	0.063		0.232
			100	0.059		0.436
			500	0.072		NA
	Si3N4E-17	E3-SI3N4	0	0.06		0.211
			100	0.027		0.888
			500	0.035		NA
	Si3N4E-9	E5-SI3N4	0	0.063		0.222
			100	0.037		0.382
			500	0.048		NA
	Si3N4E-32	E7-SI3N4	0	0.066		0.206
			100	0.034		0.389
			500	0.048		NA
				Ti	TiAl	
TiAl Exhaust	TiAl-5	E9-TiAl	0	0.121	0.071	0.187
			100	0.239	0.316	0.970
			500	0.178	NA	NA
	TiAl-6	E11-TiAl	0	0.102	0.063	0.221
			100	0.316	1.054	1.157
			500	0.181	NA	NA
	TiAl-7	E13-TiAl	0	0.121	0.054	0.211
			100	0.269	0.661	0.762
			500	0.119	NA	NA
	TiAl-8	E15-TiAl	0	0.12	0.052	0.226
			100	0.318	1.097	1.143
			500	0.165	NA	NA

Valve/seat wear

A 2x increase in valve/seat surface roughness after 100 hours for Si3N4E-32 was an indication that break-in scuffing wear occurred on the Si_3N_4 valve. Figure 2b shows a relatively constant wear scar depth of ~2mm. The scar depth continues to increase to ~8mm after 500 hours (Figure 2c). However, the 5x increase in valve/seat surface roughness for TiAl-5 was an indication that the wear exceeded standard break-in wear. This is confirmed by Figure 4b, which shows the valve/seat wear scar depth was ~15mm, a significant wear groove for only 100 engine hours. However, the wear seemed to have reached a steady state, since the scar depth was only ~16mm after 500 hours (Figure 4c).

Valve/guide wear

The minor scuffing wear moderately increased the Ra of the Si_3N_4 intake valves after 100 hours. However, the Ra decreased after 500 hours due to a polishing wear mode, which was enabled by higher stem temperatures at longer exposure times. This mechanism was seen initially in the Si_3N_4 exhaust valves because the exhaust temperatures were already at elevated temperatures after 100 hours. The Ra continued to increase after 500 hours of exposure. The TiAl valves exhibit inferior wear performance than the Si_3N_4 valves in the

valve/guide region. However, the 2x-3x Ra increase in the Ti-6-4 segment of the stem indicates that the thermal oxidation heat treatment was more effective on Ti-6-4 than on TiAl, which showed a 3x-10x Ra increase.

Laser Inspection

At the end of Phase #1 and #2, the valves were scanned with the laser-based NDE instrument outlined in the project titled "NDE of Diesel Engine Components." Figures 5 and 6 show the NDE scans for exhaust valves Si3N4E-32 and TiAl-5 (the same valves in Figures 1 and 3). The region of interest is this valve seat band because this is typically the location of highest accumulated damage. A minor amount of wear was observed between 100 and 500 hours on the Si_3N_4 seat, while a significant amount of wear was observed on the TiAl seat for the same exposure time. The smooth continuous surfaces seen on the Si_3N_4 seats indicate that no or minor wear occurred. The defined light and dark ridges on the TiAl seats indicate that more significant, uneven wear occurred.

Destructive Evaluation
Fracture Strength

The fracture strengths of the valves removed from Cylinder #1 and 4 after 500 hours and some new, untested valves were determined by fast fracturing both half-cylindrical stem and head specimens of each valve. The fracture strengths of the Si_3N_4 exhaust (E1SN-500, E3SN-500, and E3SN-0) and intake (I2SN-500, I4SN-500, and I34SN-0) valve stems, along with plus and minus one standard deviation, are presented in Figure 7. The fracture strengths from the valve head for the same samples are presented in Figure 8. A standard deviation was not plotted for the fracture strength of the head of the valves, as only one specimen was tested. The fracture strengths of both the Si_3N_4 stem and head seem to be relatively unaffected by the 500 hour engine exposure. In most cases, the stem fracture strengths of the 500-hour specimens were higher than the 0-hour specimens. The only depreciation of the fracture strength as a result of engine exposure appeared in the intake valve heads.

Similar results are plotted for a 500-hour TiAl exhaust valve (E15TiAl-500) and a new, untested TiAl exhaust valve (TiAl3-0) in Figures 9 and 10. In both the stem and head, the fracture strength of the 500-hour specimens was higher than the 0-hour specimens. The results obtained from these tests will be compared to the CARES/Life life prediction models (see 2006 Annual Report) in early-FY 2008.

Phase #3 – Engine Failure Analysis

After ~55 hours at rated conditions, the G3406 engine was stopped due to low cylinder pressures. After a complete diagnostic of the engine, it was concluded that one of the Si_3N_4 intake valves in Cylinder #6 was dropped due to a worn out metal keeper latch. The remaining valves in Cylinder #6 fractured between the head and stem of the valve as a result of the debris from the dropped valve. As a result, the piston crown and cylinder liner were also heavily damaged. The other cylinders showed similar damage to the piston and cylinder and significant damage to the face of all the valves in Cylinders #1-5. The six pressure transducers that measure heat release in each of the cylinders were destroyed, as well.

The metal keeper latch that is used to hold the valve in place was worn off for the dropped Si_3N_4 in Cylinder #6 (Valve #22), as presented in Figure 11. A typical worn keeper is shown alongside the failed keeper. Roughness

measurements from the keeper groove on the stem of Valve #22 revealed a more polished surface than the other Si_3N_4 valves, indicating the valve was moving independent of the keeper.

Measurements of the keeper groove on a stainless steel production valve and a Si_3N_4 valve, as seen in Figure 12, indicate that the groove radius for a Si_3N_4 valve is substantially larger than the production valve. Since keepers with identical keeper latch radii were used for both valves, it was concluded that the free motion of the Si_3N_4 valves caused the keeper latch to be worn away, thus allowing the valve to drop into the cylinder.[8]

No further wear analysis was done for the 55 hours between Phase #2 and the engine failure, as no significant conclusions were thought to have resulted from such a small amount of time.

Residual Stress Tests of Si_3N_4 Rods

A user proposal was developed in 2004 to research cost effective machining processes for ceramic components resulting in optimal performance and extended life and reliability. The machining conditions and results of the Weibull moduli and characteristic strength tests of machined Kyocera SN235P Si_3N_4 test rods are outlined in the 2004 Annual Report. A wide range of Weibull moduli were reported for the different machining techniques; however, the characteristic strengths were all very similar. Therefore, it was decided that experiments should be done to determine if differences in residual stresses as a result of the machining processes were causing the variation in moduli.

A test matrix was setup to compare the highest to lowest Weibull moduli test specimens, as outlined in Table 4. Measurements were to taken in the axial, radial, and hoop directions with the XRD-PTS Rotating Anode. Thus far, only the first four samples have been tested. The machining information from these four samples is presented in Table 5. The surface finishes of these samples were laser scattered and optically imaged, as shown in Figure 13.

After finding little stress in these samples by employing the conventional method of x-ray diffraction (XRD) due to averaging effects, it was determined that grazing incidence x-ray diffraction (GIXD) should be used to determine the stress at the near surface (approximately first 10μm). However, the results from GIXD are more qualitative than quantitative and will only give an approximate value of the actual residual stress. Figure 14 shows the relative comparison of the samples listed in Table 5 as a result of the GIXD analysis. There is a steep stress gradient in the first few microns of the surface. As the depth increases, the stress levels off. The samples which were finish machined and had the highest Weibull moduli, 2A and 2B, showed the highest compression stresses at the surface. This suggests that the high compression stresses prevent crack initiation in the finished samples better than the rough samples. The finished machining shears the surface more than the rough grinding, creating more of a smeared, deformed surface (see Figure 13). This suggests that the finished machining more uniformly distributes the surface flaws, since Weibull modulus is a measure of variance.

Table 4. Test matrix for residual stress tests

Sample #	Machining Rank*	XRD Scans - 1 Spot		
		Axial	Hoop	Radial
2A	1	Y	Y	Y
4A	12	Y	Y	Y
2B	1	Y	Y	Y
4B	12	Y	Y	Y
Do we see a difference? Y: Continue, N: End Testing				
12A	2	Determine if all 3 directions are necessary based on data. Perform the minimum number of directions as necessary.		
10A	11			
12B	2			
10B	11			
Do we see a difference? Y: Continue, N: End Testing				
7A	3	Determine if all 3 directions are necessary based on data. Perform the minimum number of directions as necessary.		
3A	10			
7B	3			
3B	10			

* Machining Rank: 1=Best sample, 12=Worse sample

Table 5. Machining processes for samples in residual stress test matrix

Sample ID	Machining Condition
2A	Finished
4A	Rough
2B	Finished
4B	Rough

References

1. D. Eylon et al., "Development of permanent-mold cast TiAl automotive valves," *Intermetallics*, **6**, 1998.

2. K. Maki et al., "Development of a high-performance TiAl exhaust valve," SAE Paper 960303, Warrendale, Pennsylvania, 1996.

3. M. J. Andrews and J. Chapa-Cabrera, "High-temperature advanced materials for lightweight valve train components," *Heavy Vehicle Propulsion Materials 2003 Annual Progress Report*, Energy Efficiency and Renewable Energy Office of FreedomCAR and Vehicle Technologies, March 2004.

4. J. G. Sun, "NDE development for ceramic valves for diesel engines," *Heavy Vehicle Propulsion Materials 2004 Annual Progress Report*, Energy Efficiency and Renewable Energy Office of FreedomCAR and Vehicle Technologies, May 2005.

5. J. S. Trethewey et al., "High-temperature advanced materials for lightweight valve train components," *Heavy Vehicle Propulsion Materials 2004 Annual Progress Report*, Energy Efficiency and Renewable Energy Office of FreedomCAR and Vehicle Technologies, May 2005.

6. Biery et al., "Use of Weibull statistics to quantify property variability in TiAl alloys," *Metallurgical and Materials Transactions A*, 33A, 3127–3136 (October 2002).

7. N. S. L. Phillips et al., "High-temperature advanced materials for lightweight valve train components," *Heavy Vehicle Propulsion Materials 2006 Annual Progress Report*, Energy Efficiency and Renewable Energy Office of FreedomCAR and Vehicle Technologies, May 2006.

8. M. D. Kass and H. T. Lin, "Report of the G3406 Engine Failure Investigation: Heavy-Duty natural Gas Lightweight Valve Project," ORNL Engineering Science and Technology Division and Materials Science and Technology Division, August 2007.

Presentations and Publications

H. T. Lin, N. S. L. Phillips, "Design and Implementation of Silicon Nitride Valves for Heavy Duty Diesel Engines," poster presented at the 2007 Diesel Engine-Efficiency & Emissions Research Conference, Detroit, MI, August 13-16, 2007.

N.S.L. Phillips, J. A. Jensen, J. G. Sun, H. T. Lin, "Effect of machining Procedures on the Strength of Ceramics for Advanced Diesel Engine Applications," poster presented at the 2007 Diesel Engine-Efficiency & Emissions Research Conference, Detroit, MI, August 13-16, 2007.

J. G. Sun, J. S. Trethewey, "Nondestructive evaluation of silicon-nitride ceramic valves from engine duration tests," paper presented at the American Ceramic Society's 31st Ann. Intl. Cocoa Beach Conf. & Exposition on Advanced Ceramics & Composites, Daytona Beach, Florida, January 21-26, 2007, and to be published in conference proceedings.

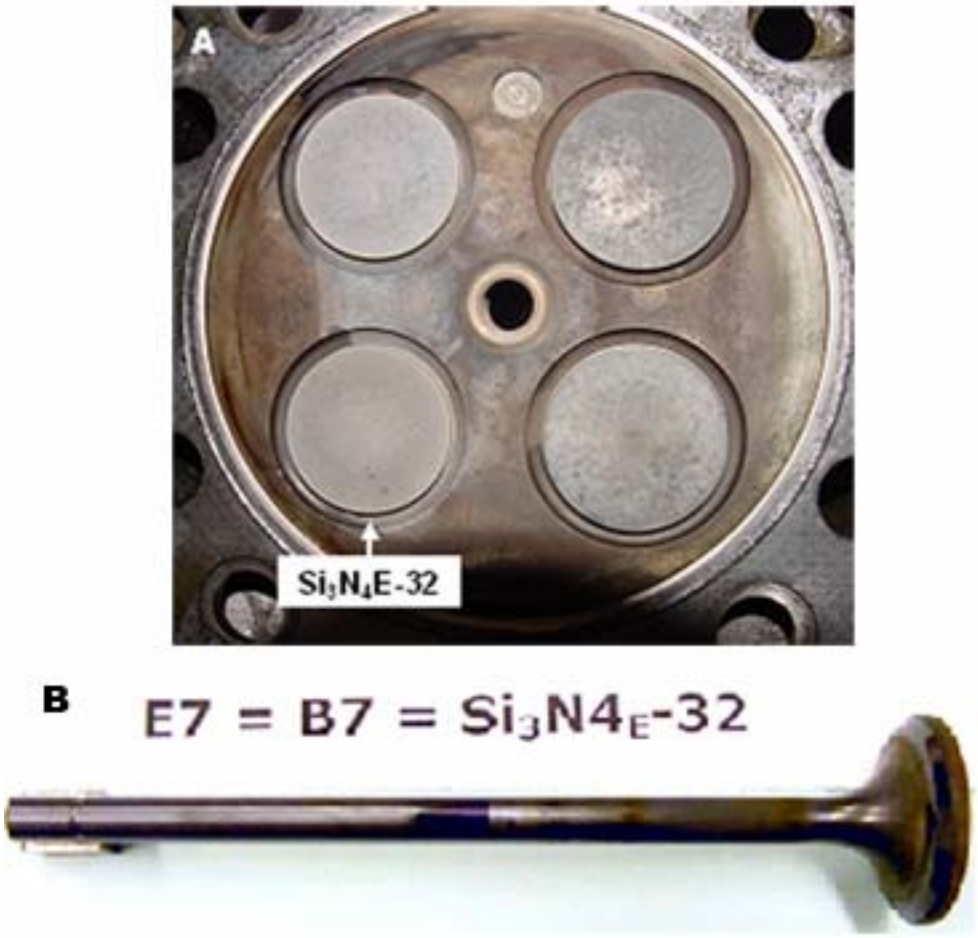

Figure 1. *(A) Cylinder 2 immediately after the completion of the first 100-hour break-in phase. (B) Valve Si3N4E-32, a representative Si_3N_4 exhaust valve after 500 hours.*

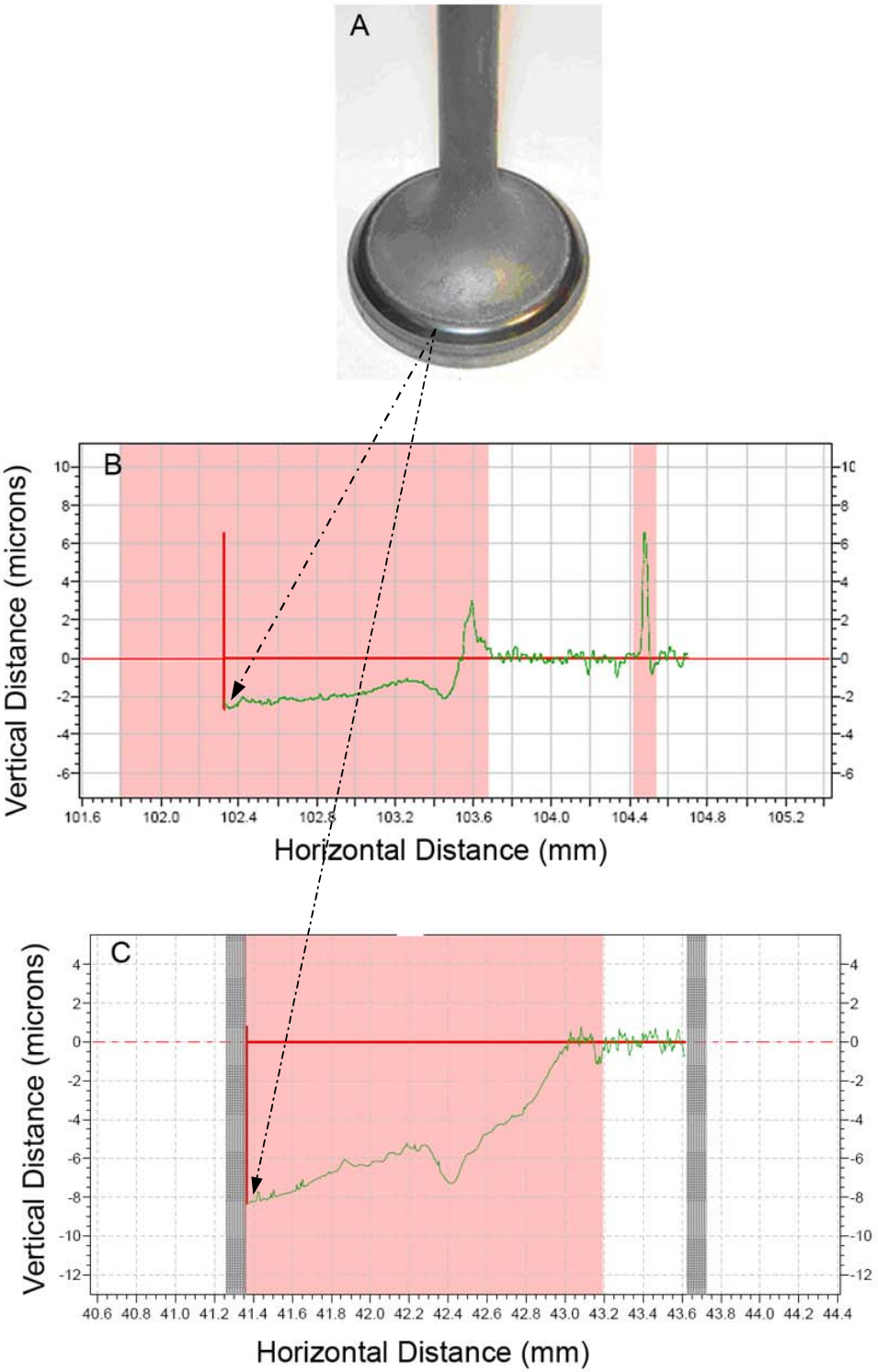

Figure 2. *(A) Seat area where profilometry was taken from (B) 100- and (C) 500-hour Si_3N_4 wear patterns.*

Figure 3. *(A) Cylinder 3 immediately after the completion of the first 100-hour break-in phase. (B) ValveTiAlE-5, a representative TiAl exhaust valve after 500 hours.*

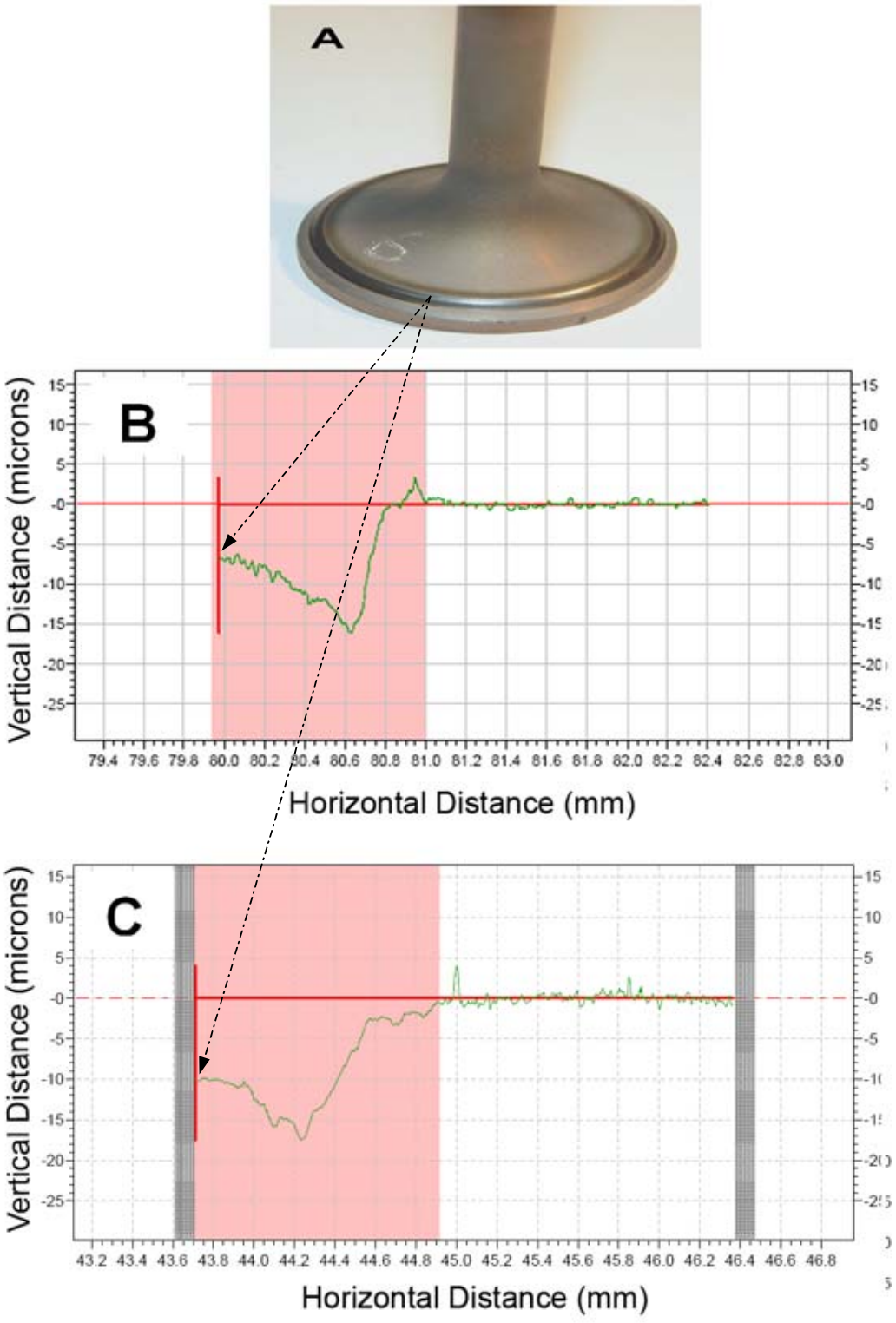

Figure 4. *(A) Seat area where profilometry was taken from (B) 100- and (C) 500-hour TiAl wear patterns.*

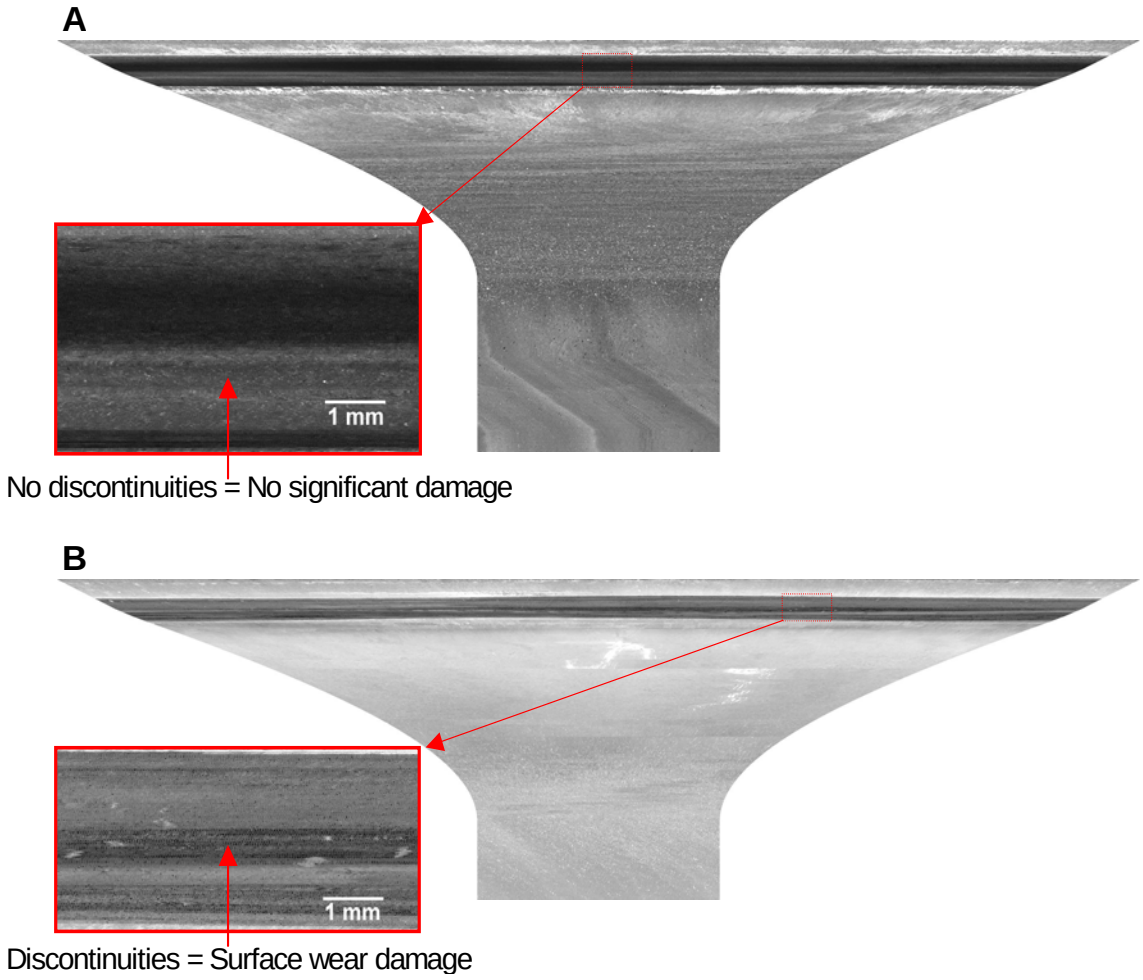

Figure 5. *Laser-based NDE scans after 100 hours of engine exposure time of (A) Si3N4E-32 and (B) TiAl-5, indicating that the Si_3N_4 valve has not sustained major wear damage, but the TiAl valve is showing signs of significant valve/seat wear.*

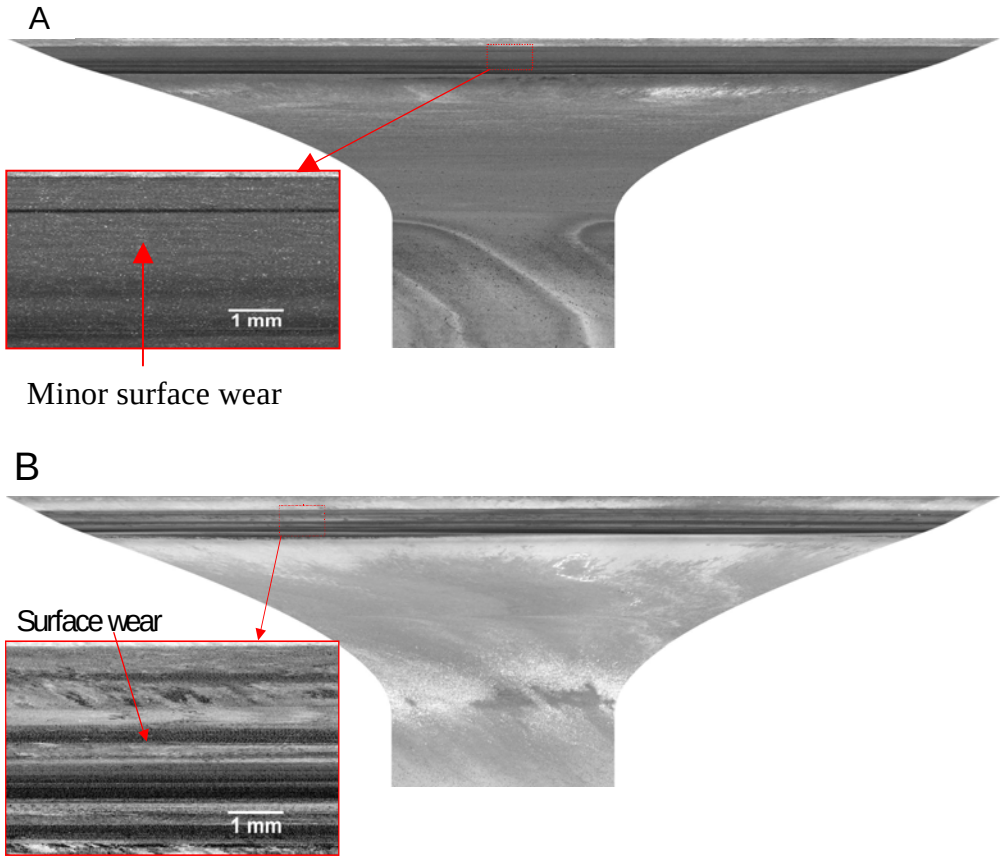

Figure 6. *Laser-based NDE scans after 500 hours of engine exposure time of (A) Si3N4E-32 and (B) TiAl-5*

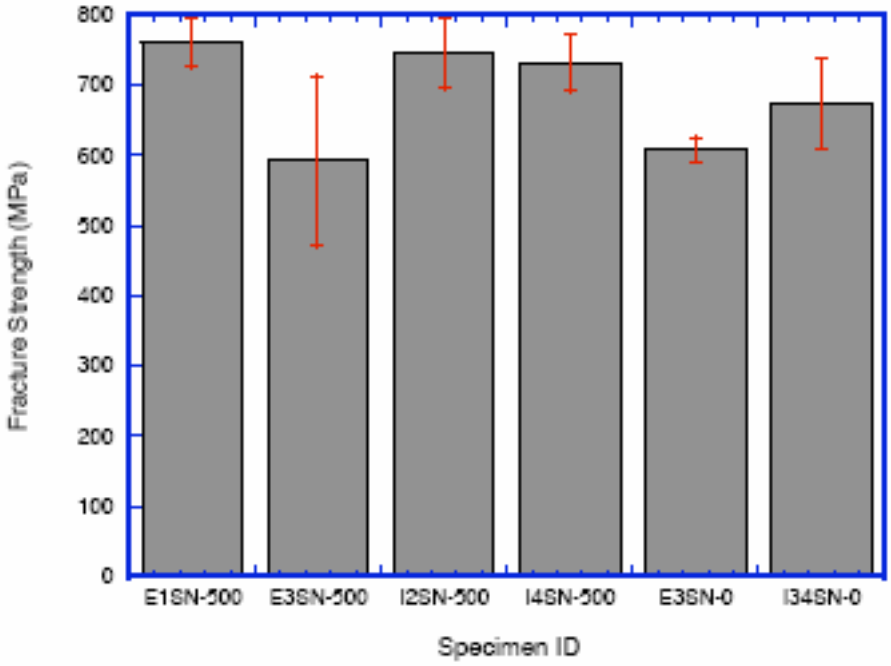

Figure 7. *Fracture strength of half-cylindrical Si_3N_4 valve stems.*

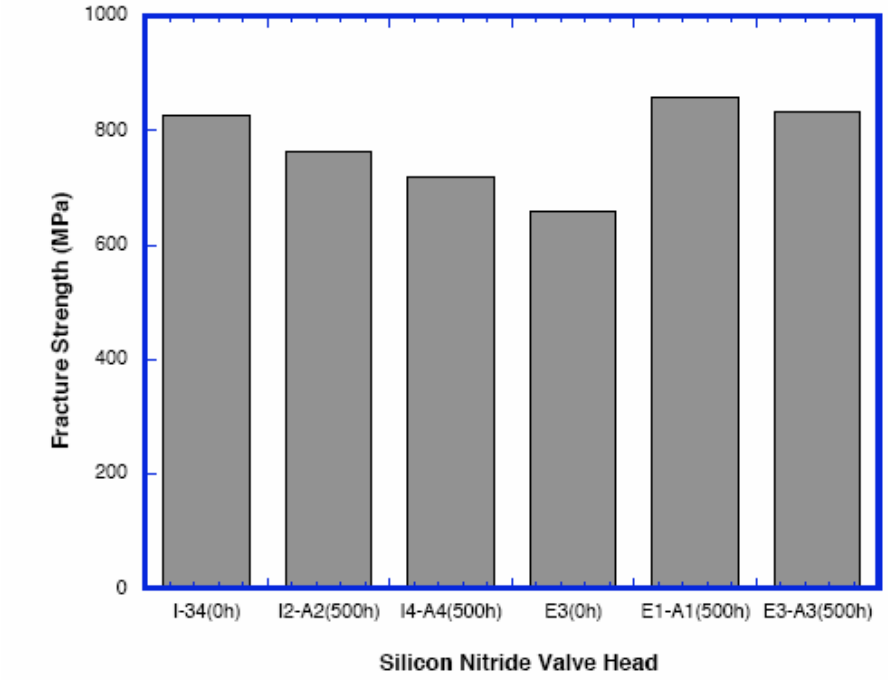

Figure 8. *Fracture strength of Si_3N_4 valve heads.*

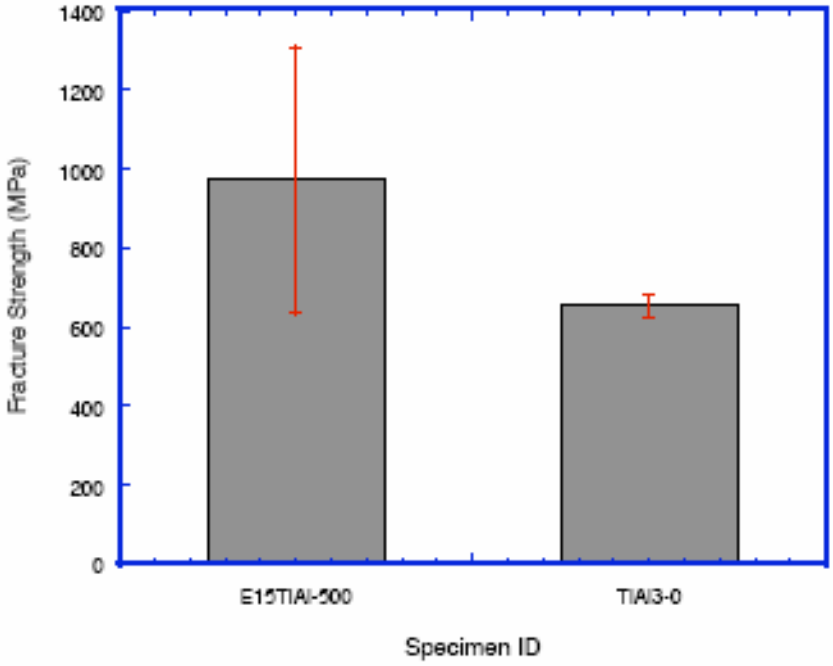

Figure 9. *Fracture strength of half-cylindrical TiAl valve stems.*

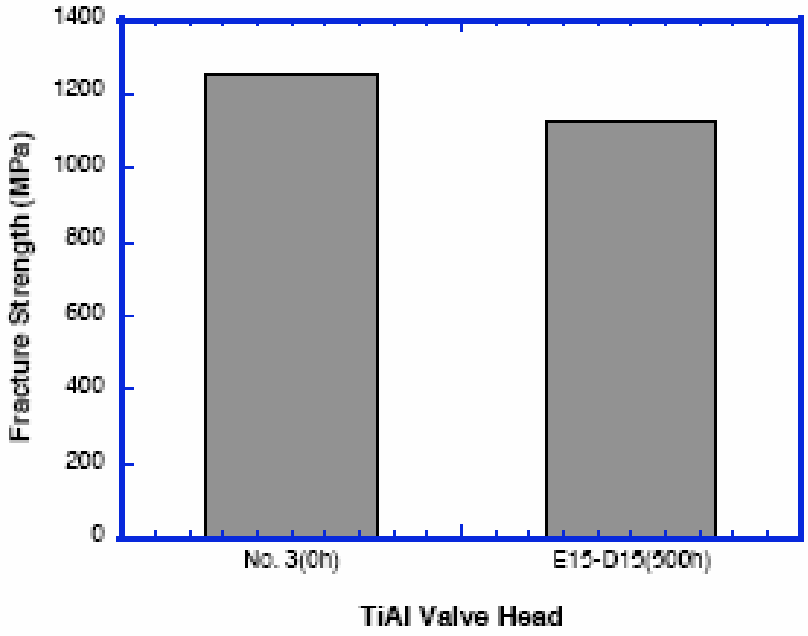

Figure 10. *Fracture strength of TiAl valve heads.*

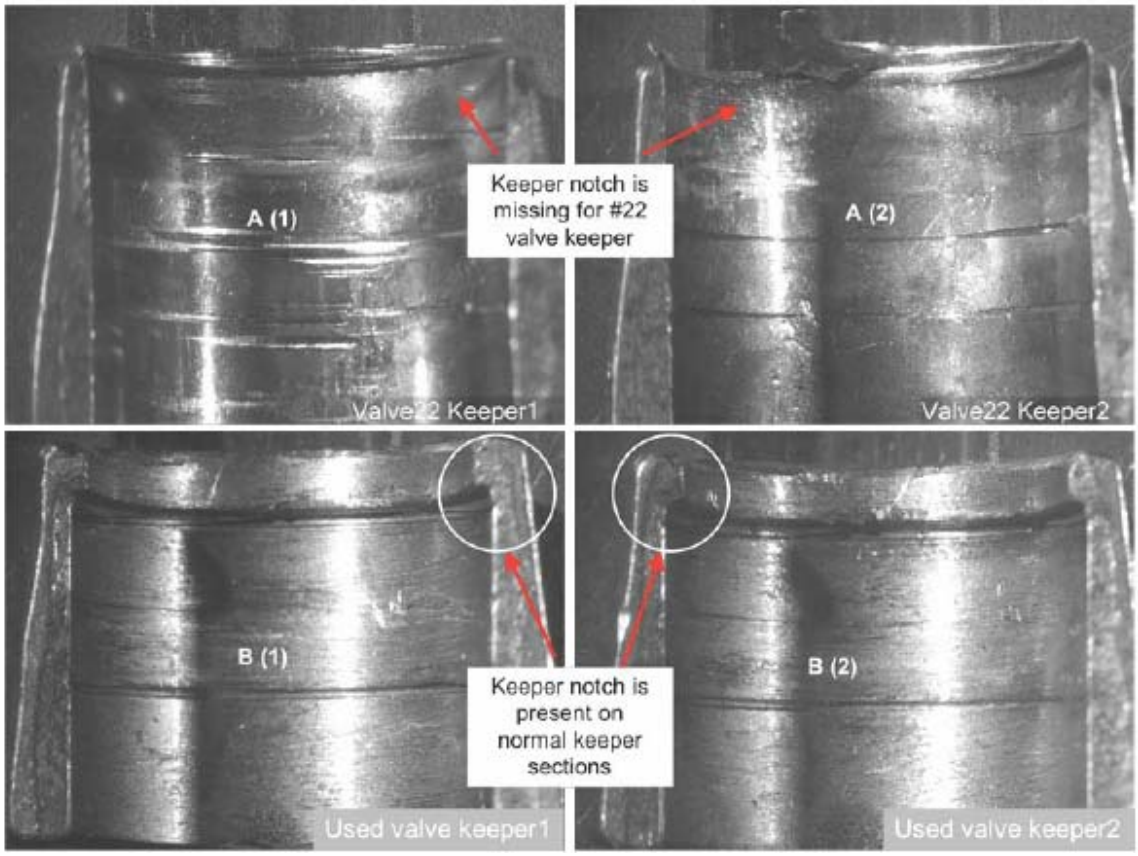

Figure 11. *(A) Failed valve keeper from Cylinder #6. (B) Engine-tested valve keeper with unworn keeper latch.*

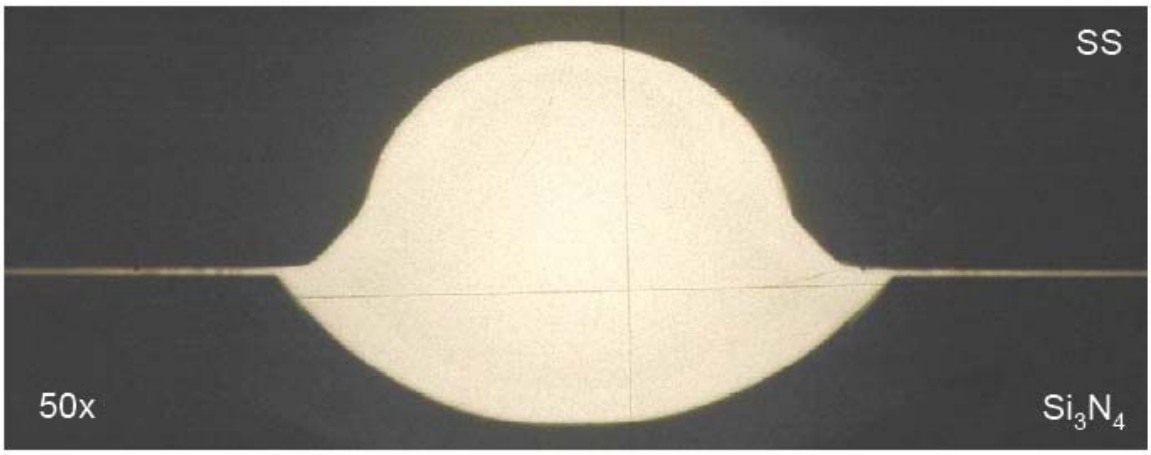

Figure 12. *Keeper groove from a production stainless steel (SS) and Si_3N_4 valve.*

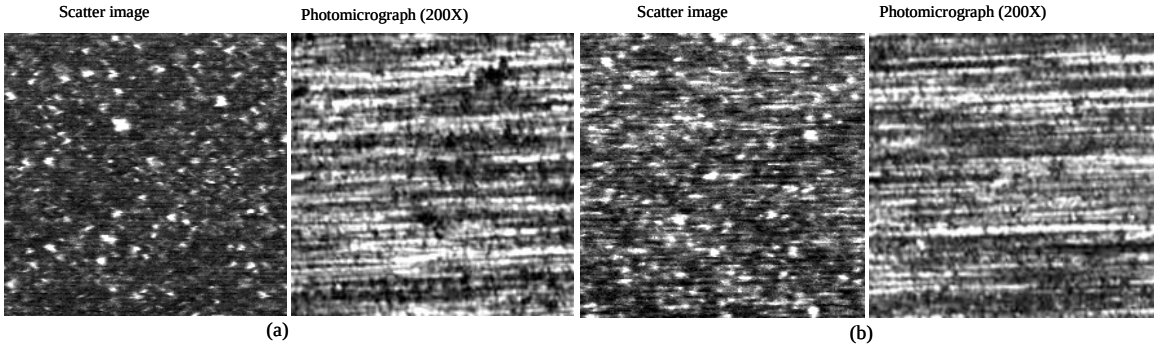

Figure 13. *(A) Finished and (B) rough machined Si_3N_4 specimens.*

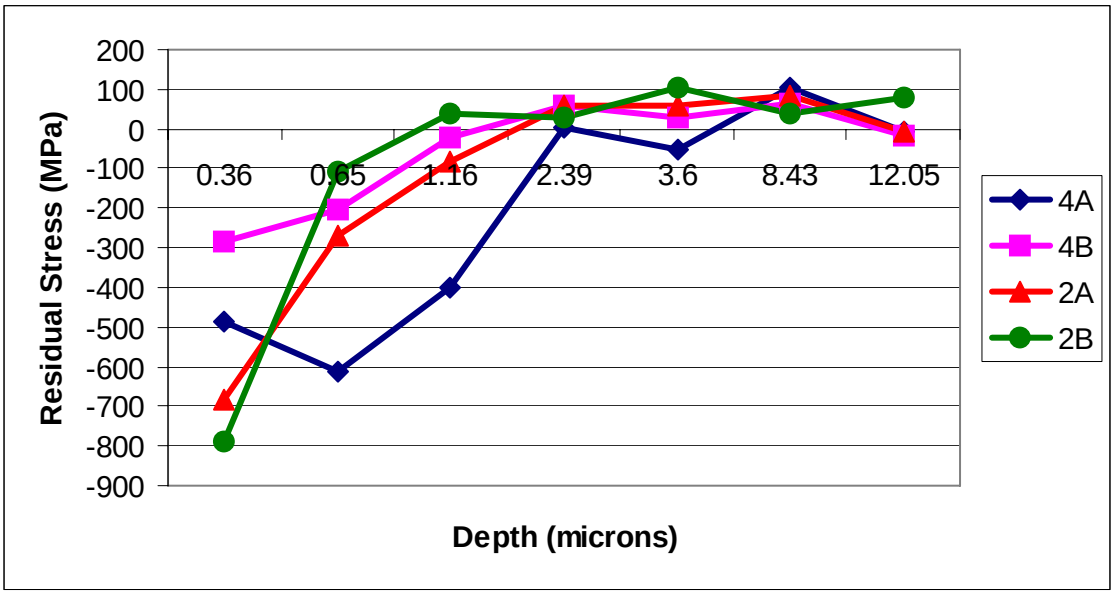

Figure 14. *Relative GIXD residual stress results as a function of sample depth for machined SN235P Si_3N_4 test rods.*

Agreement 15054 - Fatigue Enhancement in CIDI/HCCI Engine Components

Dean M. Paxton and Curt A. Lavender
Energy Materials & Manufacturing Group
Pacific Northwest National Laboratory
PO Box 9998, MS K2-44
Richland, WA 99352
(509) 375-2620; fax: (509) 375-2186; e-mail: dean.paxton@pnl.gov
(509) 372-6770; fax: (509) 375-2186; e-mail: curt.lavender@pnl.gov

DOE Technology Manager: Jerry L. Gibbs
(202) 586-1182; fax: (202) 586-1600; e-mail: Jerry.gibbs@ee.doe.gov

Contractor: Pacific Northwest National Laboratory
Prime DOE Contract Number: DE-AC05-76RL0 1830

Objectives

- Evaluate the fatigue performance impact offered by surface treatments such as laser shock peening, waterjet peening, and friction stir processing to induce compressive residual stresses in the surface of aluminum, steel and cast iron engine components.
- Compare fatigue performance and thermal stability of these novel surface treatment approaches to traditional shot peening methods.

Approach

- Apply surface treatments to induce subsurface compressive residual stresses in test specimens and evaluate the stress profile vs. depth as well as the surface roughness after treatments.
- Evaluate mechanical properties of surface treated bar specimens using roller contact fatigue and rotating beam tests methods.

Accomplishments

- Cooperative Research and Development Agreement (CRADA) signed between Pacific Northwest National Laboratory (PNNL) and Cummins, Inc. on October 22, 2007.
- CRADA project kick-off meeting held on November 29, 2007 at Cummins Technical Center.
- Complete initial characterization of stress profile and surface roughness of test specimens.
- Established rotating beam fatigue test capability at PNNL with purchase of a unit from Fatigue Dynamics, Inc.

Future Direction

- Complete mechanical testing evaluations of specimens with novel surface treatment techniques to establish fatigue enhancement capability.
- Utilize component modeling tools to determine over-stressed regions of engine components that would benefit from residual compressive stress and determine magnitude of stress state needed to improve fatigue performance.
- Develop a nondestructive evaluation (NDE) tool for estimating part failure by acoustic wave propagation, strain quantification, and stress modeling.

Introduction

The primary objective of this project will be focused on evaluating laser shock peening (LSP), waterjet peening (WJP), and friction stir processing (FSP) on the fatigue performance of aluminum, cast iron and steels. Fatigue performance is an important factor in propulsion materials, especially for fuel system components, cylinder heads and blocks, etc. With the advent of faster injector response and higher pressures for better control of combustion events, cam stresses are significantly increased leading to reduced contact and flexural fatigue life. Cyclic fatigue improvements of forming dies made from tool steels have been shown by selectively applying compressive residual stresses at the surface. Methods to apply these stresses vary, but among them LSP has been used successfully. Laser shock peening not only induces compressive residual stresses at the surface, improving cyclic fatigue life more than five times, but has also been shown to decrease the susceptibility of steels to stress corrosion cracking. However, there are some uncertainties with application of the LSP process for engine components: 1) knowing exactly where to optimally apply the process based on part starting condition and ultimate performance requirements, and 2) the parameters required to effectively improve performance based on failure modes encountered.

For softer metals, like aluminum, a lower-energy option that operates similarly to LSP is high-pressure WJP. This process is still in its infancy, but has shown promise for improving fatigue performance in aluminum castings and wrought products, with better control of residual stress distribution. Like that of LSP of high strength steels, the fatigue life enhancement mechanisms of WJP and optimum processing parameters are not yet well defined. In addition, further understanding of the effects of LSP on aluminum alloys is needed.

A cost and energy efficient way of localized processing of metals to improve their fatigue life and wear resistance is by FSP. This process is known to increase fatigue life by refining grain structure and homogenizing the microstructure of the metal, eliminating defects if any in the processed area. Porosity is inherent to a cast metal and the strength is always lower than a forged metal. By FSP the area of interest, forged properties can be attained in a cast component and by designing in the process, low cost, high strength castings can be produced. This is ideal for applications like cylinder heads and blocks, where high strength and wear properties are desired in localized areas such as the combustion chamber, bolt hole bosses, etc. This process is capable of delivering high strength in aluminum, cast iron and steel. Significant challenges exist in understanding the effect of process parameters on mechanical properties of high temperature materials like steel and cast iron.

Approach

The scope of this CRADA project will involve validation of claims that LSP, WJP, and FSP can improve fatigue performance. Recommendations will then be made if additional R&D should be pursued to develop a better mechanistic understanding of the processes. The effectiveness of these three methods will also be compared against the more traditional shot peening approach and will include comparisons of process control, thermal stability, and cost effectiveness.

Adding additional processing steps in manufacturing adds cost, and as such, it is critical to minimize such processing, or limit it to only areas where there is benefit. As such, an important aspect of applying low plasticity peening and FSP methods is to understand how best to manage and distribute stresses in components, in order to increase fatigue performance. In addition, it is important to know the stress distributions and wave propagations under static and dynamic loading. PNNL is experienced in modeling stress distributions and structure evolution in various components and with various materials processing methods. The second objective of this project is to develop a modeling methodology and analytical tools to evaluate the stress fields, and redistribution of these stresses, before and after low plasticity peening and FSP operations. Such tools will enable engineers to quickly design, evaluate, and re-design fuel system components with confidence, and would lead to successful implementation of higher pressure fuel delivery systems that will be needed for advanced combustion, higher-efficiency engines.

As part of developing better design methodologies, a third project objective will be to develop a nondestructive evaluation (NDE) tool for estimating part failure by acoustic wave propagation, strain quantification, and stress

modeling. The concept will employ acoustic excitation of injector and fuel system components at highly loaded areas; quantify strain as a function of time as the impulse wave propagates down the component, and then model stress to determine high stress regions and distribution. The stress model will also be modified to estimate behavior at higher excitation levels and predict part failure. Use of such an NDE tool, combined with modeling, will enable the prediction of part failure and, more importantly, mitigation of failure by implementing design changes, such as part dimensions or material properties. Non-contact strain measurement will be performed by optical techniques so not to alter part dynamics.

The specific tasks planned to address the objectives listed above include:

1. Mechanical Properties Testing of LSP Steel – a) Process initial M50 steel bars (cam material) with LSP and evaluate the surface finish and residual stresses of the ground surfaces after centerless grinding to 9 mm diameter. Additional M50 bars shall be processed by LSP with the goal of removing minimal material to improve surface finish and achieve target size of 3/8-inch diameter.

   b) Evaluate roller contact fatigue (RCF) of initial 9 mm diameter bars at Cummins. Test additional 3/8-inch diameter bars after LSP, centerless grinding to final diameter, and characterization of residual stresses.

   c) Evaluate flexural fatigue at PNNL via rotating beam test of 3/8-inch diameter bars after LSP, centerless grinding to final diameter, and characterization of residual stresses.

2. Mechanical Properties Testing of Waterjet Peened Aluminum – PNNL's subcontractor, Flow International, will provide waterjet peening on six cast A354 aluminum fatigue samples and Cummins will evaluate high-cycle fatigue life improvements. One sample from this initial processing lot will be dedicated to residual stress characterization.

3. Comparison of LSP and WJP to Traditional Shot Peening – Mechanical property testing in Items #1 and #2 shall be performed for companion M50 and aluminum test specimens processed using traditional shot peening. Fatigue performance and thermal stability of each method and materials will be analyzed for comparison.

4. Cam Component Modeling – PNNL will model the quasi-static stress distribution of fuel injector actuator cam to determine over stressed regions that would benefit from LSP residual compressive stress. PNNL will obtain cam and injector component drawings from Cummins to support model development. Additional modeling will identify high-tensile stress regions of the component that would be candidate areas for LSP.

5. Injector NDE Evaluation – PNNL will develop the capability to apply acoustic excitation and measurement NDE techniques to simulate wave propagation in injectors from dynamic loading in order to evaluate material behavior under such conditions and fast injector actuation. The dynamic behavior and stresses induced will be used to develop schedules for LSP to improve ultra-high cycle fatigue life.

6. Mechanical property testing of FSP cast iron
   a. Process cast gray iron (cylinder head and block material) with friction stir processing and determine optimum processing parameters

   b. Conduct microstructural analysis and understand effect of processing parameters

   c. Evaluate hardness, tensile and fatigue strength at room temperature and higher temperatures that will be seen by the component in an engine. Determine the effect of microstructure and processing parameters on mechanical properties

   d. Evaluate wear resistance and machinability of the processed areas.

   e. Residual stress analysis of the processed area

   f. Prototype components as per applications determined

i.Perform Non Destructive evaluation of prototyped components
ii.Component testing/Engine testing

This project is anticipated to be a 3-year development and demonstration effort and will include active participation by Cummins. PNNL will subcontract LSP Technologies to process steels using LSP and Flow International for water jet peening processing of aluminum. In addition, PNNL will perform the material characterization, selected mechanical properties tests, modeling and NDE development.

Results

Only preliminary work has been completed on this project, parallel with establishing a formal CRADA agreement with Cummins, Inc. Laser shock peening was used to develop residual compressive stresses in 3/8" diameter M50 steel bar specimens to be used for roller contact fatigue tests and evaluation of surface roughness and stress distributions in the specimen. A photograph of a typical specimen is shown in Figure 1 where LSP was applied to the right-hand side of the specimen and the center section remained in the as-received condition.

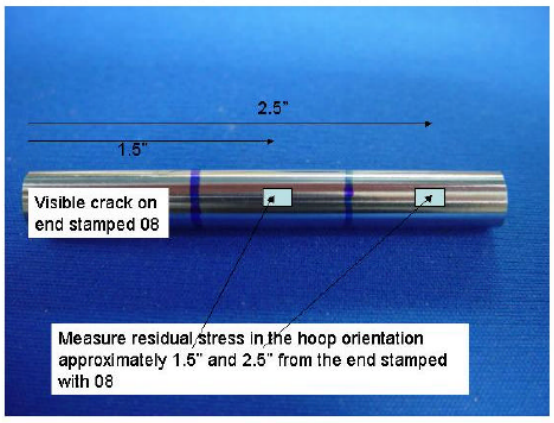

Figure 1. *Photograph of test specimen stress measurement locations.*

Surface polishing, to prepare the specimen for roller contact fatigue, was completed; the subsequent residual stresses were measured and are presented in Figure 2.

The area processed by LSP Technologies shows significant residual stresses (200 ksi at 0.001 inch depth from the surface) in the cylindrical rod specimen. Previous work on similar geometries had failed to generate high magnitude stresses, due to elastic wave reflection.

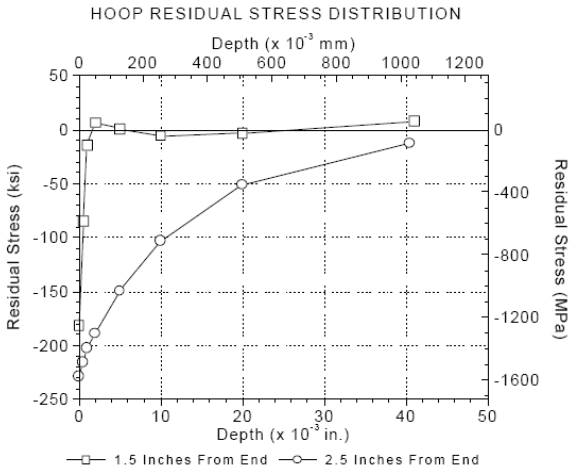

Figure 2. *Stress depth profile in M50 test specimen with LSP surface treatment.*

PNNL established the capability to perform rotating beam fatigue tests, which will better assess fatigue performance in a more prototypical stress state. Equipment to perform this test was purchased from Fatigue Dynamics, Inc. and is shown setup at PNNL in Figure 3.

Figure 3. Rotating Beam Test unit at PNNL.

Conclusions

High magnitude compressive stresses were generated using LSP in cylindrical M50 steel rods.

The surface roughness generated during LSP does require surface polishing, which was successfully completed without removing the subsurface residual stresses.

Presentations and Publications

None.

Key Words

Laser shock peening, waterjet peening, friction stir processing; roller contact fatigue

List of Acronyms Used

CRADA: Cooperative Research and Development Agreement
LSP: laser shock peening
NDE: nondestructive evaluation
WJP: water jet peening
PNNL: Pacific Northwest National Laboratory
RCF: roller contact fatigue
FSP: friction-stir processing
R & D: Research and Development

Agreement 15055 - Friction Stir Processing to Tailor Thermal and Mechanical Properties of CIDI Engine Components for Improved Energy Efficiency

Principal Investigator: Glenn J. Grant
Energy Materials and Manufacturing
Pacific Northwest National Laboratory
902 Battelle Blvd.
Richland, WA 99356
(509) 375-6890; fax:(509) 375-4448; e-mail: glenn.grant@pnl.gov

Co-Investigator: Darrell Herling
Energy Materials and Manufacturing
Pacific Northwest National Laboratory
902 Battelle Blvd.
Richland, WA 99356
(509) 375-6905; fax :(509) 375-4448; e-mail: darrell.herling@pnl.gov

Co-Investigator: M. Brad Beardsley
Advanced Materials Technology
Caterpillar Inc. Tech Center E/854
PO Box 1875
Peoria, Illinois 61656-1875
(309) 578-8514

DOE Technology Manager: Jerry L. Gibbs
(202) 586-1182; fax: (202) 586-1600; e-mail: Jerry.gibbs@ee.doe.gov

---

Contractor: Pacific Northwest National Laboratory
Contract No.: DE-AC06-76RLO1830

Objectives

- To develop Friction Stir Processing (FSP) for engine materials (cast iron, alloy steels, and aluminum alloys), with the goal of increasing their high temperature performance, durability, and thermal properties
- To deploy Friction Stir Processed components that can enable energy efficient engine design strategies, such as HCCI combustion.

Approach

- This project will develop surface modification techniques, modified materials, and components that can withstand higher temperatures and pressures without losing appreciable strength, hot hardness, or wear resistance, and at the same time, be much less thermally conductive for increased thermal efficiency

Accomplishments

- CRADA documents were finalized in October 2007, and an initial kickoff meeting took place Dec. 5-6
- Pre-CRADA accomplishments included preliminary tool design, tool material procurement, and modification of facilities to prepare for Friction Processing trials. Specific tooling and fixturing was engineered and constructed to enable us to use our existing Friction Stir equipment to process the materials and components specified by our CRADA partners.

Future Direction

- Friction Stir Processing of aluminum alloys will begin during the first quarter of 2008 with the goal of improving high temperature fatigue resistance and modifying thermal conductivity
- FSP work on steels and cast iron will begin in the fourth quarter of 2008

Introduction

The objective of this project is to investigate the application of a new material processing technology, Friction Stir Processing (FSP), to improve the thermal and mechanical properties of Compression Ignition Direct Injection (CIDI) engine components. The objective is to produce components with functionally graded surfaces that are optimized for thermal properties and for better in-service performance. The direct goal of the project is to increase the energy efficiency of the engine through better management of thermal conditions, reduced parasitic losses, and indirectly through better part durability and wear resistance. This project is in the first year of a three year effort, and is a CRADA in partnership with Caterpillar, Inc.

Background

Increases in thermal efficiency of internal combustion engines can be gained by decreasing the heat losses from the cylinder during the combustion event. Typical engine efficiencies for CIDI engines are on the order of 35%. The remaining 65% of the fuel heating value goes to approximately 35% energy lost in the exhaust (thermal and chemical) and 30% in other heat losses. These other losses can further be subdivided into: engine coolant (~14%); lubricating oil (~7%); ambient (~4%); and internal parasitic friction losses (~5%)[1] . The heat transfer associated with these other losses is through the cylinder wall, piston, and cylinder head. These components are traditionally made from cast iron, steel and aluminum alloys, which conduct heat fairly well. If thermally insulating materials or thermal barriers were employed, heat transfer would be reduced, and if taken to the theoretical extreme of no heat loss, the engine efficiency would reach the adiabatic limit.

The effective impact of improving thermal efficiency can be expressed by an increase in either fuel economy, or increase in engine power output. This improvement can be estimated by how much of the additional heat retained (reduced heat loss) is actually utilized during the expansion stroke when useful work (shaft power) is produced. Heat loss occurs over the entire 4-stroke cycle, or 720º of crankshaft rotation. However, the expansion stroke accounts for only 25% of the total cycle, or 180º. About 35% of the available energy in the fuel is converted to useful work (thermal efficiency) during the expansion stroke. If a 15% decrease in heat loss energy were accomplished, the estimated power output gained, or fuel saved would be: [(0.15)*(0.35/4)], or 1.3%. A 1% improvement in fuel economy applied to Class 8 line-haul trucks would save approximately $3x10^{13}$ BTU/yr of energy, or roughly equivalent to 5.3 million barrels of oil per year[2] .

Most of the remaining reduced heat loss energy (75%) ends up increasing the enthalpy of the exhaust gas. An added benefit is that a portion of this enthalpy increase can recovered by the turbocharger, and further increasing the overall engine efficiency. However, these efficiency improvements also result in hotter engine components, and an increase burden on materials. Therefore, materials with improved high temperature behavior with lower thermal conductivity are needed. Nickel, titanium, ceramics and similar materials or coatings can potentially be employed. However, these materials are either cost prohibitive, or have significant durability problems when used in engine applications.

To achieve improved high temperature behavior with lower thermal conductivity, surface engineering can produce an alternative to

[1] [1] W.W. Pulkrabek, Engineering Fundamentals for the Internal Combustion Engine, 2nd Ed., (2004)

[2] Annual Energy Outlook 2005 DOE/EIA-0383(2005)

monolithic materials. Conventional coatings technologies are appropriate in some environments, but often suffer durability problems in the high temperature and high stress conditions seen in the combustion chamber of a CIDI engine. Compositionally graded structures may be more appropriate, allowing for smoother property gradients while providing enhanced durability or thermal barrier properties in the near surface region.

Friction Stir Processing is a new technology that has an opportunity to be used to create compositionally graded surfaces. In recent years, PNNL has worked on developing techniques and tools that allow FSP to be accomplished in steels, cast iron and aluminum (Figure 1). The process for these materials is far from commercially ready, but early work by PNNL and the South Dakota School of Mines & Technology (SDSMT) has shown the potential for success if additional investments are made to further develop and optimize the technology.

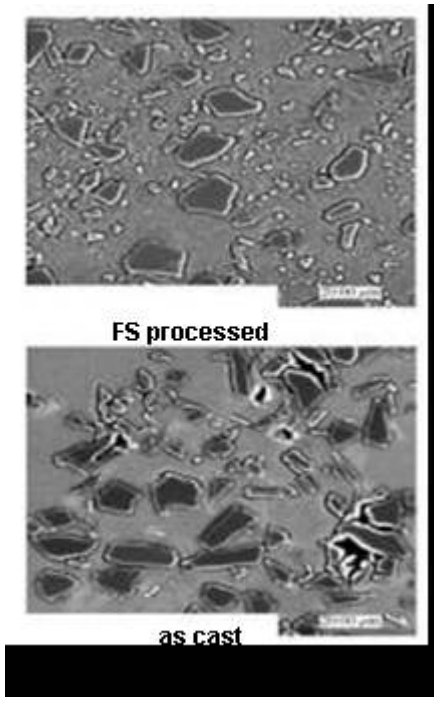

a

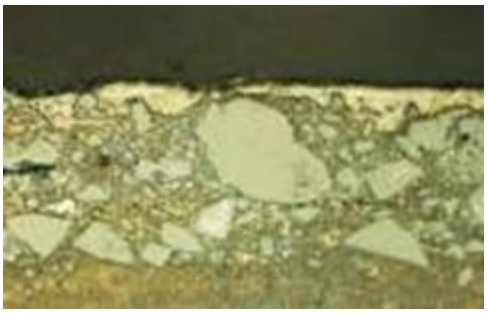

b

Figure 1 - 1a - Friction stir processing can close porosity in castings, producing better fatigue performance. The micrographs illustrate a cast aluminum MMC in the as-cast condition on the bottom, and as-friction stir processed (top) 1b - Ceramic particulate can also be stirred into the surface to produce functionally graded surfaces and near surface MMCs.

Figure 2 - Tool design is a critical component of successful FSP

FSP is an outgrowth of friction stir welding (FSW), invented by TWI, Ltd. 17-years ago. It was recognized that the same techniques and processes used to make a friction stir weld could

be used to process a material for enhanced properties. The process can be selectively applied to the surface of a material, and it alters the microstructure by the severe plastic deformation that occurs in the processed zone. FSP can create a robust and graded structure with fundamentally different properties than the underlying surface, and has been shown to produce surface regions with improved fatigue life, ductility, and strength.

Friction Stir Processing produces a surface modified region that is different from a coating. Commonly, surface treatments designed to enhance wear or thermal performance include various coating methods, or fusion-welded hard facings. Most of these processes are liquid state and often involve detrimental temperature effects on the base material. Heat affected zones in the base metal and various deleterious high temperature reactions can create a coated part with less than desirable properties. Also, traditional thin coatings can suffer from issues involving the nature of the interface between the coating and the base material (spalling, debonding, and cracking on the interface), especially under high stress, gouging wear conditions, or under cyclic thermal conditions where CTE mismatch is an issue. Also, failure of a coating under high loading conditions can occur when the substrate below a thin hard coating fails by plastic deformation. Friction Stir Processed regions can show significant robustness over traditional coatings for two reasons. First, FSP produces a modified region that transitions to the base material without a sharp interface. Secondly, the modified region is generally thicker and the transition region wider than traditional coating because the plasticized region depth is related to the tool geometry; specifically the depth and size of the pin.

It is also possible to use FSP to "stir" insoluble ceramic particles from the surface into the substrate to depths limited only by the FSP tool geometry (Fig. 2), in order to create unique surface properties, including increased hardness, wear resistance and thermal characteristics. Figure 3 shows initial trials designed to show the feasibility of stirring ceramic surface coatings into the substrate to modify the thermal conductivity of the base material. To-date the addition of up to 20% ceramic to aluminum has been demonstrated, and approximately 10% addition to steel has been achieved. These trials demonstrated the feasibility, but it is clear that more work is needed to bring the ceramic loading up to the point where it will strongly affect the thermal conductivity.

Photo courtesy South Dakota School of Mines and Technology

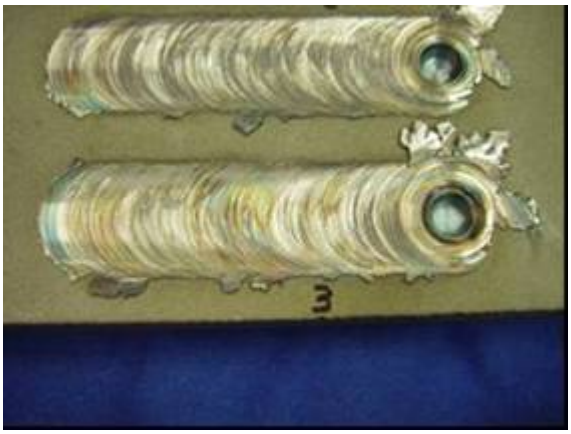

Figure 3 - Initial trials showing FSP can be used to stir thermal barrier coatings into steel plate. Surface coating was distributed into the substrate, but process parameter optimization and tool design changes will be needed to increase ceramic loading to the point where thermal conductivity is strongly affected.

Approach

This project proposes to experimentally develop the FSP processes and technologies required to engineer the surface of propulsion materials for improved properties. The application focus will be to tailor the mechanical properties and thermal conductivity of engine materials, both ferrous and non-ferrous, by using FSP techniques. This microstructural modification is expected to lead to a set of materials with enhanced surface properties

that can handle increased exhaust temperatures and lower heat losses, resulting in improved engine efficiency.

The project scope will involve developing the FSP manufacturing parameters, selecting and evaluating proper tool materials and techniques to produce defect free FSP regions. In addition, methods to introduce higher volumes of insoluble or elemental powders up to 50% will be developed. Coupon level testing and evaluation of the thermal and mechanical properties will be conducted, focusing on specific performance targets identified by project partners. If performance metrics are met for sample materials enhanced by FSP, then additional research will include developing and demonstrating the appropriate method to apply this process to a 3-D geometry. If successfully developed, this class of engineered materials can significantly impact the efficiency and durability of CIDI and potentially address some of the technical barriers to implementing Homogeneous Charge Compression Ignition (HCCI) engines.

Results

CRADA agreements and contracts were finalized in October 2007 and a project kickoff meeting was recently completed in December 2007. Pre-CRADA efforts were directed towards the design and installation of specific equipment required to FSP cast iron and steel materials. Included in this equipment is an actively cooled tool holder for our existing Friction Stir machine shown in Figure 4, and larger hardened anvils for coupon and part fixturing during FSP. In addition literature and research program reviews were completed to establish the state of the art processing techniques, and tool material suppliers were engaged to provide the required FSP tools for the program.

Figure 4 - Friction Stir machine at PNNL. This machine has an 8 ft. horizontal by ~ 5 ft. vertical working envelope, and a 30,000 lb Z force and 8000 lb X Force capability, while maintaining a 0.0002" spindle run out so that ceramic tooling can be used.

Stir tools for FSP modification of aluminum substrates will be composed of FerroTic, a tool steel based MMC with 50% TiC particulate in a matrix of high hot-hardness tool steel. Tooling for FSP of steels will initially be tungsten-rhenium, but polycrystalline cubic boron nitride, and some new tool materials will be employed as the project progresses. Many of these tool materials have been procured and will be machined into appropriate designs during the first quarter of 2008.

FSP of steels and cast iron requires that the tool itself is actively cooled. During 2007 a cooling system and cooled tool holder was designed and constructed that allow cooling fluid to directly impinge on the interior of the tool through a cooling channel in the tool itself (Fig. 5). Control systems allow for tight control of coolant flow rate and temperature.

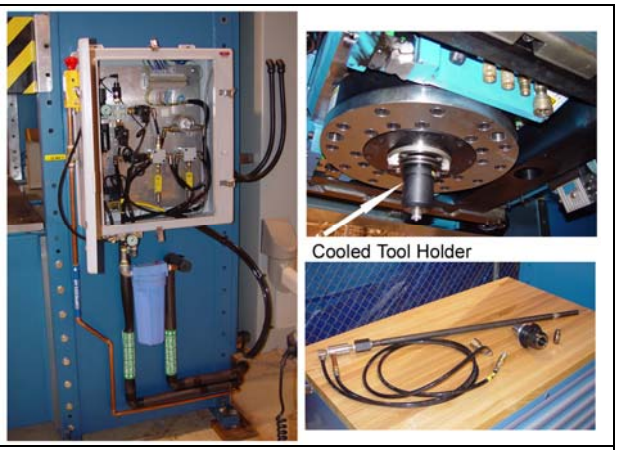

Figure 5 - Tool cooling control system and cooled tool holders

Steel and cast iron FSP also requires additional heat during the plunging phase of the processing run. This is because drastic tool wear can occur when a cold tool is driven down into a cold substrate. Induction heating of the plunge zone as been found, in earlier work by PNNL and SDSMT, to be necessary to preserve the life of the tooling. During 2007 modifications to our existing induction heating equipment were completed so that this equipment can provide the power to custom designed coils that will be mounted on the FSP spindle assembly. Induction heating will be used both to pre-heat the plunge area, and to accomplish post-processing heating to effectively slow the cooling rates after processing. It may be possible to essentially heat treat in-situ and affect the final microstructure by providing a moving induction heat source behind the stir tool. This process will be developed further towards the end of 2008.

Conclusions

The goal of this project is to increase the thermal efficiency and durability of CIDI engines using a new surface engineering strategy, Friction Stir Processing (FSP). FSP produces wide, graded structures that have shown to increase strength and durability in fatigue, compared to some conventional coating technologies. Surface modification through FSP may have an opportunity to address some emerging material problems, as seen in very high combustion pressure systems, like HCCI engines. In addition, the process allows for the incorporation of insoluble particulate into the surface, potentially decreasing thermal conductivity and increasing thermal efficiency.

Collaborative project work started in Oct 2007. The project is a three year CRADA with Caterpillar Inc. FSP of aluminum materials will be investigated during the first half of 2008 and FSP in steels will begin in the last half of 2008.

Agreement 16103 - Concept Feasibility of Bonding Similar and Dissimilar Powertrain Materials Using Reactive NanoFoils

Principal Investigator: Xin Sun
Computational Science and Mathematics Division
Pacific Northwest National Laboratory
Richland, WA 99352
(509) 372-6489; fax: (509) 372-6099; e-mail: xin.sun@pnl.gov

DOE Technology Manager: Jerry L. Gibbs
(202) 586-1182; fax: (202) 586-1600; e-mail: Jerry.gibbs@ee.doe.gov

Contractor: Pacific Northwest National Laboratory
Contract No.: DE-AC06-76RL01830

Objectives

- Provide objective bond strength evaluation for NanoFoil bond in comparison with conventional bonding methods.
- Provide cost and cycle time analyses of using reactive NanoFoil in mass production environment.

Approach

- Perform bond strength evaluations for similar and dissimilar metals joints (AHSS, Al, Mg)
- Perform bond strength evaluations for metal/non metal (ceramic, polymer) joints
- Perform economic study considering cost, bond quality and cycle time for automotive manufacturing environment.

Accomplishments

- Finished bond strength evaluations for similar and dissimilar metals joints.
- Finished preliminary cost and cycle time analyses in qualitatively identifying the cost component for NanoFoils.

Future Direction

- Perform bond strength evaluations for metal/non metal (ceramic, polymer) joints
- Perform quantitative economic study considering cost, bond quality and cycle time for automotive manufacturing environment.

Introduction

Advanced joining technology remains to be the key enabler for the engine OEMs since implementation of advanced combustion technologies will require very high fuel pressures, higher peak combustion chamber pressures, and better air handling and thermal management. Currently, fusion welding and adhesive bonding are the main joining technologies being used in the heavy vehicle production environment. While proven to be reliable in joining conventional materials, these methods have drawbacks in joining similar and dissimilar advanced lightweight materials such as advanced high strength steel (AHSS) and aluminum castings and magnesium. For example, the high heat input of fusion welding tends to destroy the designed microstructures of AHSS, rendering less than desirable joint properties.

In this project, we propose to study the performance and cost feasibility of an alternative bonding technology, namely, reactive NanoFoil bonding, in the area of heavy vehicle powertrain applications. Applications can include and range to the following: Joining of dissimilar metals in lighter weight, high performance compression ignition engines: such as high hardness steel shafting to lighter weight titanium impellers and air handling components, joining metal composite to machinable steel shafting and bearing surfaces, joining metals to ceramic high-wear inserts, joining of corrosion-resistant stainless steels and nickel-based alloys for protection of steel and iron substrates for reduced cost and improved performance.

NanoFoil is a multi-layer foil fabricated through the growth of thousands of nanoscale layers of aluminum and nickel by vapor deposition. Initiated by an energy impulse, the like-like bonds of the atoms of each layer in the foil are exchanged for more stable unlike bonds between atoms from neighboring layers. As the atoms of each layer mix, heat is generated, creating a self-sustaining reaction, therefore localized heat source, traveling along the length of the foil. This type of self-propagating exothermic formation reactions have been observed in a variety of nanostructured multilayer foils, and the reactions are driven by a reduction in atomic bond energy (Ref. 1). The instantaneous release of heat energy by this reaction is controlled by the nanolayer thickness and lay-up, such that accurate control of highly localized heat input can be realized, allowing bonding without compromising the properties/integrities of the base materials.

Since this is a very new joining technology, the scopes of PNNL's feasibility work include:

- Provide objective bond strength evaluations for NanoFoil bond in comparison with conventional bonding/joining methods;
- Provide engine OEMs with cost and cycle time analyses for using reactive NanoFoil in mass production environment.

Approach

In order to provide an objective evaluation of bond strength between similar and dissimilar metals bonds, the following material combinations, i.e., joint populations, are examined:

- 1.4 mm SAE1008/1.4 mm SAE1008 solder joint
- 2 mm AA5182-O/2 mm AA5182-O solder joint
- 2 mm AA5182-O/2 mm AZ31 solder joint
- 2 mm AA5182-O/2 mm AA5182-O braze joint

The following technical approach is followed for each joint population:

- Braze/solder each joint population with selected solder, braze material
- Examine microstructures of base material and bonded region
- Perform bond strength tests under tensile shear configuration
- Compare tested bond strength with conventional adhesive bonded joints

Results

1.4 mm SAE1008/1.4 mm SAE1008 solder joint

The tensile shear sample size is 2x4 in. with a bonded area of 2x2 in. First, 96.5Sn-3.5Ag solder material is pre-applied to the bond surfaces on a hot plate using flux. Next, a thin layer of reactive NanoFoil slightly larger than the size of the bonded area is sandwiched between the two bond surfaces.

An energy impulse is then applied at one corner of the NanoFoil by shorting the anode and cathode of a 9 volt battery. The heat generated by the exothermic reaction of the NanoFoil self-propagates over the entire bond area, melts the solder material on both sides, and forms the bond. The NanoFoil used in the current work is produced by Reactive Nano Technology (RNT) in Hunt Valley, Maryland.

After the bonding process is completed, the bonded region is scanned to ensure bond quality. Figure 1 shows the typical scanned image of the bonded region for the 1.4 mm SAE1008/1.4 mm SAE1008 solder joint. The very dark areas correspond to cracks in the NanoFoil that have been filled up with solder. Only the very bright white areas correspond to voids. The bond scan here shows that bonded region covers more than 99% of the entire surface. Therefore good quality bonds have been achieved.

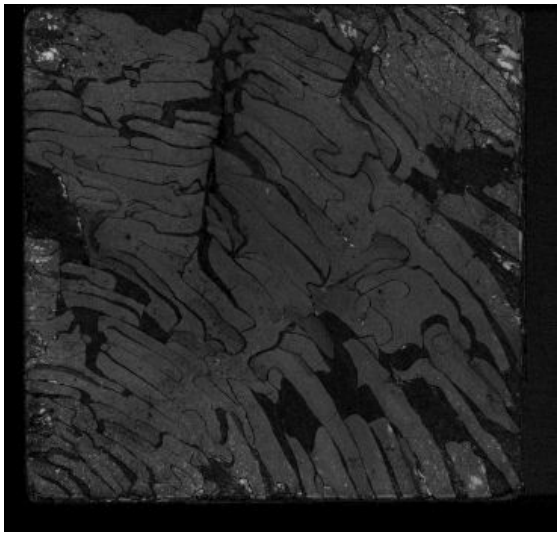

Figure 1. Scan image of the bonded area

Mechanical bond strength test is next performed by subjecting the bonded sample under tensile shear loading in an MTS test frame. Five samples are tested for each population to examine the strength variation within each joint population. Figure 2 (a) and (b) show the typical load versus displacement curve and failure mode for the 1.4 mm SAE1008 to 1.4 mm SAE1008 solder joint. Obviously, very high bond strength has been achieved since tensile shear failure for all the samples occurred in the base material. Taking the peak load from these tests and divided by the bond area, it is determined that the nominal bond strength is in excess of 10.6 MPa.

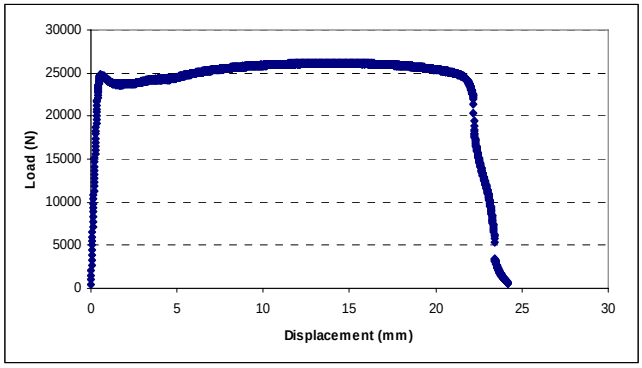

(a)

(b)

Figure 2. Typical bond strength test results for the solder joint of 1.4 mm SAE1008/1.4 mm SAE1008: (a) Load versus displacement curve; (b) Failure mode

2 mm AA5182-O/2 mm AA5182-O solder joint

Following similar procedures described above, 2 mm AA5182-O is bonded with 2 mm AA5182-O with solder material 96.5Sn-3.5Ag. The solder material is pre-applied to samples on a hot plate using mechanical agitation. Again, NanoFoil is used as the heat sources for the actual bonding process. Figure 3 shows the typical scanned image of the solder joint. Good bond quality has been obtained with respect to the coverage area.

Figure 4 (a) and (b) show the typical load versus displacement curve and failure mode for the 2 mm AA5182-O/2 mm AA5182-O solder joint. Cohesive failure is consistently observed at the bond surface for all the samples tested. The nominal bond strength is from 6.3 MPa to 9.5 MPa. The failed

samples were bent, indicating ductile bond failure for good energy absorption.

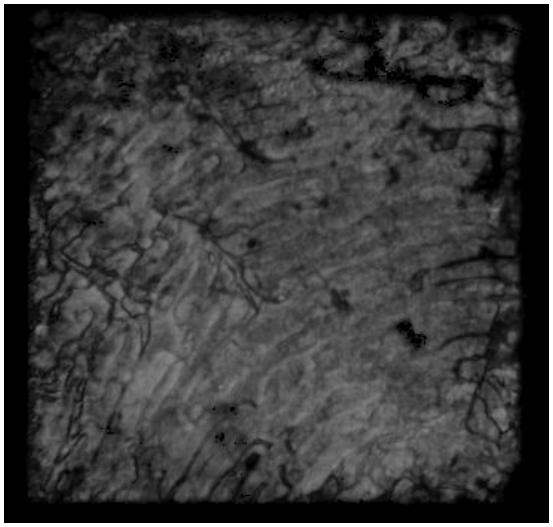

Figure 3. Scan image of the bonded area

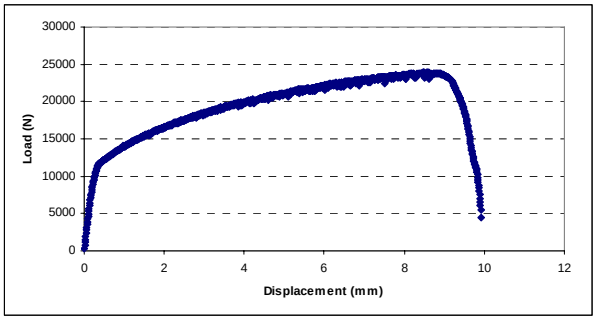

(a)

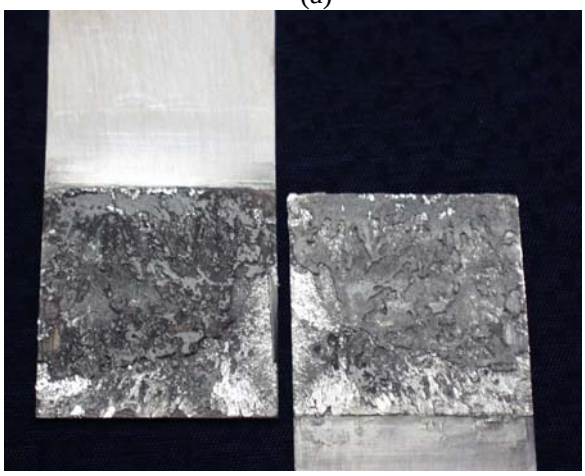

(b)

Figure 4. Typical bond strength test results for the solder joint of 2 mm AA5182-O/2 mm AA5182-O: (a) Load versus displacement curve; (b) Failure mode

2 mm AA5182-O/2 mm AZ31 solder

For this population, 96.5Sn-3.5Ag solder material is pre-applied to the aluminum samples on a hot plate using mechanical agitation. On the magnesium side, samples were vapor metalized with Ti/ Incusil (Incusil = 61.5Ag-23.5Cu-15In) braze, with freestanding Sn-Ag-Cu (SAC) solder sandwiched between metallization and NanoFoil. Figure 5 shows the typical scanned image of the solder joint. For this joint population, many small bright white regions exist at the bond interface indicating some degree of lack of bonding.

Figure 6(a) and (b) show the typical load versus displacement curve and failure mode for the 2 mm AA5182-O/2 mm AZ31 solder joint. Adhesive failure at bond surface is consistently observed for all the samples tested. The nominal bond strength is from 2.86 MPa to 4.9 MPa. The failed samples have very little bending deformation in them, indicating a brittle joint with low level of energy absorption.

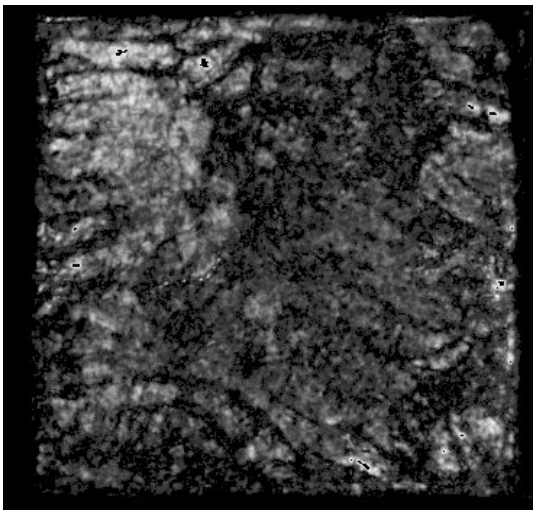

Figure 5. Scan image of the bonded area

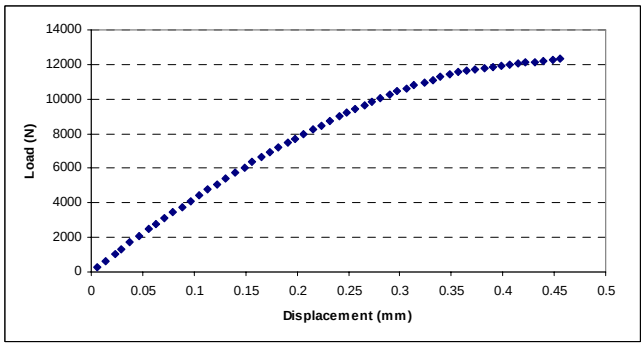

(a)

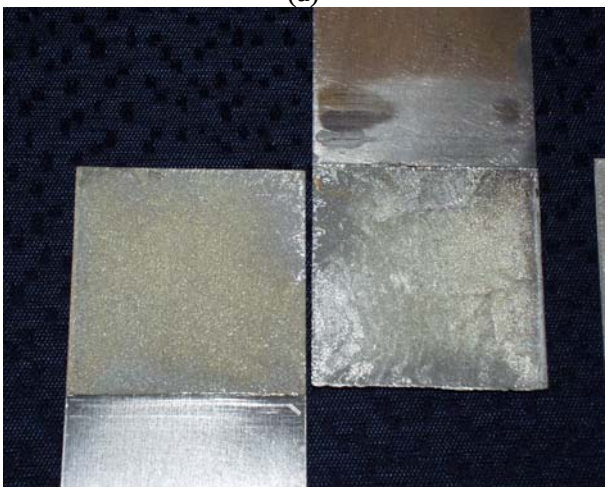

(b)

Figure 6. Typical bond strength test results for the solder joint of 2 mm AA5182-O/ 2 mm AZ31: (a) Load versus displacement curve; (b) Failure mode

<u>2 mm AA5182-O/2 mm AA5182-O braze</u>

For this population, the aluminum samples were metalized with 95Ni-5Al via thermal spray (wire arc spray). The NanoFoil is coated with thin braze (Incusil) layers. During the bonding process, the braze material (Incusil) is melted by the heat generated by the NanoFoil, then sticks to the Ni coating, which does not melt during the bonding process. Figure 7 shows the typical scanned image of the braze joint. Good bond quality has been obtained with respect to the percentage of bonded area.

Figure 8(a) and (b) show the typical load versus displacement curve and failure mode for the 2 mm AA5182-O/2 mm AA5182-O braze joint. Cohesive failure at bond surface is consistently observed for all the samples tested. The nominal bond strength is from 7.5 MPa to 8.02 MPa, with much smaller strength variation compared to the solder joint population. All the failed samples show bending deformation, indicating ductile bond failure with good energy absorption capability.

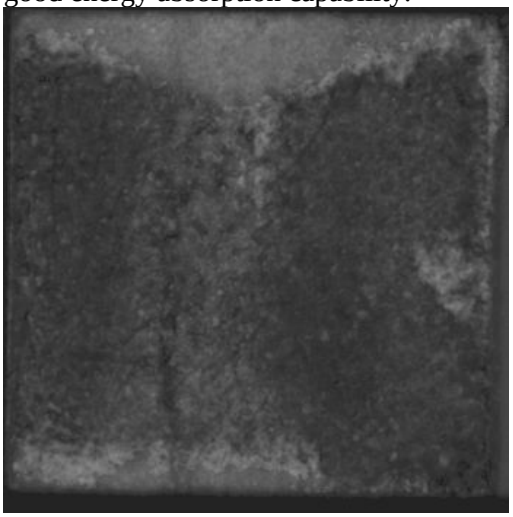

Figure 7. Scan image of the bonded area

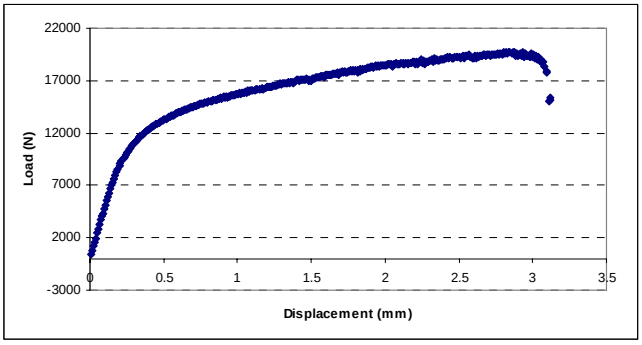

(a)

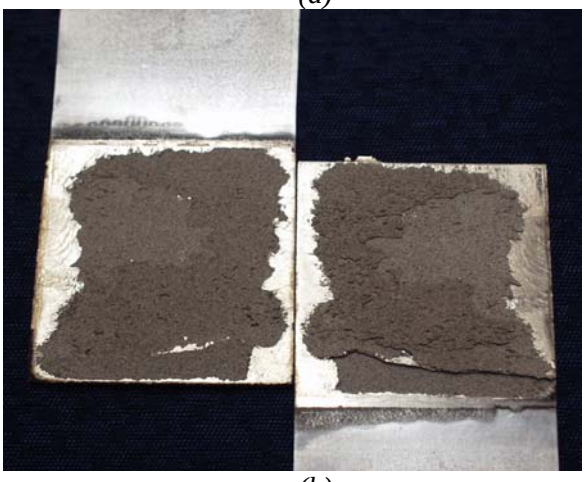

(b)

Figure 8. Typical bond strength test results for the braze joint of 2 mm AA5182-O/2 mm AA5182-O: (a) Load versus displacement curve; (b) Failure mode

Comparison with Automotive Adhesive Bonds

Figure 9 shows the typical joint strength test data for Dow Betamate 4601 and Betamate 1480 structure adhesives joining 2 mm AA5182-O to 1.6 mm DP600 steel (Ref. 2). Under tensile shear (lapshear) loading condition, cohesive failure mode is consistently observed and the nominal bond strength is around 7.2 MPa.

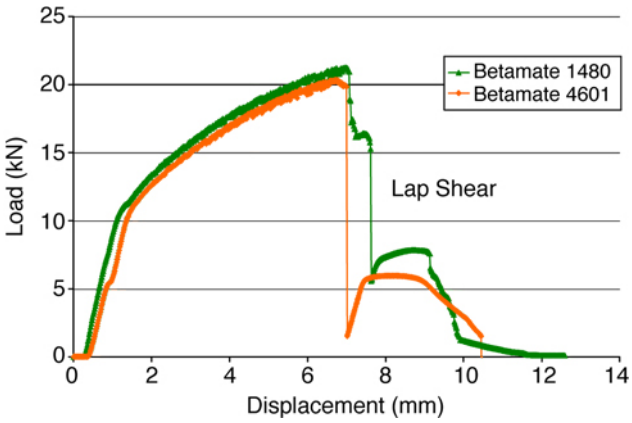

Figure 9. Bond strength test results for Dow Betamate 4601 and Betamate 1480 joining 2 mm AA5182-O to 1.6 mm DP600.

Conclusions

Comparing the bond strength of the four NanoFoil bond populations with those of the structural adhesives, the following observations/conclusions can be made:

1. Similar or higher bond strength can be obtained using reactive NanoFoil bonding for the 1.4 mm SAE1008/1.4 mm SAE1008 solder joint, 2 mm AA5182-O/2 mm AA5182-O solder and braze joints.
2. Bond strength variation is higher for the solder joints than the braze joints.
3. Bond strength for the 2 mm AA5182-O/ 2 mm AZ321 solder population is considerably lower than that of the 2 mm AA5182-O/2 mm AA5182-O solder joint. More studies on the braze material is needed to improve the joint strength and energy absorption level.

References

1. Wang, J., Besnoin, E., Duckham A., Spey, S.J. Reiss, M.E., Knio, O.M. and Weihs, T.P. *J. Appl. Phys.*, Vol. 95(1), January 2004, pp. 248-256.
2. *Joining of Dissimilar Metals for Automotive Applications: From Process to Performance*, Automotive Lightweighting Materials, FY2004 Annual Progress Report.

Presentations and Publications

1. Sun, X. and Duckham, A. "Strength Evaluation of Reactive Nano-Foil Bonded Joints for Automotive Applications," to be presented at the XIII Sheet Metal Welding Conference, Detroit, May 2008.

Project 18519 - Materials for Control of Exhaust Gases and Energy Recovery Systems

Agreement 9130 - Development of Materials Analysis Tools for Studying NO_x Adsorber Catalysts (CRADA No. ORNL-02-0659 with Cummins, Inc.)

Thomas Watkins, Larry Allard, Doug Blom, Michael Lance, and Harry Meyer
Oak Ridge National Laboratory
P.O. Box 2008
Oak Ridge, TN 37831-6064
(865) 574-2046; fax: (865) 574-3940; e-mail: watkinstr@ornl.gov

DOE Technology Manager: Jerry L. Gibbs
(202) 586-1182; fax: (202) 586-1600; e-mail: jerry.gibbs@ee.doe.gov
ORNL Technical Advisor: D. Ray Johnson
(865) 576-6832; fax: (865) 574-6098; e-mail: johnsondr@ornl.gov

Contractor: Oak Ridge National Laboratory, Oak Ridge, Tennessee
Contract No.: DE-AC05-00OR22725

Objective

- The purpose of this effort is to produce a quantitative understanding of the process/product interdependence leading to catalyst systems with improved final product quality, resulting in diesel emission levels that meet the 2010 emission requirements.

Approach

- Characterize lab-engine tested samples with X-ray diffraction (XRD), spectroscopy, and microscopy. Correlate findings with Cummins data and experience.

Accomplishments

- The evaluation of degradation of a commercial zeolite urea SCR catalysts and a model catalyst as a function of operating conditions defined by the end user has been completed.
- Supported continued characterizations of new materials from various stages of the catalyst's life cycle.

Future Direction

- Characterization of a commercial zeolite urea and model SCR catalysts subjected to hydrothermal aging for lifetime prediction model input. Focus on understanding the catalyst degradation mechanisms due to hydrothermal aging using the tools developed under this CRADA.
- Assist Cummins to competitively produce engines which attain the required emission levels for 2010 and beyond while maintaining the advantage of the diesel's inherent energy efficiency.
- Continue to characterize the soot, coke and ash formed on the catalyst from different fuels, including biodiesel.

Introduction

In order to meet the 2007 US Environmental Protection Agency (EPA) emission requirements for diesel exhaust, aftertreatment in diesel engines may be necessary. The technology necessary for 2007 will need to integrate aftertreatment with engine control systems. Currently, no commercial off-the-shelf technologies are available to meet these standards. Consequently, Cummins Inc. is working to understand the basic science necessary to effectively utilize these catalyst systems. ORNL is assisting with the materials characterization effort. Prior reports and presentations have covered the accomplishments related to the NO_x adsorber catalyst and diesel oxidation catalyst technologies, this report will focus on the study of materials used in selective catalytic reduction.

Selective catalytic reduction (SCR) is one possible method to reduce NOx emissions. Here, a gaseous or liquid reductant is added to the exhaust gases and adsorbed on to the catalyst, sometimes a zeolite. The reductant reduces NOx to H_2O and N_2.[1] Urea is a typical reducing agent which can operate under lean or oxygen rich conditions as follows:[2] $(NH_2)_2CO + 2NO + 1/2O_2 \Rightarrow 2N_2 + 2H_2O + CO_2$.

A zeolite is classically defined as a crystalline, porous aluminosilicate. More recently, zeolites are defined as porous oxide structures with well-defined pore/channel structures and a high degree of crystallinity. There are an unlimited number of structures possible, making them particularly useful as molecular sieves.[3] There are many chemical interactions with zeolites which center around $Si\text{-}O_4$ and $(Al\text{-}O_4)^{-1}$ tetrahedra and the cations within the pores, supplying charge compensation. Zeolites are often used as ion exchangers in water softeners and shape selective catalysis. The cation with H+ becomes a strong acid, which is catalytically active.

Samples and Approach

New commercial Fe-zeolite powder is being examined with diagnostic tools developed previously under this CRADA. The crystal structure, morphology, phase distribution, particle size, and surface species of catalytically active materials supplied by Cummins will be characterized using transmission electron microscopy (TEM), X-ray diffraction (XRD), X-ray photoelectron spectroscopy (XPS), and Raman Spectroscopy. These materials will come from all stages of the catalyst's life cycle: raw materials, as-calcined, sulfated, regenerated, etc. Both ORNL and Cummins personnel have participated in this work to understand zeolite degradation.

The new commercial Fe-zeolite powder, both fresh and degreened, was examined with diagnostic tools developed under the CRADA. Here, degreened means the powder was heated to 500, 700, 900 and 1100°C for 12 hours in air.

Results

The above samples were examined with microscopy, XRD and Raman from October 2006 to September 2007, which is summarized below.

Microscopy

Characterization of commercial Fe-zeolite materials by electron microscopy techniques was continued during this quarter. To date, four separate specimens have been examined, comprising either powder or ion-milled sections of monoliths, as shown in Table 1. Typical results and observations of the Fresh, Degreened and Fresh + 700°C aging samples are reported.

Powder samples were prepared typically by dry-dipping a TEM grid covered by a holey carbon film into the provided powder, shaking off the excess, and loading the grid into the TEM specimen holder. TEM samples were also prepared from sections of both "Fresh" and "Aged" catalyst monoliths, by embedding a section in epoxy, slicing a thin (<300μm) wafer normal to the monolith channels, and finally isolating a single cordierite "cross" from the wafer for grinding, dimpling and argon ion-beam milling. The milled samples had electron transparent regions that subtended the washcoat layer, so that the structure of the zeolite washcoat could be imaged. Samples were examined in either the HTML's Hitachi HF-2000 field-emission TEM which is equipped with an energy-dispersive x-ray spectrometer (EDS) system for elemental analysis, or the new JEOL 2200FS-AC aberration-corrected electron microscope (ACEM). This instrument provides high-angle annular dark-field (HA-ADF) imaging simultaneously with bright-field (BF)

imaging, and allows imaging at the sub-Ångström level.

The following sections show typical results obtained from samples shown in red in the Table 1, on both ACEM and HF-2000 instruments.

H-Beta-Zeolite (Un-doped) Powder: ACEM Results

An un-doped H-beta-zeolite powder was obtained from Cummins, Inc. Figures 1a and 1b are a HA-ADF/BF image pair acquired at a magnification suitable to show the zeolite lattice structure in the BF image. This image area represents a reasonably uniform thickness of the sheet-like morphology of zeolite structure. Note that the HA-ADF image shows a smooth, low-contrast structure, in comparison to the open network lattice structure in the corresponding BF image. There is no evidence of bright contrast regions that might correlate to the presence of dopant (viz., Fe) atoms or clusters in the structure, as are seen in all the Fe-doped samples in the following sections.

Fresh Powder: ACEM Results

HA-ADF imaging in scanning transmission mode (STEM) on the ACEM shows heavy elemental species in bright contrast relative to light element support material. A typical HA-ADF/bright-field pair of images that were acquired simultaneously is seen in Figure 2. The BF STEM image clearly shows the channels in the zeolite material, while the HA-ADF image shows the Fe-rich phase in the specimen in bright contrast. The Fe-rich phase is distributed uniformly over the surface of the zeolite and ranges between 2-7 nm in spatial extent. However, the relatively faint contrast of the Fe-rich phase, and the fact that it is not clearly evident in the associated BF image, suggests that it is distributed in thin layers either over the surface or within the bulk of the zeolite particles. This is made clearer by the observation of a discrete crystalline particle, as shown in bright contrast in Figure 3. The inset in Fig. 3a shows the lattice structure in the small crystallite; in most instances, the bright contrast in the HA-ADF images in the zeolite structure did not show such lattice structure, as shown by the fainter areas in bright contrast surrounding the crystallite in Figure 3a. The lattice spacing shown in the inset measured to be 2.02Å, via a Fourier transform analysis of the particle periodicity. This is very close to the 2.04Å {110} interplanar spacing of elemental iron. No common oxide (FeO, Fe_2O_3 or Fe_3O_4) has an equivalent spacing as close to the measured spacing as the Fe {110}. Such discrete particles were rarely observed in the fresh sample. However, it is not likely that particles of pure Fe would be present in the zeolite, given the fact that it is energetically favorable for Fe to oxidize rapidly, particularly in fine particulate form. No chemical analysis capability is presently available on the ACEM, so the primary composition of the particle could not be determined. Analysis of the Fresh Zeolite sample in the HF-2000 FE-TEM allowed energy dispersive spectra to be acquired, as discussed in the following section.

Fresh Powder: HF-2000 TEM Results

Since only BF imaging is available on the HF-2000 instrument, there was no opportunity for correlating the bright contrast features seen on the ACEM directly with corresponding features on the BF images from the HF-2000. Figure 4 is an example of a typical zeolite aggregate, showing (circled) a thin region with dark patches. Inset in Figure 4 is the EDS spectrum acquired from the circled area, which shows distinct Fe K-alpha and K-beta peaks. This strongly suggests that the dark patches are primarily Fe, but no determination of the oxidation state was possible because of the strong oxygen component of the zeolite.

Fresh Powder, Ion-milled sample: ACEM results

Cross section samples were prepared from a catalyst monolith provided in the Fresh condition; that is, with the washcoat of zeolite material equivalent to that in the Fresh powder sample. The monolith was vacuum-impregnated with a mounting epoxy, and thin slices subsequently ground, polished and dimpled for the ion milling process. This TEM sample was then argon-ion-milled using standard techniques, which allowed observation of electron transparent areas. These areas were uniformly thin, giving more reliable information on the distribution of Fe within the zeolite structure throughout the entire washcoat. Although more observations remain in order to quantify the Fe distribution, some interesting characteristics of the Fe species were made from the initial studies.

Figure 5 shows HA-ADF images of two different areas of the washcoat having the Fe patches similar to those observed in the Fresh powder

sample. However, these areas seemed to have more discrete patches of Fe than typical in the powder images. The faint patches seen in the corresponding BF images are, however, consistent with the observations of Fresh powder aggregates, suggesting that the observed patches are likely not crystallites as observed in Figure 3. Figure 5c shows an interesting contrast feature in the largest patches (~5 nm) reminiscent of a 'core-shell' structure seen often in bimetallic catalysts, but the BF image does not confirm a 3-dimensional crystallite (which would show in much better BF contrast). This contrast may be due simply to an unequal distribution of Fe within the zeolite structure in this area; it was not seen commonly in other areas.

Fe Zeolite Degreened at 500°C

The primary observation from the ACEM imaging of the degreened powder material was that there was no distinction between the Fresh and the 500°C degreened material in terms of the structure, size and distribution of the Fe patches. This is shown by typical HA-ADF images of two areas of the degreened sample (Figure 6). The Fe patches in these images and others are similar to the Fresh powder structure as shown in Figure 1, with patches 1-4 nm in size. However, degreening at 700°C produced noticeable changes in the Fe structure within the support material, as shown next.

Fe Zeolite Degreened at 700°C: ACEM results:

The primary conclusion of the initial analysis of the effects of degreening at 700°C was that the Fe species showed a non-homogeneous structure or distribution within the powder support material. Figure 7 shows HA-ADF and BF images of an area typical of most of the aggregates observed. The Fe species in the HA-ADF image appear to be essentially unchanged from the structure observed in the Fresh and the 500°C degreened samples. The BF image shows only faint dark patches (and the lattice structure of the zeolite), suggesting that the Fe patches are still not significantly 3-dimensional (where they would appear in stronger contrast in both HA-ADF and BF images). Other areas in the sample, however, showed a different morphology. Figure 8 is a HA-ADF/BF pair of images of a different area of the 700°C degreened sample. These images show very distinct Fe patches, in bright contrast in the HA-ADF image, and in dark contrast in the BF image. The patches are in some cases much larger (~5-10 nm in largest dimension), and not as uniform in size as the initial patches. This suggests that the Fe species have agglomerated into patches that are thicker and perhaps more crystalline than the original morphology. The tendency for growth into a more organized crystalline structure is seen at low and high magnification (Figure 9a and 9b, respectively). Figure 9b in fact shows a larger Fe patch (but still only 2 nm in size) with an alignment of atoms into a structure with clear periodicity. The bright contrast of this particle with respect to the fainter patches suggests a structure several atomic layers thick. This image is at high resolution, and also shows single atoms, dimers, and very small clusters of Fe, which the first resolution of Fe at the single-atom level ever, as far as we are aware.

These observations suggest that the degreening treatment causes a rearrangement of the Fe species into more discrete particles that may eventually grow into regular crystals. However, additional imaging is needed to clarify the progression of changes in the Fe species morphologies with time at temperature in further aging experiments. Results will be reported in following quarterlies.

Microscopy Summary:

1. Fresh Fe Zeolite powder shows "patches" of Fe 1-4 nm in extent, which seem to lack 3-dimensional structure. No such patches are seen in dark-field images of H-beta-zeolite blank material.
2. An occasional/atypical crystallite, or small particle on the order of 2.5 nm in size, with a single-crystal structure was seen. One particle's lattice was consistent with elemental Fe {110} planes, but it is not clear how pure Fe could exist at this particle size (it should be an oxide). Further imaging is needed to clarify this question.
3. Degreening at 500°C does not apparently affect the morphology of Fe patches; these samples show structure similar to the Fresh powder.
4. Degreening at 700°C caused some areas in the powder to show a more discrete Fe particle structure, with larger (up to 20 nm) particles that appeared to have a 3-dimensional aspect. Ultra-high-resolution HA-ADF imaging showed the organization of one 2 nm particle into a periodic crystal.
5. The 700°C degreened samples also showed single atoms of Fe and some dimers and small

clusters. The observation of single Fe atoms in the JEOL 2200FS ACEM is, as far as we have been able to determine, the first time Fe has been imaged at the atomic level.

Raman

Spectroscopic techniques provide important information about the chemical state of and identification of adsorbed surface species. Raman spectroscopy measures the characteristic vibrational energy levels of molecules and crystals and so is very sensitive to any changes in bonding, stoichiometry and phase/symmetry.

Raman spectra were acquired with a Dilor XY800 Raman Microprobe (JY, Inc., Edison, NJ) with an Innova 308c Ar^+ laser (Coherent, Inc., Santa Clara, CA) operating at 5145Å and ~10 μW at the sample. The spot size was 10 μm. Figure 10 shows the spectra acquired from a zeolite samples degreened at 500 and 1100°C. The large background is caused by color centers in the zeolite that absorb and then fluoresce the incident light making it difficult to see the Raman peaks. Nevertheless, the spectra exhibits peaks commonly associated with aluminosilicates; ~500 cm^{-1} for the Si-O-Si bending vibration and 750-1000 cm^{-1} for Si-O stretching. Peaks associated with –OH groups are also observed > 3000 cm^{-1}. After degreening at 1100°C, the sample showed a peak around 1500 cm^{-1} which has yet to be identified. Future Raman work will employ a new UV system that will eliminate the large background observed here and reduce the penetration depth of the laser so as to make the technique more surface sensitive.

X-ray

X-ray diffraction (XRD) was employed to understand the crystalline nature of the samples. For the unfamiliar, the following analogy can be applied: As a fingerprint identifies a person, so a diffraction pattern identifies a crystalline material.

The fresh Fe-zeolite powder was degreened at 500, 700, 900 and 1100°C for 12 hours in air, cooled to room temperature and scanned. The XRD patterns show little change until 900°C, where a change in relative peak intensities and shape for the reflections at ~21.5 and 22.5 °2θ is evident. The phase composition of the powder has changed after the 1100°C exposure wherein Fe_2O_3 and Crystobalite (SiO_2) are forming. Further work on Fe/zeolite fresh and aged powders

References

[1] Internet: en.wikipedia.org/wiki/Selective_catalytic_reduction.
[2] I. Chorkendorff and J. W. Niemantsverdriet, Concepts of Modern Catalysis and Kinetics, Wiley-VCH Verlag GmbH & Co. KGaA, Weinheim, 2003, p. 400.
[3] Internet: www.personal.utulsa.edu/~geoffrey-price/zeolite/zeo_narr.htm.

Acronyms

ACEM	aberration-corrected electron microscope
BF	bright-field
EDS	Energy dispersive spectroscopy
EPA	Environmental Protection Agency
HA-ADF	high-angle annular dark-field
NO_x	Nitrogen and Oxygen containing compounds
ORNL	Oak Ridge National Laboratory
SCR	selective catalytic reduction
STEM	Scanning Transmission Electron Microscopy
XPS	X-ray photoelectron spectroscopy
XRD	X-Ray Diffraction

Table I. Samples examined with microscopy.

Sample	Sample Type	Instrument/Technique
1. H-beta-Zeolite Undoped	Powder	ACEM
2. Fe Zeolite, Fresh	Powder	ACEM (ADF + BF imaging)
"	"	HF-2000 TEM (EDS analysis)
Fe Zeolite Fresh	Ion-milled monolith	ACEM
3. Fe Zeolite 500°C Degreened	Powder	ACEM
4. Fe Zeolite 700°C Degreened	Powder	ACEM
5. Fe Zeolite 3 Aged	Ion-milled monolith	ACEM
"	"	HF-2000

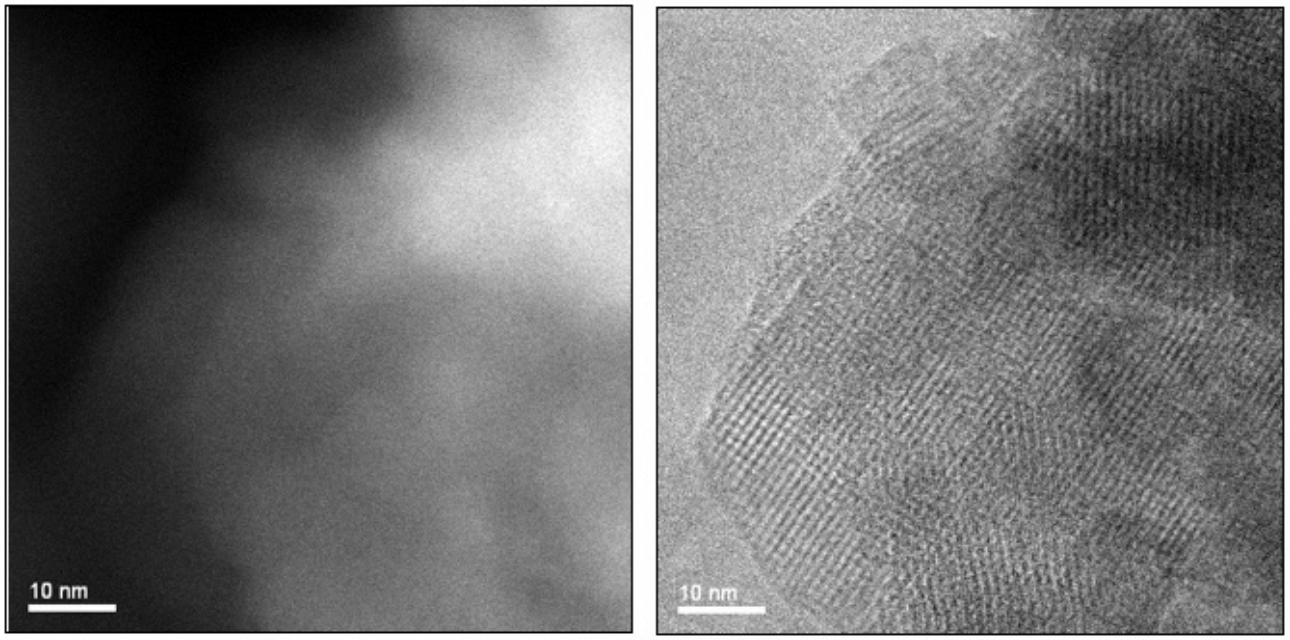

Figure 1. a) HA-ADF image of H-beta-zeolite blank material, showing uniform contrast with no evidence of heavy element scattering; b) Corresponding BF image showing crystal lattice that indicates the high resolution of the incident probe.

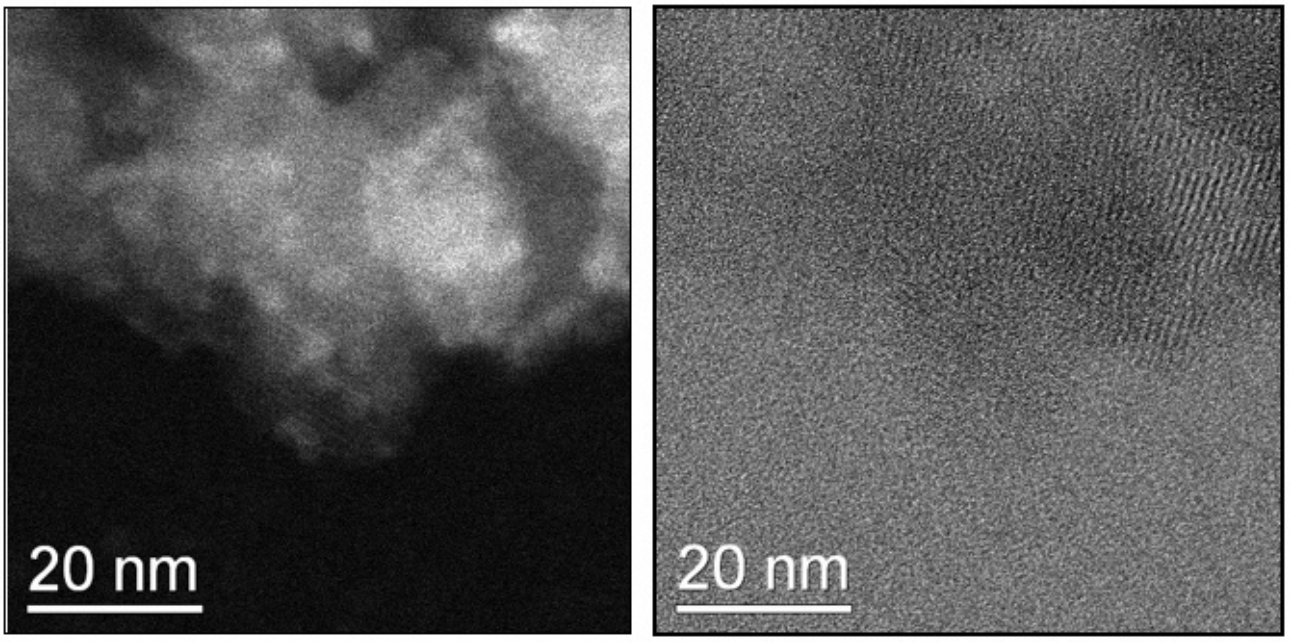

Figure 2. HA-ADF/BF pair of micrographs of fresh Fe/zeolite powder. The bright areas in the HA-ADF image are the Fe-rich phase.

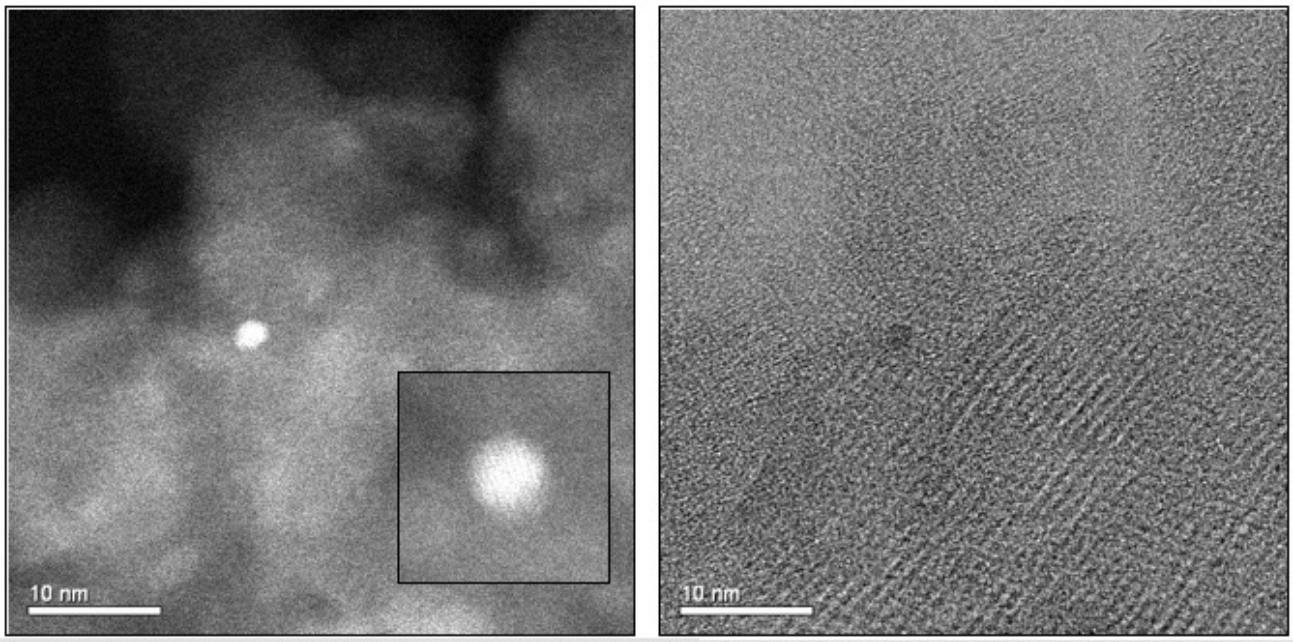

Figure 3. HA-ADF/BF pair of micrographs of showing presence of discrete crystallite. The inset in 3a shows the crystallite lattice, illustrating that it is a 2-3 nm diameter single crystal. The BF image clearly shows channels in the zeolite structure.

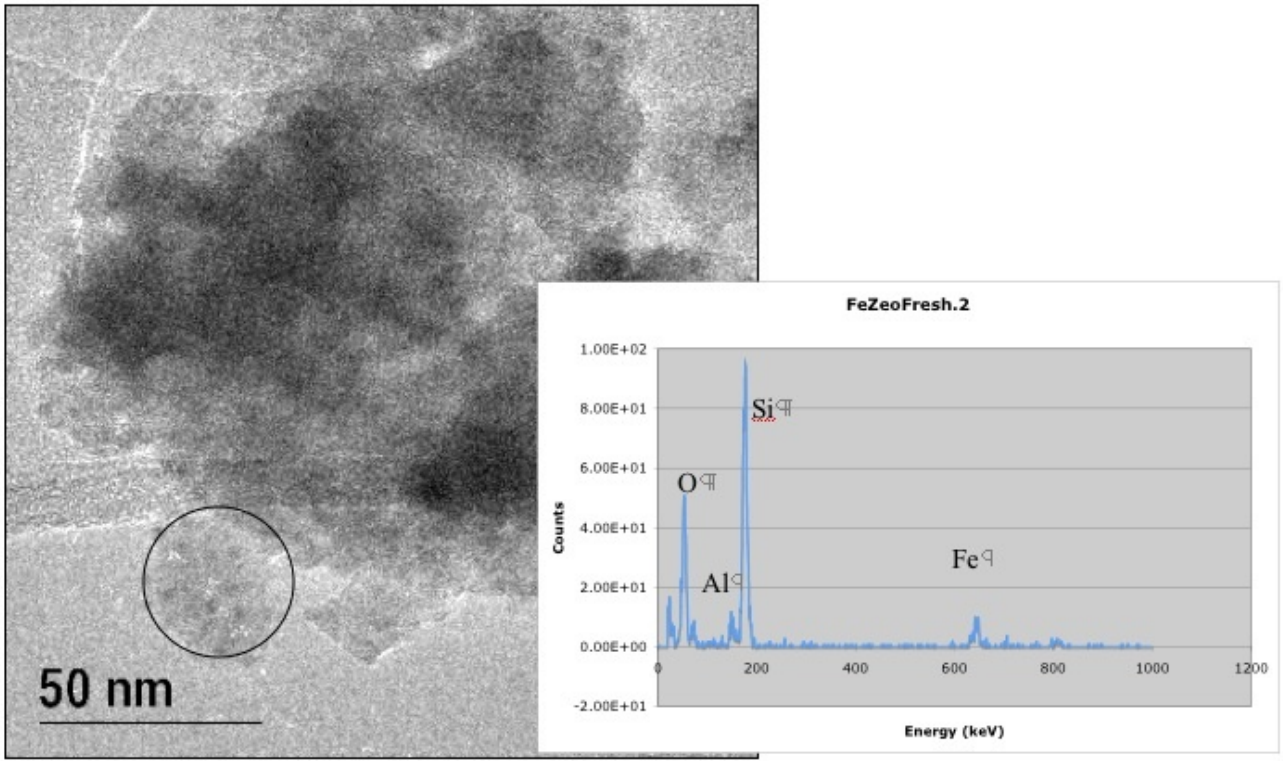

Figure 4. BF image of Zeolite aggregate in the HF-2000 TEM. Circled area shows dark patches equivalent to the bright patches seen in the ACEM HA-ADF images. The presence of Fe in this thin flake of material is confirmed by the EDS spectrum inset; the O, Al and Si peaks originate from the aluminosilicate zeolite structure.

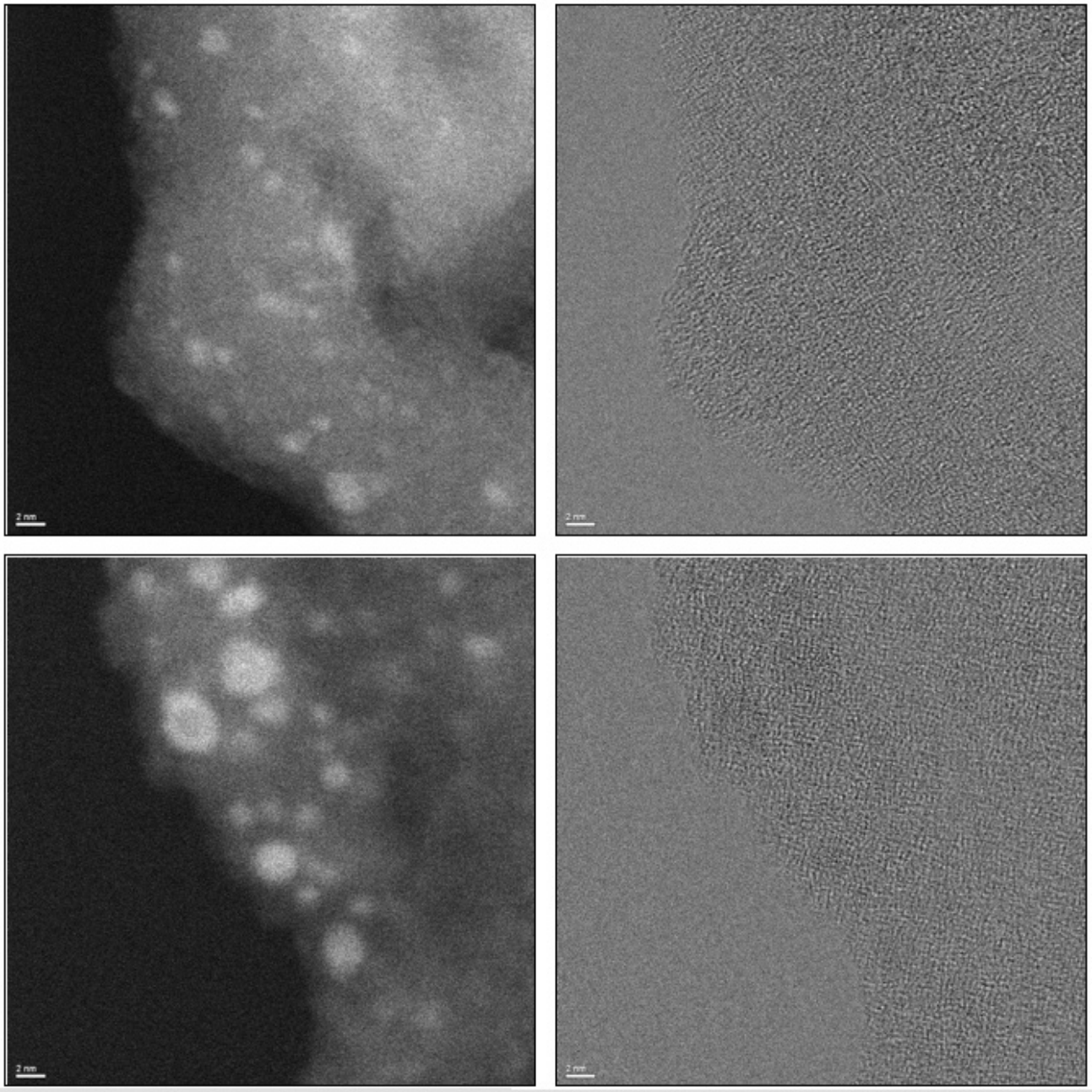

Figure 5. a,c, left) HA-ADF images of two different areas of the ion-milled Fresh powder sample, showing patches of Fe in bright contrast; b,d, right) corresponding BF images showing faint contrast from the heavy metal patches.

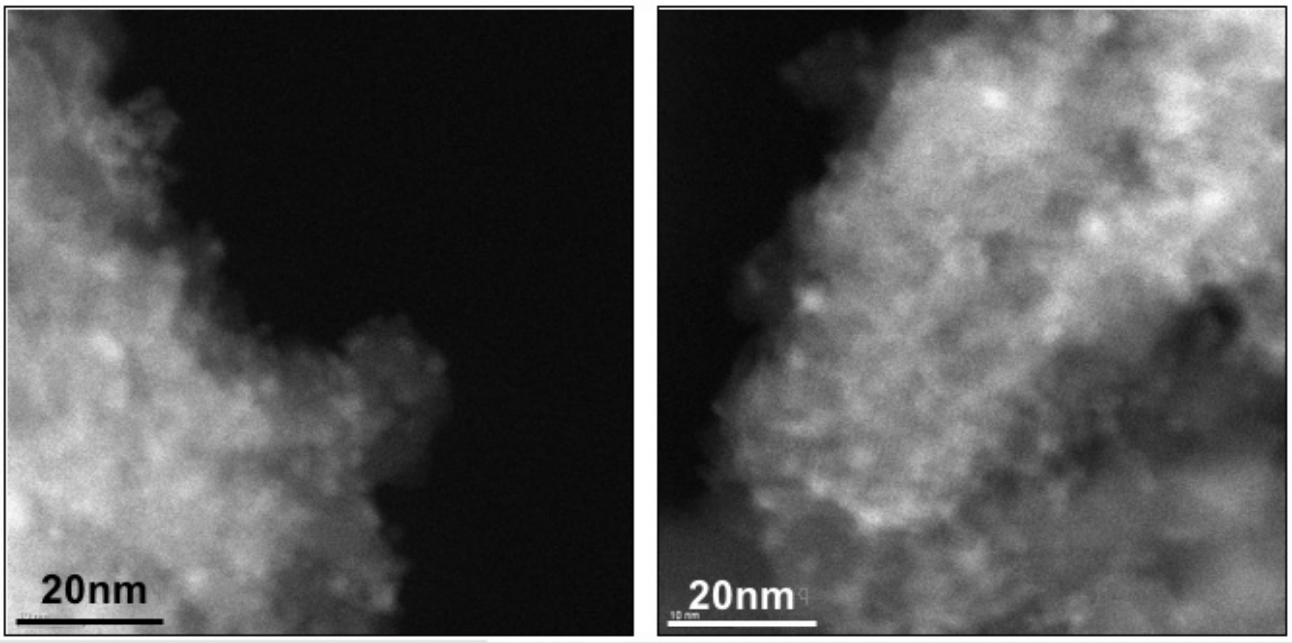

Figure 6. Two typical HA-ADF images of the 500°C degreened powder material, showing bright patches of Fe species consistent in size and distribution with those observed in the Fresh powder sample.

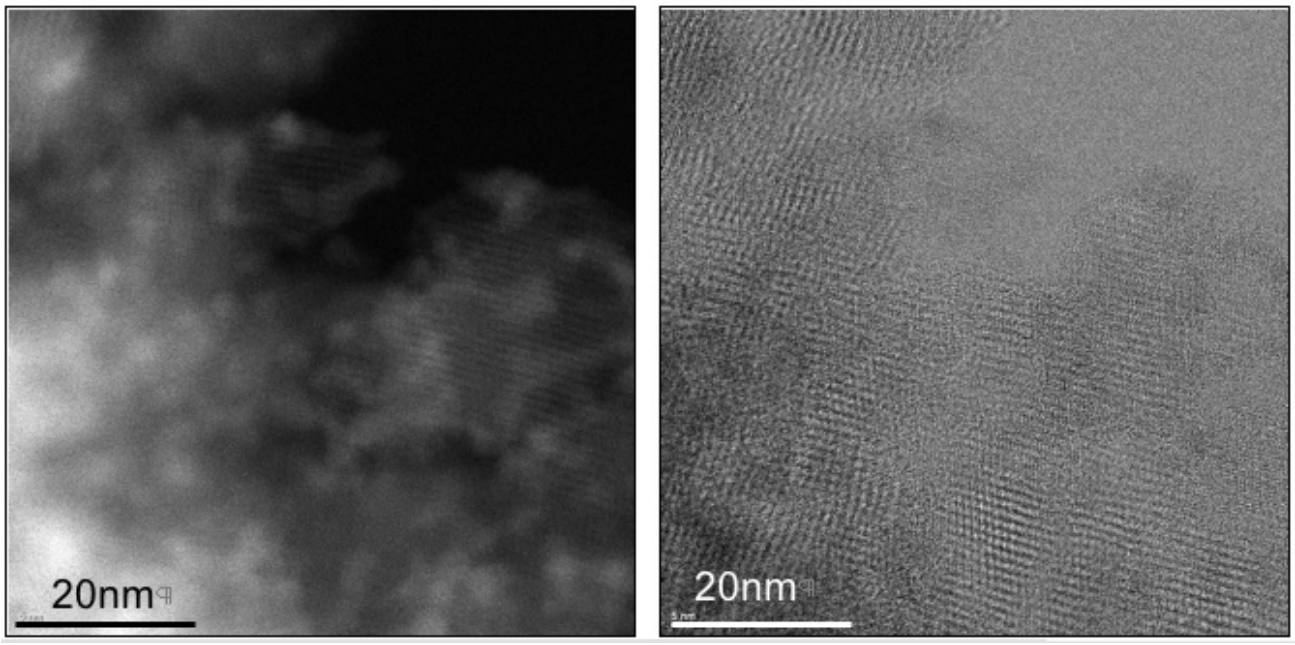

Figure 7. 700°C degreened powder sample, in HA-ADF and BF imaging. The Fe species in this area is remarkably similar to the original Fresh sample, with patches 2-4 nm in size as the predominant structure seen.

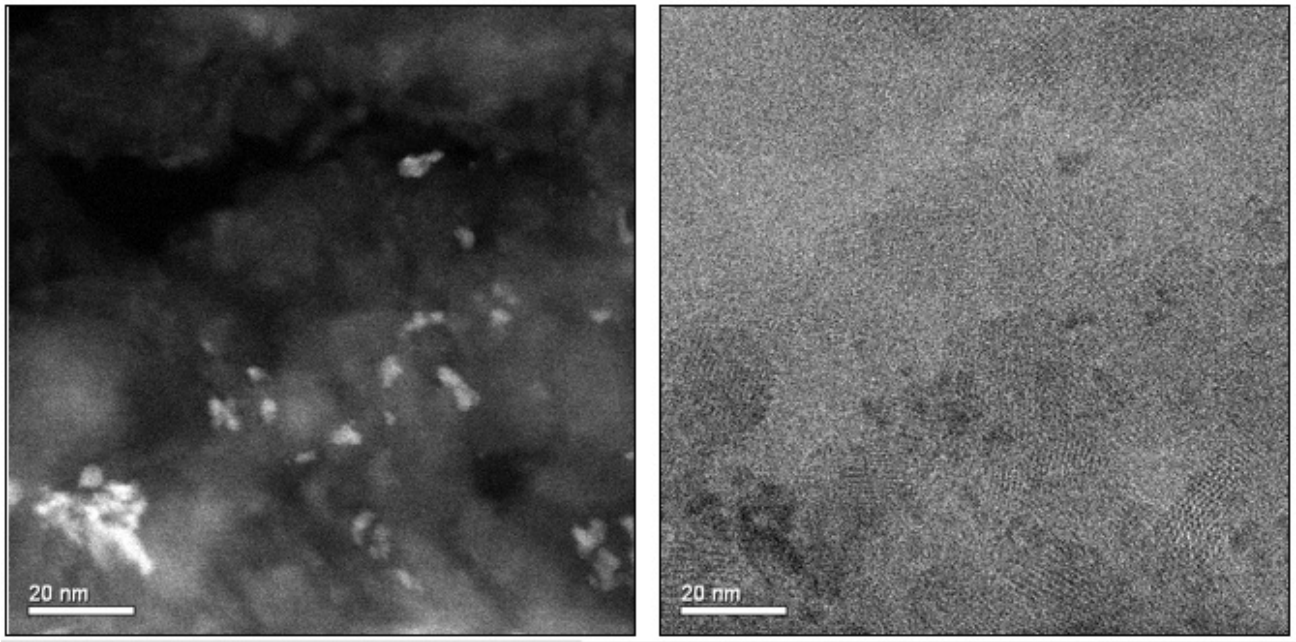

Figure 8. 700°C degreened powder sample, in HA-ADF and BF imaging. The Fe morphology in this area shows strong contrast in both images, suggesting the Fe species has formed more discrete particles of several atomic layers.

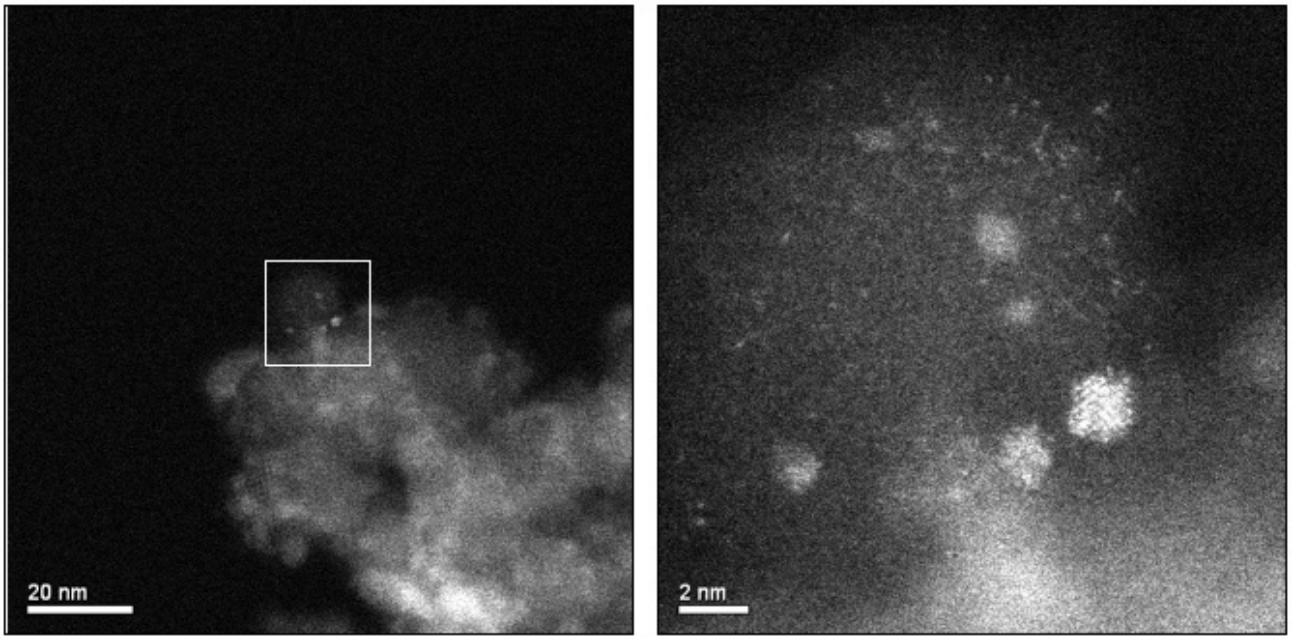

Figure 9. 700°C degreened powder sample, in HA-ADF and BF imaging; a) low magnification, and b) high magnification of the same area. Single atoms and dimers are resolved, and a larger particle with atoms showing a periodic arrangement, suggesting the aggregation into a discrete 3-dimensional crystal.

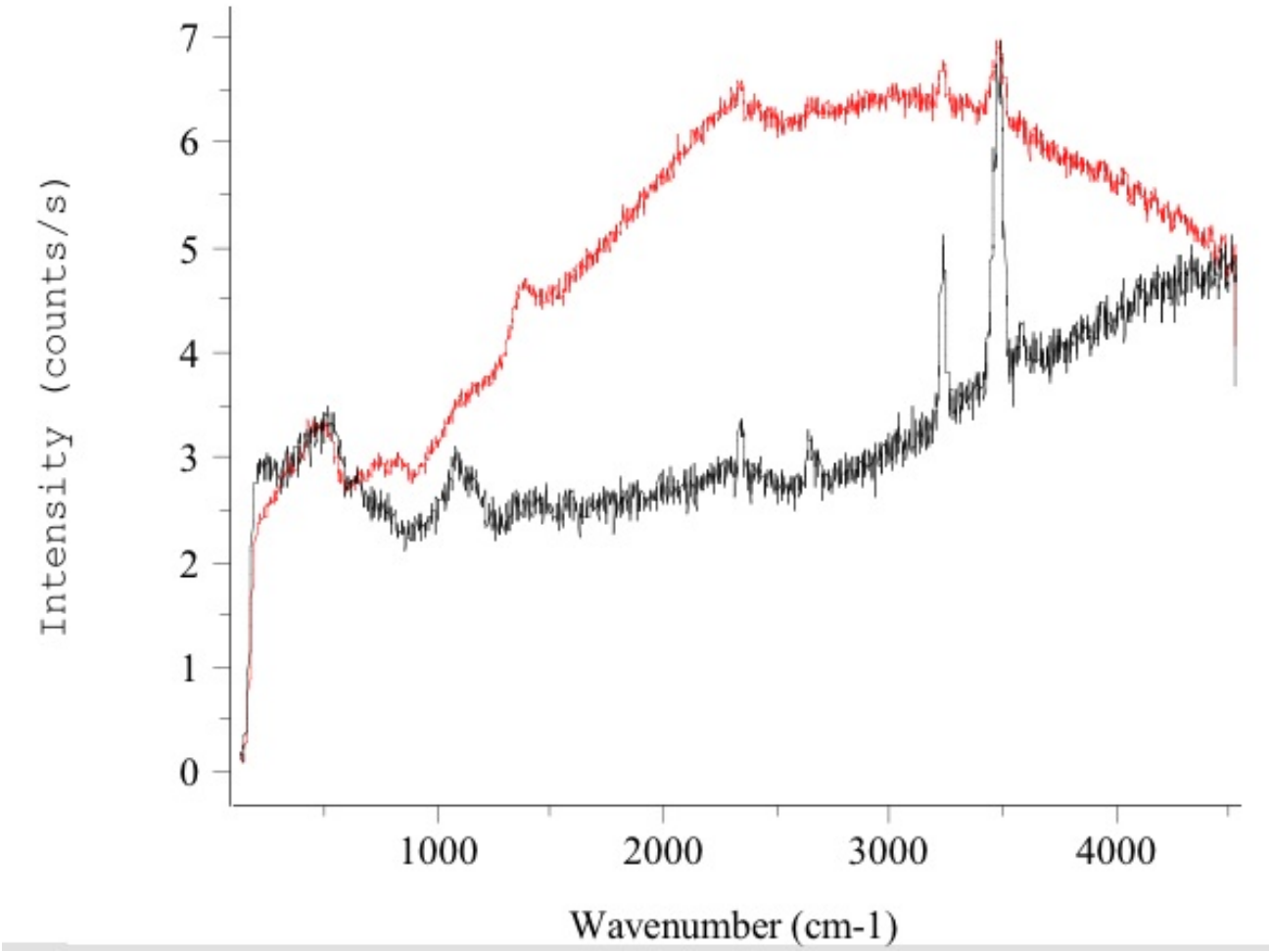

Figure 10. Raman spectra from the zeolite sample degreened at 500°C (black) and 1100°C (red).

Agreement 9112 - Austenitic Stainless Steels Alloys for Exhaust Components

P. J. Maziasz, J. P. Shingledecker, and N. D. Evans
Materials Science and Technology Division
Oak Ridge National Laboratory
P.O. Box 2008, MS-6115
Oak Ridge, TN 37831-6115
(865) 574-5082; fax: (865) 754-7659; e-mail: maziaszpj@ornl.gov

M. J. Pollard
Advanced Materials Technology
Caterpillar Technical Center
14009 Old Galena Rd.
Mossville, IL 61552
(309) 578-6133; fax: (309) 578-2953; e-mail: pollard_michael_j@cat.com

DOE Technology Manager: Jerry L. Gibbs
(202) 586-1182; fax: (202) 586-1600; e-mail: jerry.gibbs@ee.doe.gov
ORNL Technical Advisor: D. Ray Johnson
(865) 576-6832; fax: (865) 574-6098; e-mail: johnsondr@ornl.gov

---

Contractor: Oak Ridge National Laboratory, Oak Ridge, Tennessee
Contract No.: DE-AC05-00OR22725

Objectives

- Commercialize new CF8C-Plus cast austenitic stainless steel.
- Add the critical test data to the high-temperature properties database for both CF8C-Plus and CF8C-Plus Cu/W that enables component prototyping, lifing and scale-up for new end-user licensees.

Approach

- Support Caterpillar (CAT) partnership with turbocharger supplier to facilitate the upgrade from SiMo cast iron to new thin-walled highway diesel turbocharger housing made from cast CF8C-Plus and CF8C-Plus Cu/W cast austenitic stainless steels.
- Perform the critical creep, fatigue, thermal-fatigue and creep-fatigue testing that demonstrates the required properties advantages and long-term benefits of thin-section CF8C-Plus and CF8C-Plus Cu/W at 700-900^{o}C that enable commercialization for the turbocharger housing application.

Accomplishments

- Caterpillar commercialized CF8C-Plus steel for the Caterpillar Regeneration System (CRS) burner housing on all highway diesel engines at the beginning of 2007. In July, 2007 over 350,000 lb of cast CF8C-Plus steel have been made for this single commercial application.
- US Patent 7,153,373 for CF8C-Plus steel was received Dec. 26, 2006. ASTM new alloy designation HG10MNN was applied for at the end of May, 2007. Outstanding weldability of CF8C-Plus was demonstrated for the ASTM data package.

Future Direction

- Extend the CRADA for 12 more months in July, 2007, to support commercialization.
- Support commercial licensing for diesel turbocharger housings, and other applications.

Introduction

Advanced heavy truck diesel engines are increasingly required to have higher fuel efficiency and reduced exhaust emissions without sacrificing durability and reliability. The most demanding normal duty cycles require exhaust manifolds, turbocharger housing, and other exhaust component materials to withstand temperatures ranging from 70 to over 800°C. Such materials must withstand prolonged, steady high-temperature exposure (which requires tensile strength and creep and oxidation resistance) as well as more rapid and severe thermal cycling (which requires resistance to aging and thermal fatigue). New emissions reduction technology and transient power excursions can push temperatures in these critical components even higher.

Higher diesel engine exhaust temperatures push components made from SiMo ductile cast iron well beyond their current strength and corrosion limits. The first Oak Ridge National Laboratory (ORNL)/CAT cooperative research and development agreement (CRADA) (3y) developed a new, modified CF8C cast austenitic stainless steel (CF8C-Plus) as an upgrade alternative to SiMo cast iron and performed the initial mechanical properties testing on a lab-scale heat. The new CF8C-Plus steel was found to have outstanding creep resistance at 850°C. The second ORNL/CAT CRADA project (3y) capitalized on the initial success and began commercial scale-up of the new CF8C-Plus. The new material was found to have good castability, as well as much better mechanical properties at 600–850°C than standard CF8C steel, including resistance to aging, creep, and fatigue/thermal fatigue. The new CF8C-Plus cast steel won a 2003 R&D 100 Award.

In 2005-2006, efforts to commercialize CF8C-Plus expanded dramatically, so this CRADA project was extended for 2 more years. Commercial interest to upgrade diesel turbocharger housing intensified in 2006. At the end of 2006, three stainless steel foundries had taken trial licenses, and about 35,000 lb of the new steel had been cast for various applications. However, the situation changed dramatically again, when the U.S. Patent 7,153,373 B2 was obtained for CF8C-Plus steel on Dec. 26, 2006.

Approach

In 2006-2007, commercial end-users became interested in CF8C-Plus for specific applications, and the strategy switched from testing for a general properties data base, to specific application-relevant critical testing and testing to support and define component performance. With the U.S Patent granted, licensing interest in CF8C-Plus steel increased dramatically in 2007. ORNL and Caterpillar contracted with Stainless Foundry & Engineering (Milwaukee, WI) to conduct the weld testing and prepare the properties data package on commercial heats of CF8C-Plus to enable an ASTM new alloy designation. ORNL also had Stainless Foundry & Engineering make thin-section step castings of CF8C-Plus and CF8C-Plus Cu/W to determine the properties of thin sections with refined microstructures and much higher cooling rates, for data relevant to thin-wall stainless exhaust manifold and turbocharger housings. Finally, it was decided to extend the CRADA an additional 12 months beyond the July, 2007 ending date, to enable longer-term data generation in support of new commercial licensees. Upgrading various critical exhaust components to stainless steel will enable the increased engine temperatures needed to allow a 3% decrease in fuel consumption for on-highway trucks.

Technical Progress

Caterpillar

The 21st Century Truck Partnership technical goal of developing emission-compliant engine systems for Class 7–8 highway trucks is an improvement in engine efficiency from 42 to 50% by 2010. CAT has determined that replacing various SiMo cast iron exhaust components with CF8C-

Plus cast stainless steels allows a 90°C increase in exhaust gas temperatures, which translates directly into a 3% increase in fuel economy while also significantly improving performance and durability. In July, 2006 Caterpillar chose CF8C-Plus stainless steel for the Caterpillar Regeneration System (CRS) housing shown in Fig.1. The CSR became standard equipment on all heavy-duty highway truck diesel engines in January, 2007, and as of the end of June, over 350,000 lb of the new steel have been cast for this single successful application. Success of the CRS unit directly increased the interest by the turbocharger OEMs to upgrade turbocharger housings from SiMo cast iron to CF8C-Plus steel.

Caterpillar signed trial licenses with several commercial end-users for different applications of CF8C-Plus steel in 2007.

Caterpillar Regeneration System (CRS) Housing

Figure 1. The first commercial application of CF8C-Plus is the Caterpillar Regeneration System (CRS) housing, which was included on all on-highway truck diesel engines after January 2007. This combustor ignites exhaust gas and injected diesel fuel to clean filters, and must withstand high temperatures and rapid thermal cycling.

ORNL

In 2006-2007, ORNL continued the long-term creep testing of CF8C-Plus and CF8C-Plus Cu/W began earlier, and obtained new step-casting of CF8C-Plus and CF8C-Plus Cu/W from Stainless Foundry & Engineering to obtain new data on thin sections solidified at higher cooling rates, which are relevant to walls of stainless exhaust manifolds and turbocharger housings.

Figure 2 shows the considerable refinement in as-cast dendritic structure that occurs when the section thickness decreases from 1.0 inches to 0.25 inches. The thinner section microstructures tensile properties from room temperature to 800°C that are similar to or slightly better than the properties measured in thick section specimens. In particular, the thin sections of CF8C-Plus Cu/W show more strength than CF8C-Plus steel at 700-800°C. More importantly, preliminary creep-rupture testing of thinner section specimens show rupture strength as good as or better than thinner section specimens for both CF8C-Plus and CF8C-Plus Cu/W steels (Fig. 3). The creep-rupture strength and creep-resistance benefits of the CF8C-Plus Cu/W over CF8C-Plus may also in thin-section specimens compared to thicker sections with much slower cooling rates, especially at 750-800°C and above (Fig. 3 and Fig. 4). The extended secondary creep regime with low creep rate may be an important advantage for the CF8C-Plus Cu/W in applications where creep-strain rather than rupture life defines the limitations.

In late 2006 and early 2007, ORNL and Caterpillar engaged Ron Bird and Stainless Foundry & Engineering to perform the require weldability and weld-properties testing on CF8C-Plus and put together a data package for a new alloy designation (HG10MNN) for the A297 Committee of ASTM. CF8C-Plus was found to exhibit excellent weldability, and those welds more than passed the room-temperature tensile ductility and U-bend ductility tests. In addition to good ductility, the welds were also 25% stronger than the as-cast base metal. The ASTM new alloy designation package was submitted at the end of May, 2007. The ASTM alloy designation, together with the U.S. Patent, enhance the commercial marketability of the CF8C-Plus steel.

Finally, the need for additional ORNL high-temperature mechanical properties testing to support new end-user licensing agreements and interest resulted in this CRADA project being extended for 12 more months, until July, 2008.

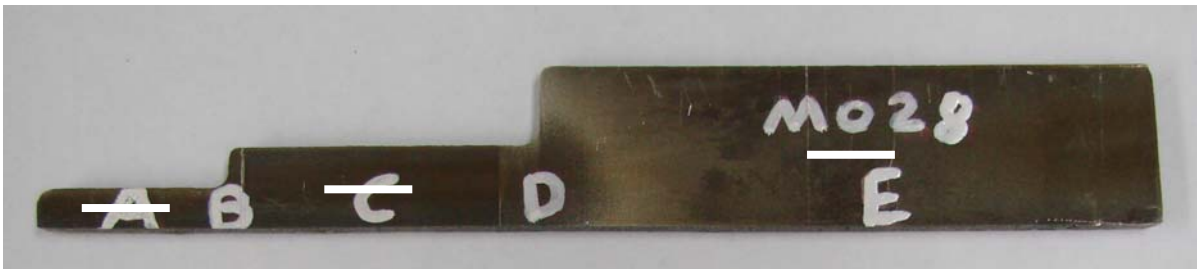

A

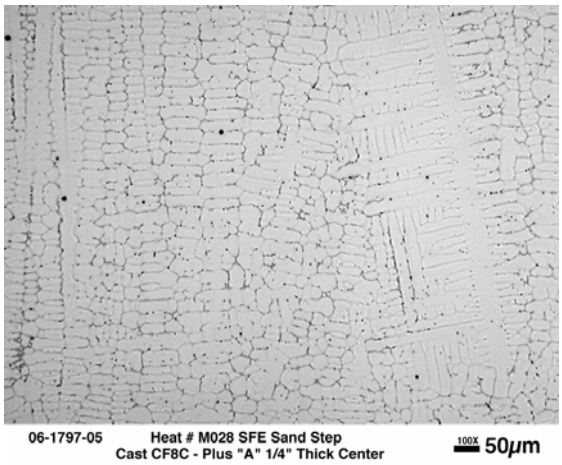

B

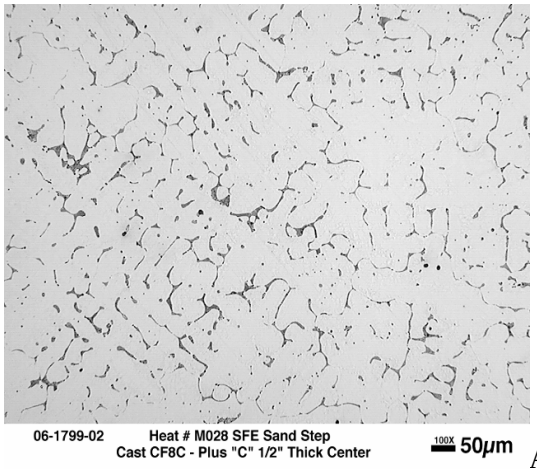

C A

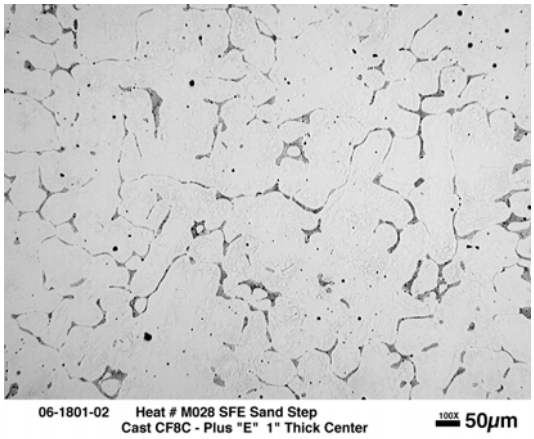

D

Figure 2 – A) Macro-photo of CF8C-Plus stainless steels step casting, with 1.0, 0.5 and 0.25 inch step thicknesses, and etched metallographic cross-sections showing the as-cast dendritic structure of the B) 0.25 inch thick section (marked A), C) the 0.5 inch thick section (marked C), and D) the 1.0 inch thick section (marked E) in the photo above.

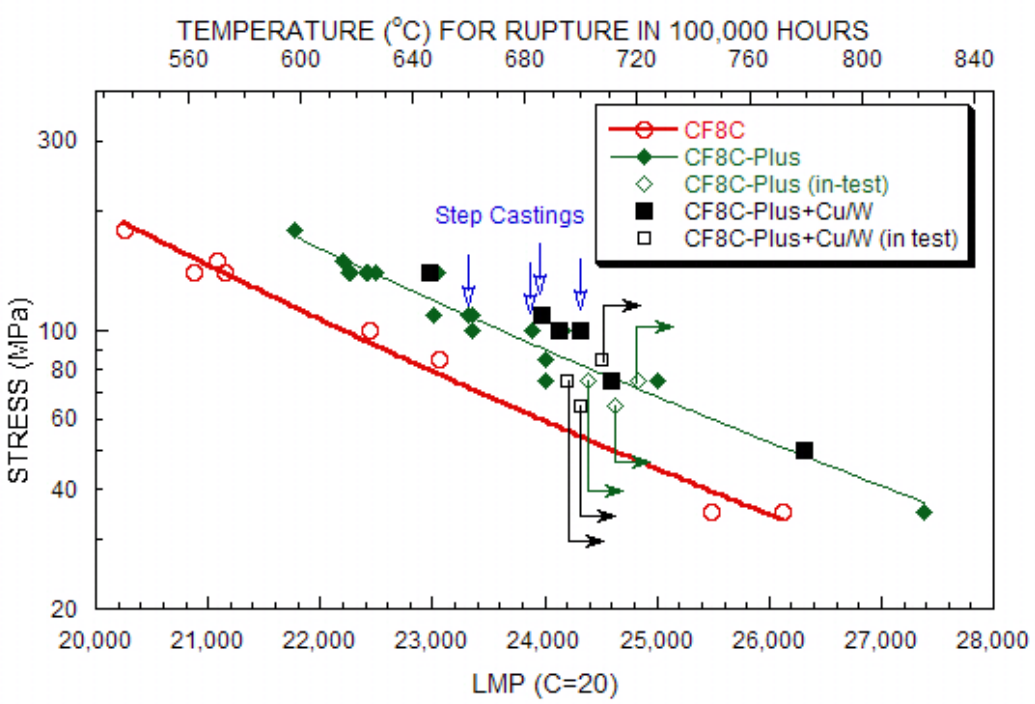

Figure 3. Creep-rupture stress plotted vs LMP for various ORNL creep-rupture tests at 500–850°C in air of various commercial heats of standard CF8C, CF8C-Plus and CF8C-Plus Cu/W stainless steels. New creep data on thin sections of CF8C-Plus and CF8C-Plus Cu/W show similar or better creep-strength compared to previous data on much thicker cast sections.

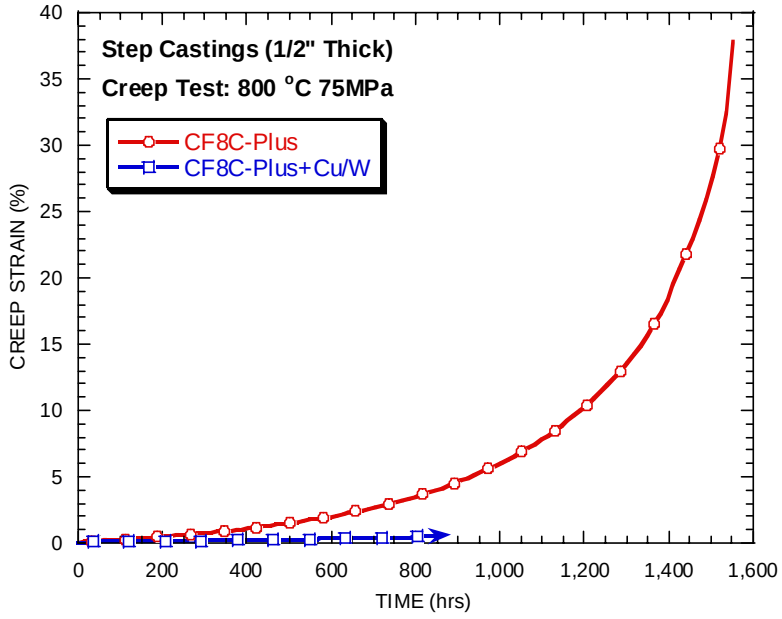

Figure 4. Plots of creep-strain vs time for new thin-section step-cast heats of CF8C-Plus and the new CF8C-Plus Cu/W, all tested in air at 800°C and 75 MPa. Clearly the CF8C-Plus Cu/W has much more creep-resistance, with an extended secondary creep-regime and a very low steady-state creep rate, which is very important for applications like turbocharger housings

Conclusions

ORNL and CAT dramatically expanded the commercialization of the CF8C-Plus cast stainless steel. The new Caterpillar CRS housing exhaust component application, applied to all new on-highway truck diesel engines beginning in January, 2007, has resulted in over 350, 000 lb of CF8C-Plus cast up to June, 2007. The U.S. Patent for CF8C-Plus was granted in December, 2006, and that led directly to several commercial end-users signing trial licenses in March-April 2007. The ORNL/CAT CRADA has been extended 12 more months, until July, 2008 to enable more high-temperature mechanical testing and critical data generation to support licensees, particularly for the thin-walled stainless turbocharger housing application for Caterpillar advanced on-highway truck diesel engines.

Publications/Presentations

J.P. Shingledecker, P.J. Maziasz, N.D. Evans, and M.J. Pollard, "Creep Behavior of a New Cast Austenitic Alloy," *International Journal of Pressure Vessels and Piping* (Special issue on New Steels) **84** (2007) 21-28.

P.J. Maziasz, J.P. Shingledecker, N.D. Evans, and M.J. Pollard, "Developing New Cast Austenitic Stainless Steels With Improved High-Temperature Creep Resistance," paper CREEP2007-26840, in Proc. of CREEP8 – 8th International Conference on Creep and Fatigue at Elevated Temperatures, ASME-PVP2007 (22-26 July, 2007, Antonio, TX), Am. Soc. Mech. Engin., New York, NY (2007).

An invited talk, "Designing New Steels for High-Temperature Service," was present by P.J. Maziasz at the American Metals Market (AMM) Conference on Stainless and Its Alloys, Panel IV: Technological – Metallurgical Advances, on April 10, 2007 in Pittsburgh, PA.

"Designing New Steels for High Temperature Uses," by P.J. Maziasz was given as an invited ORICL Lecture for the Seminar Series IR-1 R&D100 Award Winning Research at ORNL, on Feb. 1, 2007 at Roane State Community College, Oak Ridge, TN.

"CF8C-Plus: A Material Developed by the 'Engineered Microstructure' Approach" by J.P. Shingledecker, was given as an Invited Seminar at the Department of Materials Science and Engineering at the University of Tennessee, Knoxville, TN on Mar. 20, 2007.

Special Recognitions and Awards/Patents Issued

A U.S. Patent, 7,153,373 B2 was received Dec. 26, 2006 for "Heat and Corrosion Resistant Cast CF8C Stainless Steel Alloy With Improved High Temperature Strength and Ductility" by P.J. Maziasz, T. McGreevy, M.J. Pollard, C.W. Siebenaler, and R.W. Swindeman.

A U.S. Patent, 7,255,755 was received Aug. 14, 2007 for "Heat and Corrosion Resistant Cast CN-12 Type Stainless Steel Alloy With Improved High Temperature Strength and Ductility" by P.J. Maziasz, T. McGreevy, M.J. Pollard, C.W. Siebenaler, and R.W. Swindeman.

Agreement 10461 - Durability of Diesel Particulate Filters (CRADA with Cummins, Inc.)

Amit Shyam, Thomas R. Watkins and Edgar Lara-Curzio
Oak Ridge National Laboratory
P.O. Box 2008, MS-6069
Oak Ridge, TN 37831-6069
(865) 574-2046; fax: (865) 574-4913; e-mail: watkinstr@ornl.gov

DOE Technology Manager: Jerry L. Gibbs
(202) 586-1182; fax: (202) 586-1600; e-mail: Jerry.gibbs@ee.doe.gov
ORNL Technical Advisor: D. Ray Johnson
(865) 576-6832; fax: (865) 574-6098; e-mail: johnsondr@ornl.gov

Contractor: Oak Ridge National Laboratory, Oak Ridge, Tennessee
Contract No.: DE-AC05-00OR22725

Objective

- Implement test techniques to characterize the physical and mechanical properties of ceramic diesel particulate filters (DPFs) and develop analysis and inspection tools for assessing their reliability and durability.

Approach

- Implement test techniques to determine the physical and mechanical properties of DPF ceramic substrates.
- Rank the thermal shock resistance of candidate DPF substrates.
- Application of probabilistic design tools to DPF ceramic substrates. In addition, the development of non-destructive evaluation (NDE) techniques to periodically inspect DPFs and ascertain the validity of the probabilistic models.

Accomplishments

- Identified the relationship between microstructure and elevated temperature elastic-fracture property relationship in diesel particulate filter substrates.
- Carried out physical and mechanical property measurements on several coated and uncoated substrates and ranked their relative thermal shock resistance.
- Developed non-destructive evaluation (NDE) techniques for detecting cracks in diesel particulate filters.

Future Direction

- Detailed examination of the effect of coating, soot loading and field service environment on the elastic and fracture mechanical characteristics of diesel particulate filter substrates.

Introduction

The pollution emitted by diesel engines contributes greatly to the nation's air quality problems. Even with more stringent environmental regulations having taken effect in 2007, existing trucks and buses will continue to emit nitrogen

oxides (NO_x) and particulate matter (PM), both of which contribute to serious public health problems[1]. There are several technologies designed to reduce pollution from existing trucks and buses; prominent among these technologies are DPFs. A DPF is often a ceramic device that collects particulate matter in the exhaust stream. The high temperature of the exhaust heats the ceramic structure and allows the particles inside to break down (or oxidize) into less harmful components. DPFs reduce emissions of PM, hydrocarbons, and CO by 60 to 90%.

Most DPFs consist of a ceramic honeycomb with hundreds of cell passages partitioned by walls (Figure 1). Each cell passage has a square cell opening at one end and is closed at the other end so that the cell passages are alternately closed at each end. The checkerboard plugging structure forces the exhaust gases through the porous, thin ceramic honeycomb walls. When the gases carrying the carbon particles flow through the fine pores of the walls, the carbon particles are filtered out. High porosity values, in the range of 40-70%, heighten filtration efficiency to more than 90% and reduce gas-flow resistance for better engine performance.

The process of diesel PM collection continues while the engine is operating. Carbon particles are collected on the ceramic walls and, as a result, the backpressure of the system increases. This problem is alleviated by burning the trapped PM, aided by a catalytic reaction using exhaust gas heat at 400°C or more, into CO_2 and water vapor. This process, called regeneration, results in a cleaner filter. The regeneration process is dependent upon exhaust temperature, oxygen, NO_x content, time, and PM levels.

The key to the successful application of DPFs is to reliably regenerate the filter (e.g., to burn the PM that the filter continues to trap or collect). Traditionally, combustion of soot is done in an oxygen atmosphere (air). In air, soot will burn at about 500°C. However, this is not a typical operating temperature for diesel engine exhaust.

Therefore, to burn soot in air, an active system—i.e., one that increases the temperature of the exhaust using some external heat source—is required. But if an active system is not carefully controlled, or if too much PM collects on the filter walls, the filters can experience an “uncontrolled burn” where the temperature increases to 600°C or more, resulting in damage to the filter element.

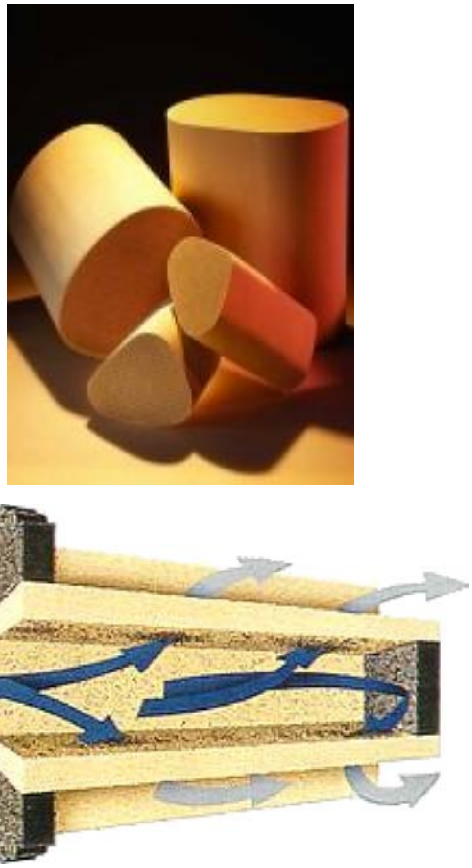

Figure 1. Corning’s cordierite-based DPFs.

The objective of this project is to develop and implement methodologies to predict the reliability of DPFs. A useful conceptual model for this purpose is the reliability bathtub curve, which describes reliability-related phenomena of a component over its life cycle.[2] A schematic of the reliability bathtub curve is represented in Figure 2. It consists of three stages: the infant mortality phase is characterized by premature failures due to improper manufacturing or assembly, poor workmanship, or defects introduced during processing. The second stage of the curve corresponds to the useful life of the component and

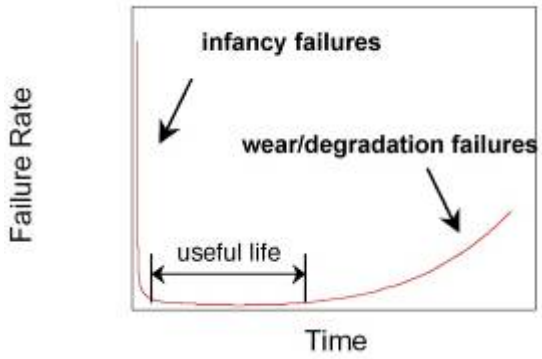

Figure 2. Reliability bathtub curves.

is characterized by a constant failure rate. In this regime, failures are typically associated with random, excessive loads. If sufficiently high safety factors are used during the design process, the magnitude of this failure rate should be negligible. The third stage of the bathtub curve is known as the wear-out phase, where the failure rate increases with time as a result of aging phenomena. Aging phenomena include thermal and mechanical fatigue, corrosion, creep deformation and environmentally assisted crack growth. The time at the onset of wear-out is often regarded as the useful life of the component.

The reliability bathtub curve can be used as a descriptor of how the failure rate of DPFs evolves over time. Infancy failures of DPFs could be related to manufacturing or process defects (large pores, inclusions, cracking) or defects introduced during assembly. Failures of DPFs during their useful life will be dictated by the intersection between the spectrum of thermomechanical loads and the distribution of DPF strengths. Such failures could result from excessive vibration, for example, or unwanted thermal excursions during transients associated with regeneration. Wear-out and degradation failures of DPFs could be associated with the growth of microcracks assisted by thermal fatigue, and/or by the chemistry of the environment, and/or by chemical and microstructural changes in the material due to long-term exposure to elevated temperatures in the exhaust environment.

The objective of this project is to implement test techniques to characterize the physical and mechanical properties of ceramic DPF substrates and to develop analysis and inspection tools for assessing the reliability and durability of DPFs. The developed tools and methods would allow the design of durable and reliable DPFs. An important outcome of the development of the test methods is the ability to rank the relative thermal shock resistance of substrates in different conditions (catalyzed, soot loaded, etc.) and of different candidate substrate materials.

Approach

The design process for making DPFs that are durable and reliable includes a complex materials selection process[3]. For example, the porosity of DPFs, which allows them to remove PM from the exhaust gas stream, has a deleterious effect on their mechanical and fracture strength. Designing mechanically reliable DPFs is important because these components will experience demanding thermomechanical conditions during service. These include, for example, thermal shock resulting from rapid heating/cooling and thermal stresses that arise from temperature gradients. Techniques to assess the elastic and fracture properties of DPF substrates have been identified and implemented. The test techniques will be applied to rank the suitability of common candidate substrates for application in DPFs. The mechanisms responsible for the mechanical property degradation in the various stages of the bathtub curve will also be determined and identified. These properties include thermal expansion, thermal conductivity, heat capacity, density, porosity, elastic properties, strength, fracture toughness, and environmentally assisted crack growth at ambient and elevated temperatures, in air and in relevant environments.

The information generated will be used in turn to implement probabilistic design tools. In particular, the applicability of the CARES code[4] to predict the reliability of DPF ceramic substrates will be investigated. Such probabilistic design methodologies are based on a combination of experimentally determined strength data, stress analyses of the component using a finite-element analysis, and selection of appropriate failure criteria. The durability (service life) of the component can also be predicted using this framework by considering the mechanisms that are responsible for the degradation of material strength, such as slow crack growth or creep. Non-destructive evaluation (NDE) techniques have been developed to periodically inspect DPFs

and the inspection schedule would be based on probabilistic model predictions.

Results

The elastic modulus of the substrate is a key property for determining the mechanical reliability and thermal shock resistance of DPFs. The determination of the modulus poses a challenge due to the fragility of the substrates. 40 mm x 20 mm x 0.375 mm flat plates of porous cordierite were prepared by dry grinding methods reported earlier. Resonant ultrasound spectroscopy (RUS) was utilized to characterize the elastic modulus of this plate. The temperature dependence of the elastic modulus of the plate for three loading and unloading thermal cycles is reported in Figure 3. The temperature dependence of elastic modulus is unusual, in that the modulus values remain nearly constant up to 500°C and subsequently increase with temperature up to 1000°C. The increase in the modulus of porous cordierite with increasing temperature is attributed to the healing of preexisting microcracks at elevated temperature. These cracks form during cooling from the sintering temperature due to the severe thermal expansion anisotropy that exists within the orthorhombic cordierite structure. The crack formation and healing process is not reversible as can be seen from the hysteresis of the elastic modulus-temperature graph in Figure 3. The initial room temperature elastic modulus value was calculated to be 11.85 GPa and it increases to 16.28 GPa at 1000°C. Thermal cycling decreases the modulus of the substrates and after three thermal cycles, the modulus of the same specimen decreased to 10.46 GPa.

The elastic modulus RUS study was repeated on porous cordierite specimens with a mean thickness of 0.275 ± 0.005 mm that had a catalytic washcoat on it. The effect of coating on the temperature dependence of the elastic modulus is demonstrated in Figure 4. The room temperature elastic moduli of the coated and uncoated specimens are similar. The elastic modulus of the coated specimens, however, starts increasing at a lower temperature and its elastic modulus is 19.35 GPa at 1000°C. The greater rate of increase of the elastic modulus of coated specimens is attributed to the interaction of the coating with the microcracks.

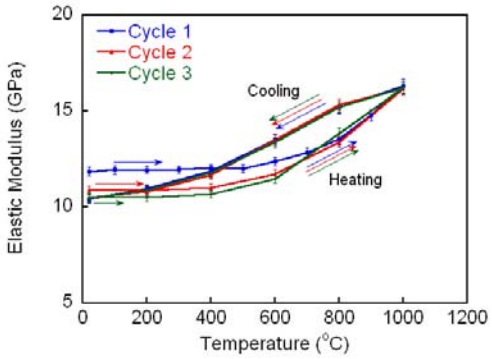

Figure 3. The temperature dependence of the elastic modulus of porous cordierite. The test specimen was subjected to three thermal loading cycles with a maximum temperature of 1000°C.

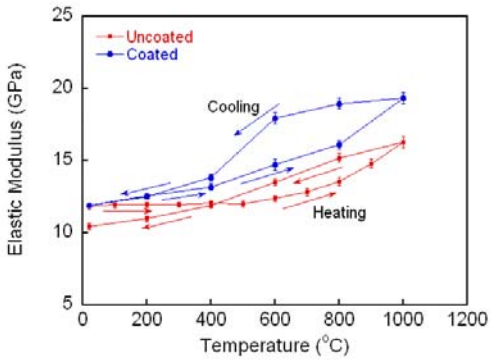

Figure 4. The effect of catalytic washcoating on the temperature dependence of the elastic modulus of porous cordierite.

During FY 2007, the procedure to prepare double-torsion (DT) test specimens was further developed and this testing technique was applied to determine the fracture toughness and slow-crack-growth behavior of porous cordierite and other candidate DPF substrates. The double-torsion test configuration is particularly attractive for determination of the fracture mechanical properties of DPF substrates. This is due to the following reasons (a) crack length measurements are difficult in porous cordierite with optical techniques and DT characterization does not require crack length measurements, (b) the DT specimen geometry is ideally suitable for plate-like specimens that can be fabricated from DPF walls and (c) the DT

configuration is also attractive for slow-crack-growth studies because of the relative stability of crack extension, in contrast to other testing configurations (e.g., SENB, CT).

The preparation of double-torsion test specimens of porous cordierite has been reported in FY 2006. The mean thickness of the DT test specimens was equal to 0.375 mm and the flatness of the test specimens was equal to 8 μm. The fracture toughness of porous cordierite test specimens was determined by loading pre-cracked test specimens to failure at a constant crosshead displacement rate of 0.01 mm/s. The fracture toughness was calculated from the peak load using Equation 1:

$$K_{IC} = PS_m\left[\frac{3(1+\nu)}{St^4\xi}\right]^{1/2}, \qquad (1)$$

where P is the peak load, S is the width of the test specimens, S_m is the moment arm, t is the specimen thickness, ν is Poisson's ratio, and ξ is a finite beam thickness correction factor given by

$$\xi = 1 - 1.26\left(\frac{t}{S}\right) + 2.4\left(\frac{t}{S}\right)e^{\left(-\frac{\pi S}{2t}\right)}. \qquad (2)$$

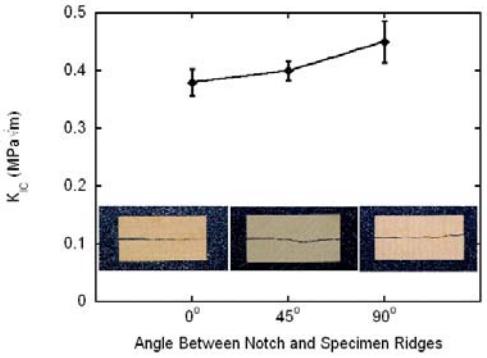

Figure 5. Fracture toughness of porous cordierite at room temperature as a function of orientation.

The effect of orientation of the notch on the fracture toughness of porous cordierite, as determined by the double-torsion test method, is reported in Figure 5. Three orientations are represented in this bar-chart where the x-axis represents angles of 0, 45 and 90°. The "parallel" or 0° orientation represents the specimen where the notch is parallel to the extrusion direction. In other words, the fracture toughness of this specimen represents the crack propagation resistance of the material parallel to the honeycomb passages (Figure 1). The "perpendicular" or 90° orientation specimen K_{IC}, on the other hand represents the crack propagation resistance of the material in a direction that is perpendicular to the honeycomb passages. The perpendicular orientation has a fracture toughness of 0.45 ± 0.036 MPa√m, nearly 20% higher than the parallel orientation value of 0.38 ± 0.023 MPa√m. The 45° orientation has an intermediate fracture toughness value of 0.40 ± 0.020 MPa√m. It is therefore, suggested that the ridges in the specimen provide a toughening mechanism. The fracture toughness of a DPF as determined by a ring crack with an arbitrary orientation would be in-between the two extreme values represented in Figure 5.

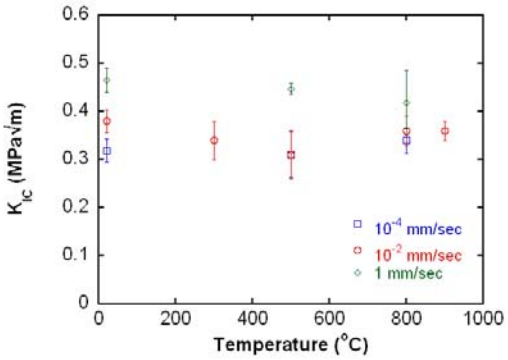

Figure 6. Fracture toughness variation of porous cordierite up to 900 °C at three different crosshead displacement rates. Every data point represents an average of five tests under that condition.

The fracture toughness and slow crack growth behavior of DPF cordierite was evaluated by the double-torsion testing methodology up to a temperature of 900°C. While the fracture toughness tests reported so far were performed at a crosshead displacement rate of 0.01 mm/sec, both slower (10^{-4} mm/sec) and faster (1 mm/sec) tests were performed to understand the effect of loading rate on fracture toughness. The effect of temperature on the fracture toughness of DPF cordierite is summarized in Figure 6. Five temperatures were tested at a crosshead displacement rate of 0.01 mm/sec because this is the rate at which the slow crack growth tests could be

performed in a controlled manner. At the intermediate loading rate of 0.01 mm/sec, the fracture toughness decreased from 0.38 ± 0.023 MPa√m at 20 °C to 0.31 ± 0.050 MPa√m at 500 °C and subsequently increased to 0.36 ± 0.020 MPa√m at 900 °C. At the fastest crosshead displacement rate of 1.00 mm/sec the average fracture toughness values have a small change with increasing temperature with the values being 0.47 ± 0.025, 0.45 ± 0.012 and 0.42 ± 0.067 MPa√m at 20, 500 and 800°C, respectively. At the slowest crosshead displacement rate of 10^{-4} mm/sec the average fracture toughness values are lower with the values being 0.32 ± 0.024, 0.31 ± 0.048 and 0.34 ± 0.026 MPa√m at 20, 500 and 800°C, respectively.

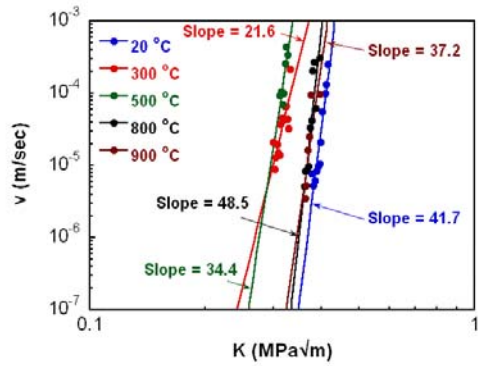

Figure 7. The effect of temperature on the slow crack growth behavior of porous cordierite in a lab environment.

The elevated temperature slow crack growth resistance of porous cordierite represented by v-K curves is presented in Figure 7. The partial pressure of water in the laboratory was monitored throughout the testing program and it varied between 0.3 - 2.1 kPa. One curve is presented for each temperature in Figure 7 and the power-law crack growth exponents for the curves are included in this figure. The relative stress intensity factor position of the curves is related to the average fracture toughness value at a crosshead displacement rate of 0.01 mm/sec with curves shifting to lower K values at 300 and 500°C and subsequently increasing K values at 800 and 900°C. The average slow crack growth exponent values (for two tests) determined by double-torsion at 20, 300, 500, 800 and 900°C are 39.6, 17.2, 26.8, 46.8 and 42.3, respectively. The low values of crack growth exponent indicate the material is susceptible to slow crack growth at all the tested temperatures. The slow crack growth susceptibility of the material is related to the presence of a glassy phase at the grain boundaries as reported in FY 2006.

In FY 2007, the comparative mechanical properties and relative thermal shock resistance of several DPF substrates was assessed. The cordierite substrates analyzed are called C-0 and C-1, corresponding to manufacturer C in the uncoated and coated conditions, respectively and B-0, B-1 and B-2 corresponding to manufacturer B in the uncoated, coated and coated+aged conditions, respectively. In addition, a mullite DPF substrate called D-1 was analyzed in comparison to the cordierite based substrates. The original wall thickness of C-0 filters was around one and a half times the other substrates and therefore, for fracture toughness comparison, some thinner C-0 specimens were fabricated. The mean thickness of the C-0 specimens for double-torsion testing and resonant ultrasound spectroscopy was 0.375 mm, whereas the mean thickness of all the other specimens (including thin specimens of C-0) was 0.275 mm.

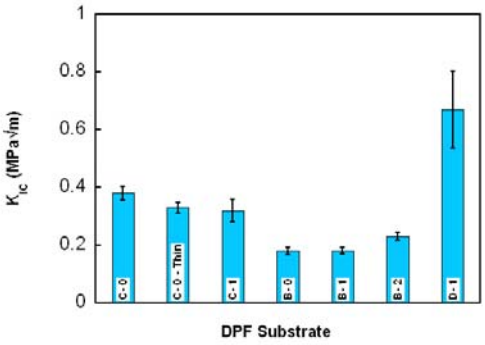

Figure 8. The average room temperature fracture toughness of the DPF substrates analyzed. The mullite substrate (D-1) has a higher fracture toughness compared to the cordierite based substrates. Five tests were carried for C-0, C-0-thin, C-1, B-0 and B-1 substrates whereas; three tests were conducted for B-2 and D-1 substrates. The error-bars represent the standard deviation of the values.

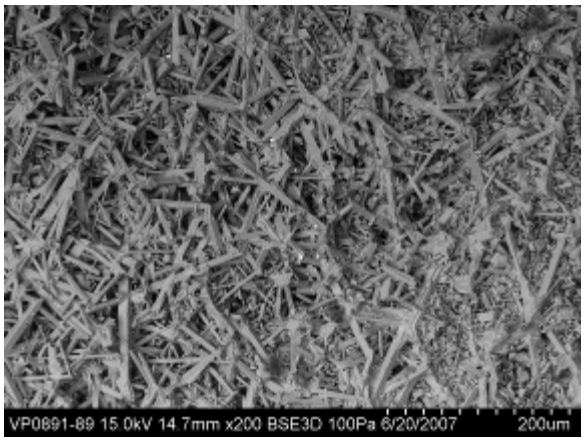

Figure 9. SEM image of the interlocking microstructure, of the mullite (D-1) DPF substrate, that is responsible for its increased fracture toughness.

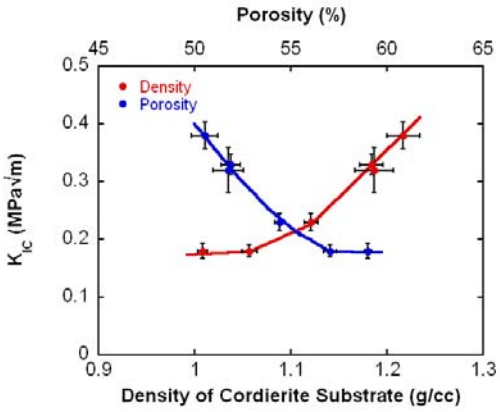

Figure 10. The variation in the fracture toughness of the cordierite substrates as a function of density and porosity of the substrate.

The room temperature fracture toughness of the substrates was calculated based on the double-torsion methodology and is summarized in Figure 8. It can be observed from this figure that the mullite substrate (D-1) has a higher fracture toughness of 0.67 $\pm$ 0.13 MPa$\sqrt{m}$ compared to the cordierite based substrates whose mean fracture toughness varies between 0.18-0.38 MPa$\sqrt{m}$. This is due to the interlocking structure of the mullite DPF substrate shown in the SEM image of Figure 9. For the cordierite substrates, there was little influence of coating on the room temperature fracture toughness for both manufacturers B and C. This can be inferred by comparing B-0 and B-1 and C-0 thin and C-1 in Figure 8. The fracture toughness of the thin C-0 specimens was marginally lower compared to C-0 specimens with a mean thickness of 0.375 mm. The average fracture toughness of the substrates from manufacturer C was, however, nearly twice the toughness of the substrates from manufacturer B. The variation in the toughness of the cordierite substrates can be explained based on results in Figure 10. For all substrates, the fracture toughness increases with increasing density and conversely the toughness decreases with increasing porosity. The density was calculated based on a mass per unit volume calculation and the porosity of the substrate was calculated assuming a bulk density value for cordierite of 2.46 g/cc. The fracture toughness is highly sensitive to porosity and a 20% increase in porosity causes a 50% decrease in fracture toughness.

The room temperature elastic modulus of the substrates was calculated based on resonant ultrasound spectroscopy and is summarized in Figure 11. Isotropic elasticity was assumed for RUS analysis. It can once again be observed from Figure 11 that the mullite substrate with an elastic modulus of 25.6 GPa is stiffer compared to the cordierite substrates where the modulus values range from 9.4–11.9 GPa. The other trends observed for fracture toughness of cordierite substrates are also observed for elastic modulus, namely (i) there is little influence of coating on the modulus of the substrate at room temperature, (ii) the modulus of the substrate from manufacturer C is higher than the modulus of the substrate from manufacturer B and (iii) there is a correlation between the modulus and porosity/density of the substrate.

The thermal expansion behavior of the substrates was analyzed on cellular structures in directions that were parallel and perpendicular to the extrusion direction. The average coefficient of thermal expansion (CTE) between 20 and 1000^{o}C are reported in Figure 12. This figure demonstrates that the coefficient of thermal expansion of the mullite substrate was much higher than the cordierite substrates. In addition, the CTE values for the cordierite substrates are higher in the direction perpendicular to the extrusion direction. The simplest thermal shock resistance parameter is R_S, the ratio of the strength (σ) of the material and the product of elastic modulus (E) and CTE (α), i.e.

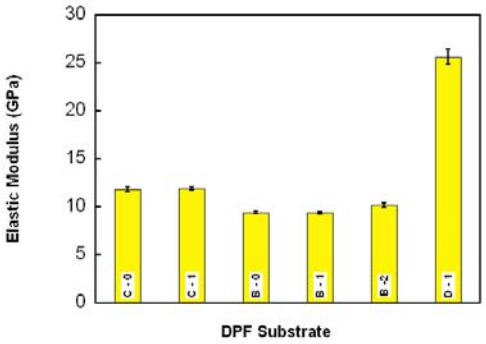

Figure 11. The room temperature elastic modulus of the DPF substrates analyzed. Isotropic elasticity was assumed. The error bars represent the RMS error of the fit for one measurement.

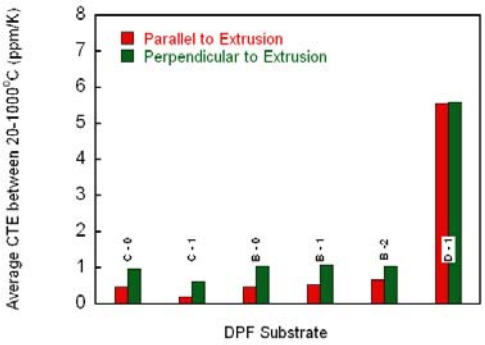

Figure 12. The coefficient of thermal expansion (CTE) of the DPF substrates analyzed. The CTE values reported are the between 20 and 1000°C and in directions that are parallel and perpendicular to the extrusion direction. One measurement each in the parallel and perpendicular direction.

$R_S = (\sigma/\alpha E)$. A modified parameter called R_K was proposed, where $R_K = (K_{IC}/\alpha E)$. The value of the R_K parameter was calculated for all the substrates and has been compared in Figure 13. The values used for the calculation are room temperature elastic modulus and fracture toughness and average CTE values between 20 and 1000°C. According to Figure 13, C-1 material will have the highest thermal shock resistance, whereas D-1 would have the lowest resistance. It is to be cautioned that the values of the R_K parameter can change drastically for a different temperature range so the comparison in Figure 13 is valid only at room temperature. Elevated temperature modulus and fracture toughness values (Figures 3, 4 and 6) can be utilized to estimate the thermal shock resistance of a substrate in a particular temperature range. It is also to be noted that a real filter has heterogeneities that a calculation like the one presented above did not take into account.

A portion of the efforts during FY 2007 was applied in developing non-destructive evaluation techniques for detecting cracks in DPFs, thus allowing the assessment of the integrity of filter structures in real time. Two techniques that were successfully developed are illustrated in Figure 14. Figure 14(a) illustrates the procedure in which crack gages (wires in parallel) are constructed on porous cordierite substrates by baking decals in the temperature range of 700-900°C. The decals are 60% silver (by volume) and can be constructed in various patterns depending on the required sensitivity of the crack length measurement. The decals adhere well to the substrate and the wires (in parallel in Figure 14a) break when a crack passes through the substrates. This causes a change in resistance across the gage and the resistance change can be monitored as a change in voltage by implementing a voltage divider (half of a wheatstone bridge) circuit and this is shown in Figure 15. Figure 15 shows a double-torsion specimen with six wires in parallel that leads to six voltage spikes in the voltage versus time curve, as the crack passes through the individual wires.

Figure 14(b) is another example of a crack gage specimen, where the crack gage is constructed via screen printing of a cermet paste on a porous cordierite substrate. The specimen was subsequently baked with an infra-red (IR) lamp to harden the cermet paste into a solid pattern. Both the methods illustrated in Figure 14 are suitable for fabricating crack-gages on diesel particulate filters. Moreover, a combination of different patterns can be applied in different sections of a filter in order to obtain desired patterns.

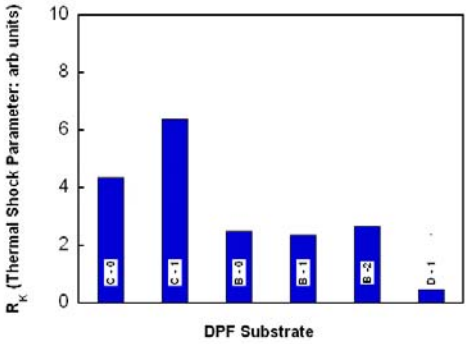

Figure 13. Comparison of the R_K, thermal shock parameter for the DPF substrates. The values are based on the average CTE (average of parallel and perpendicular values), room temperature modulus and average fracture toughness values.

Summary

A comprehensive fracture mechanics based investigation was conducted for porous cordierite; a leading candidate material for the fabrication of diesel particulate filters. Fracture toughness and slow crack growth tests were performed in the double-torsion test geometry for the service temperature range of 20-900 ^{o}C. The elastic properties of the filter wall substrate were characterized with resonant ultrasound spectroscopy (RUS) in the temperature range of 20-1000 ^{o}C. The developed test procedures were employed to rank the relative thermal shock resistance of several candidate DPF substrate materials. The properties utilized to measure the thermal shock resistance included the fracture toughness, elastic modulus and the coefficient of thermal expansion. NDE techniques were developed for detecting the integrity of diesel particulate filters.

References

1. United States Environmental Protection Agency, Office of Transportation and Air Quality EPA420-F-03-017, June 2003. “Questions and Answers on Using a Diesel Particulate Matter Filter in Heavy-Duty Trucks and Buses.”

2. G. S. Wasserman, *Reliability Verification, Testing and Analysis in Engineering Design*, Marcel Dekker, New York, 2003.

3. J. Adler, “Ceramic Diesel Particulate Filters,” International Journal of Applied Ceramic Technology, vol. 2, no. 6, pp. 429-439, 2005.

4. N. N. Nemeth, L. P. Powers, L. A. Janosik, and J. P. Gyekenyesi, “Ceramics Analysis and Reliability Evaluation of Structures Life Prediction Program: Users and Programmers Manual,” NASA-GRC, Life Prediction Branch (1993).

Presentations, Publications and Patents

T. M. Yonushonis, R. J. Stafford, E. Lara-Curzio and A. Shyam, “Apparatus, system, and method for detecting cracking within an aftertreatment device” *US Patent Application* Filed, March 2007.

A. Shyam, E. Lara-Curzio, H-T Lin and R. J. Parten, “Fracture Toughness of Porous Cordierite", *Ceramic Engineering and Science Proceedings*, vol. 27, no. 2, pp. 75-81, 2007.

T.M. Yonushonis, R. J. Stafford, C. Klepser, T. R. Watkins, A. Shyam and E. Lara-Curzio, “Ceramic Particulate Filters”, *Diesel Engine-Efficiency and Emissions Research (DEER) Conference*, Detroit, August 2007.

A. Shyam, E. Lara-Curzio and T.R. Watkins, “Fracture mechanical characterization of porous cordierite ceramics”, *Materials Science & Technology*, Detroit, September 2007.

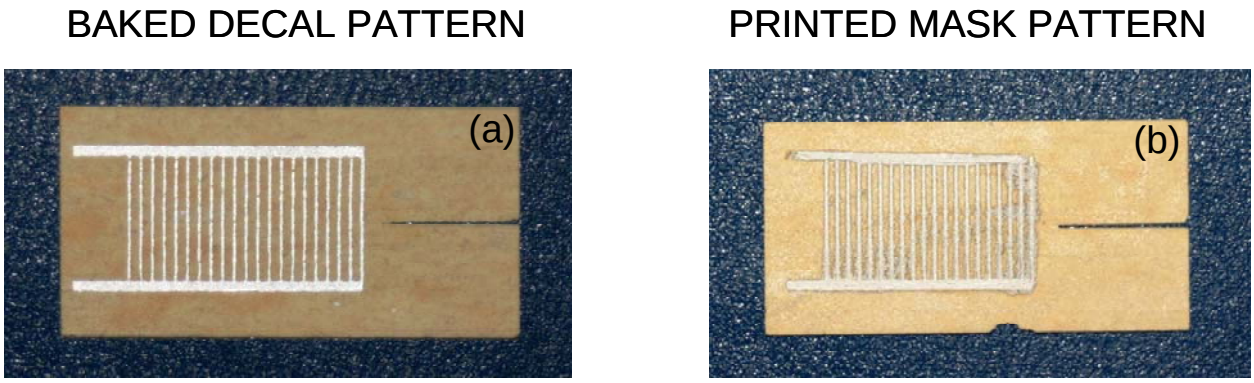

Figure 14. Images of two different kinds of crack-gages bonded to double-torsion specimens of porous cordierite. (a) Decal pattern baked on DT specimen and (b) Printed mask of cermet paste baked on ceramic substrate.

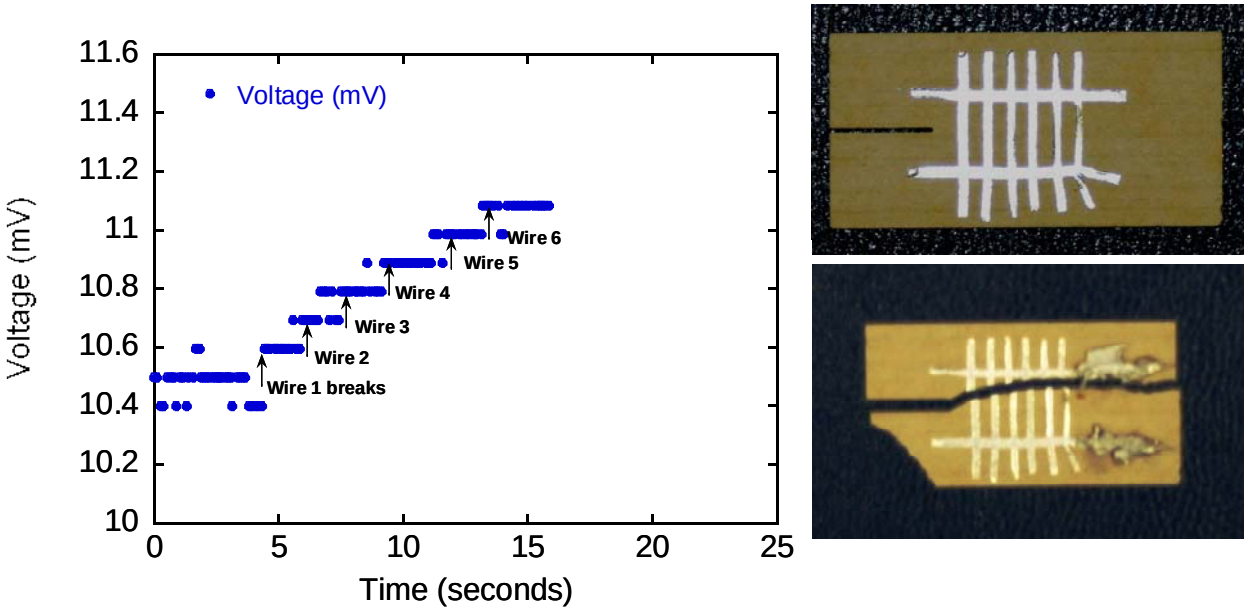

Figure 15. Implementation of developed crack-gages in voltage divider circuits to detect crack growth in porous cordierite substrates.

Agreement 10635 - Catalysis by First Principles

C. K. Narula, L.F. Allard, M. Moses-DeBusk,
Oak Ridge National Laboratory
P.O. Box 2008, MS 6116
(865)574-8445, narulack@ornl.govl

DOE Technology Manager: Jerry L. Gibbs
(202) 586-1182; fax: (202) 586-1600; e-mail: Jerry.gibbs@ee.doe.gov
Field Technical Manager: D. Ray Johnson
(865) 576-6832; fax: (865) 574-6098; e-mail: johnsondr@ornl.gov

---

Contractor: Oak Ridge National Laboratory, Oak Ridge, Tennessee
Contract No.: DE-AC05-00OR22725

Objective

The objective of this work is to search for durable emission treatment catalysts (LNT, TWC, OC) from a protocol based on

- an integrated approach between computational modeling and experimental development,
- design and testing of new catalyst materials to rapidly identify the key physiochemical parameters necessary for improving the catalytic efficiency of these materials.

Approach

- Theoretical Modeling
  - Density functional theory-based first-principles calculations
  - Optimization of Pt clusters supported on alumina
  - Interaction of CO, NO_x, and HC with Pt clusters supported on alumina
- Experimental System
  - Synthesize Pt Nanoclusters on morphologically diverse alumina supports
  - Evaluate systems for CO, NO_x, HC oxidation
  - Understand non-structural changes in catalyst under operating conditions and correlating the changes to performance.

Accomplishments

- We have previously shown by theoretical models that nano-particles of Pt are stable as oxides and metallic particles are poorer catalysts than oxides. We have found experimental evidence to validate theoretical studies.
  - After determining the nano-structure of supported Pt clusters, we evaluated a series of $2\%Pt/Al_2O_3$ catalysts with different Pt particle sizes and alumina substrate morphologies (1 nm $2\%Pt/\gamma\text{-}Al_2O_3$; 12 nm $2\%Pt/\gamma\text{-}Al_2O_3$: 1nm $2\%Pt/\theta\text{-}Al_2O_3$) by electron microscopy after testing for CO oxidation on a bench-top reactor to correlate activity with catalyst's nano-structure.
  - We have established that nano-particles of Pt on alumina support are highly prone to agglomeration and even exposure to CO-oxidation conditions at low temperatures leads to agglomeration. An increase in the average Pt nanoclusters size, as well as the quantity of larger particles/clusters occurs with all of the $2\%Pt/Al_2O_3$ catalysts. Alumina substrate morphology is not a predictor of the extent of sintering that occurs to 1 nm Pt clusters.
- ORNL ex-situ reactor studies enable us to differentiate between nano-cluster/particle agglomeration and sample-to-sample variation effects. We found that:
  - Pt particle sizes for the 1nm $2\%Pt/\gamma\text{-}Al_2O_3$ catalyst increase throughout the CO oxidation process even under CO oxidation initiation conditions.

- Our results show that large particles formed as result of nano-particles sintering should not be assumed to be metallic particles since we found oxidized ordered particles in as little as 2-3 cycles of quantitative CO oxidation.
- Our *ex-situ* study of the ~12nm 2%Pt/γ-Al_2O_3 catalyst showed that such large Pt particles are more stable than Pt nanoparticles and further sintering, if any, is gradual.

Future Direction

- Understanding of the structures of nano-clusters on support.
  - Theoretical models to understand cluster oxidation state (oxidized, reduced, in equilibrium), dependence on cluster size, and the kinetics of oxidation
  - Experimental studies on the structures of these systems using EXAFS, XANES
- Support interaction with clusters and its impact on the structure and reactivity
  - Cationic or zero-valent metals or both
  - Cationic metals at the metal–support interface
- Reactivity of the clusters
  - Theoretical and experimental studies on structure-reactivity correlation towards NO_x, and HC oxidation studies
  - The impact of cluster size on catalytic activity
- Translate these results into design of durable supported catalysts for lean NO_x catalysts and other systems such as TWC, OC for diesel etc.

Introduction

This research focuses on an integrated approach between computational modeling and experimental development, design and testing of new catalyst materials, that we believe will rapidly identify the key physiochemical parameters necessary for improving the catalytic efficiency of these materials.

The typical solid catalyst consists of nano-particles on porous supports. The development of new catalytic materials is still dominated by trial and error methods, even though the experimental and theoretical bases for their characterization have improved dramatically in recent years. Although it has been successful, the empirical development of catalytic materials is time consuming and expensive and brings no guarantees of success. Part of the difficulty is that most catalytic materials are highly non-uniform and complex, and most characterization methods provide only average structural data. Now, with improved capabilities for synthesis of nearly uniform catalysts, which offer the prospects of high selectivity as well as susceptibility to incisive characterization combined with state-of-the science characterization methods, including those that allow imaging of individual catalytic sites, we have compelling opportunity to markedly accelerate the advancement of the science and technology of catalysis.

Computational approaches, on the other hand, have been limited to examining processes and phenomena using models that had been much simplified in comparison to real materials. This limitation was mainly a consequence of limitations in computer hardware and in the development of sophisticated algorithms that are computationally efficient. In particular, experimental catalysis has not benefited from the recent advances in high performance computing that enables more realistic simulations (empirical and first-principles) of large ensemble atoms including the local environment of a catalyst site in heterogeneous catalysis. These types of simulations, when combined with incisive microscopic and spectroscopic characterization of catalysts, can lead to a much deeper understanding of the reaction chemistry that is difficult to decipher from experimental work alone.

Thus, a protocol to systematically find the optimum catalyst can be developed that

combines the power of theory and experiment for atomistic design of catalytically active sites and can translate the fundamental insights gained directly to a complete catalyst system that can be technically deployed.

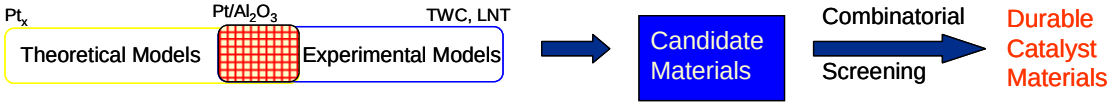

Although it is beyond doubt computationally challenging, the study of surface, nanometer-sized, metal clusters may be accomplished by merging state-of-the-art, density-functional-based, electronic-structure techniques and molecular-dynamic techniques. These techniques provide accurate energetics, force, and electronic information. Theoretical work must be based on electronic-structure methods, as opposed to more empirical-based techniques, so as to provide realistic energetics and direct electronic information.

A computationally complex system, in principle, will be a model of a simple catalyst that can be synthesized and evaluated in the laboratory. It is important to point out that such a system for experimentalist will be an idealized simple model catalyst system that will probably model a "real-world" catalyst.

Thus it is conceivable that "computationally complex but experimentally simple" system can be examined by both theoretical models and experimental work to forecast improvements to obtain optimum catalyst systems.

Approach

The theoretical modeling is based on DFT studies of Pt clusters to understand the relationship between cluster size, structure, composition, and reactivity. This coupled with first-principles thermodynamics provides insights into the effects of oxidizing atmosphere (O_2) – finite (T, p_{O_2}), structure, composition, redox potential on particle size. The results provide guidance for investigations of larger / supported clusters. The next steps of this work will model supported clusters, based on input from experimental results, and their interactions with CO, NO_x, and HC.

Experimentally, we have synthesized a series of Pt clusters/particles of different sizes supported on morphologically different alumina and evaluated the catalysts CO oxidation activity. We monitored the microstructural changes throughout the CO oxidation process to correlate microstructure and activity. We plan to extend the CO oxidation studies to other supports and to broaden our study to the NO_x and HC oxidation processes.

Guided by the theoretical models and experimental results of our study, we will synthesize new set of catalyst materials with higher durability under operating conditions.

Results

Over the last year, we have carried out experimental studies on Pt nanoclusters and nanoparticles correlating their CO oxidation activity with microstructural changes. We employed our *ex-situ* reactor[1] and scanning transmission electron microscopy (STEM) using both the Aberration Corrected JOEL 2200FS (ACEM) and the HD-2000 to study the nanostructural changes in catalysts upon exposure to CO oxidation condition. It is important to note that the *ex-situ* reactor permits duplication of the CO oxidation conditions obtained on the bench-top reactor.

The results show the correlation between nanostructural changes and their impact on the catalytic activity and are summarized in the following subsections:

EXPERIMENTAL STUDIES ON $Pt/\gamma\text{-}Al_2O_3$

1 nm 2%Pt/γ-Al_2O_3: The nanostructure of supported Pt catalysts is not well understood. The Z-contrast imaging reports in literature

describe the presence of 3-atom clusters and allocate anomalous long Pt-Pt bond to OH terminated Pt clusters.[2] Recent EXAFS studies, on the other hand, suggest thermal metal-metal bond contraction after hydrogen reduction of $Pt/\gamma\text{-}Al_2O_3$ whose TEM shows particles in 0.5-1.5 nm range centered at ~0.9 nm consisting of 15±9 atoms on average.[2]

Our dark-field STEM imaging of 1 nm $Pt/\gamma\text{-}Al_2O_3$ shows features identical to those reported previously in terms of particle size distribution. The ACEM HA-ADF STEM images of this catalyst, on the other hand, show that there are single atoms, 2-3 atom clusters, and several 10-20 atom clusters of Pt. The directly measured Pt-Pt bond distances are 2.35, 2.54, 2.7, and 3.2Å for 2-atom clusters, and 2.3, 2.8 Å for 3-atom clusters. The ACEM HA-ADF STEM images of this catalyst show that there are isolated atoms, 2-3 atom clusters, and several 10-20 atom clusters of Pt (Figure 3). The directly measured Pt-Pt bond distances are 2.35, 2.54, 2.7, and 3.2Å for 2-atom clusters. The theoretical bond distance for a Pt-Pt dimer in the gas phase is 2.34 Å. While it appears that the observed bond distance matches closely with the calculated ones for gas-phase Pt-Pt dimers, it is not a good comparison because gas-phase dimers do not include substrate interactions. Theoretical models of oxides of Pt nanoclusters suggest them to be 2-dimentsional in gas phase. The calculated Pt-Pt bond distance for Pt_2O_4 cluster is 2.77 Å and although it matches the observed value, we are reluctant to assign Pt_2O_4 structure to Pt-dimers primarily due to 2-dimensionality of calculated structure. None of the large clusters exhibit 2-dimensional structures. A better comparison is with Pt dimers supported on α-alumina where they occupy two adjacent Al_T-Al_T sites and exhibit bond distance of 2.723 Å.[3] This study also suggests that a Pt-Pt dimer undergoes dissociative adsorption on two adjacent O_{3h} sites with each Pt atom occupying an O_{3h} site. This would probably explain the larger bond distance of 3.2 Å observed for Pt dimers.

The calculated Pt-Pt bond distances for gas-phase Pt trimers is 2.5 Å and does not match with observed bond distances of 2.3 and 2.8 Å perhaps due to substrate interactions. This calculated value for a gas phase trimer is also different from the calculated value described previously for γ-alumina supported Pt trimers. Interestingly, the calculated bond distance of Pt_3O_6 clusters is 2.75 Å which is close to our observed value, but the observed Pt trimer structure is different from the two-dimensional calculate structure of gas phase Pt_3O_6. As for dimers, the calculated Pt-Pt distances of Pt trimers supported on α-alumina are a better match with our observed values. In the theoretical model, a Pt-trimer orients itself parallel to the (0001) surface forming an equilateral triangle with each Pt atom occupying an O_{3h} site. In this model, the Pt-Pt bond distance is 2.696 Å.

We had previously evaluated this catalyst for CO oxidation activity on a bench-top reactor and monitored the conversion of CO to CO_2 by gas chromatography (GC) as a function of temperature. Now, we summarize our evaluations of microstructural changes that occurred to the fresh sample after initiation testing and after 3 cycles of quantitative CO oxidation testing on the bench-top reactor.

Microstructural evaluations carried out by STEM (HD-2000) after only initiation CO oxidation (~4% oxidation) indicated significant growth in the Pt nanoparticles (see table 1). While only a 1nm increase in the average was seen compared to the fresh sample (Figure 1), particle sizes range up to 3.8. A further increase in the upper end of the Pt particles size distribution was observed after 3 cycles of quantitative CO oxidation (Figure 1) with the largest particle at ~5.5nm. Not only did the size range increase but a significant increase was also seen in the number of larger Pt particles; however, there was virtually no change in the average Pt particle size. Figure 2 compares the particle size distributions observed for the fresh 1 nm $2\%Pt/\gamma\text{-}Al_2O_3$ catalyst and the catalyst after CO oxidation initiation testing and 3 cycles quantitative conversion testing.

While the above described test-protocol is informative, it does not take sample-to-sample variations into account which is necessary

because only a very small fraction of sample can be analyzed by electron microscopy. We have developed an *ex-situ* reactor that allows us to examine a sample repeatedly after exposure to various reaction conditions, thereby, eliminating any errors caused by sample-to-sample variations. We loaded 1 nm 2%Pt/γ-Al_2O_3 catalyst onto a stainless steel TEM grid coated with $LaCrO_3$ by dry dipping the coated grid into a powder sample of our catalyst. We imaged multiple areas of the sample using ACEM to obtain atomic resolution micrographs of the fresh sample which showed Pt present as single atoms and as clusters up to ~15 atoms. The TEM sample grid was then exposed to CO oxidation conditions in our *ex-situ* reactor which mimicked the conditions observed on the bench-top reactor for CO oxidation initiation. The grid was removed from the reactor and the exact same spots were imaged again on the ACEM. This process was continued for the follow two conditions: 2 cycles of quantitative CO oxidation (FR 2x) and then a 3rd cycle of quantitative CO oxidation (FR 3x).

After initiation testing, fewer single atoms and clusters under 15 atoms could be seen and the areas were becoming dominated by large disordered Pt clusters with sizes greater than 2nm in some cases. The atomic resolution imaging of the sample areas after 2 cycles of quantitative CO oxidation showed that the Pt particles/clusters had sintered significantly and only a few clusters in the 1nm range still exist. Large 2-3 nm clusters without atomic ordering were regularly seen; however, some particles at this stage do exhibit atomic ordering. At the end of the 3rd cycle of quantitative CO oxidation exposure, Pt particles with well ordered structures had become more common. The sintering progression we observed can be seen in Figure 3 for one of the sample areas. In the FR 3x frame of Figure 3, the inset image shows a bcc Pt_3O_4 particle looking down the (120) lattice plane.

12 nm 2%Pt/γ-Al_2O_3: Imaging of multiple areas of a TEM sample grid containing this sample by STEM confirmed the presence of Pt particles ranging from 3.4 to 36.7 nm (a larger outlier at 138.1 nm also seen). The average particle size for the Pt (excluding the outlier) seen by electron microscopy was 12.9 nm (Figure 4a). Following a similar protocol as that used to test the 1nm 2%Pt/γ-Al_2O_3 catalyst discussed above, samples of the fresh 12nm Pt catalyst were tested for CO oxidation initiation (~8% CO oxidation) and for 3 cycles of quantitative CO oxidation using a bench-top reactor and a GC (results reported last year). After each of these tests, the Pt microstructure was evaluated by STEM (HD-2000), see Figure 4b-c. The average Pt particle size increased as the catalyst was exposed to CO oxidation conditions. However, the distribution ranges did not increase in a consistent fashion like that of the 1nm Pt sample, see table 1. A graph comparing particle size distribution of the fresh catalyst to each CO oxidation test is present in Figure 5.

An *ex-situ* study, similar to the one discussed above for the smaller Pt clusters, was also carried out on this catalyst. The CO oxidation conditions that were used mimicked those observed during CO oxidation of the catalyst on the bench-top reactor. These larger particles did not require atomic resolution electron imaging allowing us to follow this *ex-situ* testing process on the HD-2000 and calculate averages and distribution plots. Table 2 shows that after following multiple sample areas from fresh to initiation to 2 cycles quantitative oxidation and finally to a 3rd cycle of quantitative oxidation, only a 1nm increase in the average particle size is observed and virtually no difference in the particle size distribution plots can be seen (Figure 6). These results can be observed visually in Figure 7 which shows a single sample area progression through the CO oxidation test process.

EXPERIMENTAL STUDIES ON Pt/θ-Al_2O_3

1 nm 2%Pt/γ-Al_2O_3: θ–alumina support is the first structurally diverse alumina that we have selected to understand the impact of surface properties and structure of substrate on the behavior of nanocatalysts. Compared with γ–alumina, θ-alumina (BET surface area ~100 m^2/g) has a simple structure and its surface

properties while less attractive than sol-gel derived γ–alumina (BET surface are ~200m^2/g) are still comparable to commercial γ-alumina (BET surface are ~ 100m^2/g). θ-Al_2O_3 can be easily synthesized by sintering sol-gel derived γ-Al_2O_3 at 900°C for 34 hours. The Pt was loaded by impregnating it with $H_2PtCl_6 \bullet 6H_2O$ and subsequent calcination in air at 450°C. Analysis by electron microscopy shows that the Pt clusters sizes ranges from 0.6-1.3 nm with a 0.9 nm average (table 1). Thus, the Pt particles distribution is similar to that for fresh 2%Pt/γ-Al_2O_3, prepared from commercial γ-alumina.

We subjected the 2%Pt/θ-Al_2O_3 catalyst to the same test protocol used for evaluating the γ-Al_2O_3 supported catalyst. Previoulsy, we reported that the change in the substrate morphology had a significant impact on the catalyst CO oxidation activity with both initiation and quantitative oxidation requiring less energy for the θ-Al_2O_3 supported catalyst. Now, we have studied the microstructural changes that occurred as a result of CO oxidation initiation (~5%) (Figure 8b) and 3 cycles of quantitative oxidation by STEM (HD-2000) (Figure 8c). Pt cluster/particle averages and size ranges after both of these tests were nearly identical to those seen for the 1nm 2%Pt/θ-Al_2O_3 catalyst (table 1). Figure 9 shows the particle size distributions at each stage of testing. This is surprising because there is a significant difference between the CO oxidation reaction on γ-Al_2O_3 and θ-Al_2O_3 supported catalyst.

Conclusions

Our study on the microstructural effect of the Pt cluster/particle size on the 2%Pt/γ-Al_2O_3 catalysts demonstrated that fresh 1 nm and smaller Pt clusters agglomerate quickly even under CO oxidation initiation conditions and continue to exhibit sintering through 3 cycles of quantitative CO oxidation. Large particles (based on our tests of supported 12 nm Pt particles), on the other hand, are more stable and do not significantly change after 3 cycles of CO oxidation. These results suggest that the efforts to obtain nanometer and sub-nanometer Pt particles do not offer a significant advantage for CO oxidation.

We also studied the effect the substrate plays on the Pt microstructure under CO oxidation conditions by studying 1 nm 2%Pt/θ-Al_2O_3. While we found that there is a significant difference in activity, surprisingly, our microstructural studies show no structural differences in Pt particles supported on γ and θ alumina in fresh samples. Furthermore, agglomeration and sintering for both types of samples under various CO oxidation conditions were almost identical.

Our studies also indicate pot-mortem analysis of catalysts, while informative, can not take into account samples-to-sample variation and is not effective in determining less than dramatic microstructural changes. As such, the conclusions based on co-relation of activity with microstructural analysis could be erroneous. Our *ex-situ* reactor study presented here provides a means to accurately monitor even the minor microstructural changes since the analysis is not affected by sample to sample variations. Next, we plan to determine nano-structural changes in supported Pt catalysts under NO and HC oxidation and correlate our experimental findings with theoretical calculations before studying a complex system such as vehicle exhaust

References

1. Narula, C.K., Moses, M.J., Allard, L.F. *SAE no. 2006-01-3420*, 2006.
2. Kang, J.H.; Menard, L.D.; Nuzzo, R.G.; Frenkel, A.I. *J. Am. Chem. Soc.*, 128 (2006) 12068.
3. Zhou, C.W., J.; Dhilip Kumar, T.J.; Balakrishnan. N.; Forrey, R.C.; Cheng, H., *J. Phys. Chem. C* 111 (2007) 13786-13793.

Presentations and Publications (FY 07)

1. Narula, C.K.; Catalyst by Design – Bridging the gap between Theory and Experiments at Nanoscale Level, Encyclopedia of Nanoscience and Nanotechnology, Taylor &

Francis, (manuscript to be submitted by November 30, 2007)

2. Narula, C. K., Allard, L.F., Blom, D.A., Moses-DeBusk, M., "Bridging the Gap between Theory and Experiments – Nanostructural Changes in Supported Catalysts under Operating Conditions." *SAE no. 08PFL-355,* submitted.

3. Narula, C. K., Moses, M.J., Xu, Y., Blom, D.A., Allard, L.F., Shelton, W.A. "Catalysis by Design – Theoretical and Experimental Studies of Model Catalysts." *SAE no. 2007-01-1018*, 2007.

4. Narula, C.K.; Blom, D, A; Allard, L.F.; Moses, M.J.; Xu, Y.; Shelton, W.A.; Schneider, W.F. "Catalysts by Design – Bridging the Gap between Theory and Experiments." DEER 2007, Marriott, Detroit, August 13-16, 2007.

5. Narula, C. K., Moses, M.J., Blom, D.A., Allard, L.F. "Nano-Structural Changes in Supported Pt Catalysts during CO Oxidation." North American Catalysis Society Meeting, Houston, TX, June 2007.

6. Narula, C. K., Moses, M.J., Allard, L.F. "Analysis of Microstructural Changes In Lean NO_x Trap Materials Isolates Parameters Responsible for Activity Deterioration" *SAE no. 2006-01-3420*, 2006.

Figures

Figure 1: STEM images of fresh 1nm 2%Pt/γ-alumina (a), after CO oxidation initiation (b) and after 3 cycles of quantitative CO oxidation

Figure 2: Particle size distribution of 1nm 2%Pt/γ-alumina catalyst as determined from STEM imaging of multiple areas, for fresh sample and after exposure to various CO oxidations conditions. Sizes have been sorted into ranges for this graph and all begin and end at zero.

Figure 3: ACEM HAADF-STEM images of the exact same sample area of fresh 2%Pt/γ-Al_2O_3, after CO oxidation Initiation, after 2-, and 3-cycles of quantitative CO-conversion (left to right, respectively). The second row shows the area at higher magnification for each stage, respectively. Circles and squares are located at the same place on each image to allow monitoring of Pt growth at each stage of testing.

Figure 4: STEM images of fresh 12nm 2%Pt/γ-alumina (a), after CO oxidation initiation (b) and after 3 cycles of quantitative CO oxidation (c).

Figure 5: Particle size distribution comparison of 12nm 2%Pt/γ-alumina catalyst as determined from the STEM imaging of multiple areas, for fresh sample and those exposed to various CO oxidations conditions. Sizes have been sorted into ranges for this graph and all begin and end at zero.

Figure 6: Pt particle size distribution for 12 nm 2%Pt/ γ-Al_2O_3 fresh catalyst and after CO oxidation on the *ex-situ* reactor, as determined from HAADF-STEM micrographs. Sizes have been sorted into ranges for this graph and all begin and end at zero.

Figure 7: HAADF-STEM images of the exact same sample area throughout the *ex-situ* CO oxidation study on Fresh 12 nm 2%Pt/γ-Al_2O_3. Images after CO oxidation initiation-testing, 2 cycles of quantitative oxidation and a 3rd cycle of quantitative oxidation are shown.

Figure 8: STEM images of fresh 1nm 2%Pt/θ-alumina (a), after CO oxidation initiation (b) and after 3 cycles of quantitative CO oxidation (c).

Figure 9: Particle size distribution of 1nm 2%Pt/θ-alumina catalyst as determined from STEM imaging of multiple areas for fresh samples and those exposed to various CO oxidations conditions. Sizes have been sorted into ranges for this graph and all begin and end at zero.

Tables

Table 1. Average Pt particle sizes and ranges as determined by STEM imaging before and after the bench-top CO oxidation tests.

Table 2. Average Pt Particle sizes and ranges from multiple areas determined by STEM imaging throughout the CO oxidation *Ex-situ* study on 12nm 2%Pt/γ-Al_2O_3.

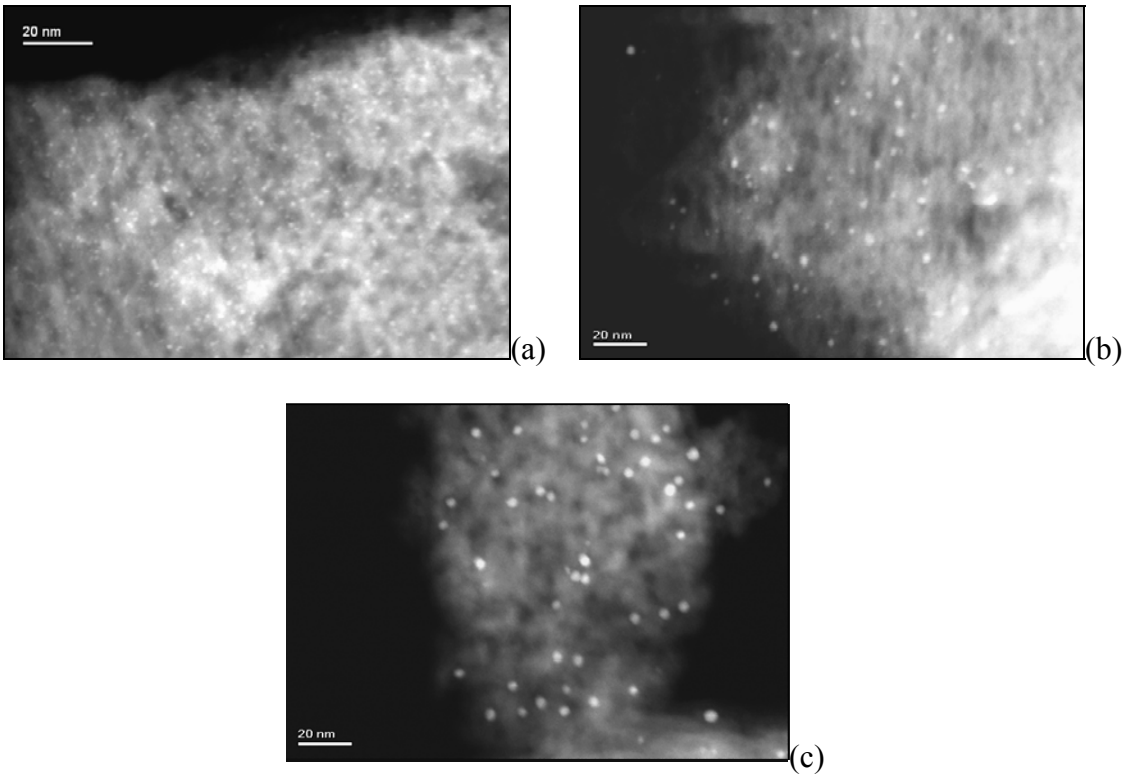

Figure 1: STEM images of fresh 1nm 2%Pt/γ-alumina (a), after CO oxidation initiation (b) and after 3 cycles of quantitative CO oxidation

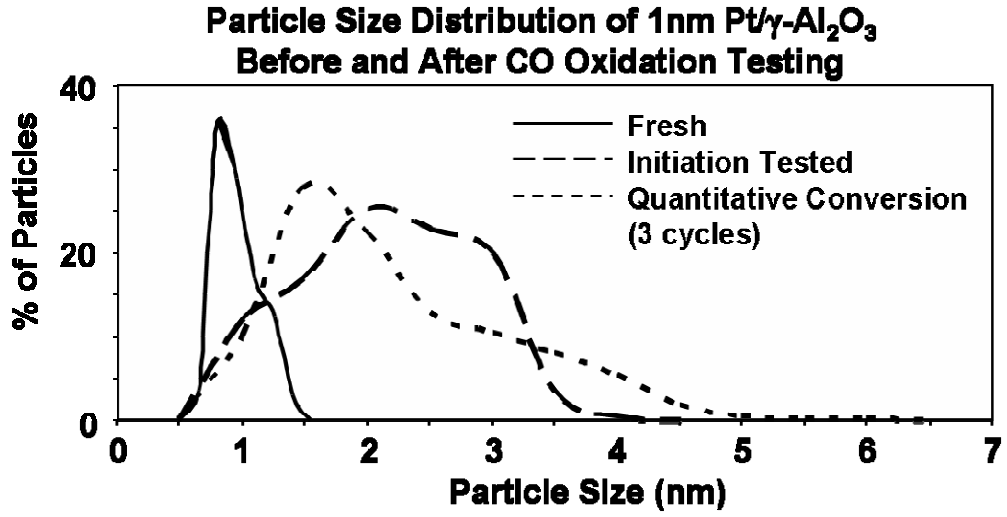

Figure 2: Particle size distribution of 1 nm 2%Pt/γ-alumina catalyst as determined from STEM imaging of multiple areas, for fresh sample and after exposure to various CO oxidations conditions. Sizes have been sorted into ranges for this graph and all begin and end at zero.

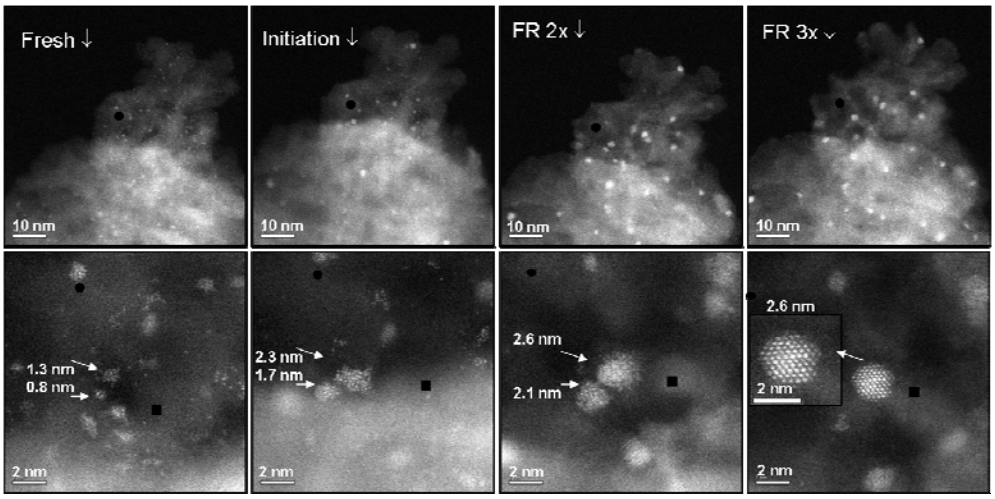

Figure 3: ACEM HAADF-STEM images of the exact same sample area of fresh 2%Pt/γ-Al_2O_3, after CO oxidation initiation, after 2-, and 3-cycles of quantitative CO-conversion (left to right, respectively). The second row shows the area at higher magnification for each stage, respectively. Circles and squares are located at the same place on each image to allow monitoring of Pt growth at each stage of testing.

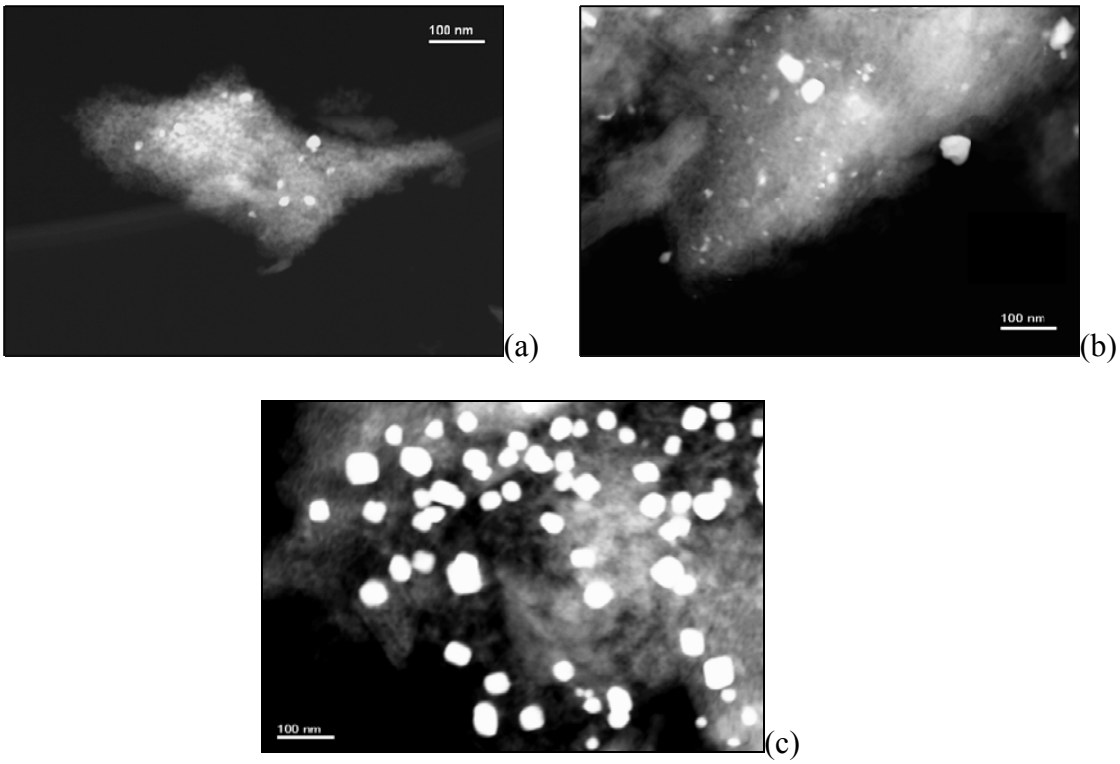

Figure 4: STEM images of fresh 12 nm 2%Pt/γ-alumina (a), after CO oxidation initiation (b) and after 3 cycles of quantitative CO oxidation (c).

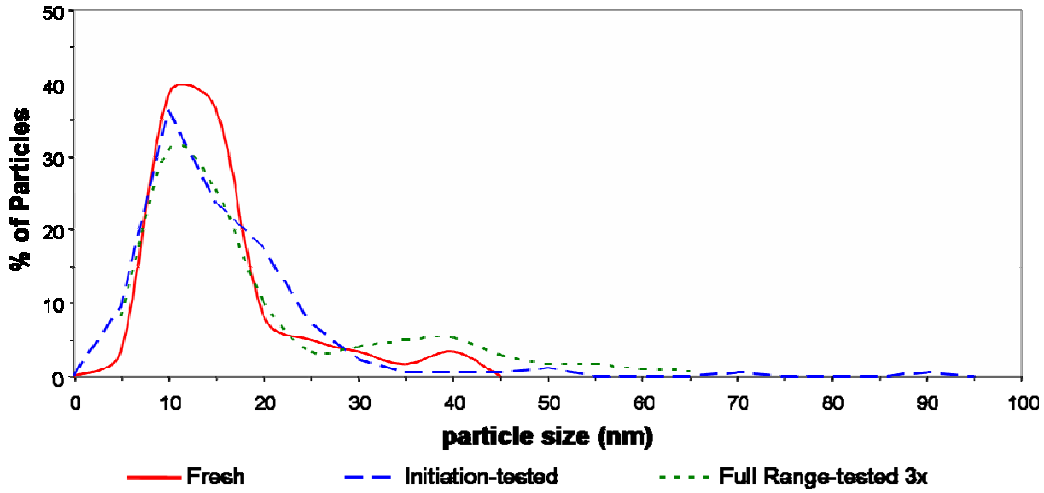

Figure 5: Particle size distribution comparison of 12 nm 2%Pt/γ-alumina catalyst as determined from the STEM imaging of multiple areas, for fresh sample and those exposed to various CO oxidations conditions. Sizes have been sorted into ranges for this graph and all begin and end at zero.

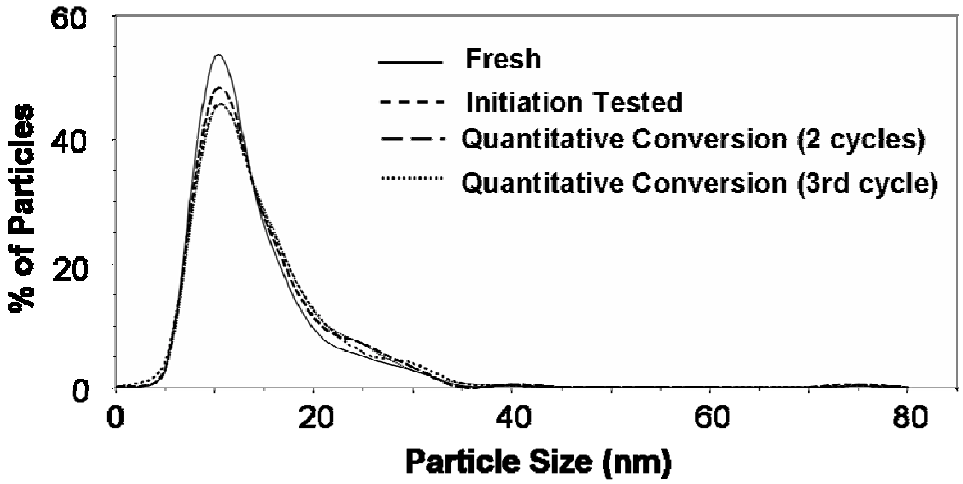

Figure 6: Pt particle size distribution for 12 nm 2%Pt/ γ-Al_2O_3 fresh catalyst and after CO oxidation on the *ex-situ* reactor, as determined from HAADF-STEM micrographs. Sizes have been sorted into ranges for this graph and all begin and end at zero.

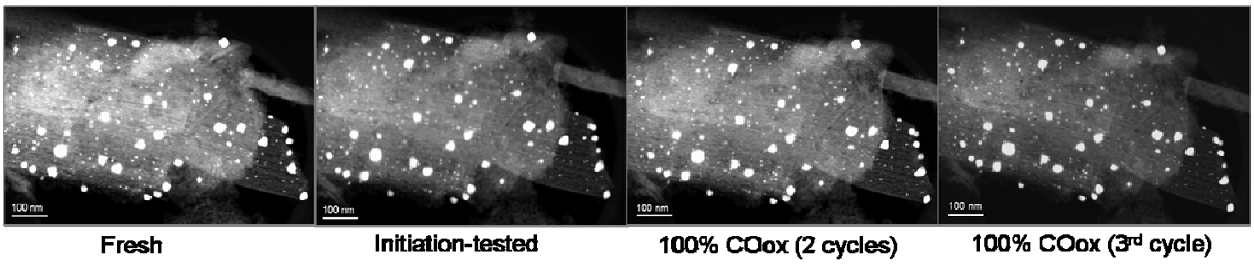

Figure 7: HAADF-STEM images of the exact same sample area throughout the *ex-situ* CO oxidation study on Fresh 12 nm 2%Pt/γ-Al_2O_3. Images after CO oxidation initiation-testing, 2 cycles of quantitative oxidation and a 3rd cycle of quantitative oxidation are shown.

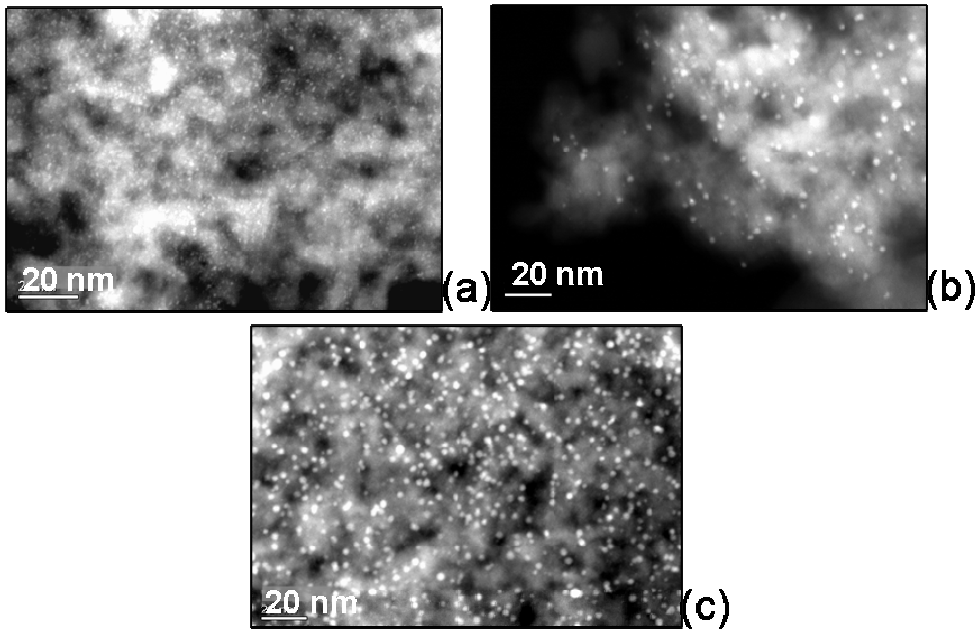

Figure 8: STEM images of fresh 1 nm 2%Pt/θ-alumina (a), after CO oxidation initiation (b) and after 3 cycles of quantitative CO oxidation (c).

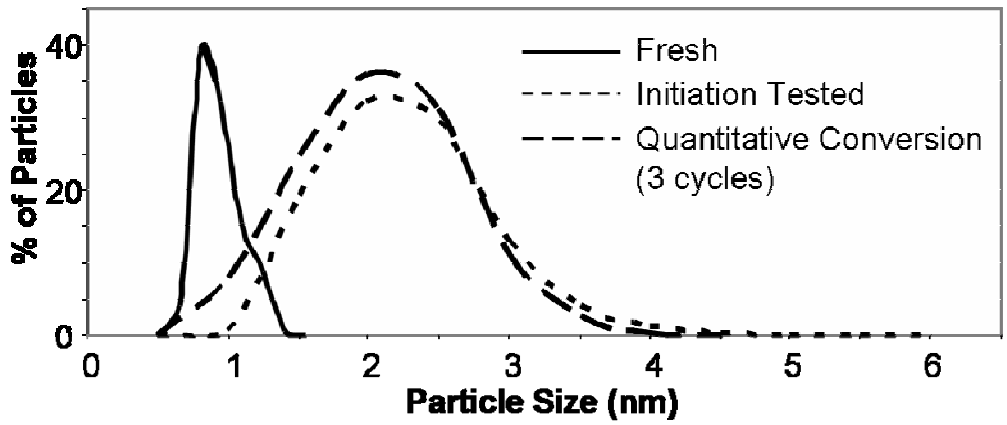

Figure 9: Particle size distribution of 1 nm 2%Pt/θ-alumina catalyst as determined from STEM imaging of multiple areas for fresh samples and those exposed to various CO oxidations conditions. Sizes have been sorted into ranges for this graph and all begin and end at zero.

Table 1. Average Pt particle sizes and ranges as determined by STEM imaging before and after the bench-top CO oxidation tests.

	Fresh	**Oxidation Initiation-Testing**	**3-cycles Quantitative Oxidation**
1nm Pt/γ-alumina	0. 9 nm (0.6-1.4 nm)	1.9 nm (0.7-3.8 nm)	2.0 nm (0.7-5.6 nm)
25nm Pt/γ-alumina	12.9 nm (3.4-36.7 nm)	13.1 nm (1.4-87.9 nm)	17.0 nm (1.7-68.7 nm)
1nm Pt/θ-alumina	0.9 nm (0.6-1.3 nm)	1.8 nm (0.6-4.0 nm)	2.0 nm (0.7-5.1 nm)

Table 2. Average Pt Particle sizes and ranges from multiple areas as determined by STEM imaging throughout the CO oxidation *Ex-situ* study on 12nm 2%Pt/γ-Al_2O_3.

Summary	**Average**	**Median**	**Range**	**# of Particles**
Fresh	11.1 nm	9.2 nm	2.8-39.9 nm + 72 nm	403
COox Initiation-Testing	11.9 nm	10.0 nm	3.0-36.7 nm + 74.3 nm	306
2 cycles Quantitative COox	11.8 nm	10.0 nm	3.4-35.4 nm + 71.1 nm	243
3rd cycle Quantitative COox	12.3 nm	10.4 nm	2.5-38.4 nm + 70.9 nm	238

Project 18865 - Materials by Design

Agreement 13723 - Residual Stresses in Thin Films*

*(This project is jointly funded by Propulsion Materials and Heavy Vehicle Systems Optimization)

Principal Investigator: D. Singh (co-investigators: J. L. Routbort, G. Chen, O. Eryilmaz, A. Erdemir)

Argonne National Laboratory

9700 S. Cass Avenue, Argonne, IL 60439-4838

630-252-5009 dsingh@anl.gov

DOE Technology Manager: Jerry L. Gibbs

(202) 586-1182; fax: (202) 586-1600; e-mail: jerry.gibbs@ee.doe.gov

---

Contractor: UChicago Argonne LLC

Contract No.: DE AC03 06CH11357

Objective

- Measure residual stresses in thin films and coatings as a function of film thickness and relate stresses to film properties such as hardness, fracture toughness, and adhesion energy to relate to film processing variables and to predict durability

Approach

- Develop X-ray technique to measure change of lattice parameter of coating constituents as a function of depth and hence to calculate the lattice strains and stresses
- Develop indentation technique to measure hardness, fracture toughness, and adhesion energy of films and coatings
- Relate stresses, properties, and processing conditions to film durability

Accomplishments

- Advanced Photon Source (APS) used to measure stresses in 3–μm thick thin films of nanocrystalline MoN and MoCuN deposited on silicon and steel substrates as a function of depth
- Stresses were found to be sensitive to deposition conditions and thermal annealing
- A paper published in Applied Physics Letters
- Preliminary coating/film adhesion energies measured using indentation

Future Directions

- Continue to refine and improve resolution of X-ray technique
- Develop indentation technique to measure film adhesion
- Investigate stresses in superhard, nanocrystalline MoCuN films as a function of deposition conditions and Cu concentration on steel substrates as well as investigate other coatings systems applicable for engine applications

---

Introduction

Because of their unusual structural, mechanical, and tribological properties, superhard, nanocrystalline coatings can have an immediate and far-reaching impact on numerous advanced transportation applications including FreedomCAR and 21st Century Truck Programs of DOE by reducing parasitic friction losses (hence increasing fuel economy) and wear (hence increasing durability/reliability). They can also be used to overcome toxic emission problems associated with exhaust gas recirculation in diesel engines. Durability of hard coatings is a critical property. The durability is determined by the surface adhesion energy, but is the result, in a large part, of the residual stresses that form as a result of materials, and processing parameters such as deposition bias voltage, ion flux, and temperature.

The approach for this effort is to use the high-brilliance X-rays produced by the Advanced Photon Source (APS) at Argonne National Laboratory, and a microfocus beam, to measure the residual stresses/strains of MoN thin films as a function of depth from the surface through the interface to the substrate. Subsequently, correlate the residual stress profiles with the film processing conditions and the resulting film/substrate adhesion and its tribological properties.

During the past year, focus has been on two coating/substrate systems: (a) MoN/Mo film on silicon (Si) single crystal wafer and (b) MoN/Mo film deposited on steel; latter system having a significant technological implication. In addition, effect of copper additions on the film was also investigated. MoN/Mo on Si system was used to measure residual stress/strains using two different approaches (edge scan and wire technique) to establish viability of each of the techniques and their pros/cons. Whereas, MoN/steel system was used for residual stress measurements and preliminary correlation of film/substrate adhesion energy to the residual stresses.

Experimental

(a) Coating/substrate systems

MoN/Mo on Si

MoN/Mo bilayer films were prepared by physical vapor deposition (PVD) using magnetron sputtering at temperatures between 250 and 300 °C. The substrate was p-type (100) single-crystal silicon wafer (cleaved into 3 cm × 3 cm × 0.1 cm pieces) with native oxide layer. Film deposition details have been described in FY 06 report and will not be repeated here. Figure 1 is a scanning electron microscopy (SEM) micrograph of the cross section of an as-deposited MoN/Mo film. The Mo and MoN layers show a dense columnar structure.

MoN/Mo on steel

MoN/Mo thin films on H 13 steel substrates (1" x 1" x 0.25" coupons) were also deposited by PVD process. Three samples were fabricated using slightly differing deposition conditions to investigate the effect of processing on film adhesion. In all the samples, initially a bond layer was deposited followed by MoN coating. The bond coat was either combination of Mo + Mo_2N or Mo_2N. Flowing nitrogen gas was used. Details for each of the samples are listed in the Table 1. Based on the deposition parameters, it is estimated that bond layer for all the samples would be approximately 100 nm. Figure 2 shows a SEM micrograph of a typical MoN/Mo film deposited on steel. The film thickness is approximately 4 μm and it dense.

Table 1. Deposition Conditions for the MoNCu/Steel Samples

Sample ID	Mo & Cu Deposition Power (kW)	Deposition Time (s)
C70109	Mo:8; Cu: 0	7200
C70110	Mo: 8; Cu: 0.5	6600
C61215	Mo: 8; Cu: 0.8	7200

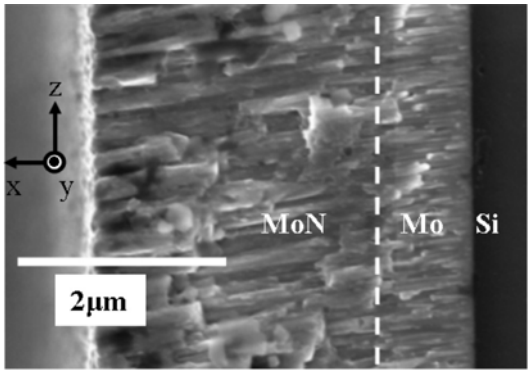

Figure 1: Cross-sectional scanning electron micrograph of MoN/Mo bilayer film deposited on Si substrate.

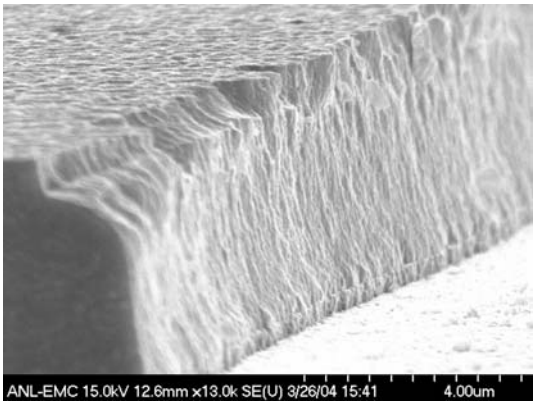

Figure 2: Cross-sectional SEM of a MoNCu/Mo film deposited on steel substrate.

b) Residual stress measurements

X-ray microdiffraction was performed on beamline 34-ID-E at the Advanced Photon Source (Argonne National Laboratory) [1]. The x-ray beam was focused by Kirkpatrick-Baez mirrors down to 0.4 (horizontal) × 0.6 (vertical) μm^2. A high-resolution charged coupled device (CCD) x-ray detector was used to collect x-ray diffraction (XRD) patterns from the x-ray microbeam with energy of 8.9 keV (1.39308 Å). Strains and stresses were evaluated from the change in the lattice spacing determined from diffraction pattern of specific diffraction planes of coating and substrate materials and their respective stress-free states. Two different approaches, namely cross-section and wire techniques, were used for the measurement of stresses.

For the cross-section or edge technique, cross-section of the sample is examined, either by fracturing the sample or aligning the sample such that one of the edges is perpendicular to the x-ray beam. Schematic of the edge technique is shown in Figure 3 (A). Sample was aligned by an x-ray fluorescence method so that the film surface (i.e., the yz plane in Figure 1) was parallel to the x-ray beam. The position of the x-ray beam was scanned along the film normal (x in Figure 1) direction with a step size of 0.25 μm. Similarly, by rotating the detector or the sample by 90°, out-of-plane strains can be determined.

Schematic for the wire technique is shown in Figure 3(B) and was originally developed by Larson et al. [2] to study the strain tensors and orientations in three-dimensional crystals. When the x-ray beam hits a series of grains within the film, a Laue diffraction pattern is generated and captured by the CCD x-ray detector. This pattern contains information on grains along the x-ray beam direction. Unlike previous two-dimensional x-ray structural microscopy, this technique uses an x-ray absorption wire (a 50-micron platinum wire) as a differential-aperture (i.e. knife edge) slit to separate Laue patterns obtained from different grains along the sample depth. Thus, by comparing the shift in Laue patterns from grains, at a specific coating depth, to that of the unstrained grains, residual strains can be determined. Currently, this technique provides ~ 0.5 μm spatial resolution along the beam direction. However, by decreasing the beam size and the step size of the wire movement, it is possible to increase the resolution to ~ 0.1 μm. Thus, this technique can be extremely useful in stress profiling in thin films and coatings.

There are pros and cons associated with both the techniques. Edge or cross-section based technique is simpler in terms of conducting experiments and analyzing data, however, results from this technique could be affected by the edge effects. On the other hand, wire technique is more

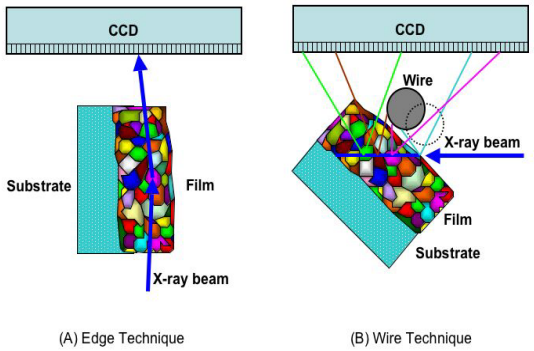

Figure 3. Experimental set-up used for stress evaluations: (A) Edge and (B) Wire techniques.

complex in terms of experimentation and analysis. At the present time, wire technique is set-up to only measure out-of-plane stresses/strains.

c) Adhesion energy measurements

An indentation technique [3] was used to evaluate the film/substrate interfacial adhesion energy. Specifically, this technique is applicable for hard brittle films deposited on relatively ductile substrates, similar to the MoN/steel system used in our study. This technique assumes that upon application of an indentation load, the sub-surface stress is concentrated at the interface. At a critical indentation load, stress concentration becomes equal or greater than the film adhesion strength, thereby leading to delamination of the film. Typically, the extent of delamination can be observed by the formation of circumferential cracks in the film.

Accounting for the complex stress state developed during indentation, residual stresses, plasticity of the substrate material, and the extent of interfacial delamination, Kim et al. [3] have developed a closed-form solution for the critical energy release rate 'G_c' or the adhesion energy given as:

$$G_c = \left(\kappa \frac{dP}{dc} + \lambda\right) t \Big/ \left(c - a\frac{da}{dP}\frac{dP}{dc}\right) \qquad (1)$$

where P is the indentation load, a is the indent radius, c is the delamination radius, t is the film thickness, and κ and λ are constants that include the material properties of the film and substrate materials and the residual stresses. Thus, by experimentally determining the variation of the indentation and delamination radii with the indentation loads (da/dP & dc/dP), material properties, and residual stresses in the film, adhesion energy of the film can be calculated.

Results and Discussion

(a) Residual stress measurements in MoN/Mo on Si using cross-section technique

Results from this technique were reported in FY 2006 annual report. Highlights of the results were that MoN and Mo layers in the as-deposited film were found to be under in-plane compression, with large strain gradients as a function of depth (Figure 4). The observed strain profiles were explained in terms of atomic peening and void-induced strain relaxation. Annealing of the film caused significant strain relief possibly due to defect reduction in the MoN layer. In contrast, residual strain in the Mo layer was only slightly relieved, and the defect concentration increased after annealing.

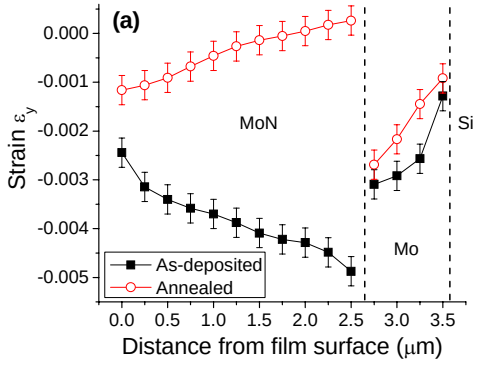

Figure 4: Depth-resolved residual strain for as-deposited and annealed MoN/Mo bilayer films as determined from cross-section technique.

(b) Residual stress measurements in MoN/Mo on Si using wire technique

Figure 5(a) shows the overall diffraction pattern of the MoN/Mo film, and Figure 5(b) shows the reconstructed patterns from different depths of the film, which were derived from the wire technique. The overall pattern shown in 5(a) comes from both the MoN layer and the Mo bond layer. The latter shows a spotty diffraction pattern, indicating a relatively larger grain size than the MoN layer. The reconstructed patterns in 5(b) indicate that the MoN layer is near the surface of the film while the Mo bond layer is near the substrate. Further analysis of the diffraction patterns shows that there are shifts in the diffraction peaks (both MoN (402) and Mo (220)) as depth of film increases (Fig. 6). The sharper peaks are the Mo and the broader peaks correspond to the MoN. The corresponding lattice parameter of the MoN (402) peak decreases from 1.1473 Å to 1.1411 Å. The corresponding lattice parameter of the Mo (220) also decreases from 1.1187 Å to 1.1174 Å. The strain free lattice parameters for MoN (402) and Mo (220) are 1.1405 Å and 1.1143 Å, respectively. Therefore, from these data, we can plot the depth-resolved out-of-plane strains for both MoN and Mo layers, as shown in Figure 7.

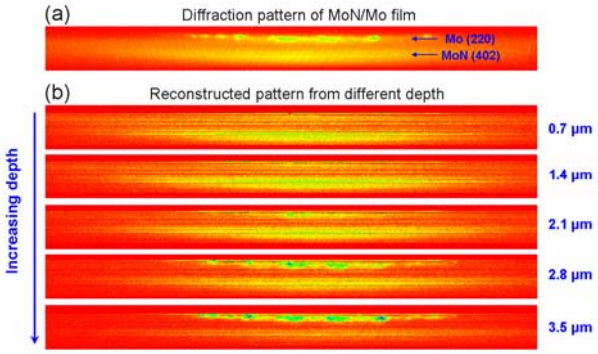

Figure 5. (a) Overall x-ray diffraction pattern of the MoN/Mo film and (b) reconstructed diffraction patterns from different film depths.

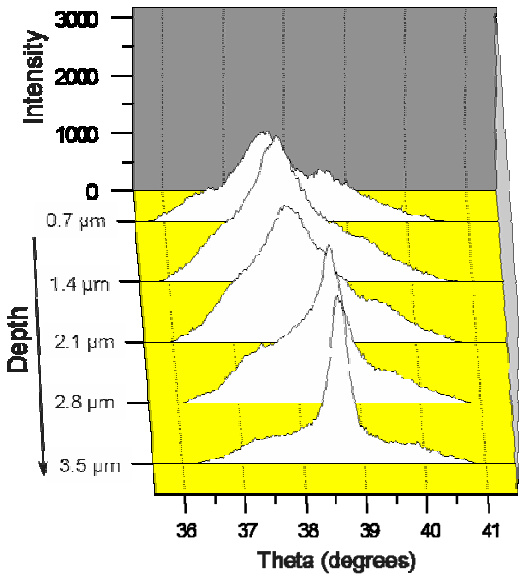

Figure 6. Shift in the diffraction peak as a function of depth indicative of variation of residual stresses as a function of depth.

Figure 7 also compares the out-of-plane strain measured by the wire technique with the in-plane strains measured by the cross-section technique. Because of the limitations in the current set-up for wire technique and associated software, independent measurements of the in-plane strains could not be made. Nevertheless, on estimating the in-plane stains based the out-of-plane strain measurements from the wire-technique gives values of in-plane strain that are significantly (20-40%) lower than those determined from the cross-section technique. This implies that sample sectioning or using the sample edge of as-deposited film/substrate, per the cross-sectional technique, alters the stress state. In this regards, cross-sectional technique should be best used for qualitative assessment of the residual stresses in thin films as opposed to accurate strain determinations.

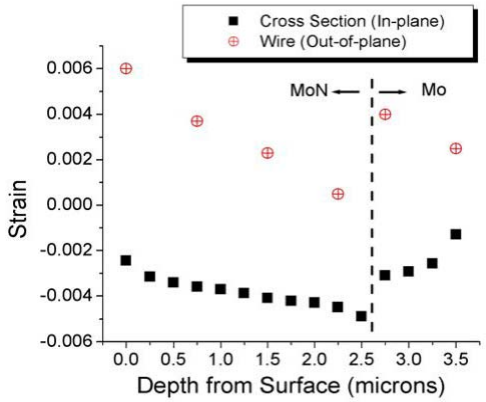

Figure 7. Depth resolved out-of-plane strain measured using the wire-technique in MoN/Mo film deposited on Si substrate.

c) Residual strain measurements in MoN-Cu using the cross-section technique

Figures 8a-c show the measured lattice parameters of in-plane biaxial, out-of-plane, and strain free MoN 222 peaks as a function of the film depth in the MoNCu thin films deposited on steel substrates. Observations from three samples processed differently (Table 1) are quite similar; in-plane lattice parameters decrease with the film depth, whereas, out-of-plane lattice parameters increase with the film depth. Strain-free lattice parameter is calculated from $\sin^2\psi$ approach [4]. These results indicate the film is in in-plane compression and in tension out-of-plane.

Figure 9 shows the residual stresses for the three MoNCu/steel samples estimated from lattice spacing changes of Fig 8. In all cases the in-plane residual stresses were compressive and increases in magnitude with film depth. The magnitudes of the residual stresses were as high as 4 GPa. There was no clear correlation between the deposition conditions and the measured residual stresses for the three samples investigated. However, it appears that sample (C70110) with the shortest deposition time has the highest compressive residual stress.

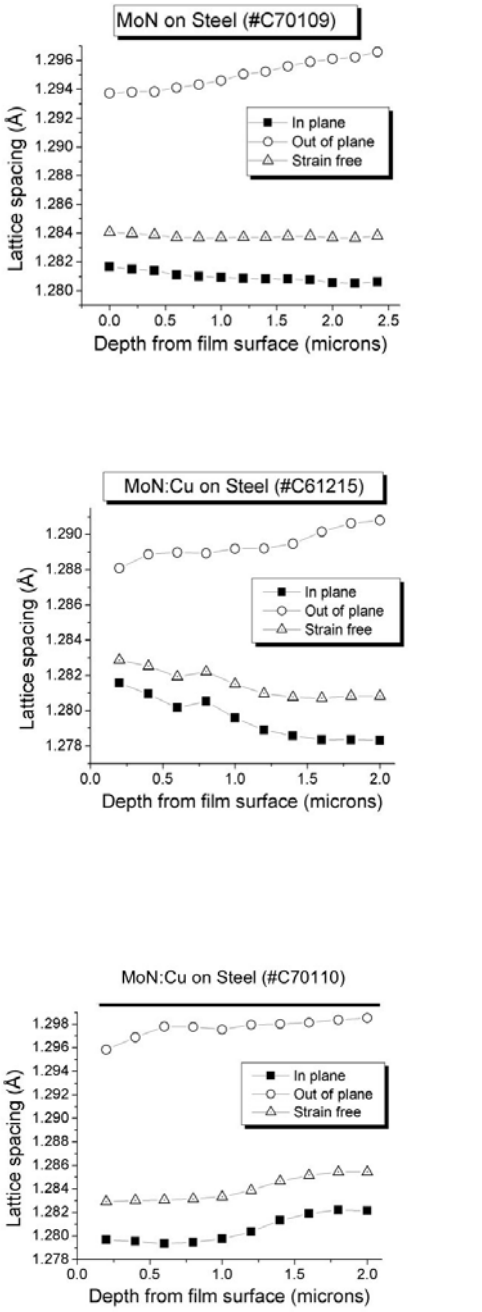

Figure 8. Lattice parameters of MoN 222 reflections for various stress-states as a function of film depth in MoNCu film deposited on steel.

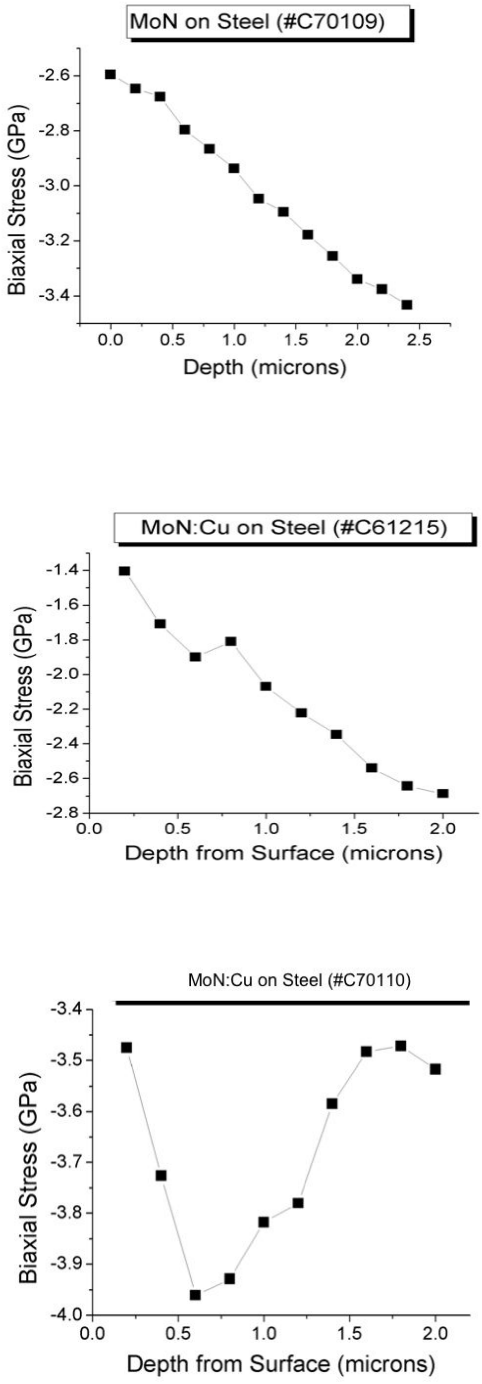

Figure 9. In-plane biaxial stress for various stress-states as a function of film depth in MoNCu film deposited on steel.

Residual strains in PVD coatings are very complex because they include both intrinsic and extrinsic strains [5]. The intrinsic strains are related to the microstructure of thin films, which varies with material as well as with film deposition conditions. Extrinsic effects refer to thermal strain caused by the thermal expansion coefficient mismatch between film and substrate. In PVD films, the intrinsic residual strain is strongly affected by deposition conditions. Nonetheless, it is believed that compressive strains in thin films that have been subjected to ion or atom bombardment are caused by atomic peening [6], which is enhanced by low sputtering gas pressure and high substrate bias during deposition [6]. The case of the MoN layer is more complicated since N_2 was introduced during the film growth to form the metal nitride.

(c) Measurement of Thin Film Adhesion Energy

Spherical Brale C indentor was used to evaluate the adhesion energy of the MoN/Cu coatings deposited on steel substrate (sample C61215), Indentations were made at three different loads (P) ranging from approximately 600 N to 1600 N. Figure 10 is an optical micrograph of a typical indent showing the circular indent and on the sample. There is a large circular indent surrounded by a region where the film debonding and cracking occurs. Indent and delamination radii are depicted on the figure. The film debonding and cracking is symmetric around the indent. This indent was from an area of the sample away from the edge.

Figure 11 shows an indent on the same sample as in Figure 10, but near the sample edge. The indentation load was 590 N. Clearly, the cracking and delamination in this case is not symmetric to the indent made near the sample center (Figure 10). Similar observations were made at all the indentation loads. It is believed that the asymmetric nature of cracking and delamination is a direct consequence of asymmetric in-plane residual stress-state near the sample edge.

Variations of the indent and delamination crack sizes as a function of

indentation loads are plotted in Figure 12 and there is a linear dependence. The slopes of the linear curve fits to the data were used in the eqn. 1, along with the material parameters, for the determination of the interfacial adhesion energy. The residual stress was assumed to be 2.5 GPa and the coating thickness was taken as 2.5 µm. The resulting value for the adhesion energy was determined to be 671 J/m^2. High measured adhesion interfacial energy is consistent with experimental observation of short delamination zone. Similarly, adhesion energies for diamond like carbon (DLC) on steel (571 J/m^2, ref. 3) and TiN/ZrN on steel (180 J/m^2, ref. 7) have been reported in the literature.

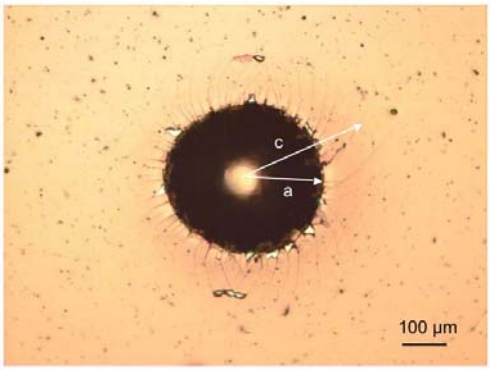

Figure 10. Optical micrograph of a 590 N indent on MoNCu/steel (C61215) sample away from the sample edge.

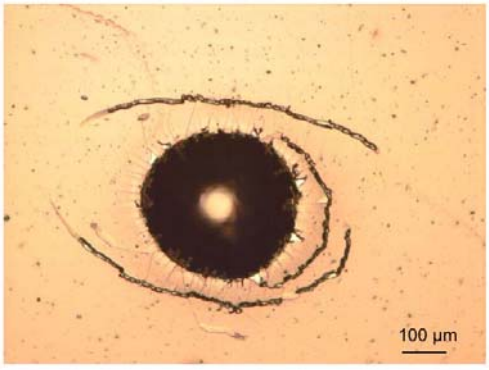

Figure 11. Optical micrograph of a 590 N indent on MoNCu/steel (C61215) sample near the sample edge.

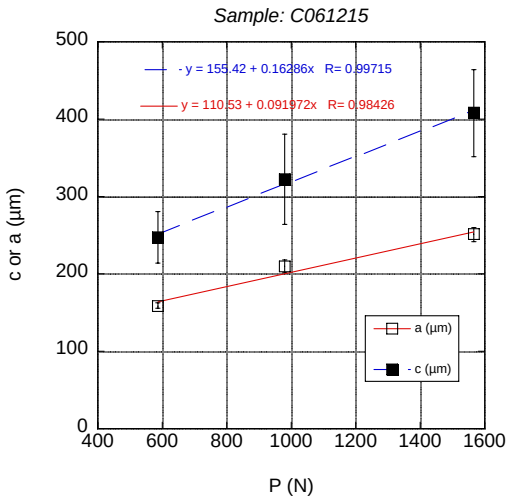

Figure 12. Plot of indentation and delamination crack sizes as a function of the indentation load for MoNCu/steel sample.

In conclusion, we have applied cross-section and wire techniques using x-ray micro-diffraction to study depth-resolved residual strain in MoN/Mo bilayer films deposited on Si and steel substrates. Preliminary evaluation of film/substrate adhesion energy made using an indentation method.

Future Direction

Residual stress measurements will be extended to superhard, nanocrystalline MoCuN thin films and to commercial films, namely Ni_3B, ZrN. The indentation technique will be further refined and exploited to measure the thin film or coating properties and the adhesion energy. The residual stress-states and adhesion energy will be related to the film deposition conditions to optimize the film tribological performance.

References

1. G. E. Ice, B. C. Larson, W. Yang, J. D. Budai, J. Z. Tischler, J. W. L. Pang, R. I. Barabash, and W. Liu, J. Synchrotron Rad. **12**, 155 (2005).
2. B. C. Larson, W. Yang, G. E. Ice, J. D. Budia, and J. Z. Tischler, Nature **415**, 887 (2002).

3. J. J. Kim et al., Thin Film Solids **441**, 172-179 (2003).
4. V. Hauk, *Structure and Residual Stress Analysis by Nondestructive Methods*, (Elsevier, Amsterdam, 1997), Chapter 2.
5. A. Misra and M. Nastasi, *Engineering Thin Films and Nanostructures with Ion Beams*, edited by E. Knystautas (Taylor & Francis, Boca Raton, FL, 2005), Chapter 7.
6. H. Windischmann, Crit. Rev. Solid State Mater. Sci. **17**, 547 (1992).
7. S. V. Hainsworth, M. R. McGurk, and T. F. Page, Surface and Coatings Technology **102,** 97-107 (1998).

Agreement 9105 - Ultra-High Resolution Electron Microscopy for Characterization of Catalyst Microstructures and Deactivation Mechanisms

*L. F. Allard, D. A. Blom, C. K. Narula, S. A. Bradley*and M. Jose-Yacaman***
Oak Ridge National Laboratory
P.O. Box 2008, MS-6064
Oak Ridge, TN 37831-6064

**UOP LLC, Des Plaines, IL 60017*
*** University of Texas-Austin, Austin, TX 78712*

DOE Technology Manager: Jerry L. Gibbs
(202) 586-1182; fax: (202) 586-1600; e-mail: jerry.gibbs@ee.doe.gov
ORNL Technical Advisor: D. Ray Johnson
(865) 576-6832; fax: (865) 574-6098; e-mail: johnsondr@ornl.gov

Contractor: Oak Ridge National Laboratory, Oak Ridge, Tennessee
Contract No.: DE-AC05-00OR22725

Objectives

- Develop and utilize new capabilities and techniques for ultra-high resolution transmission electron microscopy (UHR-TEM) to characterize the microstructures of catalytic materials of interest for reduction of NO_x emissions in diesel and automotive exhaust systems.
- Relate the effects of reaction conditions on the changes in morphology of heavy metal species on "real" catalyst support materials (typically oxides).
- Develop capability to experimentally study the effects of experimental reaction treatments on TEM samples of NO_x trap catalyst materials before and after reactions, using the High-Temperature Materials Laboratory (HTML) "ex-situ" catalyst reactor with a specimen holder designed for use in the aberration-corrected electron microscope (ACEM).
- Initiate project with Protochips Co. to develop a robust heating holder for the ACEM, to allow the behavior of catalytic materials to be studied in-situ as a function of temperature and time, with stability sufficient not to compromise the full sub-Ångström imaging capability of the instrument.

Approach

- Utilize Oak Ridge National Laboratory ACEM to characterize the atomic morphology and behavior of heavy-metal species such as platinum and rhenium on oxide support materials (alumina, silica and titania) as a function of ex-situ reaction treatments.
- Utilize ACEM ADF imaging to characterize the structure and chemistry of a series of model bimetallic nanoparticle comprising controlled compositions in the gold/palladium system.
- Utilize density functional theory for modeling bimetallic catalyst structures and computing the resultant ADF images for comparison to and support of experimental observations.

Accomplishments

- Characterized the changes in platinum catalyst structures on γ-alumina as a function of reduction treatments in the ex-situ catalyst reactor.

- Characterized the morphology and chemistry of a series of novel bi-metallic catalysts in the Au-Pd system, including nanoparticles that demonstrate a core-inner shell-outer shell structure. Compared to computed structures and images.
- Fabricated a new ACEM specimen holder designed to allow sample heating in-situ, using novel heater "chips" developed by Protochips Co. (Raleigh, NC).

Future Directions

- In a cooperative project with Protochips Co., continue to develop techniques for in-situ heating experiments, and perform the baseline experiments to allow reliable data to be obtained. Extend the heating capability further to allow in-situ gas reaction experiments to be conducted.
- Focus on the use of the ACEM to characterize the location of sulfur species on NO_X reduction catalyst materials, to enable characterization of the mechanisms of sulfur poisoning of these materials. This will involve not only imaging of the catalysts at the single-atom level, but also the use of the electron spectroscopy capabilities on the ACEM to obtain chemical information at the atomic level.
- Continue to work on the critical problem of determination of precise shapes of catalyst nanoparticles to determine the most important characteristics for control of catalytic performance.
- Perform precisely controlled in-situ thermal experiments using in-situ heating capabilities to understanding the interaction of Pt atoms with catalyst supports, and the development of catalyst nanoparticles and subsequent coarsening kinetics.

Technical Progress

The arrangement of heavy metal species in "as-prepared" catalysts on common supports is not well understood, notwithstanding decades of study on the preparation and properties of such catalysts. Aging or calcining treatments often cause atomic dispersions of heavy metals species to coarsen into discrete particles of size >2 nm, with crystal lattices that can be imaged using conventional high-resolution bright-field imaging techniques. High-angle annular dark-field (HA-ADF), or Z-contrast, imaging in an aberration-corrected scanning transmission electron microscope (STEM) is the best direct technique for studying monoatomic and multi-atom "rafts" of heavy metals which form prior to growth into discrete nanoparticles. In our present work, platinum on alumina catalysts were freshly prepared and oxidized, prior to characterization using HA-ADF imaging methods. Subsequent reduction treatments of the samples in HTML's ex-situ reactor at elevated temperatures allowed characterization of the same sample areas from treatment to treatment (details below). The goal of the investigation was to determine the evolution of the Pt dispersion from the oxidized condition to the activated reduced condition.

Studies of bimetallic catalysts continued, with progress on understanding the structure and chemistry of novel nanoparticles having a core surrounded by two shell of different chemistry. The Au-Pd nanoparticle experimental images were compared to computed HA-ADF images of model structures.

A new research thrust area was initiated in conjunction with a collaboration with Protochips Co. (Raleigh, NC). Protochips is developing novel heater elements utilizing semiconductor micro-fabrication techniques that have outstanding properties and behavior ideal for *in-situ* electron microscopy studies at the sub-Ångström level. Initial experiments demonstrated the efficacy of these techniques for *in-situ* imaging, with first results obtained that have never been (to our knowledge) equaled in the history of microscopy on earth.

Examples of the results obtained in these studies are given in the sections that follow.

Fundamental behavior of Pt species on alumina support material

The arrangement of heavy metal species in "as-prepared" catalysts on common supports is not well understood, notwithstanding decades of study on the preparation and properties of such catalysts. Aging or calcining treatments often cause atomic dispersions of heavy metals species to coarsen into discrete particles of size >2 nm, with crystal lattices that can be imaged using conventional high-resolution bright-field imaging techniques. High-angle annular dark-field (HA-ADF), or Z-contrast, imaging in an aberration-corrected scanning transmission electron microscope (STEM), which provides sub-Ångström resolution, is the best direct technique for studying monoatomic and multi-atom "rafts" of heavy metals which form prior to growth into discrete nanoparticles.

Platinum on alumina catalysts for the present study were prepared by impregnating the support materials with 0.35 wt.% Pt, and oxidizing the material at 525ºC. Several areas of the resulting catalyst were imaged in ORNL's aberration-corrected JEOL 2200FS FEG STEM/TEM. *Ex-situ* exposure of the catalyst to 4%H_2 in Ar for 15 minutes at 300°C was followed by re-examination in the microscope, followed by a subsequent series at 350°C for 15 minutes, and a final series at 700ºC, again for 15 minutes. The goal of the investigation was to determine the evolution of the Pt dispersion from the oxidized condition to the activated reduced condition.

Figure 1 shows a series of high-magnification images showing the gradual development of Pt clusters from the initial atomic dispersion seen in the as-oxidized sample (Fig. 1a), through the subsequent reduction treatments at 300°C and 350°C (Figs. 1b and 1c). The images are of the same catalyst area; some slight tilt and rearrangement of the alumina support occurred during reduction. They show aggregation of Pt atoms into small "rafts" of 10 atoms or so by the 350°C treatment, but still some individual atoms remaining pinned to the alumina. After a 700°C reduction (starting with a fresh specimen, Fig. 2), discrete rafts containing 20-30 atoms were seen. Adjacent rafts tended to rearrange slightly under beam exposure, but did not tend to be so highly mobile that they merged into a single larger raft. This suggests that while the electron beam has some effect on the instantaneous arrangement of atoms in a cluster, the effect is only minor relative to the larger contribution from reaction heat treatment. Further studies of this nature using our developing *in-situ* heating capability are clarifying these effects; initial results are detailed in the last section of the report.

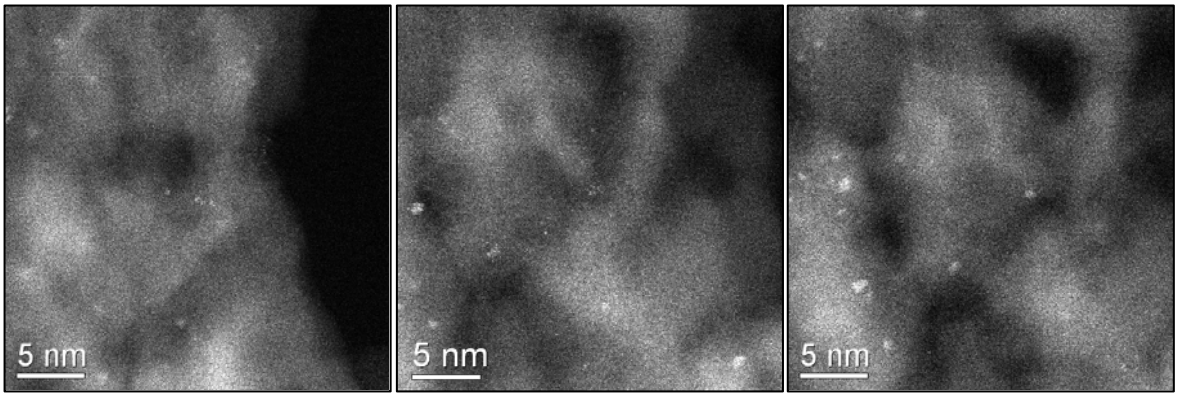

Fig. 1. a) Pt/alumina as-oxidized. Pt species dispersed almost entirely as single atoms and some dimers. b) Same area after 350°C reduction treatment for 15min. Some single atoms remain, but more small clusters of 3-4 atoms are seen. c) Same area after 350°C reduction treatment for 15min. Fewer single atoms and slight aggregation into bigger clusters.

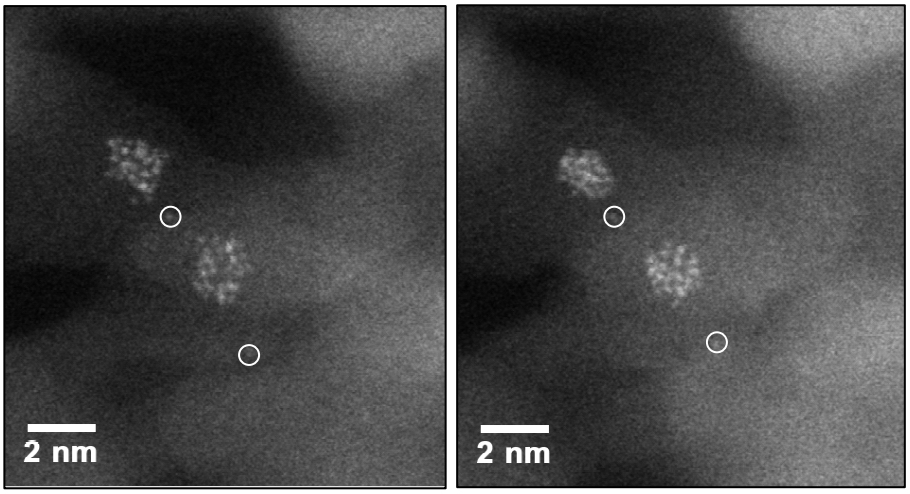

Fig. 2. Frames from a "movie" of the 700°C/15min reduction treatment (starting from a fresh as-oxidized Pt/alumina sample). Rafts of 20-30 atoms were seen, which tended to rearrange slightly under beam exposure, while single atoms (circled) are pinned to the alumina.

Structure of bi-metallic nanoparticles: Au-Pd system

Bimetallic clusters and nanoparticles attract great interest due to their unique catalytic, electronic, and optical properties that differ from those of the corresponding monometallic components.[1-5] For instance, it is well known that adding a second metallic component enhances the activity, selectivity and stability of a pure metal catalyst. The properties of bimetallic nanoparticles can vary dramatically not only with size, as happens in pure nanoclusters, but also with chemical composition. Controlling their structure and chemical ordering can be the starting point to prepare the building blocks for specifically tailored cluster-assembled materials. It has been reported in many cases that bimetallic systems display a core/shell structure, where a thin shell of metal B surrounds a core of metal A. The B overlayer is usually strained, and thus can present prominent catalytic properties. The chemical and physical properties of bimetallic nanoparticles exhibiting core/shell structure strongly depend on whether the two monometallic elements are chemically segregated or intimately alloyed. These materials can be grown by different microscopic mechanisms, either involving shell-by-shell growth on pre-existing smaller clusters, or by a structural transformation of the clusters.6-8 Our approach consists of synthesizing polymer-protected Au-Pd nanoparticles by means of the polyol method.[9] A core/shell structure was obtained in the colloids by the successive reduction of their corresponding metallic salts. Figure 1 shows the as-synthesized particles in HA-ADF imaging; each particle shows a dark core with a brighter inner shell, and a dark outer shell. The contrast is consistent with a Pd-rich core, a gold-rich inner shell, and a Pd-rich outer

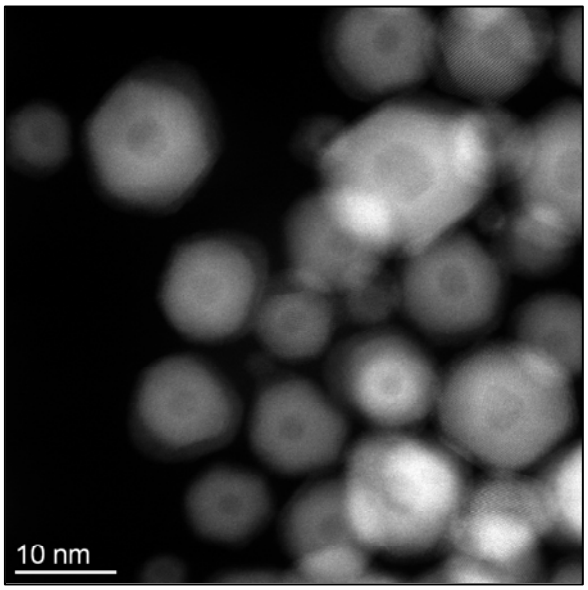

Fig. 3. As-synthesized Au-Pd particles showing core/inner/outer shell structure.

shell, since dark-field images show contrast related to the atomic number of the imaged area. The question of whether or not the particle core was in fact a void was answered by using electron holography techniques; analysis of 10 different particles conclusively showed the core to be filled. Energy dispersive analysis also was consistent with a Pd-rich core and Pd-rich outer shell.

A higher magnification image of a single particle clearly shows the regions described above. The orientation is consistent with a <110> zone axis (looking down a cube-face diagonal of the face-centered cubic structure, per inset diffractogram of the image) parallel to the electron beam. Since Pd and Au are both FCC structures with similar lattice constants, the observation that no defects (stacking faults or dislocations) were seen in any particles indicates a complete coherence between the different regions.

A major thrust of our studies of nanoparticles such as these in the Au-Pd system is ultimately to be able to model the structures, and compute the subsequent annular dark-field STEM images. Initial results have been obtained for the Au-Pd core-shell particles shown here. Three different orientations (<100>, <110> and <111>) have been modeled (a

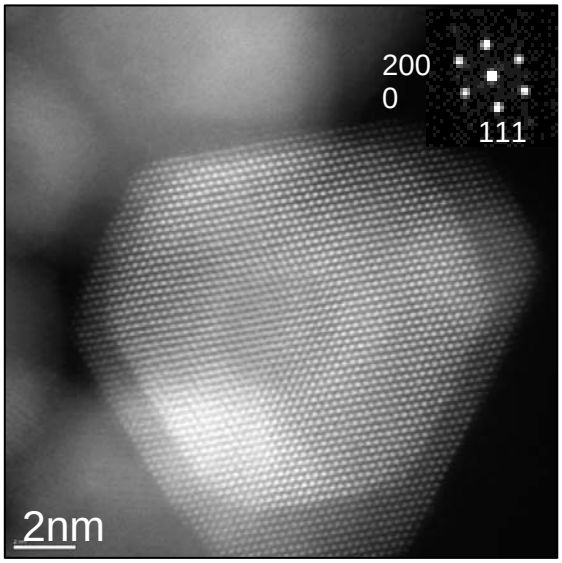

Fig. 4. Higher magnification image of a single Au-Pd nanoparticle, showing the Pd-rich core, Au-rich inner shell, and Pd-rich outer shell (see text for details).

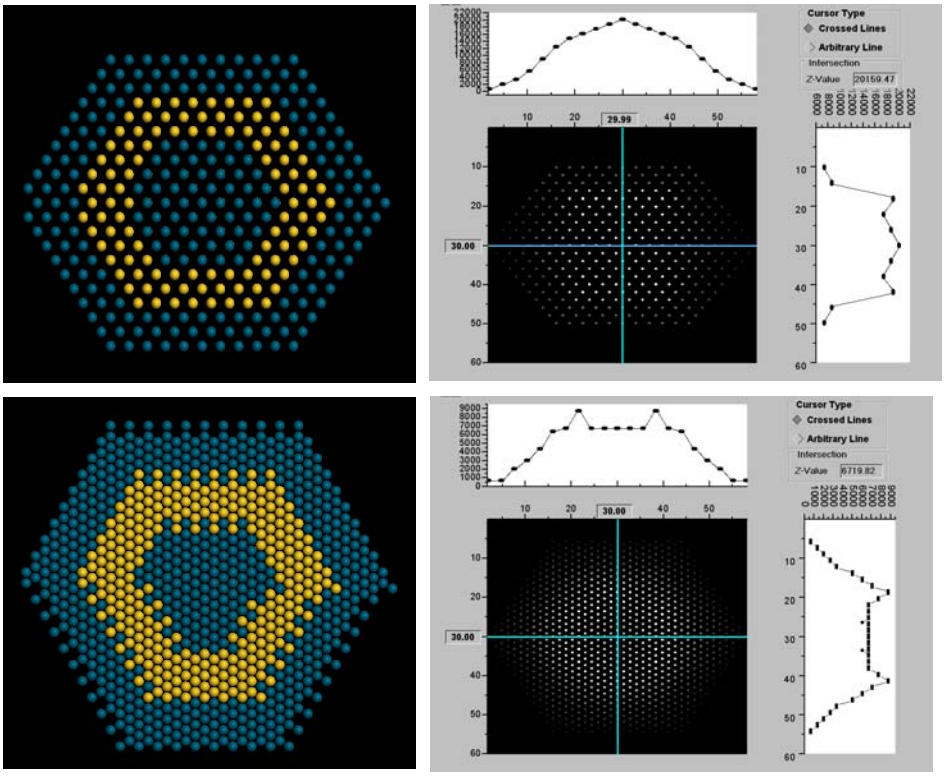

Fig. 5. Two orientations of Au-Pd model structures, with corresponding computed HA-ADF images. The <111) orientation shows a close correlation to the experimental images, while the <110> orientation shows an anomalous peak in intensity at the particle center. Further studies are underway to better understand model-simulated imaged correlations.

paper with all the details has been submitted for publication[7]); the <110> result is shown in Fig. 5.

First Results of New Thrust into In-Situ Heating and Gas Reaction Studies

We have begun developing a new capability to study catalyst reactions via in-situ techniques, i.e. to be able to heat and react samples inside the ACEM during imaging experiments, while retaining the capability to record images at the highest resolution levels. This effort is being done in collaboration with the company Protochips (Raleigh, NC), which provides heater elements of novel design, fabricated using semiconductor manufacturing techniques. The initial phase of the work involves testing of the heating capability alone, requiring a new specimen rod that is designed to provide electric leads in to the heating elements. There are many experiments that we are interested to conduct in which heating in vacuum (with no gas reactions) will give significant useful information. The second phase of the work will involve the development of gas reaction "cells," which will be able to be installed in a second new specimen holder that will provide gas inlet and outlet feeds. The geometry of the new technique and first imaging experiments are described below.

Figure 6 shows a scanning electron micrograph illustrating the general design of the Protochips heater element. The "chip" has a 3mm diameter silicon base, with a 500 micron square area etched out to expose a very thin (~20-30nm) ceramic film (here presumed to be Si nitride). The film is patterned with an array of 3-micron holes, and Au electrodes also laid down as indicated. This structure acts as the support for catalyst powder specimens, after a holey carbon support film is picked up over the surface of the sample. Figure 7 shows a catalyst powder aggregate suspended on the holey carbon film (which is not seen in this dark-field image). When a voltage is applied to the Au electrodes, only the ceramic film heats up. Since the mass is so infinitesimally small, heating is almost instantaneous; tests have shown that, remarkably, the ceramic film can be heated from room temperature to 1100°C in a single millisecond (and cooled nearly as quickly back to RT)!

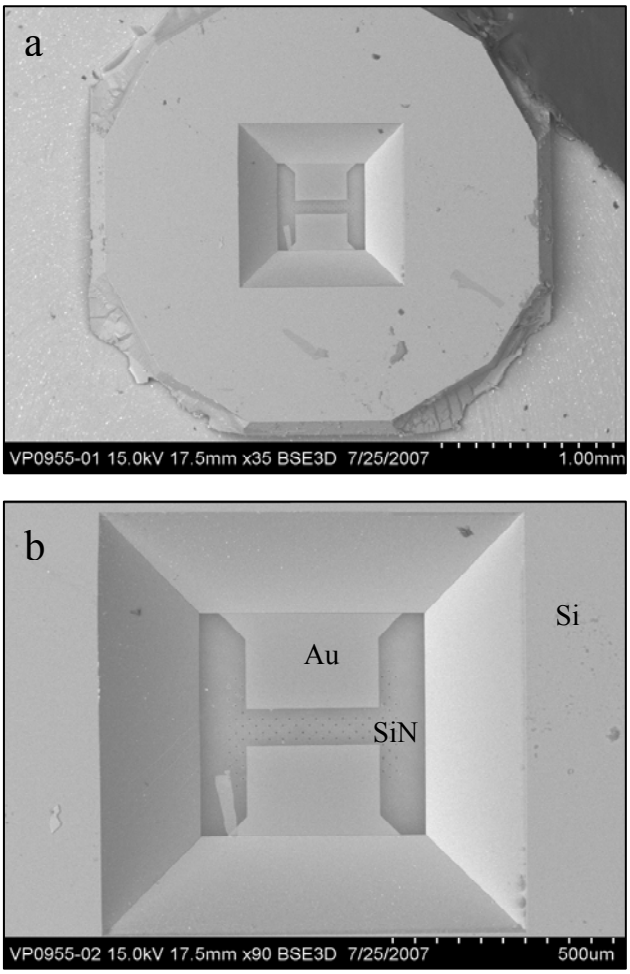

Fig. 6. a) Scanning micrograph of the back side of the Protochips heater element. b) Ceramic film (SiN) and Au electrodes shown at higher magnification.

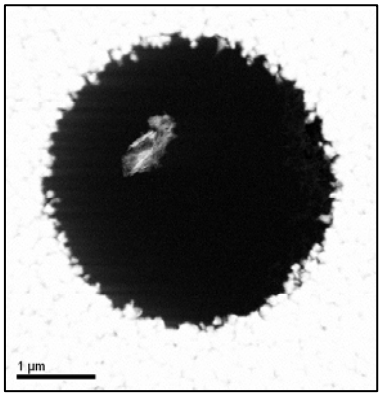

Fig. 7. View of single hole in ceramic heater element, showing catalyst powder aggregate supported by holey carbon film.

The first tests of the Protochips heater elements have been conducted, with initial outstanding results. The heater chip is retained in a specially fabricated ACEM specimen rod, which provides two leads to be connected to the respective Au electrodes of the chip. Figure 8a shows the tip of the new heater rod, with a chip in place. (The rod was designed and fabricated by our consultant, Prof. Emeritus Wilbur Bigelow of the University of Michigan.) Because of the symmetrical design of the chip, we have observed essentially zero specimen drift at high temperatures, even at the highest magnifications needed for ultimate image resolution (typically 10Mx). The only apparent effect of the heating of the ceramic film is a change in focus, since the film expands on heating and thus changes in position vertically (Z-direction) in the lens of the microscope. A change in temperature of 1000°C causes about 5 microns change in focus, but only a few nanometers shift in X-Y position; this focus change is easily tracked manually within a few seconds, since temperature stability is apparently achieved within a second or so.

An example of the kind of result we can get with this new in-situ holder is shown in Figs. 8b and 8c. A sample of Pt on alumina catalyst from a project with our colleague Dr. Charles Peden of PNNL was collected on a heater chip, and gradually heated from RT to 1000°C, with images made at the various temperature steps. A series of 20 images of a 4nm particle was made when the temperature reached 1000°C; Fig. 9 shows two "frames" from the movie. The particle, aggregated from Pt clusters and rafts into a discrete crystal, shows an ordered structure in these images (originally recorded at 10Mx direct magnification). We suspect that it is a Pt oxide composition, but have not positively identified the most likely compound that would be consistent with the dark-field image computation and image diffractogram results. We have found no other examples of images with the resolution and image information that compares to these images; *it is likely that these are the best such images taken in all of the history of electron microscopy.*

Fig. 8. New ACEM specimen heater rod, fabricated to accommodate Protochips heater chip, as indicated.

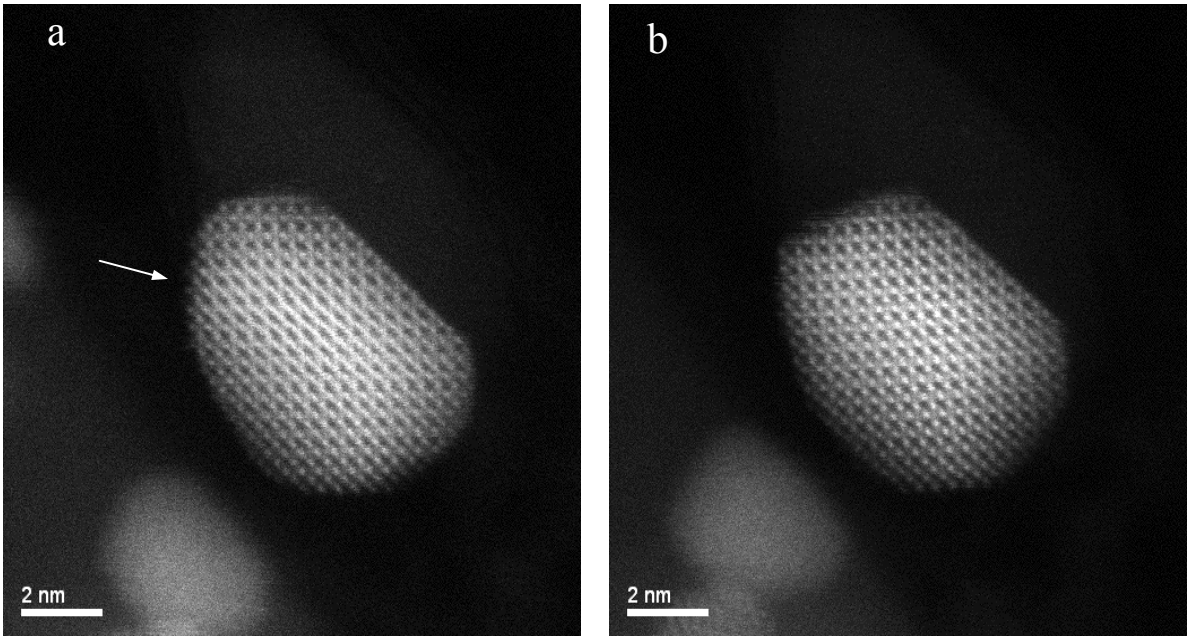

Fig. 9. HA-ADF images of Pt on alumina, at a nominal 1000°C, taken at an original magnification of 10Mx. These images show two "frames" from a 20-image "movie" that followed the changes in particle morphology with time. The particle structure is clearly ordered, indicating a compound has formed, likely a Pt-oxide composition, under these treatment conditions. Note changes in facets, and the details of exposed atomic columns on the surface, such as at the arrows in a).

Concluding Remarks

Our research activities on the forefront studies of the behavior of catalyst clusters and nanoparticles with reaction treatments, imaged at ultra-high resolution with the aberration-corrected electron microscope, are building a foundation towards a better understanding of the phenomena, which control performance in real systems. The initiation of a new thrust into in-situ studies with a remarkable specimen heating capability offers real promise for breakthrough results as we carry our research studies forwards.

References

1. N. Toshima and T. Yonezawa, "Bimetallic nanoparticles—novel materials for chemical and physical applications," *New J. Chem*. 1179, 1998.

2. T. Fujikawa, K. Idei, T. Ebihara, H. Mizuguchi and K. Usui, "Aromatic hydrogenation of distillates over SiO_2-Al_2O_3-supported noble metal catalysts," *Appl. Catal. A* **192**, 253-261, 2000.

3. M. Jacquin, et al., "Cetane improvement of diesel with a novel bimetallic catalyst" *J. Catal.* **228**, 447, 2004.

4. B. Pawelec, R. Mariscal, R. M. Navarro, S. van Bokhorst, S. Rojas and J. L. G. Fierro, "Hydrogenation of aromatics over supported Pt-Pd catalysts," *Appl. Catal. A* **225**(1-2), 223-227, 2002.

5. S.-C. Kim, H.-H. Park and D.-K. Lee, "Pd–Pt/Al_2O_3 bimetallic catalysts for the advanced oxidation of reactive dye solutions," *Catal. Today* **87**, 51, 2003.

6. S. Mejia-Rosales, J C. Fernandez-Navarro, E. Perez-Tijerina, D. A. Blom, L. F. Allard and M. Jose-Yacaman, "On the Structure of Au/Pd Bimetallic Nanoparticles," *J. Phys. Chem. C,* **111**(3), 2007.

7. Nitani, H., et al., "Sonochemically synthesized core-shell-structured Au - Pd nanoparticles supported on γ-Fe_2O particles," *J. Nanopart. Res.* **8**(6), 951-958, 2006.

8. Steinbrueck, A., Csaki, A., Festag, G. & Fritzsche, W., "Preparation and optical characterization of core-shell bimetallic nanoparticles," *Plasmonics* **1**(1), 79-85, 2006.

9. Domingo I. Garcia-Gutierrez, Claudia E. Gutierrez-Wing, Lisandro Giovanetti, Jose M. Ramallo-Lopez, Feliz G. Requejo, and Miguel Jose-Yacaman. *J. Phys. Chem. B*, **109**(9), 3813-3821, 2005.

10. Pérez-Tijerina, E., et al., "Highly size-controlled synthesis of Au/Pd nanoparticles by inert-gas condensation," *Faraday Discuss.* **138**/20, 2007.

11. Kickelbick, G. & Liz-Marzan, L. M., "Core-shell nanoparticles," *Encyclopedia of Nanoscience and Nanotechnology* **2**, 199-220, 2004.

Publications and Presentations

1. "Observation of Pt Atoms, Clusters and Rafts on Oxide Supports, by Sub-Ångström Z-Contrast Imaging in an Aberration-Corrected STEM/TEM," D. A. Blom, S. A. Bradley, W. Sinkler and **L. F. Allard**, *Microscopy and Microanalysis (Supp 2)* Cambridge University Press, 50, 2006.

2. "Early Results from an Aberration-Corrected JEOL 2200FS STEM/TEM at Oak Ridge National Laboratory," D. A. Blom, **L. F. Allard**, S. Mishina, and M.A. O'Keefe, *Microscopy and Microanalysis* **12**, 483-491 (Dec 2006).

3. **Invited Talk** "Looking at Atoms with the Aberration-Corrected Electron Microscope: The World Through "Rose-Colored" Lenses," **L. F. Allard**, Keynote Address at the University of Texas, Austin Department of Chemical Engineering *Workshop on Aberration-Corrected Electron Microscopy*, March 2007.

4. "Studies of Pt Cluster Evolution During Reduction;" D. A. Blom, S. A. Bradley, W. Sinkler and **L. F. Allard**, Microscopy Society of America, August 2007.

5. "Cluster Evolution during Reduction of Pt/Alumina Catalysts," D. A. Blom, S. A. Bradley, W. Sinkler and **L. F. Allard**, Poster presentation, Frontiers of Electron Microscopy in Materials Science, Sonoma, CA, September 2007.

6. "Atomic Structure of Three-Layer Au/Pd Nanoparticles Revealed by Aberration-Corrected Scanning Transmission Electron Microscopy," D. Ferrer, D. A. Blom, **L. F. Allard**, S. Mejia, E. Perez-Tijerina and M. Jose-Yacaman, submitted to *ACS Nano*, September 2007.

7. "On the Structure of Au/Pd Bimetallic Nanoparticles," S. J. Mejia-Rosales, C. Fernandez-Navarro, E. Perez-Tijerina, D. A. Blom, **L. F. Allard** and M. Jose-Yacaman: *J. Phys. Chem. C* **111**(3), 2007.

8. "High-Resolution Electron Microscopy of Bimetallic Nanoparticles," D. Ferrer, A. Torres-Castro, D. A. Blom, **L. F. Allard** and M. Jose-Yacaman, *Microscopy and Microanalysis* **13**(Suppl 2), 84-85, 2007

Agreement 9110 - Life Prediction of Diesel Engine Components

H. T. Lin, T. P. Kirkland, A. A. Wereszczak, and H. Wang
Oak Ridge National Laboratory
P.O. Box 2008, MS-6068
Oak Ridge, TN 37831-6068
(865) 576-8857; fax: (865) 475-6098; e-mail: linh@ornl.gov

Nate Phillips and Jeff Jenson
Caterpillar, Inc.
Peoria, IL 61656-1875
(309) 578-2969; fax: (309) 578-2953; e-mail: Jensen_Jeff_A@cat.com

DOE Technology Manager: Jerry L. Gibbs
(202) 586-1182; fax: (202) 586-1600; e-mail: jerry.gibbs@ee.doe.gov
ORNL Technical Advisor: D. Ray Johnson
(865) 576-6832; fax: (865) 574-6098; e-mail: johnsondr@ornl.gov

---

Contractor: Oak Ridge National Laboratory, Oak Ridge, Tennessee
Contract No.: DE-AC05-00OR22725
Subcontractor: Caterpillar, Inc., Peoria, Illinois

Objective

- Generate a database and characterize damage mechanisms of candidate advanced ceramics and intermetallic alloys.
- Apply and verify probabilistic life prediction and component design and verification methods for advanced diesel engine components.

Approach

- Evaluate the dynamic fatigue, rotary bending fatigue, and high-temperature fatigue and creep performance of candidate silicon nitride ceramics and TiAl alloys at elevated temperatures in air before and after long-term exposure to simulated engine environments, as well as engine field tests.
- Characterize the evolution and role of damage mechanisms, and changes in microstructure and chemistry, linked to the long-term mechanical performance and reliability of ceramics and intermetallic alloys.
- Predict the failure probability and reliability of complex-shaped diesel engine components subjected to application conditions via the use of life prediction codes.

Accomplishments

- Completed characterization of surface profiles, microstructure analysis, and retained mechanical properties evaluation of selected 500-h engine tested TiAl and silicon nitride valves. The results generated were provided to end user for verification of probabilistic component design and life prediction.
- Completed dynamic scratch studies for both Daido and Howmet TiAl alloys after surface modification treatment. The test results showed that the surface modification process employed significantly improved the surface wear resistance, which could have substantial impact on the long-teem durability of TiAl valve components.

- Completed generation of long-term tensile creep database for Daido and Howmet TiAl alloys at different applied stress levels and temperature conditions. The database was provided to end users for probabilistic component design and life prediction of turbo wheel.

Future Direction

- Characterize the mechanical properties and microstructure of candidate material such as TiAl alloys and silicon nitride under the operating conditions relevant low temperature combustion engines.
- Develop mechanical database for complex-shaped TiAl components for verification of probabilistic component design and life prediction, and also process optimization.

Introduction

There has been considerable interest in the potential for extensive use of advanced ceramics and intermetallic alloys in advanced diesel engine systems because of their superior thermomechanical properties at elevated temperatures. The implementation of components fabricated from these advanced materials would lead to significant improvement in engine efficiency and long-term durability and reduced nitrogen oxides (NO_x) and CO exhaust emissions as required in the 21st Century Truck Program. Interest has focused primarily on research into characterization and design methodology development (life prediction) for advanced silicon nitride ceramics and TiAl alloys to enable the manufacture of consistent, reliable complex-shaped components for diesel engine. The valid prediction of mechanical reliability and service life is a prerequisite for successful use of these materials in internal combustion engine components.

This research project has three primary goals: the generation of a mechanical engineering database, from ambient to high temperatures, of candidate advanced materials before and after exposure to simulated engine environments; the microstructural characterization of failure phenomena in these advanced materials and in components fabricated from them; and the application and verification of probabilistic life prediction methods using diesel engine components as test cases. For all three stages, results will be provided to both material suppliers and component end-users for use in refining and optimizing processing parameters to achieve consistent mechanical reliability, and in validating the probabilistic design and life prediction of engine components made from these advanced materials.

Approach

The retained mechanical strength of both silicon nitride and TiAl alloy valve stems after 500-h testing in natural gas engine was measured using a four-point bending fixture with 30/60 mm spans (Fig. 1a). Each valve stems were machined into four half cylindrical type stems for post strength evaluation. In addition, the valve-heads of silicon nitride and TiAl alloy were also evaluated using a customer design fixture (Fig. 1b) under a compressive load via a bench type universal testing machine. These mechanical tests would allow one to evaluate the effect of engine environment on the microstructure and chemical stability and thus mechanical performance of materials. The mechanical data generated would then be provided to the end users to verify their probabilistic component design and life prediction results of valve components. Both fractography and scanning electron microscopy analysis were also carried out to characterize the surface morphology and microstructure of fracture surfaces for selected valve stems and valve heads after mechanical test.

Studies of long-term creep behavior in air of TiAl alloys manufactured by Daido and Howmet were continued to be carried out in FY2007. Two types of TiAl creep specimens different in final densification process (i.e., one is HIP and the other one is Non-HIP) manufactured by Daido, Tokyo, Japan and designated as RNT650 were received from end user. Also, TiAl tensile specimens manufactured by Howmet, Michigan, USA and designated as 45XD were also received for evaluation. The creep specimens are cylindrical buttonhead type as shown in Fig. 2. The test conditions specified (temperatures: 600-750°C, stress levels: 120-390 MPa) are importantly relevant to the temperature and tensile stress profiles

encountered by TiAl turbo wheel under the application conditions based on the FEA modeling. The database generated will then be used by the end users to verify probabilistic life prediction of turbo wheel under engine operation conditions, and could also provide important feedbacks to material suppliers for process modification to further improve its high-temperature mechanical performances.

Results

Characterization of engine-tested Si_3N_4 and TiAl valves

The 500-h engine field tests using Caterpillar G3406, which is an in-line 6 cylinders natural gas (NG) engine, were successfully carried out to validate the valve component design and life prediction tasks carried out for advanced lightweight silicon nitride and TiAl valves. In this 500-h engine test those metallic valves currently employed in the engine were also included for benchmark reference. Following the successful engine tests the surface morphology and roughness both silicon nitride and TiAl valves were characterized in details and also the detailed NDE analysis was also carried to identify the surface flaws/damages that might be introduced during engine testing. These results were summarized in FY2006 annual report [1].

The effect of the surface roughness and/or flaws introduced after 500-h engine test on the mechanical performance of both silicon nitride and TiAl valves was evaluated in FY2007. Figure 3a shows the flexural strength results of the SN235P silicon nitride, half-cylindrical stems after 500h engine test. The results generated for the as-received silicon nitride valve stems were also included for comparison. Note that the SN235P silicon nitride valves blanks were manufactured by Kyocera, Japan. Results show that the engine tested silicon nitride valve stems exhibit strength values that are about 10% higher than those in as-received condition. Previous studies reported that the SN235P silicon nitride bend bars showed no apparent mechanical strength degradation measured after 1000h oil immersion test at 850°C [2]. Furthermore, the detailed SEM analysis showed that the SN235P silicon nitride exhibited superior oxidation/corrosion resistance to those currently used steel alloys under a simulated engine diesel engine environment (i.e., long-term oil immersion test. Similarly, the tested TiAl valves exhibited ~10-15% higher strength than the as-received ones (Fig. 3b).

Subsequently, the detailed SEM analysis was carried out to provide insight into the effect of engine operating environment on the surface roughness and thus retained mechanical strength of tested valves. Figure 4 compares the SEM stem surface features between as-received and 500h-tested valve stem. Many of the original machined groves disappeared due to the repeatedly reciprocating frictional movement between the valve guide and stem (Fig. 4b), resulting in a much smoother surface, consistent with the measured higher retained fracture strength reported above (Fig. 3). In regions that were in close contact with valve guide the surfaces exhibited smooth features similar to the etched surfaces (Fig.4c). In addition, Fig. 5 shows the SEM fracture surface of as-received and 500h-tested valve stems. In general, all of the as-received specimens failed from the original machined flaw, critical grove ~ 150-200 μm in length (Fig.5a). As for the 500h-tested specimens there are also many failing from the remnant machining flaws (Fig. 5b), while few failed from the processing flaw, i.e., pores (Fig. 5c).

On the other hand, Figure 6a and 6b compares the valve head strength of SN235P silicon nitride and TiAl before and after 500-h engine test, respectively. In general, the mechanical results showed that the two tested intake valves exhibited about 10% lower fracture strength, while the two tested exhausted valves exhibited ~10-12% higher fracture strength than the as-received ones (Fig. 6a). Similar trend was also observed for the TiAl valve head strength measurement (Fig. 6b). Since there were limited valves tested thus the observed increased or decreased in strength (10% deviation) is within the statistic error of the materials, and thus it could be concluded that there was no influence of engine condition on the valve head mechanical strength. The fractography analysis of the valve heads again showed that the strength-limiting flaw was due to the presence of the originally machined flaws (Fig. 7).

High temperature creep behavior of TiAl alloys

Studies of long-term creep behavior in air of TiAl alloys manufactured by Daido and Howmet were carried out in FY2007. Tensile creep results of Daido TiAl alloy showed that there was a minor

effect of processing method (HIP vs. non-HIP) on the high temperature creep behavior at 650°C (Fig. 8a). However, at temperatures ≥ 700°C the non-HIP TiAl specimens exhibited 10-times lower creep than that obtained for HIP TiAl specimen (Fig. 8a). In addition, the creep rates of non-HIP TiAl are less temperature dependent, while the creep rate of HIP TiAl increases with increasing temperature under the present test conditions employed. On the other hand, the creep exponents (n) obtained from the slope of creep rate vs. applied stress curves showed the n valve obtained for Daido TiAl alloys at 650°C is ~ 2.4 and it then transitioned to a much higher n valve of 13.4 at 750°C for HIP TiAl, indicating a change in creep controlling mechanism. However, the n value for the non-HIP TiAl exhibited low values even at higher test temperatures. Note that the high creep exponent value of n is in general attributed to enhanced creep cavitation process.

The limited creep data indicated that the Daido HIP TiAl tended to exhibit 10 times lower creep rates as compared with those obtained for Howmet TiAl under similar test conditions, especially under a high applied stress valve (Fig. 8b). However, at lower stress regime the difference in creep response between these two alloys became less apparent. The slope of lifetime versus creep rate for all of the TiAl specimens tested showed an m value of ~1.3-1.9 under the test conditions employed in the present study. Note the m would be ~ 1 based on the Monkman-Grant creep law. Note that similar higher m valves have been reported for siliconized SiC ceramics after tensile creep test [3]. Nonetheless, more creep tests under various test temperatures and applied stress levels would be carried out to understand the effect of microstructure on the creep response and also the creep controlling mechanism as a function of temperature and stress level.

References

1. H. T Lin et al, "Life Prediction of Diesel Engine Components," 2006 Annual Report for Heavy Vehicle Propulsion Materials.

2. H. T. Lin, T. P. Kirkland, A. A. Wereszczak, and M. J. Andrews, "Strength Retention of Silicon Nitride After Long-term Oil Immersion Exposure," *J. Mater. Sci.* 41, 8313-8319 (2006).

3. S. M. Wiederhorn, B. J. Hockey, and T. J. Chuang, "Creep and Creep Rupture of Structural Ceramics," pp. 555-575 in Toughening Mechanisms in Quasi-Brittle Materials, Kluwer Academic Publishers, Norwell, MA 1991.

Presentations and Publications

Presentation

1. H.-T. Lin, T. Kirkland, A. A. Wereszczak, M. D. Kass, N. Domingo, T. J. Theiss, N. Phillips and J. A. Jensen Design and Implementation of Silicon Nitride Valves for Heavy Duty Diesel Engines", was presented at the 2007 DEER Conference, August 12-16, Detroit, MI..

Publications

1. H. Wang, H. T. Lin, A. A. Wereszczak, J. A. Jensen, and N. Yang, "Specific Energy and Scratch Hardness of Gamma Titanium Aluminides Subjected to Single-Grit Pendulum Scratching," ICEF2006-1532, in the Proceedings of ASME Internal Combustion Engine Division 2006 Fall Technical Conference, November 5-8, Sacramento, CA.

2. H. T. Lin, T. P. Kirkland, A. A. Wereszczak, and M. J. Andrews, "Strength Retention of Silicon Nitride After Long-term Oil Immersion Exposure," *J. Mater. Sci.* 41, 8313-8319 (2006).

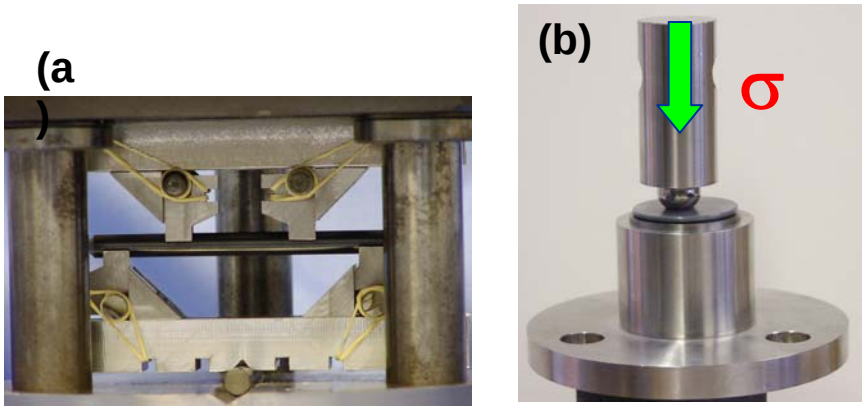

Figure 1. *Photo of four-point bending fixture used for testing the half-cylindrical valve stems (a) and custom-designed fixture for the valve head testing.*

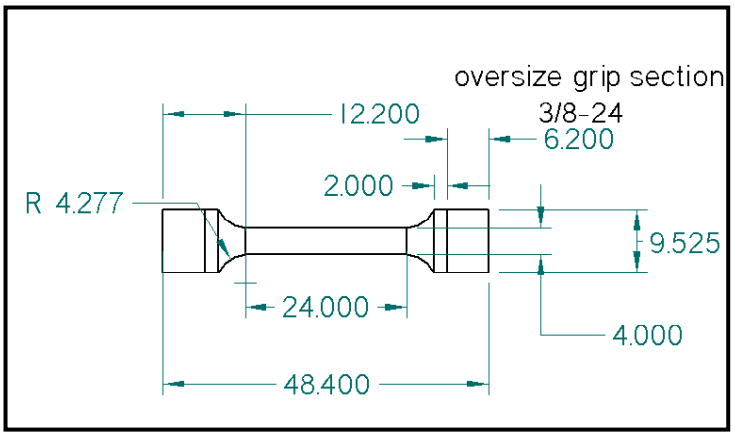

Figure 2. *Schematic of cylindrical buttonhead tensile creep specimen of TiAl alloys.*

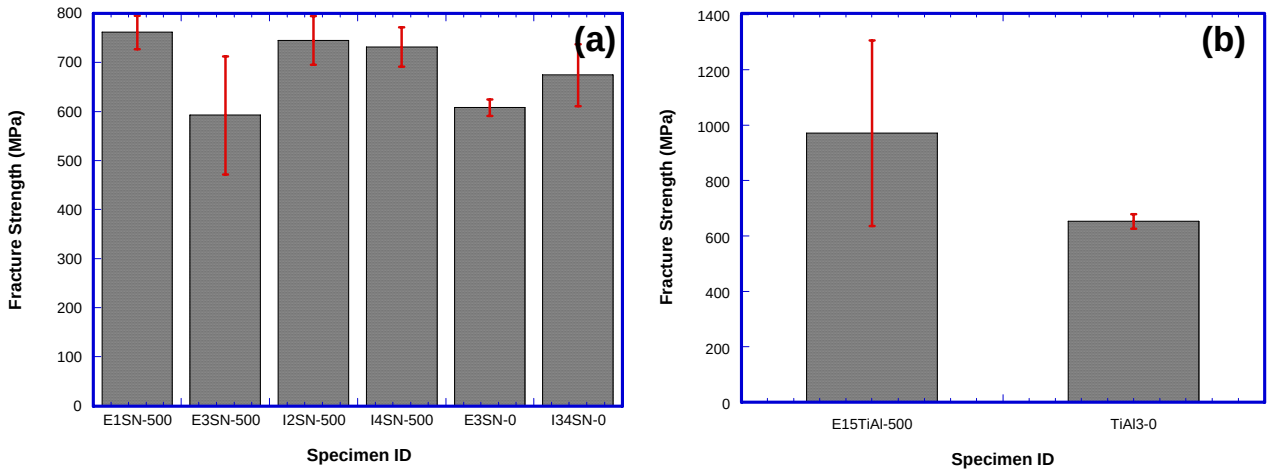

Figure 3. *Fracture strength of half-cylindrical valves before and after engine test of (a) SN235P silicon nitride and (b) TiAl alloys.*

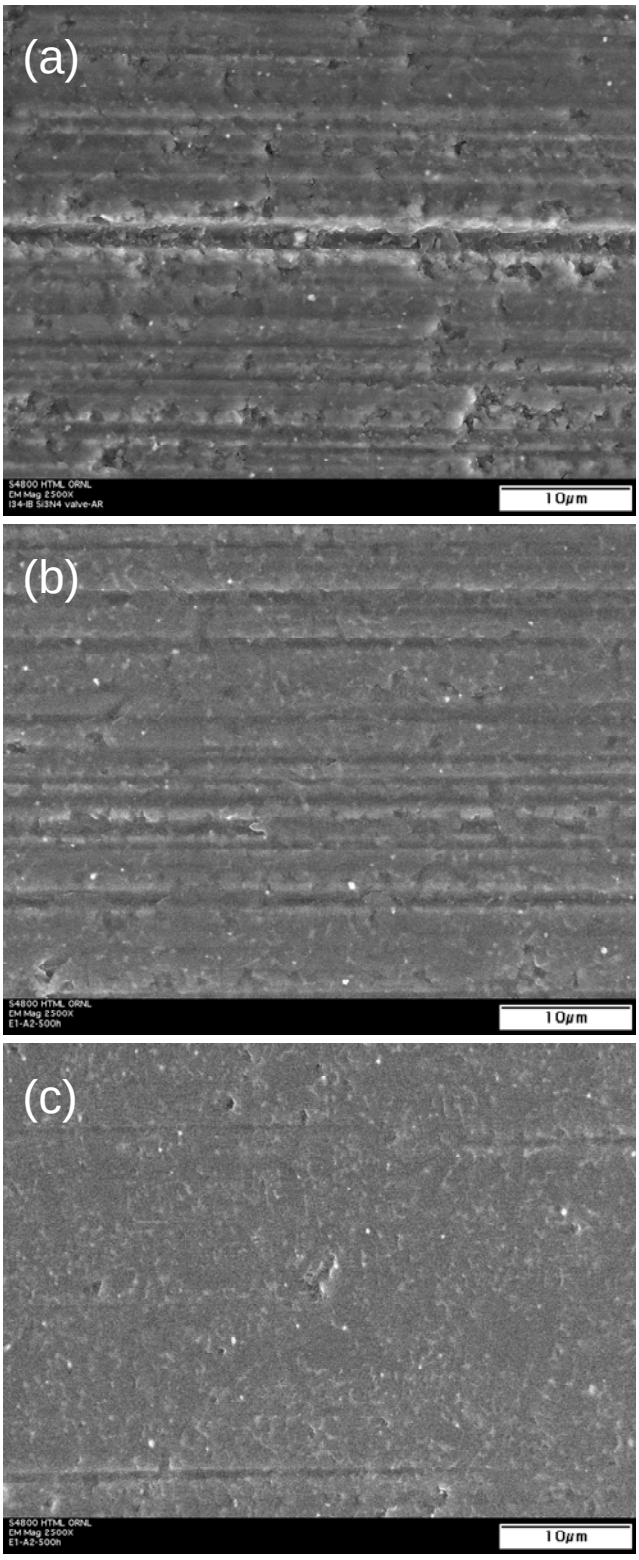

Figure 4. *Scanning electron microscopy surface features of silicon nitride valve stem region before (a) and after engine test (b and c).*

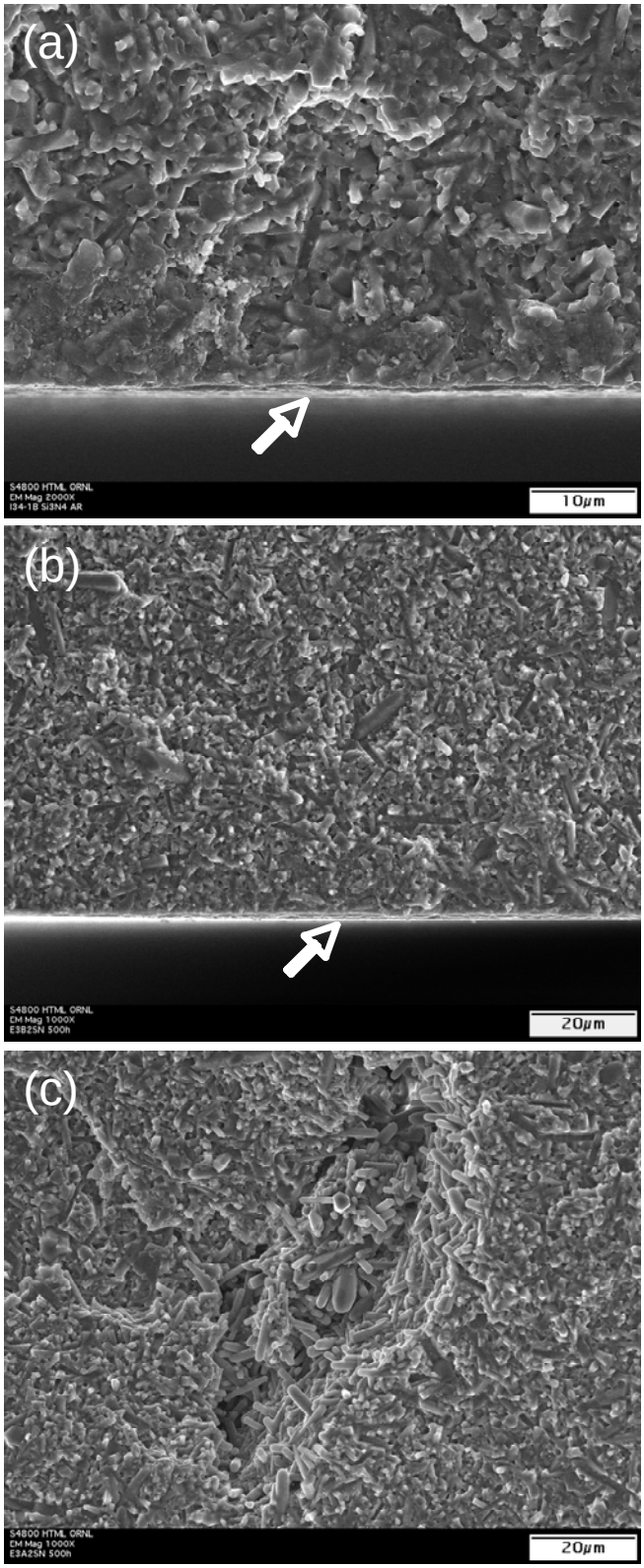

Figure 5. *Scanning electron microscopy fracture surface features of silicon nitride valve stem before (a) and after engine test (b and c).*

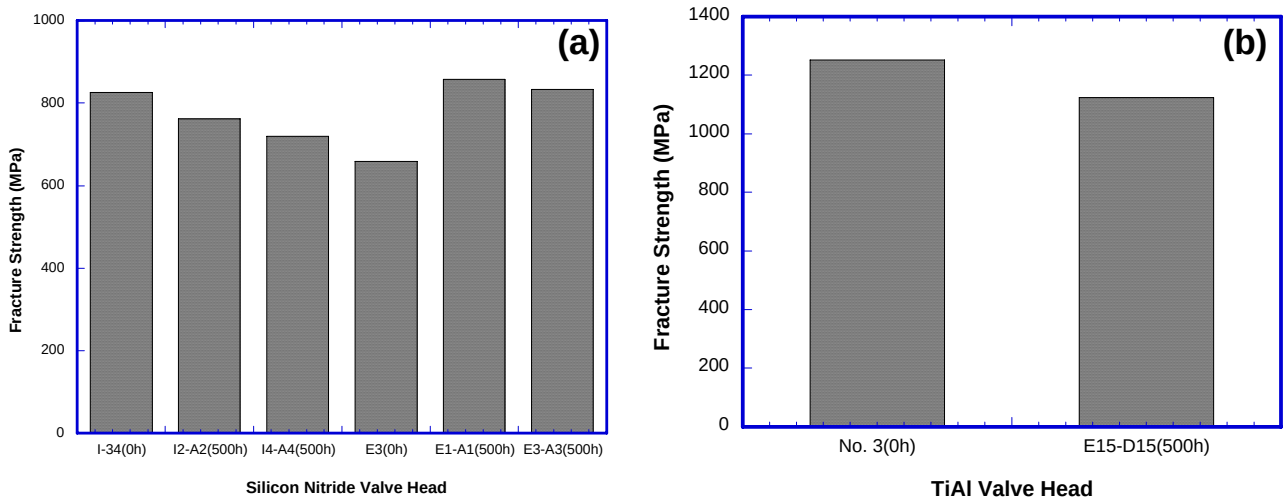

Figure 6. *Comparison of fracture strength of valve head before and after engine test. (a) SN235P silicon nitride valves and (b) TiAl valves.*

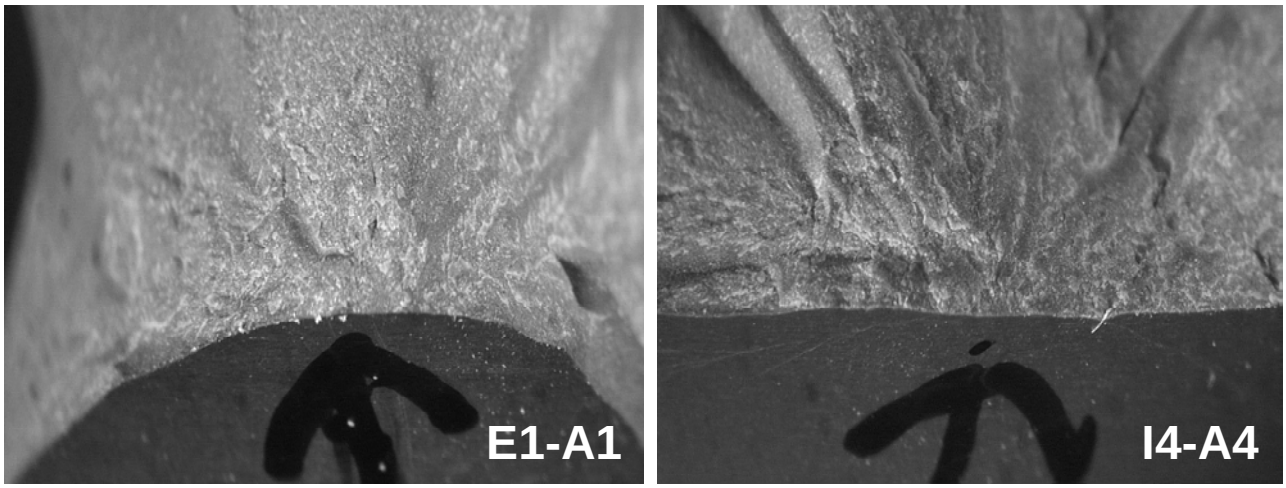

Figure 7. *Fractography photo of tested SN235P exhaust (a) and intake (b) valve head.*

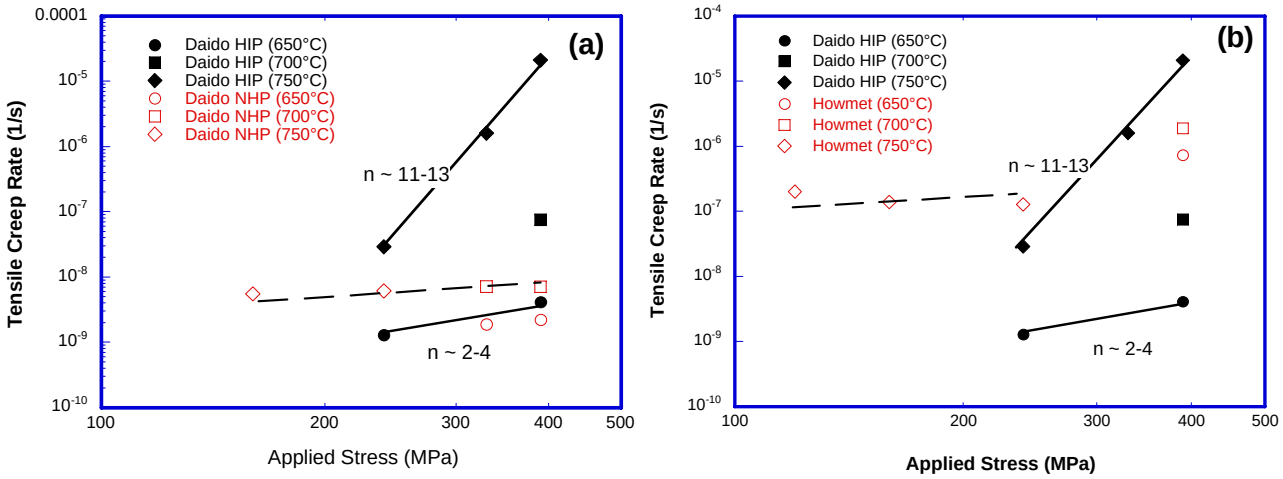

Figure 8. *Tensile creep rates versus applied stress curves of Diado TiAl alloy (a) and Howmet TiAl alloy (b).*

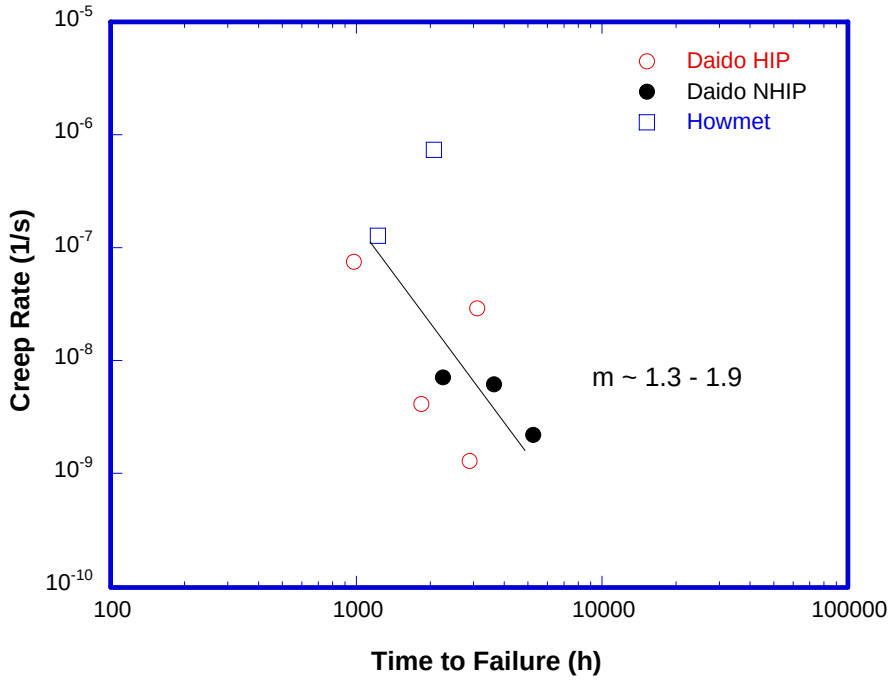

Figure 9. *Monkman-Grant creep rate versus lifetime curve of all of the TiAl alloys evaluated.*

Agreement 14957 - Modeling of Thermoelectrics

A. A. Wereszczak and O. M. Jadaan
Ceramic Science and Technology Group
Oak Ridge National Laboratory
P.O. Box 2008, MS 6068, Bldg. 4515
Oak Ridge, TN 37831-6068
(865) 576-1169; fax: (865) 574-6098; e-mail: wereszczakaa@ornl.gov

DOE Technology Manager: Jerry L. Gibbs
(202) 586-1182; fax: (202) 586-1600; e-mail: Jerry.gibbs@ee.doe.gov
ORNL Technical Advisor: D. Ray Johnson
(865) 576-6832; fax: (865) 574-6098; e-mail: johnsondr@ornl.gov

Contractor: Oak Ridge National Laboratory, Oak Ridge, Tennessee
Prime Contract No.: DE-AC05-00OR22725

Objectives

- Interpret thermomechanical stress development in thermoelectric materials (TE) in a TE device, and use to guide development of future mechanical test matrices of TE materials.
- Examine which material properties or dimensions have the largest effect on reliability.

Approach

- Execute finite element analysis (FEA) to model thermomechanical stresses in TE materials and TE devices.
- Execute probability design sensitivity (PDS) analysis on the TE material within an arbitrary TE device, and identify and rank those material properties or dimensions that have the largest effect on reliability.

Accomplishments

- Developed a FEA model for a TE device to enable the interpretation of stress development in it.
- Identified parameters that have the greatest effect on reliability in a TE device.

Future Direction

- Generate statistically significant thermomechanical property data on existing commercially available TE materials as well as higher-temperature-capable TE materials under development.
- Refine FEA and PDS analysis models and examine other TE device architectures.

Introduction

Potential next generation thermoelectric (TE) devices comprised of p- and n-type materials enjoy strong interest for implementation in high temperature and oxidizing environments because their waste heat could be used to generate electricity. However, the intended TE function of these devices will only be enabled if the device is designed to overcome the thermomechanical limitations (i.e., brittleness) that are usually inherent to these materials. A TE material with a combination of poor strength and low thermal conductivity can readily fail in the presence of a thermal gradient thereby preventing the exploitation of the desired thermoelectrical function.

This seemingly insurmountable problem can be overcome with the combined use of established probabilistic design methods developed for brittle

structural components, good thermoelastic and thermomechanical databases of the candidate material comprising the TE device, and iteratively applied design sensitivity analysis. This project executes this process to involve TE devices.

There will be several outcomes from this work that will benefit TE material and device developers and end-users of these potentially high temperature TE devices: mechanical reliability of prototypical TE devices will be evaluated from a structural brittle-material perspective and suggested redesigns will be identified, thermomechanical reliability of developmental TE materials will be assessed, and minimum required thermomechanical properties of hypothetical TE materials would be identified that produce desired reliability in a TE device.

Results

Finite element stress analysis and subsequent probability design sensitivity (PDS) analysis was conducted with a TE device. Eleven geometric and material parameters were varied to minimize two response variables. These two response variables were the maximum principal stress in the two outer alumina plates and the maximum principal stress in the TE legs. The PDS analysis yielded sensitivity plots showing which random input variables among those 11 parameters most affected the stresses in the alumina plates and TE materials.

The geometry of the TE device is shown in Fig. 1. Various views of the TE module with the insulator plates removed are shown in Fig. 2 to clearly display the geometric arrangement of the steel contacts, and the TE legs are shown in Fig. 3.

Three-dimensional thermal and structural elements were used to simulate the device and conduct the thermomechanical stress analysis. The mesh distribution used in the simulation is shown in Fig. 4. It contained 142899 elements and 240989 nodes. The following properties were used: alumina - E = 375 GPa, ν = 0.22, κ = 35 W/mK, and CTE = 8 ppm/°C; steel - E = 200 GPa, ν = 0.33, κ = 25 W/mK, and CTE = 12 ppm/°C; and the TE material - E = 24.5 GPa, ν = 0.267, κ = 5 W/mK, and CTE = 18 ppm/°C. Steady state analysis was used setting the top plate to 533°C and the lower to 78°C. The produced thermal gradient is shown in Fig. 5.

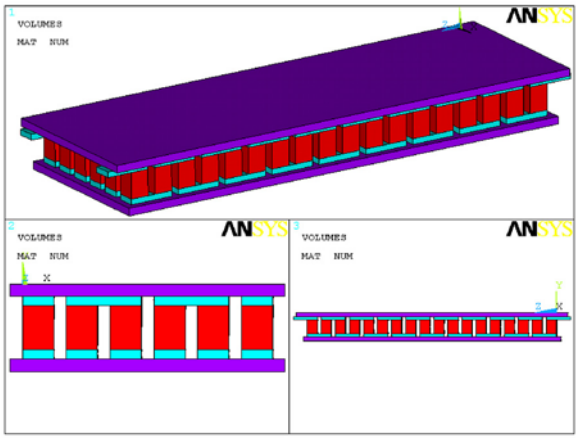

Figure 1. *Various views of the TE module with colors corresponding to material sequence. Purple is the alumina, turquoise is the steel, red is the TE legs.*

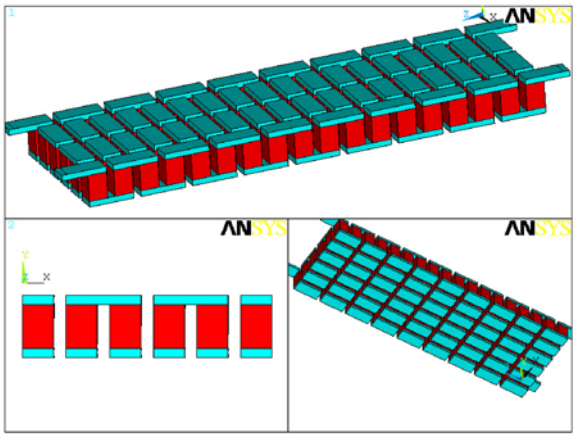

Figure 2. *Views of the TE module with the insulator plates removed to show the arrangement of the steel and TE legs.*

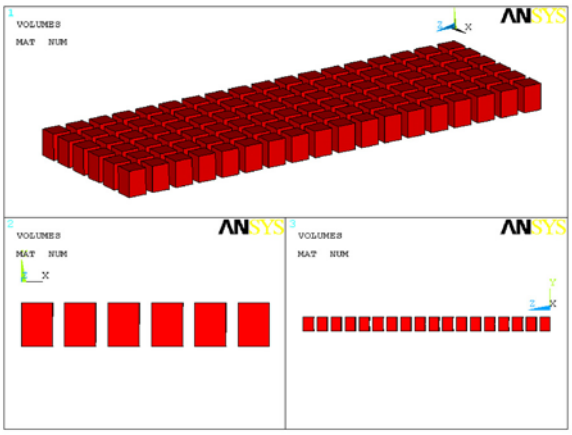

Figure 3. *A 18 x 6 array of TE legs was considered.*

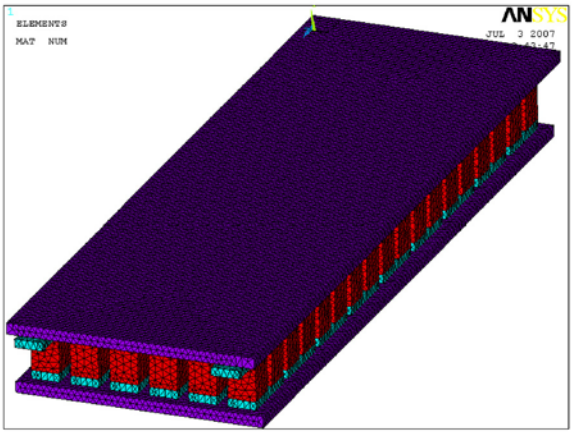

Figure 4. *The mesh distribution contained 142899 elements and 240989 nodes.*

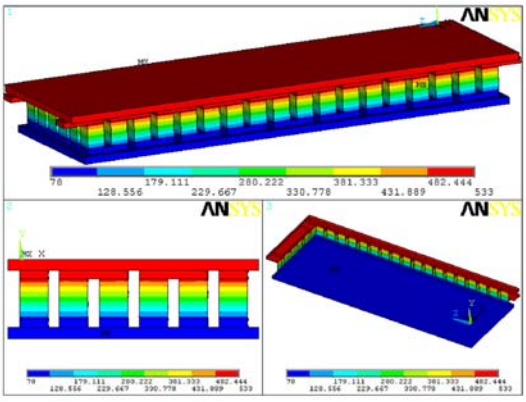

Figure 5. *Temperature distribution in °C.*

The first principal stress of the whole device is shown in Fig. 6, and those within the alumina and TE legs are shown in Figs. 7 and 8, respectively. The resulting maximum tensile stresses do not have complete confidence because more trustworthy input material properties are needed for the TE material; however, their (relatively large) values in the several hundred MPa range suggest that strategies for stress mitigation are needed in order to prevent fracturing of both.

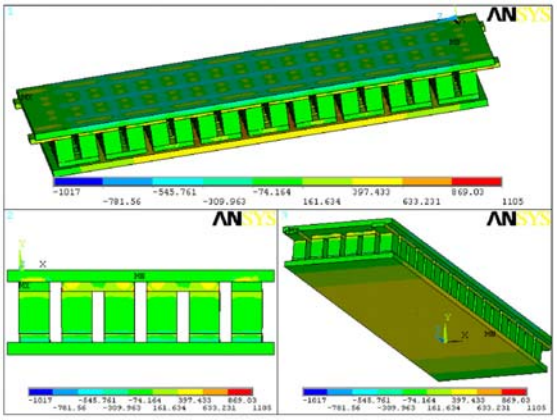

Figure 6. *First principal stresses in the TE device due to the thermal loading.*

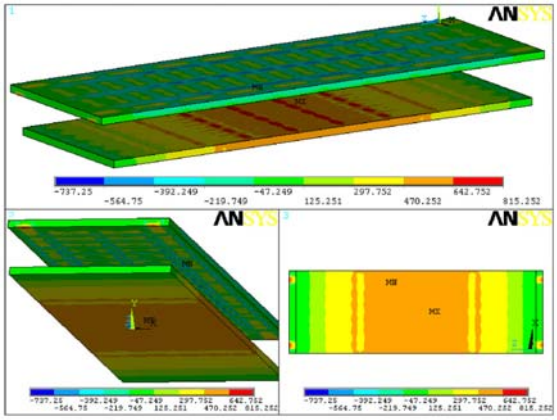

Figure 7. *First principal stresses in the alumina plates due to the thermal loading.*

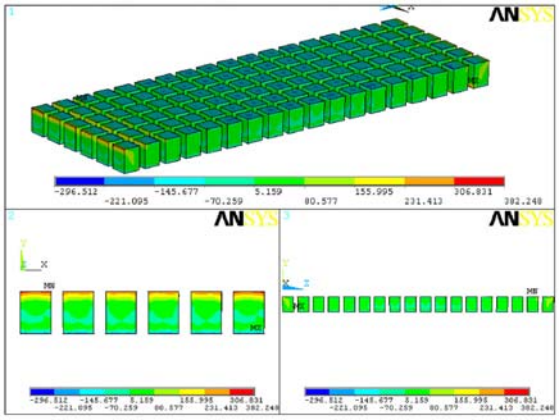

Figure 8. *First principal stresses in the TE legs due to the thermal loading.*

The PDS analysis performs Monte Carlo simulations with multiple input random variables. Geometric, material, and load parameters can be varied by assigning statistical distribution functions to them. Response variables are defined so that minimizing or maximizing them can optimize the device. The PDS analysis can then be used to perform sensitivity analysis to determine which random input variables should be altered and how, in order to optimize the selected response variables. In this analysis, two response random variables were defined and were the maximum principal stress in the (1) alumina plates, and (TE legs). The goal was to determine which geometric and/or material parameters have the most influence on those stresses. The 14 parameters considered are listed in Fig. 9. One hundred simulations were performed for both response variables.

The PDS analysis results found for the alumina plates (Fig. 10) that the tensile stress in them increases as the: elastic modulus of the contact material increases, CTE mismatch between contact and TE material increases, and the TE leg height increases.

Random input variable	Distribution	Minimum value	Maximum value	comments
Material Random Variables				
E3 (GPa)	uniform	25	125	Representing TE materials with different Moduli
v3	uniform	0.2	0.3	Representing TE materials with different Poisson's ratios
K3 (W/m.K)	uniform	3	25	Representing TE materials with different thermal conductivities
CTE3 (ppm/C)	uniform	6	24	Representing TE materials with different CTEs
E2 (GPa)	uniform	350	400	Representing insulation materials with different Moduli
V2	uniform	0.2	0.25	Representing insulation materials with different Poisson's ratios
K2 (W/m.K)	uniform	20	50	Representing insulation materials with different thermal conductivities
CTE2 (ppm/C)	uniform	7	9	Representing insulation materials with different CTEs
E1 (GPa)	uniform	10	200	Representing contact materials with different Moduli
K1 (W/m.K)	uniform	20	60	Representing contact materials with different thermal conductivities
CTE1 (ppm/C)	uniform	12	30	Representing contact materials with different CTEs
Geometric Random Variables				
LH (mm)	uniform	2	10	Range of heights for TE leg
LWX (mm)	uniform	3	6	Range of widths for TE legs
IH (mm)	uniform	1.5	4	Range of thicknesses for insulation plates

Figure 9. *Specifications of random input variables.*

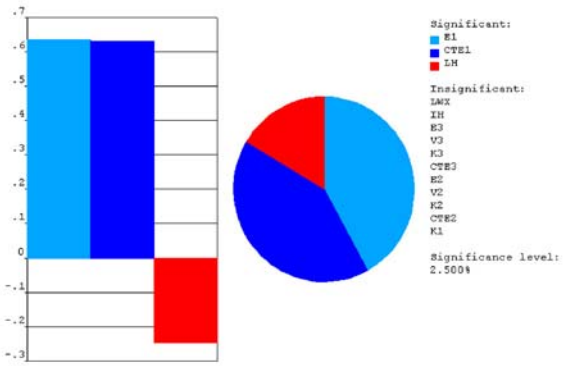

Figure 10. *Sensitivity plot for the maximum principal stress in the alumina plates.*

The PDS analysis results found for the TE legs (Fig. 11) that the tensile stress in them increases as the: CTE mismatch increases, thermal conductivity of the TE material decreases, and elastic moduli of both the contact and TE materials increase. Geometric variable had little effect.

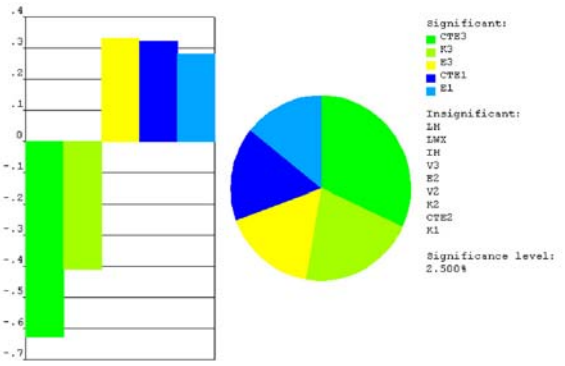

Figure 11. *Sensitivity plot for the maximum principal stress in the TE legs.*

Conclusions

Specific material properties and geometrical descriptors can greatly affect tensile stress development in a TE device. These analyses provide guidance on which should be focused on in order to mitigate them.

Agreement 15529 - Erosion of Materials in Nanofluids

(This project is jointly funded by Propulsion Materials and Heavy Vehicle Systems Optimization)

Principal Investigator: J. L. Routbort and co-workers: D. Singh, Cinta Lorenzo-Martin, R. K. Smith, D. J. Cookson (APS) and Gang Chen (now at Ohio University)

Argonne National Laboratory

9700 S. Cass Avenue, Argonne, IL 60439-4838

(630) 252-5065; fax: (630) 252-5568; e-mail: routbort@anl.gov

DOE Technology Manager: Jerry L. Gibbs

(202) 586-1182; fax: (202) 586-1600; e-mail: jerry.gibbs@ee.doe.gov

---

Contractor: UChicago Argonne LLC

Contract No.: DE AC03 06CH11357

Objective

- Determine if the use of fluids containing a variety of nanoparticles result in erosive damage to radiator materials.
- Develop models to predict the erosive damage.

Approach

- Develop an experimental apparatus to measure erosive loss.
- Conduct experiments to study erosive damage of fluids containing various types and sizes of nanoparticles on typical radiator materials.
- Develop methods to characterize nanofluids and analyze erosion results.

Accomplishments

- Little erosion damage to a typical radiator material, aluminum Al3003, was observed in experiments performed using CuO nanoparticles in ethylene glycol having impact angles of 30 and 90° and velocities up to 10m/s for impact for a total time of 3620 hrs. Particle concentration varied between 0.1 and 0.85 vol %.
- Utilized small-angle x-ray scattering technique to measure nanoparticle size, distribution, and shape.

Future Direction

- Erosion of typical radiator materials using fluids containing a variety of well-characterized nanoparticles will be measured, varying the angle, size of the nanoparticles, impact velocity, nanoparticle volume percent, and temperature.
- If erosion occurs, a predictive model will be developed.
- Initial friction and wear tests using nanofluids as lubricants.

Forward

Efforts have shifted away from the in-house production of nanofluids, to development of advanced characterization techniques and establishment of working relationships between companies that produce nanofluids. As commercial nanofluids become available, ANL will measure their thermal properties. Fluids that show promise from a heat transfer perspective will then be characterized using SAXS. Finally, liquid erosion tests will be performed to determine if the nanofluid will cause deleterious damage to radiator materials.

Introduction

Many industrial technologies face the challenge of thermal management. With ever-increasing thermal loads due to trends toward greater power output for engines and exhaust gas recirculation for diesel engines, cooling is a crucial issue in transportation. The conventional approach for increasing cooling rates is use of extended surfaces such as fins and microchannels. Reducing radiator size will reduce the frontal area and hence the aerodynamic drag. However, current designs have already stretched this approach to its limits. Therefore, an urgent need exists for new and innovative concepts to achieve ultra-high-performance cooling. Nanofluids seem to show enormous potentials as a coolant for radiators. Choi et al. have shown that fluids containing 1 vol % Cu nanoparticles increase thermal conductivity by 40% [1] while 1 vol % carbon nanotubes increase thermal conductivity by 250% [2].

In order for the enhanced thermal conductivity to be utilized it must be shown that liquid erosion of typical radiator materials will be tolerable. If nanofluids result in excessive erosive wear, they cannot be used. Hence, the Office of FreedomCAR and Vehicle Technologies funded a program on liquid erosion of radiator materials using nanofluids.

Results and Discussion of Erosion

An apparatus was built and calibrated as described in the FY05 annual report. Baseline data was obtained using a fluid consisting of 50% ethylene glycol and 50% water impacting an aluminum Al3003 target, typical of a radiator material. Results are tabulated in table 1. As can be seen, the liquid, over the entire range of angles and velocities, produced no erosive wear even for the conditions in which the maximum kinetic energy was transferred to the Al3003 target. It should be mentioned that typical flow velocities in truck radiators are about 1 m/s and hence 10 m/s would be expected to accelerate damage by a factor of 100.

Table 1. Erosion results on Al3003 measured using a baseline fluid, a mixture of 50% ethylene glycol and 50% water.

Impact Angle (°)	Velocity (m/s)	Time (h)	Weight loss (mg)
90	8.0	236	0 ± 0.2
90	10.5	211	0 ± 0.2
50	6.0	264	0 ± 0.2
50	10.0	244	0 ± 0.2
30	8.0	283	0 ± 0.2
30	10.5	293	0 ± 0.2

A previous series of experiments using a very low concentration of Cu (0.01 vol %) nanoparticles in triethylene glycol reported in the FY6 annual report also showed no erosion of the aluminum target for long times at both 30 and 90° impact angles using velocities up to 9.6 m/s. The size, shape, and distribution of the nanoparticles were not known. It was also speculated that since the volume concentration of the nanoparticles was so low that one would not expect damage. Additionally, Cu is softer than the hardened Al3003 and hence might not be expected to cause damage

In order to determine whether the erosion rate is affected by the particle loading and or the particle type, a long (3620 h) series of experiments using various concentrations of CuO in ethylene glycol at two impact angles, 30 and 90°, at velocities up to 10m/s were performed. The results are tabulated in table 2.

Table 2. Results of erosion of Al3003 using CuO in ethylene glycol.

Vol %	V (m/s)	Angle (°)	Time (h)	Weight Loss (mg)
0.1	7.7	30	848	3.3 ± 0.2
0.4	7.7	30	643	0 ± 0.2
0.85	7.7	30	692	0 ± 0.2
0.85	10.0	30	771	0 ± 0.2
0.85	10.0	90	500	0 ± 0.2

The first test performed at 7.7 m/s and with an impact angle of 30° indicated a weight loss of 3.3 mg. This result is plotted in Fig. 1. The rate of material removal is very small, 4 x 10^{-2} µm/hr, corresponding to a loss of 0.003 inches/year for a truck radiator. The results also looked as if there were a threshold.

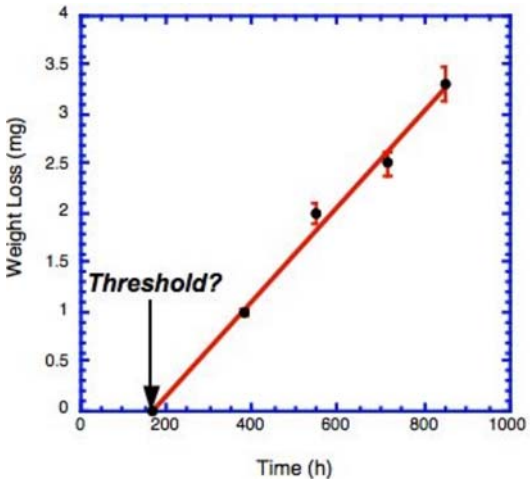

Fig. 1. Weight loss vs. time for an impact angle of 30°, velocity of 7.7 m/s using a 0.1 vol % CuO nanoparticles in ethylene glycol

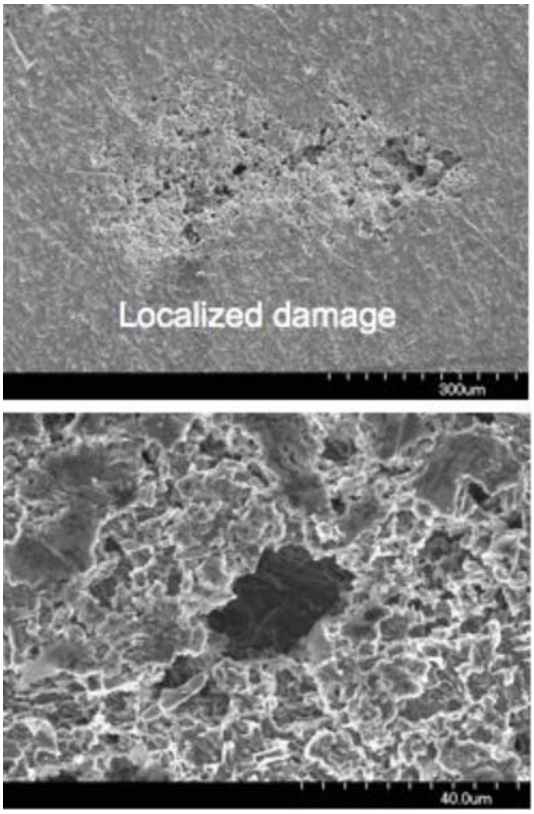

Fig. 2. Scanning electron microscopy of the damage resulting from impacts of 0.1 vol % CuO nanoparticles impacting at 7.7 m/s and 30°

However, closer examination with a scanning electron microscope revealed that the damage was highly localized. It looks as if there was a flaw in the original aluminum that was enlarged by the impact of nanofluid. The fact that the weight loss was not observed using higher velocities substantiates the fact that the weight loss, as small as it was, was an anomaly. Results of thermal conductivity enhancements for this nanofluid were presented in the previous chapter.

While we have not observed erosive wear as a result of the CuO nanofluid, we have only begun to investigate the parameter space that would include nanoparticle material, concentration, shape, size, and size distribution. These are critical parameters. While the material and concentration can be controlled, the shape, size, and size distribution are generally not accurately

determined. One might expect that since the thermal conductivity is such a strong function of nanoparticle size [3] and the kinetic energy imparted to the target by the nanofluid is proportional to the size, it is a very important parameter. The size of the nanoparticle also enters into all theoretical treatments of thermal conductivity. Shape is probably also important, as a sphere is less likely to cause damage than a nanoparticle with sharp edges. Furthermore, one might expect that more damage will result if the dynamic hardness of the nanoparticle is greater or equal to that of the target.

Typically nanoparticle sizes have been determined two ways. First, the particle size of the raw powder is measured, typically, by microscopy, and it is assumed that when added to the fluid, remains the same. The second method uses laser scattering to measure nanoparticle size of a transparent nanofluid. Laser scattering emphasizes the large particles because of the dependence of the scattering factor on R^6, where R is the particle radius. We have refined a much more accurate method of measuring the particle size, shape, and distribution, based on small angle x-ray scattering (SAXS) using high-intensity x-rays from the Advanced Photon Source at ANL.

In order to obtain a definitive result on the effect of particle size/distribution on thermal conductivity, we have chosen to use commercially available nanofluids, "Ludox" (W.R. Grace & Co., Columbia, MD), primarily used for coatings, metal casting, refractory products, and catalysts. It is a colloidal silica solution using a water-based fluid (buffered to pH = 10) containing amorphous SiO_2 particles. Ludox is available in three SiO_2 sizes.

SAXS on nanofluids was performed on beamline 15-ID-D (ChemMatCARS) at the Advanced Photon Source, Argonne National Laboratory. General description of the beamline setup can be found elsewhere [4]. The nanofluids were drawn in with a syringe pump to an open-ended 1mm glass capillary and irradiated with a 0.5×0.3mm mono-chromatic x-ray beam (λ = 1.5Å). X-ray scattering was measured with a charge-coupled device x-ray detector, with intensity calibrated from pure water measured in the identical capillary. All nanofluid SAXS profiles were background-subtracted using profiles obtained from pure buffer solution. For comparison purpose, we also measured the particle size with dynamic light scattering (DLS) using a lab-based instrument (Brookhaven Instruments Corp., Holtsville, NY).

Analysis of x-ray scattering from particles in a liquid can be complicated by interference between the x-rays elastically scattered from individual particles. This particle-particle interference becomes detectable at volume fractions larger than about 0.5%. Figure 3 shows the 1-D SAXS patterns of a silica nanofluid (i.e., Ludox SM) with three different particle volume fractions. The plot of x-ray scattering intensity versus scattering momentum change ($q = 4\pi \sin\theta/\lambda$), where θ. is the scattering angle, and λ is the wavelength) on a log-log scale provides information about the nanoparticles. The x-ray scattering intensity shows a maximum in the region $0.01 < q < 0.05$ Å^{-1} for the 1 and 16 vol % samples due to the interparticle interference effect [5]. The oscillations observed above 0.1 Å^{-1} arise from the inherent form-factor scattering from the particles. These oscillations are often 'washed-out' by poly-dispersity in particles size. The fact that they are still intact for these fluids is due to the narrow size distribution of the nanoparticles. That no change in this oscillatory feature was observed in these three samples indicates that dilution does not affect the particle size distribution. To simplify the data analysis, we use data taken from the most diluted samples, where the effect of interparticle interference can be neglected.

Quantitative data analyses of the SAXS patterns were performed using solid-sphere

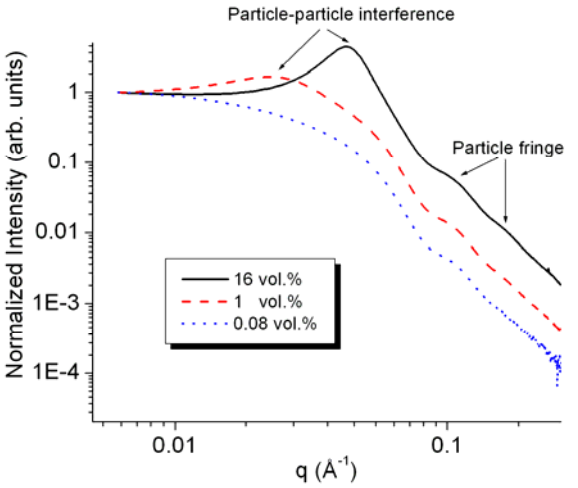

Fig. 3. SAXS patterns of Ludox SM nanofluid with three different particle volume fractions

form factors fitted with a variety of least-squares methods implemented in the program suite IRENA (Ilavsky et al. 2005). Figure 4 shows the 1-D SAXS pattern of a 0.02 vol % silica nanofluid fitted with a maximum entropy algorithm [6]. This method assumes no particle-particle interference and, apart from a non-negative criteria, imposes no further restriction on the resulting size distribution profile. Figure 5 shows the normalized particle size distribution of three diluted silica nanofluids. The concentrations of the samples SM, HS, and TM are 0.08, 0.02, and 0.02 vol %, respectively. Only one major peak is observed in each of the size distribution profiles, confirming the mono-dispersity of the nanoparticles. The presence of small satellite peaks in the distributions may be due to a small amount of aggregation – but are just as likely to be artifacts of the maximum entropy technique. Further analysis of the dominant peaks in these profiles shows that the peak centers (average particle sizes) are located at 107, 167, and 286 Å, and the corresponding full widths at half maximum are 49, 43, and 68 Å. In comparison, the average particle sizes measured by the DLS were 104, 174, and 303 Å that correlate well to the SAXS results.

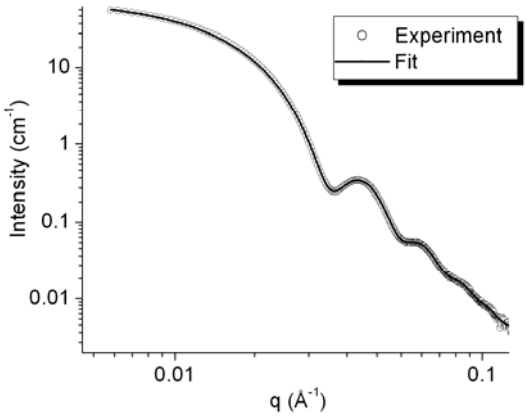

Fig. 4. SAXS data of a 0.02 vol% SiO_2 nanofluid and a fit using the maximum entropy method assuming spherical particles with an average diameter of 17 nm.

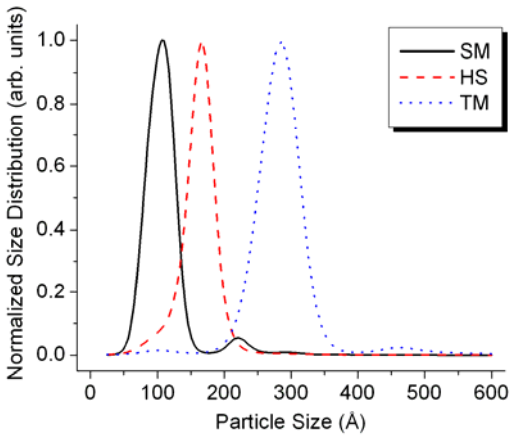

Fig. 5. Particle size distribution of three silica nanofluid samples

In summary, the use of SAXS allows determination of nanoparticle size, shape, and distribution in all types of nanofluids. Therefore, it will be used to

characterize all nanofluids that exhibit promising thermal properties. The accurate determination of particle size and shape combined with thermal conductivity, heat transfer, and erosion will allow a rigorous comparison with theoretical models and their extensions.

Issues & Future Direction

Understanding mechanism(s) of weight loss of target metal is vital to developing predictive models to describe the erosion behavior from nanofluids. At the present time, it appears that erosion behavior by nanofluids is not severe. However, this observation is based on a limited set of data. We have not yet tested a wide-variety of nanofluids containing well-characterized, and controlled volumes of larger percentages of nanoparticles. For example, we have not tested the erosion of a nanofluid containing nanoparticles that are much harder than the target, such as Al_2O_3, or SiC and would be more likely to cause erosion. Similarly, we haven't tested nanofluids containing larger well-characterized particles and particle size distributions. We plan these tests in FY08.

Conclusions

Long-term liquid erosion tests using CuO nanoparticles whose vol % varied between 0.1 and 0.85 in ethylene glycol, at 30 and 90° impact angles, and at fluid velocities of up to 10 m/s indicated that erosion of a typical radiator material, Al3003, was not a problem. However, it was felt that the soft CuO nanoparticle characterization (i.e. nanoparticle size) was not very adequate to describe the nanoparticle parameters in the fluid.

Therefore, we have refined a small angle x-ray scattering technique with x-rays from the Advanced Photon Source at ANL to measure the particle size, distribution, and even the shape. A model nanofluid, consisting of a water-based solution containing three different sizes of SiO_2 colloids was used to calibrate SAXS. The technique provides a wealth of information that will be used in the future to characterize nanofluids and hopefully, help to remove some of the ambiguities in the thermal property data that have resulted from poorly characterized nanofluids.

References

1. J. A. Eastman, S.U.S. Choi, S. Li, W. Yu, and L. J. Thompson, "Anomalously Increased Effective Thermal Conductivities of Ethylene Glycol-Based Nano-Fluids Containing Copper Nano-Particles," *Applied Physics Letters*, **78**, 718-720 (2001).
2. S. U. S. Choi, Z. G. Zhang, W. Yu, F. E. Lockwood, and E. A. Grulke, "Anomalous Thermal Conductivity Enhancement in Nano-tube Suspensions," *Applied Physics Letters*, **79**, 2252-2254 (2001).
3. W. Yu, D. M. France, J. Routbort, S.U.S. Choi, "Review and Comparison of Nanofluid thermal Conductivity and Heat Transfer Enhancements, J. Heat Transfer, in press
4. D. J. Cookson, N. Kirby, R. Knott, M. Lee, and D. Schultz, "Strategies for data collection and calibration on the small angle x-ray scattering cameras at ChemMatCARS", Advanced Photon Source. J. Synchrotron Rad. **13**, 440-444 (2006).
5. Y. Xu, P. L. Hiew, M. A. Klippenstein, Y. Koga, "Study of a commercial SiO_2 sol and gel by small angle x-ray scattering: effect of sample thickness and interoperation by means of Smoluchowski scheme", Clays and Clay Minerals **44**, 197-212 (1996).
6. J. A. Potton, G. J. Daniell, B. D. Rainford, "Particle size distributions from SANS data using the maximum entropy method", J. Appl. Cryst. **21**, 663-668 (1988).

Agreement 10460 – Nanocrystalline Materials via Machining

S. Chandrasekar, K. P. Trumble, and W. D. Compton
Purdue University
315 North Grant Street
West Lafayette, IN 47907-2023
(765) 494-3623; fax: (765) 494-5448; e-mail: chandy@purdue.edu

DOE Technology Manager: Jerry L. Gibbs
(202) 586-1182; fax: (202) 586-1600; e-mail: Jerry.gibbs@ee.doe.gov
ORNL Technical Advisor: D. Ray Johnson
(865) 576-6832; fax: (865) 574-6098; e-mail: johnsondr@ornl.gov

Contractor: Oak Ridge National Laboratory, Oak Ridge, Tennessee
Prime DOE Contract No.: DE-AC05-00OR22725
Subcontractor: Purdue University, West Lafayette, Indiana

Objective

- Develop manufacturing technologies for producing bulk nanostructured alloys with enhanced mechanical properties for transportation applications.

Approach

- Develop machining methods for direct production of bulk forms (e.g., sheet, bar) and particulate materials with nano-scale microstructure.
- Characterize microstructure, structure and mechanical properties of nanostructured chip particulate and bulk forms.
- Develop low-temperature consolidation routes for converting the chip particulate into monolithic and composite materials without significant coarsening of the nanocrystalline microstructures.
- Characterize microstructure, mechanical properties, and performance of the bulk forms after the consolidation.

Accomplishments

- Scale-up and continued development of a new process, large-strain extrusion-machining (LSEM), to directly produce bulk forms (e.g. sheet, bar) with ultra-fine grained (UFG) microstructure and enhanced mechanical properties. The process has been scaled up for producing sheet a few inches in dimension. The process has been applied to materials such as Al alloys, Ti, Inconel 718, and steel.
- A new Modulation –Assisted Machining (MAM) method for making nanostructured particulate of controlled size (30-500 micrometers) and shape (e.g., equiaxed, platelet, needle) directly by chip formation.
- Innovative, low-temperature processing routes for producing bulk nanostructured alloys from chip particulate using polymeric binders. These polymer-bonded alloys show promising enhancements in hardness and wear properties.
- Low-temperature consolidation routes that limit coarsening in Al6061-T6. Achieved a high degree of densification and interparticle bonding in room temperature powder extrusion of nanostructured Al6061-T6.

Future Direction

- Continue development of the extrusion machining process to make sheets of nanostructured Ti and Mg alloys, and steels for potential automotive applications (e.g., fuel system components, diesel engine structural components, coil springs)
- Continue development of low-temperature consolidation routes to produce bulk monolithic and/or composite alloys with nanocrystalline microstructure.
- Determine tensile and wear properties of bulk forms to demonstrate integrity of the consolidated alloy samples and guide application.
- Continue intensive efforts to scale-up these processes for prototype applications in the transportation and energy sectors.

Introduction

This program builds on the discovery of a low-cost means of producing nanostructured materials in essentially any alloy via machining. Notable achievements have been further development and scaling up of a large-strain extrusion machining process (LSEM) for direct production of bulk forms, (e.g., sheet and bar) with ultra-fine grained (UFG) microstructures; and a Modulation–Assisted Machining (MAM) process for direct production of nanostructured particulate alloys with highly controlled shape and size distributions. The bulk forms can serve as pre-cursor materials for component applications. Particulates may be used as continuous or discontinuous reinforcements in metal or polymer matrices to create advanced composites; or consolidated into monolithic bulk forms using low-temperature consolidation routes such as powder extrusion.

Progress from FY 2007 in three main areas is highlighted in this report: (1) LSEM for direct production of sheet and bar of high-strength materials with an UFG microstructure (2) particulate production of lightweight materials by MAM and (3) production of bulk alloys by low-temperature pressing of particulate using a very thin layer of polymer as binder.

Approach

Two routes were pursued for the creation of bulk forms with nanocrystalline and/or UFG microstructures. The first utilized LSEM, wherein the chip is produced with a controlled geometry by constraining its shape and size at the point of its formation. This method combines microstructure refinement by large-strain deformation with simultaneous dimensional control of chip shape by extrusion in a single step of deformation. The resulting sheet offers enormous promise for ground transportation applications.

Second, by incorporating controlled superimposed modulation into a conventional machining process - Modulation-Assisted Machining (MAM) - nanostructured chips could be directly created in micron-sized particulate form. The particulate have controlled size and shape, a tight particle size distribution, and macroscopic dimensions resembling those of powders used in current Powder Metallurgy (PM) processes. MAM has provided a cost-effective solution to the problem of making nanostructured particulate suitable for consolidation. The resulting particulate has served as pre-cursor material for shear-based consolidation processes such as powder extrusion and pressing with a polymer binder, and as reinforcements for metal and polymer matrices in composites processing.

Bulk Al 6061T6 alloys have been produced using a low-temperature consolidation (LTC) pressing process wherein a very thin layer of polymer is used as a binder. The polymer bonding is a new approach in which a thermosetting polymer resin is used, together with high-pressure compression molding in a steel die to yield a structure consisting of low-volume fractions of polymer bonding the nanostructured metal particles. The goal of this approach is to bond the machining chip particulate with as fine a polymer bond layer as possible. The availability of particulate created by MAM is opening up new opportunities for this LTC route, including realization of higher alloy packing density (volume fractions) with the equiaxed particles now being produced by the MAM.

Results

Bulk Nanostructured Materials by LSEM

Simplicity of chip formation in plane-strain machining enables grain refinement by Severe Plastic Deformation (SPD) at near-ambient temperatures in the full range of commercial alloys, including high-strength alloys which are difficult to process by conventional SPD. LSEM is the experimental configuration used to create bulk foil samples under controlled conditions of strain and strain rate. Figure 1 illustrates an LSEM process wherein a bulk foil/sheet sample (chip) of controlled thickness is produced by machining and extrusion imposed in a single step using a specially designed tool. The tool consists of two components – a bottom section with a sharp cutting edge inclined at a rake angle (α) and a wedge-shaped top section that acts as a constraining edge. The tool moves radially into a disk-shaped workpiece rotating at a constant peripheral speed, V. The chip is simultaneously forced through an 'extrusion' die formed by the bottom rake face and the top constraining edge, thereby effecting dimension and shape control. The velocity of the material at the exit of the tool is $V_c = Vt/t_c$, where t and t_c are the undeformed and deformed thickness of the chip, respectively.

LSEM, unlike conventional machining, involves chip formation by constrained deformation where the deformed chip thickness is controlled *a priori*. Thus, microstructure refinement by large-strain machining is effected in combination with shape and dimensional control. The LSEM process has also been implemented in a linear machining configuration on a press. The large force capacity available with a press has enabled macro-sized samples of various alloys to be produced.

Application of the LSEM process to high-strength alloys is illustrated using the example of creation of nickel-base superalloy Inconel 718 sheet with nano-scale microstructure. Figure 1 (inset) shows a typical Inconel foil produced by LSEM of the solution-treated material. The foils were approximately 600 mm long and 6 mm wide, with a thickness of at least 400 μm. The straightness of the foils facilitated subsequent processing. The hardness values of the foils created with shear strain (γ) of 2.1 and 3.5 were 494 kg/mm^2 and 562 kg/mm^2, respectively. These values are much greater than the hardness of the bulk microcrystalline Inconel 718 (220 kg/mm^2), suggesting a significant level of microstructure refinement during LSEM. Indeed, the foil hardness values are nearly that of aged microcrystalline Inconel 718 (500 kg/mm^2). Uniaxial tensile test results from the foils showed increases in strength that are directly proportional to the increases in hardness.

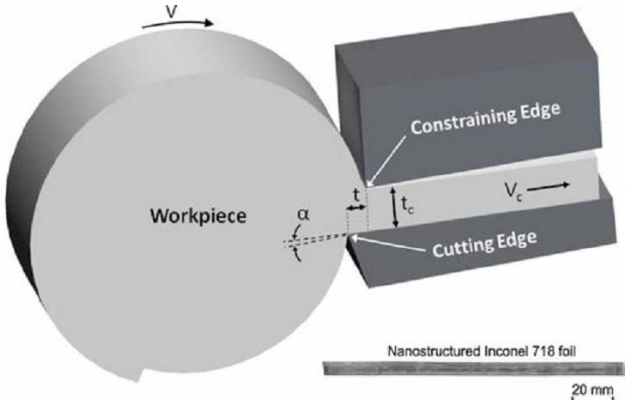

Fig. 1 Schematic of large-stain extrusion machining (LSEM). Inset at bottom right shows a typical Inconel 718 sheet strip created using this process.

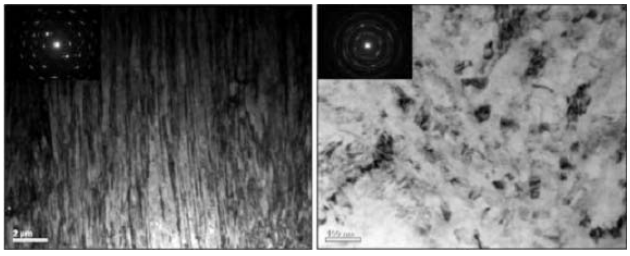

Fig. 2 Bright-field TEM micrograph of Inconel 718 sheets created with shear strains of (a) 2.1 and (b) 3.5, showing nano-scale microstructure.

Direct evidence for ultrafine microstructures of the foils is seen in the TEM images and selected-area diffraction (SAD) patterns shown in Figure 2. The micrographs illustrate increased microstructure refinement and formation of nano-scale and UFG structures with increasing strain, which is consistent with the well-known dependence of microstructure on strain. The foil produced at lower strain has a predominantly elongated UFG microstructure (Fig. 2a). The foil with the higher level of strain shows increased grain sub-division and a finer scale microstructure with equiaxed grains of size 50 to 200 nm (Fig. 2b). Simultaneous with the refinement of the microstructure, the diffraction pattern evolves from a smeared single-crystal pattern (Fig. 2a) to a

more ring-like pattern indicative of high misorientation angles (Fig. 2b). This has also been confirmed by sample-tilting experiments in the electron microscope.

Direct measurements of strain and strain rate in chip formation using Particle Image Velocimetry (PIV) have shown the deformation to be uniformly distributed across the chip thickness. Thin surface layers (~10 μm thick) on both faces of the chip are, however, affected by secondary deformation arising from tool-chip friction. The uniform distribution of strain is consistent with observed uniformity of the hardness through the chip volume. Additional support for homogeneity of the deformation comes from electron backscattered diffraction (EBSD) investigations that have revealed a uniform microstructure through the foil thickness.

Nanostructured Particulate by Modulation-Assisted Machining (MAM)

Metal and alloy powders are produced by a wide range of physical, chemical and mechanical routes, each of which imparts characteristic morphology and microstructure to the particles. These processes typically yield broad particle size distributions, requiring subsequent classification. Although particle shape (e.g., spherical, flake, dendritic, irregular) is process specific, there is generally little control of shape within a given process. Particle internal structure is also process dependent. High-energy milling, for example, imparts severe plastic deformation, which enables mechanical alloying, dispersion of fine oxide particles, as well as extreme grain-substructure refinement (nanocrystalline structure) within the particles. But the process is often limited by contamination associated with high surface area exposure during repetitive comminution and agglomeration steps and there is limited control of particle (agglomerate) size.

Continuous production of Al 6061-T6 particulate using modulation-assisted machining (MAM) has been demonstrated. Superimposition of a controlled, low-frequency modulation in conventional machining causes chips to form as discrete particles. By adjusting the conditions, equiaxed, platelet, and fiber shaped particles having narrow size distributions can be produced directly without a need for comminution of the chips. The large strains imposed by the machining result in nanostructured particulate of high hardness and strength.

Figure 3 shows examples of equiaxed-, needle- and platelet-type Al 6061-T6 particles produced by MAM under various process conditions. The extraordinary uniformity in sizes of the particles is apparent from the SEM micrographs (Fig. 3). Other experiments have demonstrated production of particles with sizes ranging from 20 to 2000 μm and aspect ratios of up to 200. The standard deviations for distributions of particle sizes are less than 3% of the mean size. This demonstrates the ability of MAM to produce particles of uniform size in each of the different shapes, a consequence of the deterministic nature of the particle formation process.

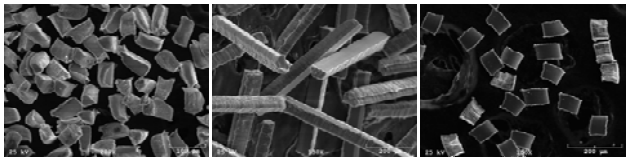

(a) (b) (c)

Fig. 3 Scanning electron micrographs of Al 6061-T6 particulate showing (a) equiaxed, (b) needle, and (c) platelet shapes.

Figure 4 shows an enlarged view of a needle shaped particle with an aspect ratio of ~7. One surface of the particle is seen to be smooth; this is the surface that was in contact with the tool rake face.

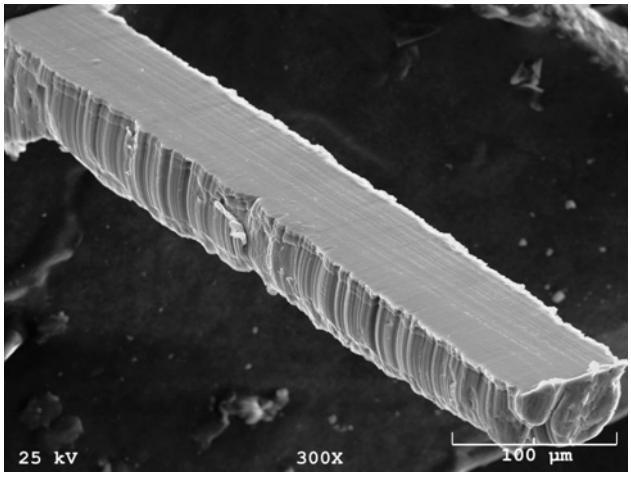

Fig. 4 SEM picture of a needle particle with aspect ratio ~7. The geometry and size are controlled by the MAM conditions. The smooth surface is the

surface that was in contact with the rake face of the tool.

The strain imposed in the particles can be estimated from the dimensions of a platelet particle prior to (l_o) and after (l_c) its detachment from the bulk material. This resulted in a shear strain estimate of $\gamma = 3.45$ in the platelet particles. Furthermore, the data fit implied that the average strain is constant over the range of modulation conditions and uniform over the particle volume. Therefore, the deformation process in MAM is self-similar at different particle thicknesses, and dependent only on the tool rake angle, as in conventional machining. Additional confirmation of this self-similarity is provided by estimates of strain in continuous chips created under the same machining condition, but without modulation. For this conventional machining condition a strain value of $\gamma = 3.50$ was obtained, very similar to that for the particles.

The Vickers hardness of the particles was 154 ± 3 HV, a 30% increase over that (110 ± 2 HV) of the bulk Al 6061-T6. A similar, high hardness value has been measured in millimeter-sized Al 6061-T6 chips created by machining, and Al 6061-T6 bars produced by Equal Channel Angular Pressing, wherein the high hardness has been attributed to the fine grain size resulting from the SPD. Transmission electron microscope observations of 3-mm size, Al 6061-T6 chips created with a shear strain similar to that of the particles have shown the microstructure to consist of equiaxed, nano-scale grains with an average size of 80 nm. Therefore, it is likely that the particles created by the MAM also have an ultrafine grained microstructure. This will be verified in the near future.

The particle dimension and geometry are determined to first order by the tool/workpiece motions; hence, it is feasible to precisely set the modulation and machining conditions to achieve desired particulate characteristics. The ability to control the shape of the particle while simultaneously achieving uniformity in particle sizes is a consequence of the deterministic nature of the particle formation process in MAM. This is to be contrasted with other particle production processes such as atomization, ball-milling, and attrition-milling, wherein particle formation is governed at least partially, if not fully, by stochastic mechanisms.

The MAM process is inherently scalable for large-volume production of particulate from a variety of metals and alloys. The particulate can serve as pre-cursor materials for powder metal consolidation methods such as pressing, spraying and shear-based processes. The uniformity of particle size offers potential for achieving enhanced densification and production yield. Current work is exploring application of the process to a broader range of materials (e.g., Ti alloys and steels), consolidation of particulate by spray, shear-based deformation and polymer bonding processes, and characterization of microstructure of the particles.

Bulk Al Alloys using a Polymer Bonding Agent

Die press bonding has been used to produce bulk Al-6061-T6 samples from nanostructured 6061 T6 particulate using a small amount (<10%) of epoxy as binder. The goal of this approach is to bond the machining chip particulate with a thin polymer bond layer, the epoxy cure at 100°C only slightly degrading the hardening imparted in chip formation. Two routes have been developed, (1) premixing the alloy powder and liquid epoxy and pressing in a closed die having sufficient clearance that the excess epoxy is squeezed out and (2) prepressing the alloy powder alone followed by isostatic pressure infiltration. Premixing the liquid epoxy seems to introduce bubbles that are not eliminated in pressing since the effective pressure on the liquid is only atmospheric pressure. Whereas, prepressing the powder results in the formation of closed pores, which are not penetrated by the liquid epoxy during high-pressure infiltration (210 MPa). Nevertheless, composites containing over 90 volume percent metal have been produced.

Figure 5 shows optical micrographs of composites produced using two different epoxies and two different pressing pressures. The low-viscosity M-bond epoxy (η~1 mPa·s) comes with the disadvantage of high cure shrinkage. Figure 5(a) and (b) show the effect of doubling the pressing pressure from 500 to 1000 MPa, whereas Fig. 5(c) shows the effect of using an epoxy of more conventional viscosity (η~600 mPa·s) at a pressing pressure of 1000 MPa. The higher viscosity resulted in a thicker "glue" layer between the particles.

Density measurements combined with quantitative stereology yield the volume fractions of all three phases (V_{Alloy}, V_{Epoxy}, and $V_{Porosity}$).

Measurement of the metal volume fraction by systematic point counting allows the volume fraction of porosity and epoxy to be distinguished. The results are shown in Table 1.

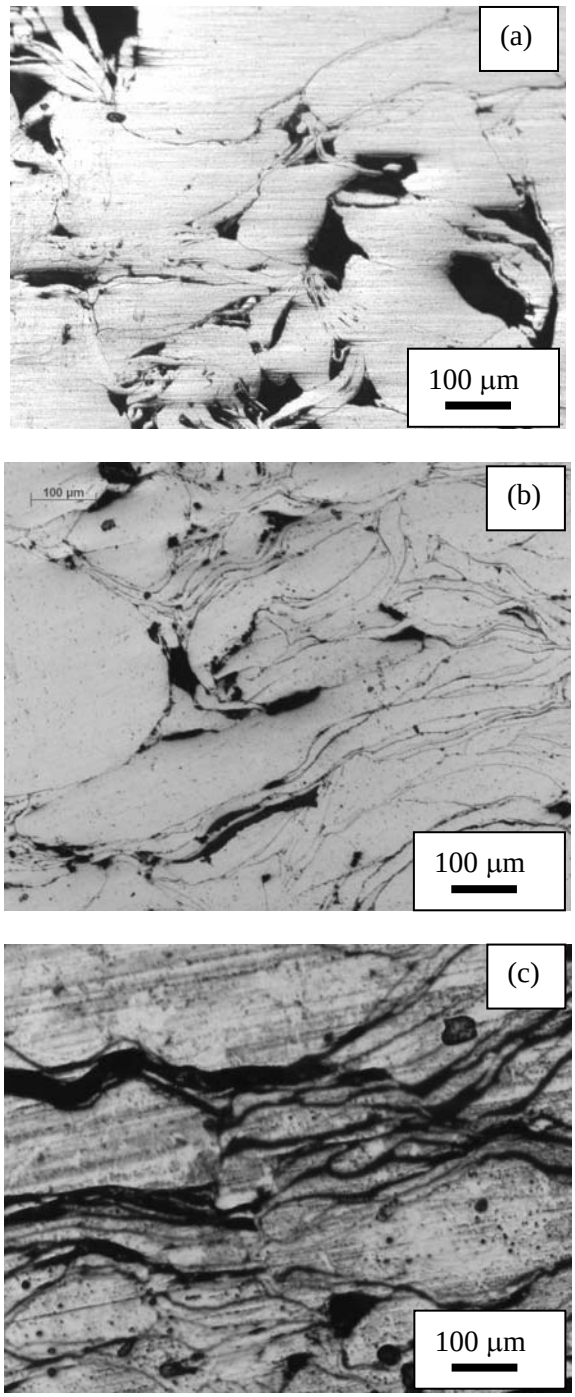

Fig. 5 Optical micrographs Al-6061-T6 chip powder produced by milling and mixed with liquid epoxy: M-bond epoxy (η~1 mPa·s) pressed at 500 MPa (a) and 1000 MPa (b), Epoxide epoxy (η~600 mPa·s) pressed at 1000 MPa

The primary effect pressing pressure (P) increasing the alloy volume fraction is apparent. Since the density of the alloy is the highest of the three constituents (ρ_{alloy} = 2.70 g/cm^3, ρ_{epoxy} = 1.04 - 1.12 g/cm^3) and $V_{alloy} = 1 - (V_{epoxy} + V_{porosity})$, pushing the alloy particles closer together (squeezing out more epoxy) yields a higher density.

Table 1 - Composite processing conditions and resulting density, phase volume fractions and average hardness (kg/mm2).

η_E mPa-s	P MPa	ρ g/cm^3	V_A	V_E	V_P	H kg/mm^2
~1	500	2.22	0.81	0.04	0.15	108
~1	1000	2.39	0.88	0.02	0.10	116
~600	1000	2.42	0.88	0.05	0.07	120

The metal volume fraction also has a primary effect on the composite hardness. These values are the average of 10 measurements using a 100-kg load. The starting chip hardness is about 150 kg/mm^2, whereas the starting alloy before machining (T6 condition) is about 107 kg/mm^2. These results indicate that a significant fraction of the hardening imparted by the machining is retained in this process.

Analogous experiments using equiaxed particles produced by modulation-assisted machining (MAM) showed more uniform alloy packing, although the metal volume fraction was comparable to that achieved with the high aspect ratio powders produced by milling.

The results to date point out the need for a model to describe the composite hardness in terms of the constituent hardness values and composite microstructure. With such a model we hope to be able to determine the relative importance of alloy volume fraction and strength of the alloy-epoxy bond. Applications for lightweight, wear-resistant components are envisioned.

Publications

W. Moscoso, M. R. Shankar, J. B. Mann, W. D. Compton, and S. Chandrasekar, Bulk nanostructured materials by large-strain extrusion machining, *Journal of Materials Research*, **22-1**, 201, 2007.

S. Swaminathan, M. R. Shankar, B. C. Rao, W. D. Compton, S. Chandrasekar, A. H. King, and K. P. Trumble, Severe plastic deformation and nanostructured materials by machining, *Journal of Materials Science,* **42**, 1529, 2007.

S. Swaminathan, T. L. Brown, S. Chandrasekar, T. R. McNelley and W. D. Compton, Severe plastic deformation of copper by machining: microstructure refinement and nanostructure evolution with strain, *Scripta Materialia,* **56,** 1047, 2007.

J. B. Mann, C. Saldana, S. Chandrasekar, W. D. Compton and K. P. Trumble, Metal-particulate production by modulation-assisted machining, *Scripta Materialia*, **57**, 909, 2007.

M. R. Shankar, R. Varma, B. C. Rao, S. Chandrasekar, W. D. Compton, A. H. King and K. P. Trumble, Severe plastic deformation of difficult-to-deform materials at near-ambient temperature, *Metallurgical and Materials Transactions* A, **38**, 1899, 2007.

S. Lee, M. R. Shankar, J. B. Mann, W. Moscoso, S. Chandrasekar and W. D. Compton, Direct measurement of large-strain deformation field in machining, Proceedings of the CIRP workshop on modeling and simulation of machining operations, Reggio Calabria, Italy, September 2007.

M. Sevier, H. T. Yang, S. Lee and S. Chandrasekar, Severe plastic deformation by machining characterized by finite element simulation, *Metallurgical and Materials Transactions* B, in press.

Presentations

S. Chandrasekar, W. D. Compton, A. H. King, K. P. Trumble et al., Severe plastic deformation and nanostructured materials, Indian Inst. Sci., Bangalore, India, March 2007.

S. Chandrasekar, W. D. Compton, A. H. King, K. P. Trumble et al., Severe plastic deformation and nanostructured materials by machining, International Institute for Advanced Research in New Materials and Powder Metallurgy (ARCI), Hyderabad, India, July 2007.

C. Saldana, W. Moscoso, J. B. Mann, M. R. Shankar, S. Chandrasekar, W. D. Compton, A. H. King, K. P. Trumble and P. Yang, Bulk nanostructured materials by large strain extrusion machining and micro/meso scale components thereof, Bulk Nanomaterials 2007, Ufa, Russia, August 2007.

S. Chandrasekar, K. P. Trumble, and W. D. Compton, Bulk nanostructured materials by large strain extrusion machining, Diesel-Engine Efficiency and Emissions Reduction (DEER) 2007 Conference, Detroit, August 2007.

S. Chandrasekar, K. P. Trumble, W. D. Compton and A. H. King, A study of material behavior at large plastic strains using plane-strain machining with a wedge indenter, Third International Indentation Workshop, Cambridge University, U. K., July 2007.

K. P. Trumble, J. B. Mann and S. Chandrasekar, Severe plastic deformation and nanostructured materials by machining, Cummins Engine Company, Columbus, IN, July 2007.

K. P. Trumble, S. Chandrasekar, and W. D. Compton, (Invited) Extreme grain refinement via novel machining processes, General Electric Global Research Center, Nishkayuna, NY, October 2007.

K. P. Trumble, J. B. Mann, W. Moscoso, M. Efe, S. Chandrasekar, W. D. Compton, Nanostructured commercial alloys via large-strain extrusion machining, Commercialization of NanoMaterials 2007, TMS, Pittsburgh, PA, November 2007.

K. P. Trumble, J. B. Mann, S. Chandrasekar, and W. D. Compton, Severe plastic deformation and grain refinement via machining-based processes, Kennametal Corporate Technology Center, Latrobe, PA, November 2007.

Related Patents

S. Chandrasekar, W. D. Compton, T. N. Farris and K. P. Trumble, Method of forming nanocrystalline structures and product formed thereof, U. S. Patent, 7, 294, 165, issued November 13, 2007.

S. Chandrasekar, W. D. Compton, T. N. Farris and K. P. Trumble, Method of forming nanocrystalline structures, European Patent No. 1347852 issued August 15, 2007.

Four patent applications pertaining to the machining technology for making bulk and particulate materials are pending. The patents and several of the patent-pending technologies have already been licensed/sub-licensed to multiple companies.

Other Commercialization Besides licensing of the technologies, a start-up company has been started by one of the students involved in the project, James Mann. The company, M4 Sciences, is focused initially on commercialization of MAM technologies for manufacturing and materials processing.

Project 18516 - Materials for Electric and Hybrid Drive Systems

Agreement 9648 - Mechanical Characterization of Electronic Materials and Electronic Devices

A. A. Wereszczak, T. P. Kirkland, and O. M. Jadaan
Ceramic Science and Technology Group
Oak Ridge National Laboratory
P.O. Box 2008, MS 6068, Bldg. 4515
Oak Ridge, TN 37831-6068
(865) 576-1169; fax: (865) 574-6098; e-mail: wereszczakaa@ornl.gov

DOE Technology Manager: Jerry L. Gibbs
(202) 586-1182; fax: (202) 586-1600; e-mail: jerry.gibbs@ee.doe.gov
ORNL Technical Advisor: David Stinton
(865) 574-4556; fax: (865) 241-0411; e-mail: stintondp@ornl.gov

Contractor: Oak Ridge National Laboratory, Oak Ridge, Tennessee
Prime Contract No.: DE-AC05-00OR22725

Objectives

- Mechanically evaluate new dielectric polymer films processed by Sandia National Laboratories (SNL).
- Mechanically evaluate developmental ceramic capacitors processed by Argonne National Laboratory (ANL).
- Model residual stresses in an arbitrary ceramic multilayer capacitor and evaluate which parameters could have the largest effect on its mechanical reliability.

Approach

- Measure tensile strain-to-failure of SNL-supplied dielectric polymer films as a function of temperature.
- Estimate strain-to-failure of ANL-supplied ceramic capacitors.
- Use finite element analysis and probability design sensitivity analysis to rank which geometrical, material property, and service conditions could have the largest effect on mechanical reliability on ceramic multilayer capacitors.

Accomplishments

- Quantified strain-to-failure of PPOD dielectric polymer films.
- Quantified allowable strain-to-failure of ANL ceramic capacitors.
- It was identified that, in descending order, that reducing the CTE mismatch between ceramic dielectric and metal electrode, reducing the elastic modulus of the metal electrode, and increasing the ceramic dielectric's Weibull modulus would have the largest effect on increasing the reliability of the ceramic dielectric in a multilayer capacitor.

Future Direction

- FY07 was the project's last.

Introduction

A primary focus of the power electronics effort in the Propulsion Materials Program is to develop novel polyfilm and nano-ceramic dielectrics that address high-temperature/electric requirements for dc bus capacitors for power electronic modules in hybrid electric vehicles. Polymer film capacitors are the most cost-effective; ceramic capacitors are smaller and have better high-temperature characteristics. Ultimately, the objectives are to make the power modules more compact while maintaining tight voltage and temperature requirements and long service life. These specifications are to be achieved without compromise caused by mechanical breakdown of the candidate dielectric film or nano-ceramic dielectrics.

The mechanical reliability of polymer and ceramic dielectrics can be a limiter of their intended electronic function. Both Sandia National Laboratory (SNL) and Argonne National Laboratory (ANL) are developing polymer and ceramic dielectric materials, so the present project is working with both laboratories to mechanically evaluate them. Lastly, residual stresses are created in ceramic multilayer capacitors because of their relatively high sintering temperature and mismatches of coefficient of thermal expansion of the materials comprising them, so a modeling effort was pursued to identifying which parameters had the largest effect on the magnitude of the first principal tensile stress within the ceramic dielectric material. For a ceramic material, it is this tensile stress that limits its reliability.

Results

Results are grouped into three categories: polymer film testing, ceramic capacitor characterization, and the modeling of a ceramic multilayer capacitor.

Polymer dielectric testing - Subtask 1

A primary goal of this subtask has been to mechanically evaluate developmental polymer dielectric films and predict the manufacturability and long term reliability of capacitors that would contain them. An example of such a capacitor is shown in Fig. 1. Ultimately, the objectives for the capacitor community (and power electronics community) is to make power modules more compact, and maintain tight voltage and temperature requirements and promote long service life without compromise from mechanical failure of the polymer dielectric film.

Figure 1. *A 0.2-µF wound capacitor. Photo provided by Sandia National Laboratory.*

The strain-to-failure of PPOD dielectric polymer film was measured as a function of temperature. The PPOD film was supplied by Sandia National Laboratory, and was produced as part of their Power Electronics and Electronics Machines project entitled "High Temperature Film Capacitors." Its response, compared to that measured for the dielectric film from a capacitor from an inverter from a Toyota Prius hybrid, is shown in Fig. 2.

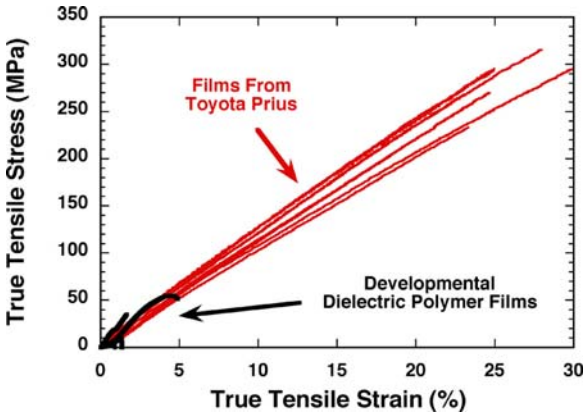

Figure 2. *Comparison of tensile strain-to-failures of PPOD dielectric film and the film from capacitor from a Toyota Prius hybrid.*

Ceramic dielectric characterization - Subtask 2

The evaluated ceramic dielectric system was supplied by Argonne National Laboratory, and was produced as part of their Power Electronics and Electronics Machines project entitled "High Performance Embedded Film-on-Film Capacitors for HEV Power Electronics."

The (thin) film-on-film capacitors were deposited on a relatively thick nickel substrate. Being that the nickel substrate was much thicker and likely to have a higher strain-to-failure than the ceramic dielectric, we employed a simple mechanical test to estimate the strain-to-failure of the ceramic dielectric using a "continuously changing radius-of-curvature bend test. Its principal is illustrated in Fig. 3 and Fig. 4 represents its analysis. The specimen is permanently deformed, and the radius of curvature where cracking in the dielectric is measured, and its value is used to calculate strain-to-failure.

Two supplied capacitors were mechanically evaluated using this method, and the strain-to-failure of the ceramic dielectric was at least 50%. An example of which is shown in Fig. 5. The nickel substrate actually cracked and the adhered ceramic dielectric remained so with no observable (Mode I) cracking in it. Caution needs to be exercised with the interpretation of that 50% strain-to-failure value though because it will dramatically decrease with an (expected) increase in total dielectric thickness.

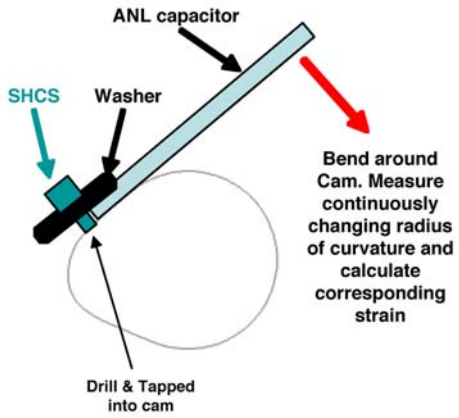

Figure 3. *Schematic of the bend test used to estimate strain-to-failure of the ceramic dielectric.*

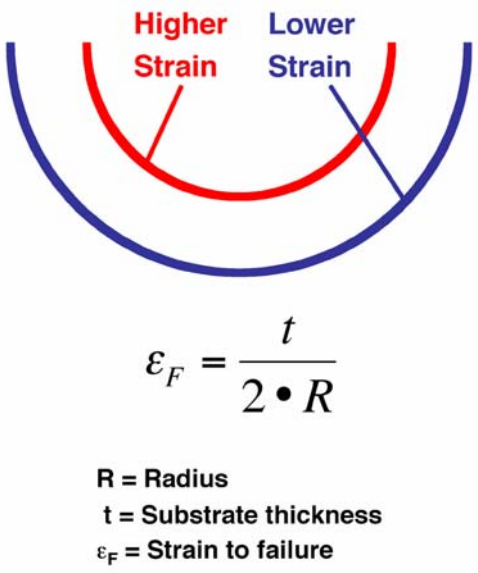

Figure 4. *Strain-to-failure relationship.*

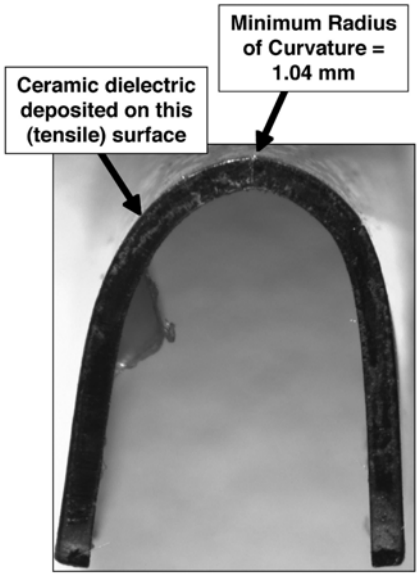

Figure 5. *Mechanically evaluated ceramic dielectric - nickel substrate system.*

Stress Sensitivity Analysis - Subtask 3

Ceramic multilayer ceramic capacitors (MLCC) are processed at elevated temperatures, and because they are comprised of dissimilar materials having different coefficients of thermal expansion (CTE), residual stresses are created within them at temperatures below that of processing. This subtask

explored which parameters would have the largest effect on the first principal stress (or probability of failure) within the ceramic dielectric.

A 2-dimensional model of a MLCC was constructed and it is shown in Fig. 6. The resulting first principal stress field is shown in Fig. 7. Ten parameters were then considered to see which would have the largest effect on probability of failure, and they are listed in Fig. 8. The probability design sensitivity (PDS) analysis showed that three parameters (see Fig. 9) could significantly affect that probability of survival. In descending order of importance, they were CTE mismatch, Weibull modulus of ceramic strength, and the elastic modulus of the metal electrode.

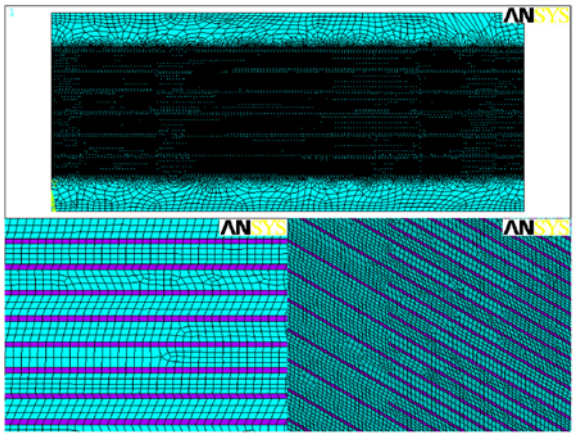

Figure 6. *The MLCC 2-D mesh contained ~96,000 elements and ~290,000 nodes.*

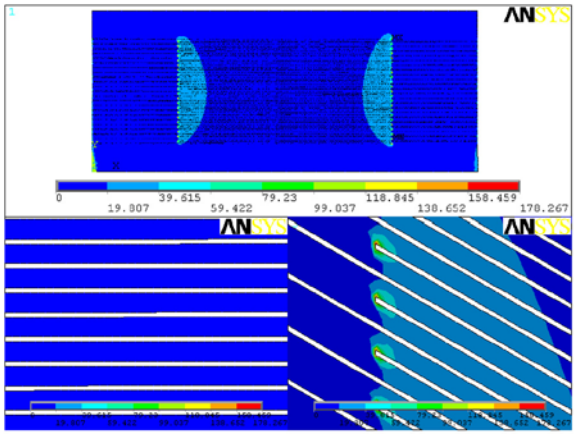

Figure 7. *First principal (residual) stress distribution in the dielectric ceramic.*

Random input variable	Distribution	Minimum value	Maximum value	comments
Material Random Variables				
E1 (GPa)	uniform	90	130	Elastic modulus for dielectric material
CTE1(1/C)	uniform	10e-6	18.0e-6	CTE for dielectric material
E2 (GPa)	uniform	40	220	Elastic modulus for electrode material
Weib_slope1	uniform	4	10	Weibull modulus for dielectric material
Weib_scale1 ($MPa.mm^{3/m}$)	uniform	150	600	Scale parameter for dielectric material
Geometric Random Variables				
TE (μm)	uniform	2	4	Electrode plate thickness
TD (μm)	uniform	4	12	Electrode layer thickness
B (μm)	uniform	70	300	Dielectric thickness of bottom cover layer
G (μm)	uniform	1876	2176	See figure 2
Thermal Load				
TSF (C)	uniform	600	850	Strain free temperature

Figure 8. *Variable examined that could affect residual stress field in the MLCC.*

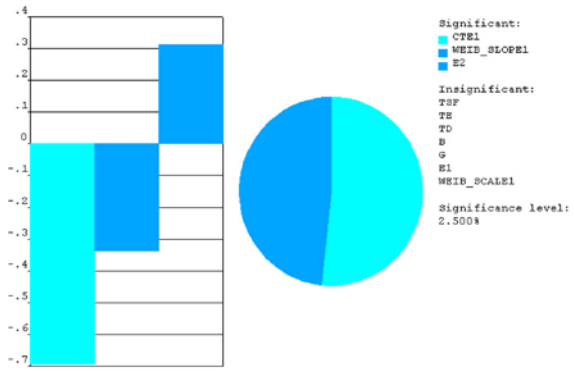

Figure 9. *CTE mismatch, Weibull modulus, and electrode elastic modulus had the largest effect on ceramic probability of failure.*

Conclusions

The PPOD dielectric film processed by SNL may not possess a sufficiently high strain-to-failure that would enable confident capacitor manufacture and tolerance to thermomechanically-induced operational stresses.

The ANL-processed ceramic capacitor system was very strain tolerant. Additional tests need to be performed as its thickness is increased because that tolerance will decrease with increasing thickness.

CTE mismatch, Weibull modulus, and electrode elastic modulus can have significant effects on the probability of failure in MLCCs.

Agreement 9237 - Graphite Foam for Cooling Power Electronics

Nidia C. Gallego
Oak Ridge National Laboratory
P.O. Box 2008, MS 6087, Bldg. 4508
Oak Ridge, TN 37831-6087
(865) 241-9459; fax: (865) 576-8424; e-mail: gallegonc@ornl.gov

Anthony G. Straatman
Department of Mechanical and Materials Engineering
University of Western Ontario
London, Canada

Brian E. Thompson and Qijun Yu
Foam Application Technologies, Inc.
Mayaguez, Puerto Rico

DOE Technology Manager: Jerry L. Gibbs
(202) 586-1182; fax: (202) 586-1600; e-mail: jerry.gibbs@ee.doe.gov
ORNL Technical Advisor: David P. Stinton
(865) 574-4556; fax: (865) 241-0411; e-mail: stintondp@ornl.gov

Contractor: Oak Ridge National Laboratory, Oak Ridge, Tennessee
Prime Contract No.: DE-AC05-00OR22725

Objective

- Collaborate with an automotive partner to develop an optimized heat exchanger/heat sink design that best utilizes the heat transfer properties of graphite foam to significantly reduce the size and weight of the thermal management system.

Approach

- Study fundamental mechanisms of heat transfer in graphite foam and develop an engineering model that can be used to design and/or evaluate optimized thermal management systems using graphite foam.
- Study the boiling heat transfer on the surface of graphite foam and evaluate the performance of graphite foams as a heat spreader in such a system.

Accomplishments

- Designed and built proof of concept thermal siphon utilizing high thermal conductivity graphite foam.
- Demonstrated that the cooling rates from a proof-of-concept thermal siphon that utilizes graphite foam elements are improved by about 20% over conventional thermal siphon.

Future Direction

- Design, build and evaluate the performance of a thermal siphon unit to be tested in an experimental HEV.

Introduction

Porous graphite foam developed at Oak Ridge National Laboratory (ORNL)[1,2] is being investigated as a material to improve both single-phase and multiphase heat transfer. Graphite foam has a high effective conductivity (40–160 W/m K) because of the high material conductivity of the graphite material (800–1900 W/m K). In comparison, similar porous aluminum foams have effective conductivities of 2–26 W/m K, resulting from material conductivities of only 140–237 W/m K (for various aluminum alloys).[3] The high effective conductivity of the porous graphite foam combined with the open, interconnected pore structure facilitates high internal heat transfer and the potential for high convective heat transfer enhancement. However, previous work at ORNL demonstrated that to fully exploit the benefits of high thermal conductivity graphite foam in thermal management applications it is necessary to access the internal surface area of the foam.

A combination of improved process and precursor has lead to foams with more open porosity that are currently being produced by Koppers. Our enhanced understanding of the thermal performance of new types of conductive graphite foam has led to innovative heat sink designs that capitalize on the properties of graphite foams.

Work performed in FY 2007 was carried out in collaboration with Thermal Centric and it was directed at designing, fabricating and testing a proof-of-concept thermal siphon that utilizes graphite foam elements to establish and quantify the benefits of graphite foam.

Experimental Set-up and Results

A proof-of concept thermal siphon was fabricated using high-thermal conductivity graphite foam for both the boiling and condensing surfaces. The experimental set up comprises of an air supply system, a power supply system and a test section instrumented to measure the air temperature and pressure, the air mass flow rate, the pressure drop across the graphite foam element on the air convection side, the vapor pressure and temperature, the copper heat spreader surface temperature and the case temperature of the CPU simulator and power applied (V, A) onto the heat sink made from graphite foam elements (Fig. 1).

The heat sinks made from graphite foam were used on both the air convection side and the evaporating side. The one for the air side consisted of graphite foam elements attached on the copper liner tubes that are glued onto the tube sheets of the top and bottom headers. The heat sink for the evaporating side consisted of a graphite foam block in contact with the inside top surface of the copper heat spreader. The copper heat spreader is in contact with the top surface of the CPU simulator (Fig. 2). Cold air is pumped by the air blower at a controlled flow rate and passes through the graphite foam elements. A photograph of the actual graphite foam-based thermal siphon is shown in Fig. 3

The refrigerant used was HFE 7000 from 3M, as recommended from preliminary experimental results from the University of Michigan. All air in the evaporating chamber was purged before testing. Tests were conducted to compare two different thicknesses of graphite foam coatings with boiling on a bare copper surface. First, a carbon foam element of 11 mm thickness was installed on the evaporating surface and tested under air-side conditions of natural convection and forced convection with different air flow rates and power inputs. Then, the graphite foam coating was replaced with an 8-mm thickness and tests were repeated. Finally, tests were repeated once more under the same thermal conditions but without graphite foam on the evaporating surface both with and without a heat sink made from Aluminum fins with copper liner tubes and heat spreader covering the heated surface.

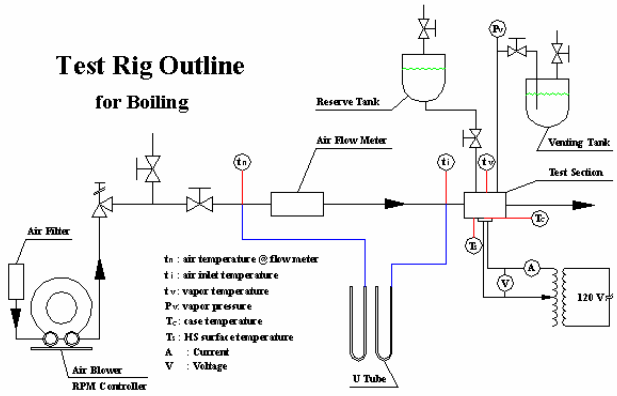

Figure 1. Test rig outline for boiling experiments

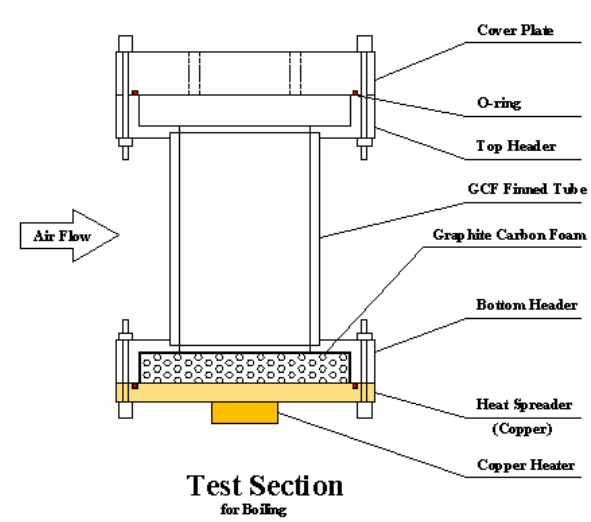

Figure 2. Schematic of test section

Figure 3. Instrumented thermal siphon with airside heat exchanger and boiling enhancements both made from high thermal conductivity graphite foam.

To evaluate the performance of the system, a thermal circuit model was developed to represent the heat path from the CPU to the cooling air through the thermal siphon. The various thermal resistances of the system were grouped into three quantities that can be measured experimentally:

R_s: the sum of the thermal interface resistance plus the heat spreader resistance

R_e: evaporating resistance in the interior surface of the graphite foam element

R_c: the sum of the condensation resistance on the inside wall surface of the liner tube, the conduction through the copper line tube wall and air convection in the foam element and on the outside baser surface of the liner tube.

The overall thermal resistance R_t, was obtained by: $R_t = R_s + R_e + R_c$

Initially tests were run using natural convection cooling on the air-side of the graphite foam element installed on the evaporating surface, and with boiling of HFE700 liquid at saturated conditions of 0 psig inside the thermal siphon. Results showed that utilizing high-thermal conductivity graphite foam enhances the evaporation rate. It was also found that the overall thermal resistances, R_t, corresponding to the 8 and 11 mm thickness foam elements were, respectively, about 80 and 70% of that of the bare surface alone.

Next tests were run with the air-side of the heat-exchanger exposed to forced air convection at flow rates of 10 and 17 cfm and varying values of heating power applied to the boiling element. In the case of the air flow rate of 10 cfm, the evaporating resistance, R_e, of the graphite foam heat sink with the 11 mm thick sample was about 23% of that of the bare surface, and this resulted in an overall thermal resistance, R_t, of about 80% of that of the bare surface. Similarly, for the case of airflow rate of 17 cfm, the evaporating resistance was about 44% of that of the bare surface, and the overall thermal was 87% of that of the bare surface.

Summary

Work in FY 2007 focused on designing, fabricating and testing a proof-of-concept thermal siphon that utilizes graphite foam elements and it was carried out in collaboration with Thermal Centric. Experimental results showed that cooling rates the graphite foam-based thermal siphon improved by about 20% over conventional thermal siphons. The next phase of the research will be directed at quantifying the performance of the thermal siphon in an experimental HEV engine.

References

1. W. J. Klett, R. Hardy, E. Romine, C. Walls, T. Burchell, "High-thermal-conductivity, Mesophase-pitch-derived Carbon Foam: Effect of Precursor on Structure and Properties," *Carbon* **38**, 953–973 (2000).
2. N. C. Gallego and W. J. Klett, "Carbon Foams for Thermal Management," *Carbon* **41**, 1461–1466 (2003).
3. W. J. Paek, H. B. Kang, Y. S. Kim, and M. J. Hyum, "Effective Thermal Conductivity and Permeability of Aluminum Foam Materials," *Int. J. of Thermophysics* **21**(2), 453–464 (2000).

Publications/Presentations

Publications

Straatman AG, Gallego NC, Yu Q, Thompson BE, "Characterization of porous carbon foam as a material for compact recuperators", Journal of Engineering for Gas Turbines and Power-Transactions of the ASME **129** (2): 326-330, 2007 .

Straatman AG, Gallego NC, Thompson BE, Hangan H "Thermal characterization of porous carbon foam - convection in parallel flow", International Journal of Heat and Mass Transfer **49** (11-12): 1991-1998, 2006.

Agreement 16307 - Modeling/Testing of Environmental Effects on Automotive PE Devices

A. A. Wereszczak
Ceramic Science and Technology Group
Oak Ridge National Laboratory
P.O. Box 2008, MS 6068, Bldg. 4515
Oak Ridge, TN 37831-6068
(865) 576-1169; fax: (865) 574-6098; e-mail: wereszczakaa@ornl.gov

DOE Technology Manager: Jerry L. Gibbs
(202) 586-1182; fax: (202) 586-1600; e-mail: Jerry.gibbs@ee.doe.gov

Contractor: Oak Ridge National Laboratory, Oak Ridge, Tennessee
Prime Contract No.: DE-AC05-00OR22725

Objectives

- Assess materials needs for automotive power electronics. This objective served as a kick-off effort because this project started in 3QFY07.

Approach

- Discuss materials limitations and needs with Principal Investigators of projects sponsored by FreedomCAR and Vehicle Technologies Automotive Power Electronics and Electrical Machines (APEEM) Program

Accomplishments

- Summarized materials issues of primary interest to APEEM Program. Results guide FY08 work.

Future Direction

- Determine effect of water ethylene glycol on mechanical strength of electrically insulating ceramics.
- Collaborate on APEEM Direct Cooling project and provide input on environmentally compatible ceramic material choices and structural design strategies.
- Model and interpret thermomechanical stress states of automotive power electronic devices in support of APEEM Program and, where applicable, recommend alterative material constituents that will lessen stresses.
- Develop alternative electrically insulating ceramics having high thermal conductivity and prospects for low-cost production.

Introduction

Research performed under the FreedomCAR and Vehicle Technologies Program's Vehicle Systems subprogram seeks to lessen technical and cost barriers and enable development that will benefit advanced vehicles such as hybrid fuel-cell-powered automobiles. Weight, volume, and cost targets for the power electronics and electrical machines subsystems of the traction drive system in those vehicles must be attained to achieve success. Research areas include more powerful novel traction motor designs, more efficient and higher temperature-capable inverter technologies, reduced footprint and weight of converters, more effective thermal control and packaging technologies, and motor/inverter concepts.

Many, if not most, technical barriers are directly linked to the contemporary material limitations of subcomponents found within devices that comprise inverters, converters, and motors. For automotive power electronic and electric machines (APEEM),

contemporary material limitations include the following:

- Insufficient temperature capability,
- Excessive thermal insulation,
- Excessive electrical insulation (i.e., generates excessive heat),
- Insufficient power density in permanent magnets, and
- Insufficient bandgap

Many of these issues are being already addressed in the Vehicle Systems APEEM Program, but there is interest in exploring additional means to overcome some of those materials limitations through the application of advanced materials science and engineering that are not currently being considered. Interviews with principal investigators (PIs) on the APEEM Program were conducted during the last quarter of FY07 to better understand what materials issues were encountered or studied on the APEEM Program and to identify where additional materials R&D could help.

Results

Discussions were held with the following individuals at the National Transportation Research Center (NTRC) during (mostly) one-on-one meetings: M. Olsweski, B. Ozpineci, L. Tang, G. -J. Su, M. Chinthavali, L. Tolbert, C. Ayers, L. Marlino, and J. Hsu. Additionally, based on advice from several of the interviewees, Professor F. Barlow of the University of Idaho was also interviewed.

The need for alternative higher-temperature-capable materials at reduced or sustained cost was the common theme in all discussions. While 250°C capability would be ideal, 200°C capability would be enabling. The national laboratories, universities, and perhaps industry are all well-suited to carry out the necessary R&D, but the somewhat uncompromising need for low cost sustenance means that industry collaboration is definitely required.

The use of parallel paths was advocated (1) to pursue the R&D of high temperature packaging that uses high band gap semiconductors (e.g., SiC), and (2) to develop improved cooling so that Si-semiconductors can continue to be used in the near-future.

Long-term reliability of alternative materials must be evaluated or known or they will not be considered seriously as candidates.

The summary of the all the discussions is broken down and combined by using power electronic and motor components as the subjects.

1. Power Electronics (PEs)

Inverters

Power modules. Near- and future-term cooling strategies are directing much of the PE work. Because 105°C cooling from water-ethylene glycol (WEG) is anticipated, the operating temperature (both ambient and junction) is expected to increase. Within power modules, higher temperature capability of the packaging, die, die attach, direct bonded copper (DBC) substrate, solder and wire bonds is needed. Specifically, solders and wire bonds are subjected to higher temperatures, so higher temperature alternatives are needed that can effectively bond to DBCs and the silicon semiconductor. AlN-DBC substrates are viewed as expensive, but they perform well. Lower-cost ceramic dielectric in the DBC with high thermal conductivity, high breakdown voltage, and thermal shock resistance between -40 and 200°C are of interest. It would be very desirable if wire bonding temperature capability could be increased by 25°C if it cannot be completely eliminated. Alternatives to (dielectric) sil-gel are desired to 200°C. Thermomechanical modeling of the stress state will be important for package optimization and improved reliability. That is because of sought higher service temperatures, the continued use of dissimilar materials (and CTE mismatch effects they produce), and the continued use of brittle silicon or silicon carbide and ceramic dielectrics that need probabilistic design to manage their service stresses.

Control circuitry and gate drivers. Higher temperature-capable resistors, capacitors, inductors, integrated circuits, printed circuit boards (PCB), and wires are needed.

Capacitors. Capacitors must be able to handle ripple currents to 200°C, benignly fail, and be inexpensive. Wound polymer-film and electrolytic capacitors are considered to be too large, so they would benefit from films having a higher dielectric

constant and higher temperature capability. They are desirable, however, because they benignly fail. It may be desirable to actively cool them to enable higher ambient temperature use. Ceramic capacitors may be the only alternative at high temperatures, but perceived lack of benign failure mechanism and high cost hinder its consideration. Cost of contemporary alternative capacitors is an order of magnitude too high. R&D would benefit greatly from direct industry involvement.

Hardware. More corrosion-resistant materials are needed for the bus bar, wiring, nuts, and bolts, or strategies need to be introduced to suppress corrosion-effects on existing hardware materials.

Converters

Transformers. There will be a need for higher-temperature-capable cores and wiring as temperature goes to 250°C.

Power modules, control circuitry, gate drivers, inductors, capacitors, and hardware. Same issues that affect them for inverters affect them for converters.

Thermal management

Strategies. Promoting minimum operating temperature of the semiconductors is directly related to the health of the over PE device. Some estimates indicate that reliability of the power electronics can be compromised by 10% for every 1°C. Choosing materials with high thermal conductivities within the PEs promotes more effective and rapid cooling. Engineered architectures can also promote more effective cooling, so a specific material choice is not necessarily the only option. If the efficiency and temperature capability of contemporary thermoelectric materials and devices could be increased, then it may be an option for cooling. Thermomechanical modeling is paramount.
Thermal interface materials (TIMs). Presently, a thermal conductivity (TC) of only ~3 W/mK has been achieved, so it limits the overall TC of many packages. TCs up to 20 W/mK would be a substantial improvement.
Coolants. More effective coolants are of interest. They must be chemically compatible with the materials comprising the heat exchanger containing them. For direct cooling, any coolants considered must have a high dielectric constant. The consideration of suspended particles in the cooling media may have merit.

2. Motors

Coils, core, and insulation. Need to have lower mass, volume, and be cheaper. However, smaller size means more rapid temperature changes, so materials must withstand thermal cycling.

Permanent magnets (PMs). Higher Curie temperature to 200°C needed, so bonded magnets may not be a candidate. A desire exists to be less reliant on foreign suppliers. Cheaper PMs needed. If motors are to be air-cooled, then PMs need to be corrosion-resistant.

Cores. Need better soft ferrites with higher saturation flux density and lower losses. Need to increase working temperature.

Conclusions

Both the engineering and the introduction of alternative higher-temperature-capable materials are required to enable higher-temperature-capable PE devices. Neither engineering nor the substitution of high temperature materials for contemporary used materials alone can accomplish this goal.

There is a need for alternative higher-temperature materials with reduced or sustained costs. When materials research or power electronics occurs, then collaboration with industry is necessary to increase the likelihood that cost minimization is an inherent priority in the research.

Parallel paths should continue (1) to pursue the R&D of high temperature packaging that uses high band gap semiconductors (e.g., SiC), and (2) to develop improved cooling so that Si-semiconductors can continue to be used in the near-future.

Long-term reliability of alternative materials must be known or established or they will not be considered seriously as candidates.

Project 18518 – Combustion System Materials

Agreement 11752 - Advanced Materials Development through Computational Design for HCCI Engine Applications

Vinod K. Sikka, G. (Murali) Muralidharan, and Rick Battiste
Materials Science and Technology Division
(865)574-5112: fax: (865) 574-4357; e-mail: sikkavk@ornl.gov

Bruce G. Bunting
Engineering Science and Technology Division
(865) 946-1512; fax: (865) 946-354; e-mail: buntingbg@ornl.gov

DOE Technology Manager: Jerry L. Gibbs
(202) 586-1182; fax: (202) 586-1600; e-mail: jerry.gibbs@ee.doe.gov
ORNL Technical Advisor: David P. Stinton
(865) 574-4556; fax: (865) 241-0411; e-mail: stintondp@ornl.gov

Contractor: Oak Ridge National Laboratory, Oak Ridge, Tennessee
Prime Contract No.: DE-AC05-00OR22725

Objectives

- Identify and catalog the materials operating conditions in homogeneous charge compression-ignition (HCCI) engines and use computational design concepts to develop advanced materials for such applications.
- Interact with designers of HCCI engines and manufacturers of components in order to identify the components that will be affected by the harsh operating conditions resulting from the HCCI design.

Approach

- Identify engine components, currently used materials, and current operating conditions and compare them with the expected component operating conditions for HCCI engines.
- Demonstrate the feasibility of the "materials-by-design" approach for the highest-priority item. Improve material performance for HCCI applications through computational modeling and experimental validation.

Accomplishments

- An initial database has been assembled on the high temperature fatigue properties at 870^{o}C of several Ni-based superalloys and an initial correlation with strengthening phase content has been established.
- Received currently used Ni-based valve alloy material for testing from a valve manufacturer and a commercial Ni-based alloy supplier to enable comparison with other alloys.
- Collaborated with University of Virginia in exploring the accuracy of thermodynamic predictions of phase equilibria in Al-based multicomponent alloys.
- Presented a paper on the application of computational design technique to designing Ni-based alloys at the DEER 2007 conference in Detroit, Michigan.

Future Direction

- Continue to communicate with automotive companies, valve manufacturers, Diesel Cross-Cut Team, FreedomCAR, and 21st Century Truck on the progress made through computational design.
- Initial correlations established between high temperature fatigue properties and microstructure of Nickel-based superalloys will be expanded and used to identify optimum microstructures for desired fatigue properties.

Introduction

There has been an increasing interest in HCCI combustion in recent years because of its potential to increase engine combustion efficiency and reduce emissions. However, the use of HCCI combustion will subject the engine components to significantly higher temperatures and pressures. The temperatures for diesel engines will reach over 1600°F, and pressure may reach > 2000 psi, which is approximately four times that of the normal combustion engine. Such severe engine operating conditions will require a significant improvement in materials performance in order to take advantage of the HCCI engine concept. This project deals with identifying materials requirements for HCCI engines for automotive and truck applications and the development of advanced, yet cost-effective, materials through computational design.

"Materials-by-design" is an Oak Ridge National Laboratory (ORNL) concept that encompasses a collection of materials-related techniques including modeling, correlation, and materials modification. The premise behind materials-by-design is that mechanical properties are correlated to microstructure and phase chemistry. The phase composition and microstructure can be achieved through thermodynamic equilibrium or through non-equilibrium techniques such as quenching, rapid casting solidification, or mechanical working. These characteristics can then be correlated to desired mechanical properties through equilibrium thermodynamics or through a variety of correlation techniques. The correlations allow untested compositions or treatments to be modeled so that desired trends can be rapidly established. Small heats of targeted materials can then be processed to confirm the modeled properties and to broaden the correlation data base.

Finally, there are several techniques, such as magnetic processing or low-temperature carburizing, that can be applied to allow further modification and optimization of desired properties. Materials-by-design is ideally suited to cast materials and heavily thermally processed materials (e.g., stainless steels, Ni alloys, cast irons, alloy steels, and brazed wrought aluminum alloys), and the concept has been successfully applied in such diverse areas as high-temperature furnace components, exhaust valves, exhaust manifolds, and tube fittings. Figure 1 and Table 1 provide an outline of the materials-by-design approach and a summary of the techniques that can be applied.

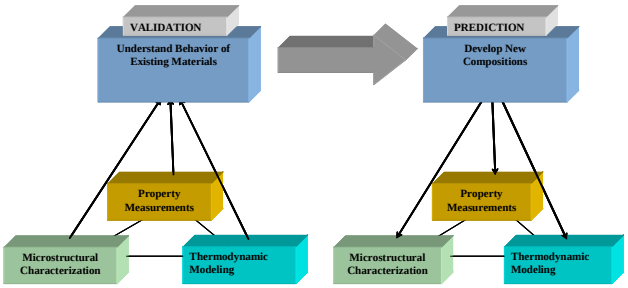

Figure 1. Overall approach for materials-by-design.

In our approach, we examined critical heavy-duty diesel engine materials and identified means to reduce their cost for acceptance in HCCI applications. This was accomplished through the following tasks:

Task 1. Identify critical material requirements for HCCI engines based on their operating conditions. This task will be accomplished through interactions with advanced engine and component designers. The interactions will include personal visits to six companies: Caterpillar, Cummins Engine, Deer, International Truck, Eaton Corp., and General Motors. Visits will be supplemented by a literature search, a review of advanced engine design studies, and follow-up discussions afterward. The key outcomes from this task will include (1) identifying operating conditions for advanced engine concepts, with a focus on the HCCI concept; (2) identifying components most affected by these operating conditions; (3) identifying currently used materials, new requirements, and performance targets; and (4) ranking the highest-priority items for study by the materials by design approach.

Task 2. Demonstrate the feasibility of materials-by-design approach for the highest-priority item. In this task, we will identify the details of the currently used material for the highest-priority item. Specifically, we will examine material compositions, processing methods, mechanical properties, corrosion properties, and cost.

Based on the available mechanical properties data, microstructural analysis, and thermodynamic phase stability calculations, we will identify the

Table 1. ORNL materials-by-design toolbox

Modeling	Experimentation	Characterization
Thermodynamic modeling of material properties vs alloy composition	Ultra-high-gauss magnetic stabilization of alloy steels	Advanced microscopy techniques
Neural-network modeling of diverse, nonlinear materials properties and process variations	Low-temperature gas carburization of finished components	X- ray and neutron scattering
Detailed microstructure based empirical modeling	Ability to produce small quantities of materials and fabricate them into test bars for property measurements and production of prototype components by a variety of methods, including sand and die casting, extrusion, forging and rolling	Surface and bulk property measuring techniques
Non-equilibrium modeling of solidified structures		
Extrapolation of properties from simple alloy systems to complex systems using interaction parameters		

underlying mechanism that delivers the current properties.

Task 3. Improve materials performance for HCCI application through computational modeling and experimental validation. In this task, we will use computational modeling (key basis for the material-by-design concept) to identify compositions that will deliver the desired phases for two purposes: (1) improving property performance and (2) finding alternatives to reduce cost for both current and improved performance. The outcome of the analysis will be validated through experimentation. The validation will be carried out in the following steps:

1. Prepare compositions identified based on computational design in 1-lb heats for microstructural analysis and very limited property determination; compare the results with output based on computational analysis for validation.
2. Scale up the validated composition into 20-lb to 100-lb heats and cast them into ingots for processing trials. In most cases, the material is expected to be used in the wrought condition. However, if it is to be used in the cast condition, we will save part of the ingots for analysis of as-cast properties.
3. Subject cast ingots to processing steps that are currently used by industry. Develop optimum processing and heat-treatment conditions to obtain the desired microstructure.
4. Carry out microstructural analysis and mechanical properties analysis on the material processed and heat-treated with optimum conditions.
5. Prepare prototype components for HCCI engine tests.

Extensive interaction with industrial partners will occur during all three tasks. This collaboration is expected to result in the rapid transfer of materials improvement from this project to industry for use in HCCI and other advanced engine concepts.

Results

Materials Development through Computational Design

Ni-based alloys have been identified as potential candidates for improved valve materials. There is particular interest in increasing the operating temperature of exhaust valves to about 1600°F (870°C). High temperature fatigue strength has been identified as a critical factor in determining the performance of these alloys in the valve application. An evaluation of the microstructure of various Ni-based alloys and correlation with limited information on the fatigue properties that are available show that the volume fraction of the γ' phase is likely to be a dominant factor in determining the performance of these alloys at high temperatures. Since the size of the strengthening precipitates is also critical, it is anticipated

that the kinetics of coarsening this phase would also be influential in the long-term performance of the alloys in this application. Based upon discussions with various users and suppliers, a range of Ni-based alloys with potentially varying weight fractions (or volume fractions) of γ' have been identified in efforts to correlate the fatigue properties with the microstructure of the alloys. Table 2 shows a summary of these alloys and the compositions of specific heats procured for this study. IN 751 is the alloy currently used, and it has been added to the matrix as a reference.

To obtain initial information on the microstructures of these alloys at equilibrium, thermodynamic calculations have been carried out using JMatPro V4 for all the alloys shown in Table 2. Comparison of the results of the calculations shows that all alloys have a matrix of γ with the major strengthening phase as γ'. One or more carbide phases such as $M_{23}C_6$, MC, and M_7C_3 may also be present in different alloys. The primary difference between the microstructures of the various alloys is in the weight percent of the γ' phase at a given temperature and the highest temperature at which the γ' phase is stable in the different alloys. Figure 2 shows a summary of the amount of γ' and carbide phases present in the down-selected alloys.

Mechanical Property Measurement

In order to develop relationships between the microstructures of the alloys and their mechanical properties high-temperature fatigue property data is being obtained as a part of the project. Table 3 shows a summary of aging treatments used for the alloys being tested. Load-controlled, fully reversed fatigue tests are being conducted *in-situ* at a temperature of 870°C. Stresses of 21.8 (150) Ksi (MPa), 29 (200 MPa), 39.9 (275 MPa), 43.5(300 MPa), 50.8(350 MPa), and 54.4(375 MPa)

Figure 3 shows a typical S-N (Stress vs. Number of Cycles to failure) observed in fatigue tests conducted on two different alloys, Udimet 720 and Waspaloy, at 870°C. The number of cycles to failure measured from tests on various alloys was then tabulated as a function of the calculated amounts of strengthening phases present in the alloys. Figure 4 shows a plot of the cycles to failure at two different stress levels 29 Ksi (200 MPa) and 39.9 Ksi (275 MPa) as a function of the calculated wt. % of γ' present in the alloys. Both curves show similar trends in that the cycles to failure increase as the amount of γ' increases. An exception is observed in Udimet 720 where the fatigue life does not seem to increase in proportion to the increase in γ' phase contents. Microstructural characterization is on-going in these alloys to understand other factors that may influence the observed trend. Particular emphasis will be placed on effect of grain size and the presence of carbides.

Table 2. Compositions of various alloys selected for studying the correlation between microstructure and mechanical properties

Alloy	C	Si	Mn	Al	Co	Cr	Cu	Fe	Mo	Nb	Ni	Ta	Ti	W	Zr
X750	0.03	0.09	0.08	0.68	0.04	15.7	0.08	8.03	–	0.86	Bal	0.01	2.56	–	–
Nimonic 80A	0.08	0.1	0.06	1.44	0.05	19.6	0.03	0.53	–	–	Bal	–	2.53	–	–
IN 751	0.03	0.09	0.08	1.2	0.04	15.7	0.08	8.03	–	0.86	Bal	0.01	2.56	–	–
Nimonic 90	0.07	0.18	0.07	1.4	16.1	19.4	0.04	0.51	0.09	0.02	Bal	–	2.4	–	0.07
Waspaloy	0.03	0.03	0.03	1.28	12.5	19.3	0.02	1.56	4.2	–	Bal	–	2.97	–	0.05
Rene 41	0.06	0.01	0.01	1.6	10.6	18.4	0.01	0.2	9.9	–	Bal	–	3.2	–	–
Udimet 520	0.04	0.05	0.01	2.0	11.7	18.6	0.01	0.59	6.35	–	Bal	–	3.0		
Udimet 720	0.01	0.01	0.01	2.5	14.8	15.9	0.01	0.12	3.0	0.01	Bal	–	5.14	1.23	0.03

Table 3. Summary of alloys and heat-treatment conditions used in the study	
Alloy	**Heat-treatment**
X750	2100°F/ 2 hr/ Air Cool, 1550°F/ 24 hr/ Air Cool, 1300°F/ 20 hr/ Air cool
Nimonic 80A	1292°F/16 hrs/ Air cool
Inconel 751	1600°F/4 hours/Air cool, 1350°F/4 hours/Air Cool.
Nimonic 90	1292°F/16 hrs/ Air cool
Waspaloy	1544°F/4 hrs/Air Cool, 1400°F/16 hrs/Air Cool
Udimet 41	1400°F/16 hrs/ Air cool
Udimet 520	2050°F/ 4 Hrs/Air cool, 1550°F/ 24 hrs/Air cool, 1400°F/16 hrs/Air cool 1500°F/8 hrs/ Air cool
Udimet 720	2012°F/4 Hrs/Furnace cool, 1202°F/4 hrs/ Air cool, 1400°F/16 hrs/ Air cool (As-received)

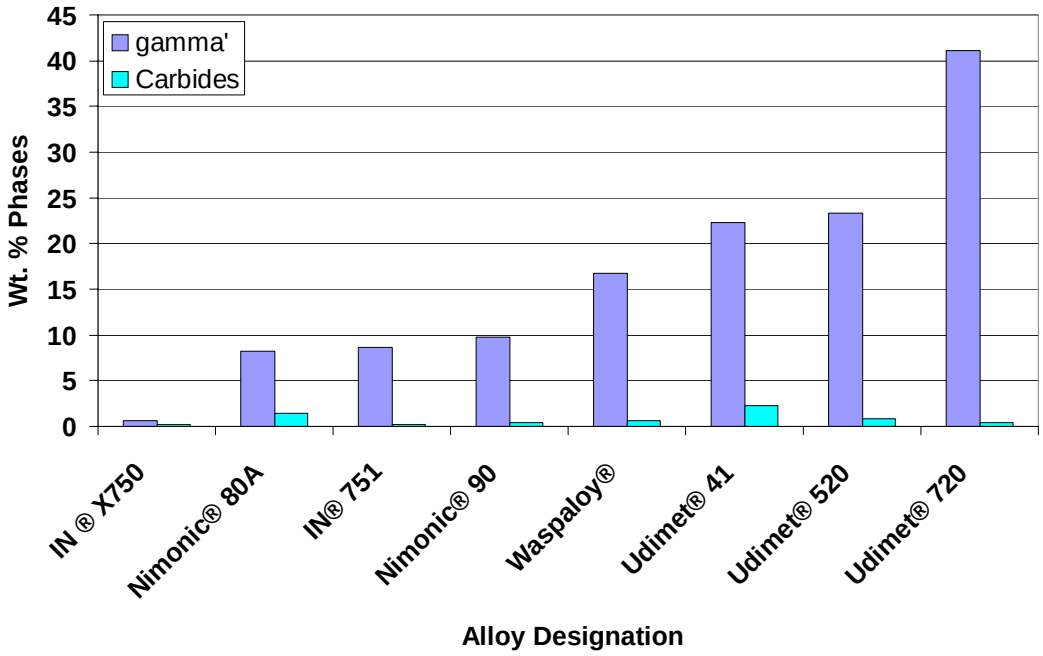

Figure 2. *Variation in wt. %of γ' and carbides at 870°C in the various alloys used in the study.*

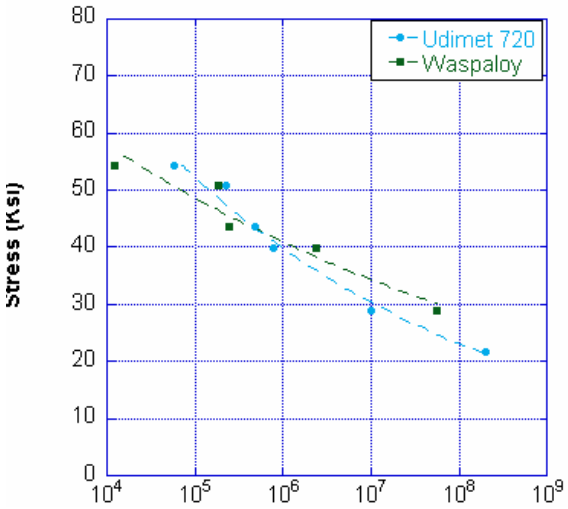

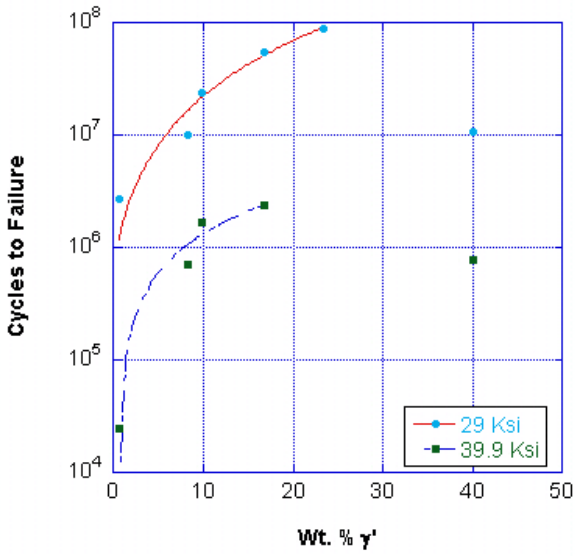

Figure 3. *Typical Stress vs. Number of Cycles to Failure (S-N) curve for Udimet 720 and Waspaloy at 870°C.*

Conclusions

- Much needed database of high temperature fatigue data for various Ni-based superalloys with emphasis on automotive valve. applications is currently being assembled.
- In general, for a given stress, the cycles to failure have been observed to increase with increase in γ' contents.
- Further microstructural characterization is ongoing to evaluate the role of carbides and other microstructural features in influencing this trend.
- The database will be used to identify required microstructural characteristics and corresponding alloy compositions for achieving optimum fatigue properties at temperatures of interest.

Publications/Presentations

G. Muralidharan, V. K. Sikka, Rick Battiste, and Bruce Bunting "Advanced Materials Development Through Computational Design," presented at the Diesel Engine-Efficiency and Emissions Research Conference 2007, Detroit, Michigan, Aug. 13- 16, 2007.

S. K. Eswaramoorthy, James M. Howe, and G. Muralidharan, "Determining the Nanoscale Chemistry and Behavior of Solid-Liquid Systems," Conditional Acceptance by Science (subject to acceptable revisions to manuscript).

Appendix A - Combustion Chamber Catalysts for HCCI

Bruce G. Bunting
Fuels, Engines, and Emissions Research Center

Homogeneous charge compression ignition engines depend on kinetic reactions of the fuel during the compression stroke for ignition. In order to achieve maximum thermodynamic efficiency, this ignition must take place at the correct place in the engine cycle (at or slightly before top dead center) and burning must be completed during the correct time interval. Motor fuels ignite in the range of about 700ºK to 1000ºK, depending on properties and chemistry. Diesel fuels ignite at the lower of these temperatures because of low temperature or cool flame chemistry most associated with normal paraffins. In-cylinder conditions must be set up to achieve the required ignition temperature at the desired timing, through a combination of compression ratio, intake air temperature, and amount of exhaust gas recirculation. In addition to achieving the correct ignition timing, burning rate must be moderated to achieve complete combustion while limiting the maximum rate of heat release and subsequent rate of pressure rise in the cylinder. The interplay between achieving ignition and controlling burning rate is one of the complex challenges of HCCI engines. Normally, it is achieved by combinations of EGR or dilution for slowing burning, fuel chemistry or properties, and a balance between compression ratio and intake temperature. It is very difficult to achieve this balance across the entire desired load/speed range of engine operation and research HCCI engines generally are incapable of running the complete set of operating conditions needed by modern applications.

It has been suggested that an in-cylinder coating or catalyst might help ignition or might help moderate burning rate through a combination of catalytic assist and adsorption / desorption of reactive fuel components or oxygen. In-cylinder temperatures during compression match light-off temperatures for diesel oxidation catalysts (i.e. 250 to 350ºC), and these catalysts commonly contain precious metals, such as platinum, to assist light-off, ceria to act as an oxygen storage/donor material, and high surface area alumina to support these catalytically active materials. In planning and setting up these experiments, the author consulted with people in the engine, substrate, and catalyst industries in order to determine the best experimental pathway to follow. It was decided to plan some simple experiments and then perform analysis and modeling of results if a favorable outcome was achieved, since no one was able to predict with certainty what results would be achieved.

The in-cylinder temperature and pressure conditions under firing conditions for the engine selected for these experiments are shown in Figures 1 and 2 respectively. This engine is an HCCI engine converted from a single cylinder 1D50Z diesel engine, single cylinder with 517 cc displacement. The conversion consisted of adding port fuel injection to create a homogeneous fuel charge, adding an intake air heater for control of combustion phasing, and lowering the compression ratio to 10.5 in order to allow the burning of a wide range of diesel and gasoline fuels.

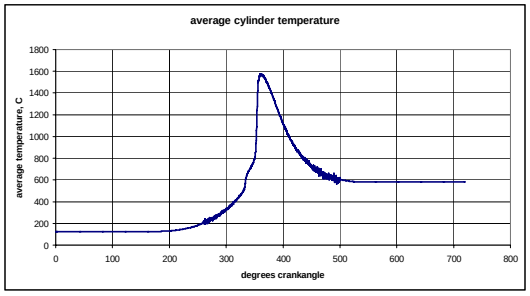

Figure 1. In-cylinder temperature conditions during HCCI combustion.

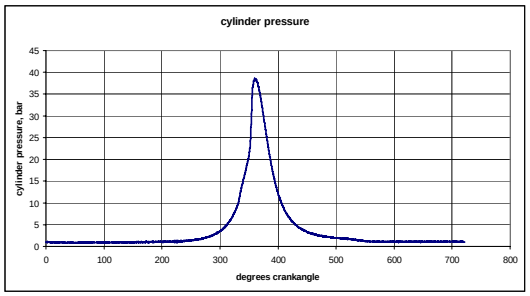

Figure 2. In-cylinder pressure conditions during HCCI combustion.

The engine piston was modified to accept a corrugated metal substrate obtained from Emitec of 50 mm diameter, 12 mm height, and 200 cpsi equivalent. This substrate was held in place by three screws. The assembly is shown in Figure 3.

These catalyst substrates were coated by Sud-Chemie in two formulations; the first contained alumina, ceria, and a high level of precious metal. The second configuration contained only alumina and ceria with no precious metal. These two formulations were chosen to provide different light-off temperatures for fuel and different levels of catalyst activity.

Figure 3. HCCI engine piston showing HCCI catalyst mounted in specially machined piston bowl.

After installing in the engine and reassembly, an attempt to run the engine was made. The catalyst was found to promote multi-stage combustion with properties varying based on intake temperature and resulting combustion phasing. At low intake temperatures, in the range of 50ºC, a small amount of very early heat release was observed with bulk quenching of the main heat release effect. Catalyst heat release occurred at about 20 degrees BTDC but temperatures remained too low to promote a main HCCI heat release. HC emissions were very high, indicating unburned fuel passing through the engine. CO was low, indicating a lack of overall combustion, and the engine produced no useful work. At medium intake temperature (100ºC), some main heat release became evident, combustion phasing remained about 20 degrees BTDC, HC emissions decreased, CO emissions increased, and the engine began to generate a small amount of

positive work. At high intake temperature (200ºC), the engine began to show very strong HCCI combustion with very early combustion phasing (40 degrees BTDC). This early phasing resulted in the engine showing negative work again. HC and CO emissions were low. Many combinations of intake temperature were run in an attempt to find an operating region where combustion was complete without phasing being too early. Overall, the engine was operated about 3.5 hours before strong internal noises began and the test was discontinued. Upon disassembly, it was found that the metal catalyst substrate had disintegrated, due to a combination of high temperatures and mechanical stresses. A picture of the failed piston crown catalyst is shown in Figure 4, which can be contrasted with Figure 3 to assess the high degree of damage.

Figure 4. HCCI engine piston shown after catalyst failure.

The catalyst substrate was removed from the piston and returned to Emitec for inspection. Their examination found that this application exceeded the maximum thermo-mechanical stress limit of the material, resulting in failure under the motion of the piston. In addition, regions of substrate melting were found, which requires temperatures above 1450ºC. Some evidence of high temperature corrosion was also found. A probable sequence of failure might include the build up of raw fuel in the substrate and piston crown, followed by light-off and uncontrolled burning, resulting in catalyst substrate failure. It appears that the catalyst promoted some very early heat release but served to quench the bulk burning reactions unless intake temperature was set high enough for complete burning. Unfortunately, this complete burning occurred during early in the compression stroke, did not lead to useful work output, and generated high enough temperatures to cause catalyst failure.

After engine rebuilding, and a period of about 6 months to conduct research in other areas with the engine, this test was repeated with the non-platinum formulation of the catalyst and using n-heptane for fuel. It was hoped that the non-platinum formulation would be less aggressive with the early heat release and allow closer matching of burning to the desired timing for the engine. It was also hoped that the n-heptane fuel, being more volatile, would be less likely to build up in the catalyst and piston bowl area. Unfortunately, results were substantially similar and the catalyst again failed after about 4 hours.

This research path has been discontinued. What we learned was that a catalyst can indeed affect in-cylinder processes. In this case, the catalyst promoted early heat release, quenched the main heat

release, and allowed build up of fuel in the piston bowl area, leading to eventual failure. No further work will be done in this area unless subsequent reviews suggest a way to solve these problems and better match the catalyst characteristics to the needs of the combustion process. One possible change which will be discussed is the use of only a thin catalytic coating on the piston crown and cylinder head. This coating may provide some slight ignition assist, but mainly may reduce combustion quenching at the chamber walls. In HCCI engines, this quenching occurs and results in high HC and CO emissions.

Agreement 8697 - Electrochemical NO_x Sensor for Monitoring Diesel Emissions

Leta Y. Woo, L. Peter Martin, and Robert S. Glass
Lawrence Livermore National Laboratory
P.O. Box 808, L-367
Livermore, CA 94551-9900
(925) 423-7140; fax: (925) 423-7914; e-mail: glass3@llnl.gov

DOE Technology Manager: Jerry L. Gibbs
(202) 586-1182; fax: (202) 586-1600; e-mail: jerry.gibbs@ee.doe.gov

Contractor: Lawrence Livermore National Laboratory, Livermore, California
Prime Contract No.: W-7405-Eng-48

Objectives

- Develop a compact, rapid-response electrochemical nitrogen oxide (NO) or total nitrogen oxides (NO_x) sensor for compression-ignition, direct-injection (CIDI) exhaust gas monitoring
- Explore and characterize novel, effective sensing methodologies based on impedance measurements
- Collaborate with the Ford Research Center to optimize sensor materials, operating parameters, and performance
- Characterize aging mechanisms and the effects on long-term performance of candidate sensor materials

Approach

- Use an ionic (O^{2-}) conducting ceramic as a solid electrolyte and metal or metal-oxide electrodes
- Apply sinusoidal voltage between a working and counter electrode and measure impedance or phase angle shifts to correlate with NO_x concentration
- Evaluate sensing mechanism using electrochemical techniques
- Work with Ford to evaluate sensor performance in dynamometer and vehicle tests and develop a sensor platform that can be used for a pre-commercial prototype

Accomplishments

- Characterized sensing mechanisms responsible for impedancemetric NO_x sensing
- Successfully performed both engine and vehicle dynamometer testing on prototype sensors at Ford facilities
- Evaluated preliminary accuracy limits and temperature dependence
- Awarded U.S. patent, published two conference proceedings and two journal articles (one additional journal article has been accepted), and presented four talks at conferences

Future Direction

- Continue to explore sensing mechanism and apply findings to optimization of the sensing strategy
- Evaluate cross-sensitivity to other species present in exhaust gas and perform dynamometer testing
- Demonstrate the commercialization potential of the impedance-based sensor methodology
- Transfer the technology to a commercial entity

Introduction

Increasingly stringent emissions regulations will require the development of advanced gas sensors for a variety of applications. For example, compact, inexpensive sensors are needed for detection of regulated pollutants, including hydrocarbons (HCs), CO, and NO_x, in automotive exhaust. Of particular importance will be a sensor for NO_x to ensure the proper operation of the catalyst system in the next generation of diesel (CIDI) automobiles.

Because many emerging applications, particularly monitoring of automotive exhaust, involve operation in harsh environments that include high temperatures and corrosive or chemically reactive conditions, ceramic-oxide–based electrochemical sensors are of considerable interest. Sensors using yttria-stabilized zirconia (YSZ) as an oxygen-ion-conducting electrolyte have been widely reported for both amperometric and potentiometric modes of operation.[1,2] These include the well-known exhaust gas oxygen (EGO) sensor.

Recently, an ac impedance-based (i.e., impedancemetric) sensing technique using YSZ has been reported for sensing water vapor, hydrocarbons, CO, and NO_x.[3-6] A typically small-amplitude alternating signal is applied, and the sensor response is measured at a specified frequency. Previous impedancemetric techniques have used the modulus (or magnitude) at low frequencies (< 1 Hz) as the sensing signal and attribute the measured response to interfacial phenomena.[3-5] More recent work by our group has also investigated using phase angle as the sensing signal at somewhat higher frequencies (10 Hz).[6,7] The higher frequency measurements would potentially allow for reduced sampling times during sensor operation.

Another potential advantage of impedancemetric NO_x sensing is the similarity in response to NO and NO_2 (i.e., total-NO_x sensing).[3,4,6,7] Potentiometric NO_x sensors typically show higher sensitivity to NO_2 than NO, and responses that are opposite in sign. However, NO is more stable than NO_2 at temperatures > 600°C, and thermodynamic calculations predict ~90% NO, balance NO_2.[8] Since automotive exhaust sensors will probably be required to operate at temperatures > 600°C, NO is the dominant component in thermodynamic equilibrium and the target NO_x species. Also, the use of upstream catalysts could further promote the conversion of NO_x species to NO. Therefore, the focus of current work is to investigate the response to NO.

Mitigating the effect of interfering gases (e.g., O_2, water vapor, HCs, etc.) is also necessary for sensor operation. This is an area of current study. For impedancemetric NO_x sensors, our previous work has demonstrated that the cross-sensitivity to O_2 may be accounted for by comparing measurements at multiple frequencies.[6] We have recently begun to evaluate cross-sensitivity to a variety of other species in automotive dynamometer testing. These results will be published in a separate study.

Previously, we reported the impedance response of a symmetric Au/YSZ/Au cell to O_2 and NO_x.[7] The cell had a symmetric, in-plane geometry consisting of a dense YSZ electrolyte and two planar Au plates, with a porous YSZ layer separating the Au and dense YSZ. Both electrodes were co-located on the same side of the dense electrolyte pellet and exposed to the same gaseous environment (i.e., no reference gas). Constant spring-loaded pressure was used to maintain contact between cell components. For real-world sensor applications, spring-loaded devices are obviously not practical.

To further understand the impedancemetric NO_x sensing mechanism and incorporate a sensor design that does not require spring-loaded pressure, current work has focused on the role of the dense Au electrode. The sensing behavior of symmetric samples consisting of a porous rectangular slab of YSZ with two metal wire loop electrodes (i.e., no dense YSZ present) is investigated. The impedance response of Au electrodes in different gas concentrations is compared with the impedance response of Ag and Pt electrodes. The role of microstructure is also investigated by comparing the impedance response of dense and porous Au. Preliminary sensor performance is also presented.

Experimental

Rectangular slabs of porous YSZ were fabricated using a slurry of YSZ powder and graphite pore formers. The slabs were sintered at 1550°C and had pore sizes between 1 to 2 μm, as shown in the SEM picture in Fig. 1a. Symmetric electrodes consisted of two tightly wrapped Au, Ag, or Pt wire loops wound around the long axis of the rectangular slab, as shown in Fig. 2a. Additional YSZ slurry was applied on the wires and fired at 1000°C and is shown in the SEM picture in Fig. 1b.

To elucidate the role of the Au electrode, another electrode configuration was also investigated using symmetrical thin Au plates pressed against

either side of the porous YSZ slab, as shown in Fig. 2b, with and without a layer of Au paste between the Au plate and porous YSZ.

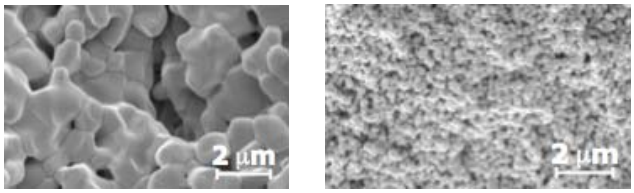

(a) (b)

Figure 1. SEM pictures of (a) rectangular porous YSZ slab and (b) fired YSZ slurry on top of wires.

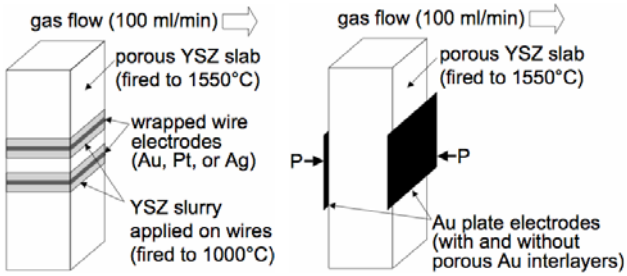

(a) (b)

Figure 2. Schematic of (a) wire setup to investigate composition (Au, Pt, and Ag) and (b) plate setup to investigate microstructure (dense and porous Au)

Gas sensing experiments were performed in a quartz tube placed inside a tube furnace with both electrodes exposed to the same environment. Gas composition was controlled by mixing air, N_2, and 1000 ppm NO using a standard gas handling system equipped with thermal mass flow controllers. Electrochemical measurements were performed using a Solartron 1260 Impedance Analyzer with the Solartron 1287 Electrochemical Interface.

The microstructure of the rectangular porous YSZ slabs, with pore sizes between 1 to 2 μm, allowed sufficiently rapid gas phase diffusion to prevent differential gas concentrations at the two electrodes in the current testing configuration. The sensor did not respond to changes in gas flow rate and only depended on reactions at the two electrodes.

Results

For gas concentrations containing both O_2 and NO_x, the following redox reactions may occur:

$$\frac{1}{2}O_2 + 2e^- \Leftrightarrow O^{2-}$$
$$NO_2 + 2e^- \Leftrightarrow NO + O^{2-} \quad (1)$$

We have proposed parallel contributions from the O_2 and NO_x reactions to the measured impedance in the Au/YSZ/Au system in previous work.[7] For gas mixtures containing 100 ppm or less of NO_x and 2-18.9% O_2, based upon the relative concentrations alone, the contribution of the O_2 reaction to the measured impedance would be expected to be much greater than the NO_x reaction. However, the relative rate constants for the two reactions also comes into play in determining the sensitivity to both gases. If the rate constant is much higher for the NO_x reaction, then it can be measured in the presence of a much larger concentration of O_2. In any case, O_2 is the most important interferent gas that must be accounted for. Therefore, it is important to understand response of the sensor to O_2 as a function of materials and design. This study constituted a large part of our work this FY.

Electrochemical redox reactions involve a complex series of steps (e.g., adsorption of gas species, transport along surfaces, electron transfer, diffusion of products away from reaction sites, etc.). In the current work, changes in the rate-limiting step for the O_2 reaction, accomplished by altering the electrode composition or microstructure, are shown to affect the ability to detect NO. This is a direct consequence of the parallel contributions of the O_2 and NO_x reactions to the measured impedance, where the contribution of the O_2 reaction affects the relative influence of the NO_x reaction.

A commonly used method to investigate the rate-limiting step is measuring the electrode resistance R_{el} over a range of O_2 partial pressures (P_{O2}):

$$R_{el} \propto P_{O2}^{\beta} \quad (2)$$

where the value of β is used to characterize the type of species involved and the corresponding elementary reaction step that could be rate-limiting.

Figure 3 shows the Nyquist behavior of the porous YSZ slab with wrapped Au wires at 650°C in 10.5% O_2, 10.5% O_2 + 100 ppm NO, and 18.9% O_2. Numbers corresponding to darkened points represent log of frequency in Hz. Two frequency ranges of impedance behavior are clearly evident, separated by

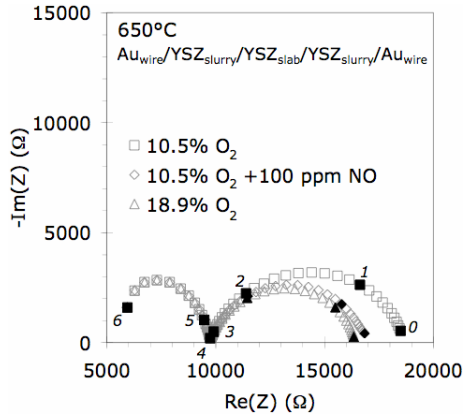

Figure 3. Nyquist plot of Au/YSZ/Au cell at 650°C in 10.5% O_2, 10.5% O_2 + 100 ppm NO, and 18.9% O_2.

a distinct cusp. The addition of either NO or increasing O_2 concentration causes similar changes in the low-frequency behavior (< 1 kHz), while the high-frequency behavior (> 1kHz) remains unaffected.

The change in concentration for NO (0 to 100 ppm) is about three orders of magnitude smaller than the change in O_2 concentration from 10.5% to18.9%, but both result in similar reductions in impedance. Therefore, the changes in the low-frequency behavior, associated with the electrode and electrode/electrolyte interface, are much more sensitive to NO than O_2.

The high-frequency behavior does not change with gas concentration and represents ohmic contributions (from leads, etc.) and resistance contributions from the ionic conduction in YSZ and related phenomena such as current constriction.

To determine the O_2 dependence of the electrode resistance (R_{el}) and possible rate-limiting mechanisms (see Eq. 2), equivalent circuit analysis was used to model the measured impedance behavior in the low-frequency range (< 1 kHz).

We have previously measured the P_{O2} dependence of a symmetric Au/YSZ/Au planar cell and shown that R_{el} scaled with $\beta = -0.62$.[7] A P_{O2} dependence with $\beta = -0.5$ has been suggested when dissociative adsorption of oxygen or transport of atomic oxygen to the electrochemical reaction site are the rate-limiting steps.[9-11] In the porous YSZ slab with wrapped Au wires, we measured $\beta = -0.37$ over a concentration range of 2-18.9% O_2, which is similar to the ideal $\beta = -0.5$ behavior, but only allows a tentative conclusion to be made about the rate-determining step. In the work described following we have compared the differences in NO sensitivity and P_{O2} dependence of the Au wire loop electrode in to that of other electrode materials (Pt and Ag), and sensor structures incorporating a porous Au interlayer between the substrate (YSZ) and Au electrode.

Comparison of the behavior of Au-, Pt-, and Ag-wire wrapped porous YSZ cells shows that only Au-wire electrodes demonstrate sensitivity to NO. For the case of Ag, the large thermal expansion mismatch with YSZ damages the interface during processing and causes only the high-frequency behavior to be discerned, which does not vary with O_2 or NO concentration. For Au and Pt, a closer thermal expansion match with YSZ (see Table 1) allows the values of the electrode resistance at lower frequencies to be examined separately from the higher frequency behavior.

Table 1. Linear thermal expansion coefficients (α) for YSZ[12] and metal electrodes at 25°C.[13]

Composition	$\alpha \times 10^6$ (K^{-1})
YSZ	~10.5
Au	14.2
Pt	8.8
Ag	18.9

The O_2 dependence of the Au-wire electrodes ($\beta = -0.37$) differs significantly from the behavior of the Pt-wire electrode, indicating a difference in the rate-limiting step. Over a concentration range of 7-18.9% O_2, we measured $\beta = 0.17$ for the Pt-wire electrode resistance. Further decreases in O_2 concentrations (from 7 to 2% O_2) seem to suggest a change in β to negative values. The complex behavior of the Pt-wire cell with two apparently different power-law exponents at lower and higher O_2 concentrations seems to agree with previous work where charge transfer at the triple phase boundary is the rate-determining step.[9]

A possible explanation for the difference in behavior for Au- and Pt- wire electrodes is the relative catalytic activity for the O_2 reduction reaction. Au is a poor catalyst compared to Pt, which is known to be a very effective O_2 reduction catalyst. More work is needed to clarify the mechanisms involved and the role of the O_2 reduction catalytic activity of the electrode material. Nevertheless, based on parallel contributions from O_2 and NO_x reactions to the total measured impedance, increasing the contribution of the O_2 reaction relative to the NO_x reaction would then decrease the influence of the NO_x reaction path, i.e., reduce NO_x sensitivity.

For Pt, the high O_2 catalytic activity may be responsible for the different rate-limiting step compared to Au and also for an increase in the contribution from the O_2 reaction compared to NO_x. Similarly, the Ag electrode, due to the high solubility and mobility of O_2 within the Ag bulk, may also cause an increase in the contribution of the O_2 reaction relative to NO_x. Differences in the rate-limiting step for the O_2 reaction, and its effect on the ratio between the contributions of O_2 and NO_x reactions to the total measured impedance, seems to be an important factor in determining the sensitivity to NO.

The role of the Au electrode microstructure was investigated using a symmetric cell consisting of the porous YSZ slab in contact with two dense Au plates, with and without a porous Au interlayer between the Au plate and porous YSZ (Fig. 2b). The sample without the porous Au interlayer demonstrated sensitivity to 100 ppm NO and is analogous to the behavior of the dense Au-wire electrode albeit with different contact areas. When present, the porous Au interlayer served to increase the electrode/electrolyte interfacial contact area and the amount of electrode surface area compared to the dense Au-wire electrodes. However, unlike the dense Au electrode, the cell with porous Au was insensitive to 100 ppm NO.

Over a concentration range of 2-18.9% O_2, we measured $\beta = -0.13$ for the porous-Au cell. As discussed with the Pt-wire electrode, β ranging from -1/4 to 1/4 have been attributed to charge transfer at the triple phase boundary as the rate-determining step. The O_2 dependences of the cells with either porous-Au or dense Pt-wire electrodes seem to suggest the same rate-limiting step.

The rate-limiting mechanism for the O_2 reaction may provide information about the relative contributions of O_2 and NO reactions to the measured impedance and the resulting NO sensitivity. Modification of the electrode surface microstructure by increasing the surface area relative to the triple phase boundary (i.e., porous Au vs. dense Au) seems to alter the rate-limiting mechanism for the O_2 reaction, indicating an increase in the relative contribution of the O_2 reaction compared to NO and the inability to sense NO.

Sensor Response to NO

Figure 4 shows the sensing behavior for the Au-wire wrapped sensor (see Fig. 2a) at 650°C and 2% O_2 over a range of NO concentrations from 5 to 50 ppm. The impedancemetric sensing signal is the phase angle measured at 10 Hz using 25 mV excitation, and demonstrates sensitivity down to 5 ppm NO.

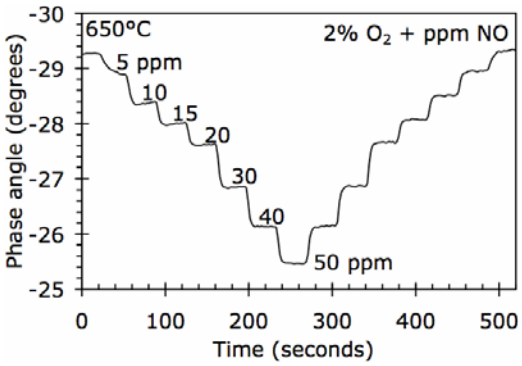

Figure 4. Impedancemetric sensing behavior of Au-wire wrapped porous YSZ slab using the phase angle response at 10 Hz as the sensing signal.

Dynamometer Testing

Preliminary engine and vehicle dynamometer testing of prototype sensors fabricated at LLNL have been performed at Ford Research Center. Initial results indicate the sensitivity of the sensor in the actual exhaust stream from an operational diesel engine and vehicle. However, due to the simultaneous changes of NO_x concentration with other interfering gases (e.g., hydrocarbons and ammonia) and temperature, only tentative conclusions can be made concerning the efficacy of the sensor. Further refinements in the dynamometer testing procedure and setup are necessary to produce more conclusive results about the sensor capabilities. Nevertheless, the sensor was successfully tested in actual engine exhaust and the preliminary results are invaluable in guiding sensor development.

Conclusions

For impedancemetric NO sensors based on YSZ-electrolyte, both the electrode composition and microstructure alter the sensitivity. Only dense Au electrodes exhibit sensitivity to NO, while other compositions for dense wire electrodes (Pt and Ag) and porous Au electrodes do not respond to changes in NO concentration. The NO sensitivity seems to be related to the rate-determining step for the O_2 reaction. The importance of the O_2 reaction cannot be neglected because of its overwhelming relative concentration. However, for parallel contributions from the NO_x and O_2 reactions the relative rate constants

also factors into the relative contributions to the overall measured impedance.

Both dense Pt wire and porous Au electrodes show impedance behavior consistent with charge transfer at the triple phase boundary as the rate-limiting step for the O_2 reaction. Dense Au electrodes show impedance behavior consistent with either adsorption or diffusion as the rate-limiting step for the O_2 reaction. The results suggest that a rate-limiting step for the O_2 reaction occurring away from the triple phase boundary may be important for impedancemetric NO sensing.

References

1. F. Menil, V. Coillard, and C. Lucat, *Sensors and Actuators B* **67**, 1 (2000).
2. W. Göpel, G. Reinhardt and M. Rösch, *Solid State Ionics* **136–137**, 519 (2000).
3. N. Miura, M. Nakatou and S. Zhuiykov, *Ceram. Int.*, **30**, 1135 (2004).
4. N. Miura, M. Nakatou and S. Zhuiykov, *Sensors and Actuators B* **93**, 221 (2003).
5. N. Wu, Z. Chen, J. Xu, M. Chyu and S. X. Mao, *Sensors and Actuators B* **110**, 49 (2005).
6. L. P. Martin, L. Y. Woo, and R. S. Glass, *J. Electrochem. Soc.*, **154**, J97 (2007).
7. L. Y. Woo, L. P. Martin, R. S. Glass, and R. J. Gorte *J. Electrochem. Soc.*, **154**, J129 (2007).
8. J. Yoo, F. M. Van Assche, and E. D. Wachsman, *J. Electrochem. Soc.*, **153**, H115 (2006).
9. Y. Takeda, R. Kanno, M. Noda, Y. Tomida, and O. Yamamoto, *J. Electrochem. Soc.*, **134**, 2656 (1987).
10. H. Fukunaga, M. Koyama, N. Takahashi, C. Wen, an K. Yamada, *Solid State Ionics*, **132**, 279 (2000).
11. M. Koyama, C. Wen, T. Masuyama, J. Otomo, H. Fukunaga, K. Yamada, K. Euguchi, and H. Takahashi, *J. Electrochem. Soc.*, **148**, A795 (2001).
12. N. Q. Minh, *J. Am. Ceram. Soc.*, **76**, 563 (1993).
13. "Thermal and Physical Properties of Pure Metals", in *CRC Handbook of Chemistry and Physics, Internet Version 2007, (87th Edition)*, David R. Lide, ed., Taylor and Francis, Boca Raton, FL.

Publications/Presentations

"Effect of electrode composition and microstructure on impedancemetric nitric oxide sensors based on YSZ electrolyte," accepted by *J. Electrochem. Soc.*, (2007).

"Impedance Characterization of a Model Au/Yttria-stabilized Zirconia (YSZ)/Au Electrochemical Cell in Varying Oxygen and NO_x Concentrations," *J. Electrochem. Soc.*, **154**(4):J129–J135, (2007).

"Impedancemetric NO_x Sensing Using YSZ Electrolyte and YSZ/Cr_2O_3 Composite Electrodes," submitted to *J. Electrochem. Soc.*, **154**(3):J97–J104, (2007).

Presentations made at the 211th Electrochemical Society Meeting, May 6 - 11, 2007 in Chicago, IL: "Investigating the Stability and Accuracy of the Phase Response for NO_x Sensing 5% Mg-modified $LaCrO_3$" and "Role of Electrode Composition and Microstructure in a YSZ-Based Impedancemetric NO_x Sensor."

U.S. Patent 7,153,401 B2 entitled "Current biased potentiometric NO_x sensor for vehicle emissions," by L.P. Martin and A.Q. Pham was awarded December 26, 2006.

Presentations/published conference proceedings from the Fall Meeting of the Materials Research Society, Nov. 27 – Dec. 1, 2006 in Boston, MA: "Impedancemetric Technique for NO_x Sensing Using a YSZ-Based Electrochemical Cell," and "Impedance Analysis of Electrochemical NO_x Sensor Using a Au/Yttria-Stabilized Zirconia (YSZ)/Au cell."

Agreement 9440 - Fabrication of Micro-orifices for Diesel Fuel Injectors

George R. Fenske
Argonne National Laboratory
9700 South Cass Avenue
Argonne, IL 60439
(630)252-5190; fax (630)252-4798; e-mail: gfenske@anl.gov

DOE Technology Development Manager: Jerry Gibbs
(202) 586-1182; fax: (202) 586-1600; e-mail: jerry.gibbs@ee.doe.gov

Contractor: Argonne National Laboratory, Argonne, Illinois
Prime Contract No.: W-31-109-Eng-38

Objectives

- Develop a methodology for reducing the diameters of fuel injector orifices to 50 μm by applying material to the internal diameter (ID) of the orifice. Micro-orifices should improve fuel distribution, increase efficiency, and reduce emissions in compression-ignition, direct-injection (CIDI) engines.
- Characterize the spray and combustion properties of the fuel injector system coated with electroless nickel (EN) and other advanced ID coating processes.
- Transfer the developed technology to DOE industrial partners.

Approach

- Evaluate the potential of EN plating for improving the surface finish and reducing deposit formation on injector nozzles.
- Evaluate the potential of vapor deposition processes to form uniform nickel (Ni) coatings.
- Evaluate the potential of laser micro-drilling processes to form uniform orifices in high length-to-diameter configurations.

Accomplishments

- Devised a new approach for preparing test nozzles in concert with the U.S. Environmental Protection Agency–National Vehicle and Fuel Emissions Laboratory (EPA-NVFEL). Also initiated collaboration with a major fuel injector manufacturer for further engine testing of plated nozzles for deposit mitigation.
- In concert with Imagineering, Inc., a commercial plating company, developed a method for improving the surface finish of commercial-scale plated nozzles.
- Developed an X-ray phase contrast imaging technique for nondestructive examination of thin EN coatings applied to the interiors of diesel injectors.
- In collaboration with Weber Manufacturing, demonstrated the feasibility of a nickel vapor deposition process to deposit thick nickel coatings on commercial fuel injectors.
- In collaboration with the U.S.-EPA, characterized the spray characteristics of EN-coated commercial nozzles.

Future Direction

- Characterize spray characteristics of coated injectors in collaboration with Argonne National Laboratory–Energy Systems (ANL–ES) and ANL–Advanced Photon Source (ANL–APS).
- Provide coated injector tips to EPA-NVFEL personnel for spray characterization and combustion tests.
- Apply advanced characterization methods for detailed examination of surface chemistry during deposit formation, particularly extended X-ray absorption fine structure.
- Characterize the uniformity and properties of laser processed micro-orifices and adjacent heat-affected zones.

Introduction

In 2007, EPA regulations mandate reduction in diesel engine emissions to 0.01 grams of particulate matter (PM) per engine horsepower per hour and 0.2 grams of nitrogen oxides (NO_x) per engine horsepower per hour. Further reductions are expected for 2010. To achieve these levels, CIDI engines are being redesigned to reduce in-cylinder soot production. One design change under consideration is the reduction of the diameter for the fuel injector orifice.

Pickett and coworkers[1,2] demonstrated significant reductions of soot in a test cylinder using experimental injectors with orifice diameters of 50 μm, even with high levels of exhaust gas recirculation and concomitant reduction in NO_x emissions. NVFEL researchers have observed reduced PM emissions from a light-duty diesel engine equipped with 75-μm-diam injector orifices. These reductions arise from increases in fuel atomization efficiency, leading to more complete combustion.[3] Although it is currently possible to economically mass-produce injectors with 100-μm-diam orifices by using electrodischarge machining, further reductions in hole size are accompanied by unacceptable fabrication error rates.

Reducing the orifice diameter (e.g., from 150 to 50 μm) carries with it a number of penalties, however. It will lead to a reduction in the amount of fuel that can be delivered to the combustion chamber without increasing the number of spray holes, the injection pressure, and/or the discharge coefficient. The potential impact of coking on smaller orifices is also much greater, as smaller holes will be more readily blocked by coking deposits on the injector tip and in the spray holes themselves. Coking deposits are a particular problem with tapered-orifice nozzles, another technique for increasing fuel atomization and thus reducing PM emissions.

Another issue is alternative fuels. One method to minimize dependence on foreign oil is the increased use of bioderived fuels such as vegetable oil esters. Because of the presence of carbon-carbon double bonds in the carboxylic acid chain precursors, these fuels readily form coking deposits in the combustion chamber—a major problem in concert with smaller spray holes. Other alternative fuels include alcohols such as methanol or ethanol. These are not typically used neat but are blended with conventional diesel fuel. One emissions reduction strategy is to inject an ethanol/water mixture along with conventional fuel, reducing the combustion temperature and NO_x emissions. However, alcohol partial oxidation products can include corrosive carboxylic acids, which will damage the steel nozzles over time. In concert with more commonly used fabrication techniques, EN plating has been used to prepare fuel injector nozzles with orifice diameters as small as 50 μm. EN plating also promises to mitigate or solve all of the difficulties described above. The plated surface is corrosion-resistant and smoother, and the discharge coefficient of the plated orifices is higher. This method can be used to deposit a wide variety of alloys, offering the possibility of tailoring surface chemistry to reduce or eliminate deposit formation.

Advances in the development of two alternative processes, laser micro-drilling and nickel vapor deposition, warrant an investigation to determine their ability to fabricate small orifices. Nickel vapor deposition (NVD) is a relatively low-temperature method for chemical vapor deposition capable of rapidly coating inner surfaces. Questions that remain to be addressed with NVD include coating adhesion, hardness, coating composition/alloying, and scale-up. Drilling micro-orifices with lasers by using trepanning shows promise – small (<50-μm Ø) holes have been reportedly drilled through steel plates >5 mm thick. The properties of the heat-affected zone (HAZ) in regions immediately adjacent to the holes, their potential impact on fatigue, and methodologies to mitigate formation of the HAZ need to be addressed. The deposition of re-cast material and back-wall protection

also need to be addressed before commercialization.

Approach

As described in previous reports, the orifice diameter can be reduced by coating the orifice interior with EN plating. This technique has been used to deposit nickel/phosphorus or nickel/boron alloys onto metallic surfaces from aqueous solutions. It has been successfully used in previous years to reduce orifice diameter from 200 to 50 μm on a bench scale, and from 180 to 75–80 μm on a commercial scale. Other metal alloys have been deposited by the same technique.

Having demonstrated that EN plating reduces orifice diameter to the desired size, we next sought to demonstrate the usefulness of EN-plated nozzles for solving the problems described in the Introduction: improving spray properties and discharge coefficient, reducing deposit formation, and resisting corrosion. To this end, the use of Argonne's APS was explored for nondestructive examination of plated nozzles. This technique is capable of measuring coating thicknesses on internal passages, and it will be applied as a quality check on nozzles that have been sent to the EPA for engine tests.

Collaborative efforts were established with industrial firms to investigate the potential of nickel vapor deposition and laser processing to produce 50-μm Ø orifices. A series of commercial nozzles was sent to Weber Manufacturing, who designed a fixture to coat the interior surfaces by using nickel carbonyl. Test coupons (obtained from commercial injectors) were also prepared and sent to two commercial laser processing labs to determine the feasibility of producing small orifices with high length-to-diameter characteristics.

Results

Initial research focused on demonstrating the feasibility of coating internal passages with EN. The early laboratory results on single nozzles were very successful. Commercial nozzles with orifices 200 μm in diameter and 1 to 1.55 mm long were plated with EN, producing an orifice 50 μm in diameter.[4,5] The coatings were uniform in thickness along the orifice and as smooth, or smoother, than the original orifice surface. Figure 1 shows a scanning electron micrograph of a coated nozzle that was cross-sectioned to measure the thickness of the coating. The image illustrates the excellent continuity and adhesion of the coating.

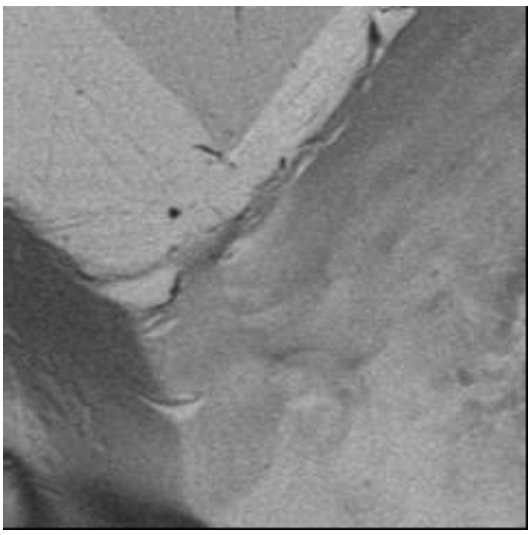

Figure 1: Scanning electron micrograph of EN-plated orifice.

The EN plating concept was transferred to a commercial plating company (Imagineering) specializing in electroless coatings—particularly Ni-phosphorus coatings. Imagineering modified its coating process to eliminate surface blemishes/pits observed on initial coating trials.

Imagineering also attempted to develop Ni stripping processes to remove EN plating from selected (non-orifice) regions. The company's method of removing EN from a plated surface without damaging the substrate did not keep the needle guide free of plating, and the conventional maskants used on the guide area did not allow sufficient plating bath flow to coat the orifices uniformly. Imagineering suggested that the plating be removed mechanically, as

EN plating can be ground off. This approach proved to be feasible. The same approach can remove overcoating from the needle seat area,[4] which might otherwise adversely affect needle sealing. In production, this additional step is not expected to increase the overall cost – the current grind and lap procedures will be the final stage. Previous studies[4] also indicated deposit formation was not an issue for the EN plating – in fact, the EN plating reduced the formation of deposits in high (500 ppm) diesel fuel.

Recent tests[6] at the APS indicated a phase contrast x-ray imaging technique developed to image the motion of a pintle inside an operating injector had sufficient resolution to differentiate the Ni coating from the surrounding ferrous body. This technique was applied to validate the thickness of EN coatings applied to a series of light-duty injectors that were sent to the EPA-NVFEL lab for engine and flow visualization studies. As-received, the nozzles contained seven 100-µm Ø orifices. Half of the nozzles were EN coated and treated to a final orifice diameter of 75 µm, the other half were coated to produce a final orifice with 50-µm Ø. After treatment, the nozzles were internally ground to remove EN plating from the needle guide and seat.

Flow tests, performed to confirm flow through all seven orifices of each nozzle, revealed that two of the 50 µm nozzles were partially plugged. The phase contrast x-ray imaging technique was used to examine one of the plugged nozzles. As seen in Figure 2, the individual orifices are readily observed, as well as the coating. The thickness of the coating is approximately 25 µm, resulting in a final orifice diameter of 50 µm. The coating thickness was uniform over the length of the orifice, and the plugging that was observed in the flow test was the result of a particle lodged in one of the orifices, as seen in the lower left quadrant of Figure 2. Thus, the plugging was not the result of a non-uniform deposition of EN plating, but to a particle that became trapped in the orifice during the post-coating grind.

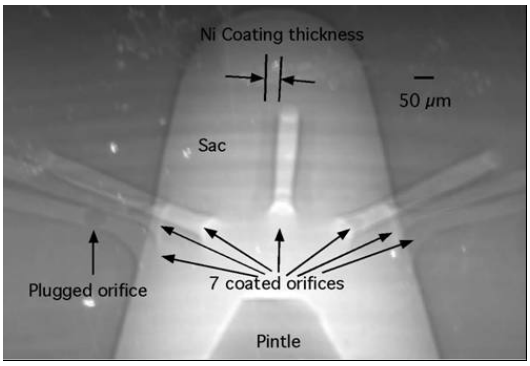

Figure 2: Phase contrast X-ray images of commercial nozzle plated with EN

Two nozzles, one with 50 µm orifices, and one with 75 µm orifices, were sent to the EPA-NVFEL to investigate the flow characteristics by high-speed laser imaging. The test rig uses a hydraulically intensified fuel system (3,000 psi intensified 11:1) injecting fuel into a 500 psi chamber. The pulse width in all cases was 1 msec. Figure 3 shows snapshots taken 0.6 msec after start of injection for three nozzles[7]: one with 50 µm orifices (far left), one with 75 µm orifices (center), and one that was uncoated – 100 µm orifices. Figure 4 shows quantitative data on the fuel penetration as a function of time for each of the cases shown in Figure 3. Qualitatively, the 100 µm sprays in Figure 3 appear denser (as indicated by the color - white vs. green) than the 50 and 75 µm sprays. Aside from a slightly deeper penetration, the fuel penetration data for the 75 µm orifice do not differ dramatically from those of the uncoated, 100 µm nozzle. The 50 µm nozzle, however, shows a dramatic difference in the fuel penetration profile. The penetration is not only shallower than that of the 75 and 100 µm orifices – as expected, but, also is linear with time in contrast to the non-linear dependence observed for the 75 and 100 µm nozzles.

Plans are being developed to demonstrate the feasibility of producing multi-sized orifices on experimental nozzles for spray visualization studies and, if successful, for engine emission studies. Argonne is also exploring application of the EN process to provide cavitation-erosion

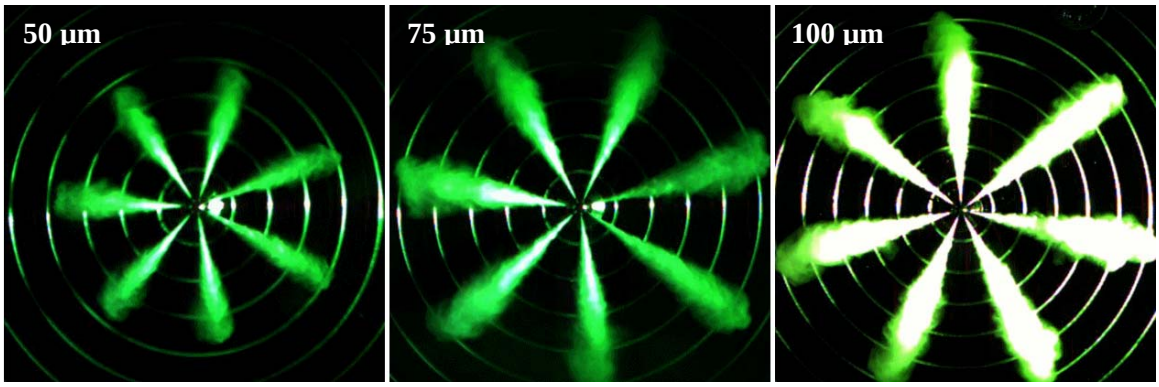

Figure 3: Laser images of fuel sprays from 50, 75, and 100 µm orifices.[7]

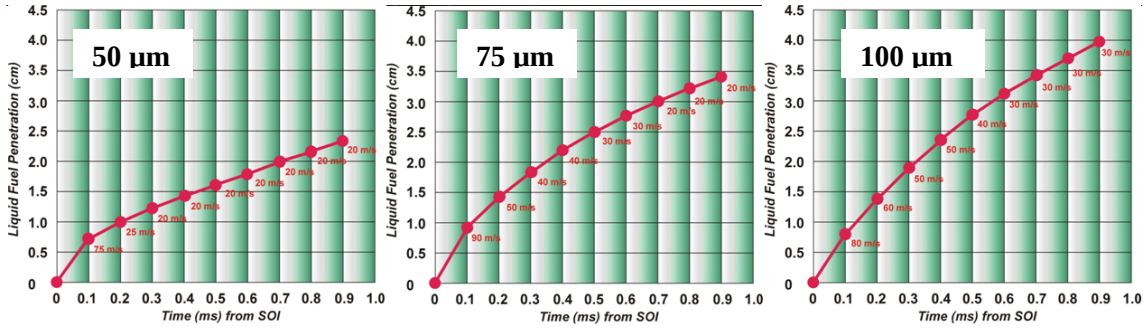

Figure 4: Fuel penetration as a function of time from start of injection (SOI) for 50, 75, and 100 µm nozzles.[7]

A process[8] developed in late FY 2006 utilizing nickel vapor deposition to deposit nickel on internal orifice surfaces was examined in closer detail in FY 2007. It is similar to the EN process, but instead of flowing an aqueous-based solution through a nozzle with a pre-existing orifice, a nickel-bearing vapor compound flows through the orifice. It is based on the NVD process[9] employed by Weber Manufacturing to fabricate molds and nickel shells with wall thicknesses up to 25 mm in thickness. The process involves the formation and decomposition of nickel carbonyl, $Ni(CO)_4$, via control of temperature and CO partial pressure in sealed chambers. The process is used by Weber to form large molds and dies for automotive applications. Argonne and Weber are collaborating to evaluate the potential for NVD to deposit Ni coatings on commercial diesel injectors. Weber designed a small, compact reactor to process test injectors at different operating conditions. Initial results on as-received nozzles showed marginal success, with coating thicknesses limited to 5 to 20 µm. A cleaning procedure was subsequently developed to degrease and remove native oxides prior to deposition. This procedure proved to be successful, with coating thicknesses up to 100 µm achieved (plugging the orifice) within 2 to 4 hours.

Figures 5a and b show optical micrographs of a commercial, six-hole nozzle after NVD of nickel for approximately 2 hours. The orifices were originally 200-µm Ø. Figure 5a indicates the presence of nickel not only inside of the orifice, but also residual coating on the outside and inner sac regions. The presence of the coating in the latter regions should not pose a problem since the outer coating could be removed by a grinding step, while the coating on the inner surface will either be

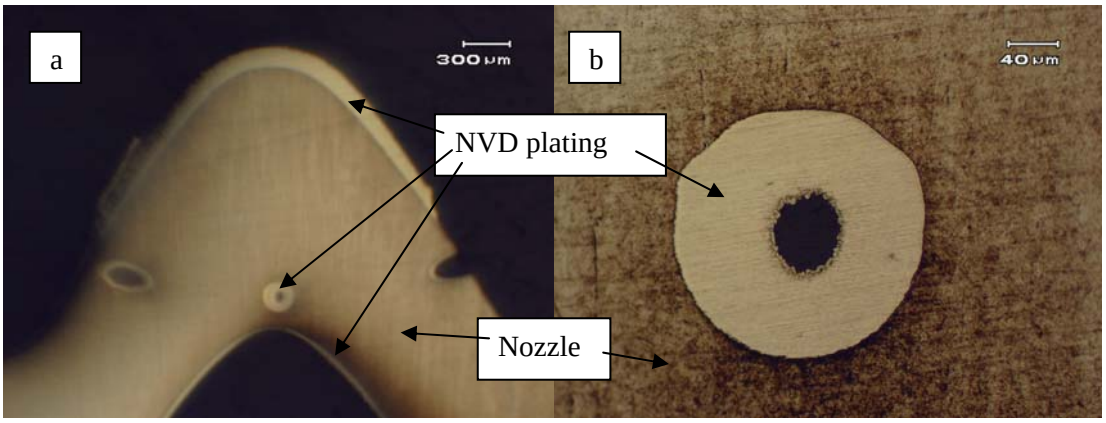

Figure 5: Low (a) and high (b) magnification optical images of a cross-sectioned, polished, and etched (Nital) six-orifice nozzle after NVD.

removed by a post-deposition grinding step for the pintle seat, or will not be sufficiently thick to be of concern for the sac region around the entrance of the orifice. The coating thickness changed along the length of the orifice – the coating near the outer surface of the nozzle was approximately 40 µm, while the coating near the inner surface was closer to 80 µm. The cause of this non-uniformity has not been studied in detail. Differences in the relative compositions of the gas reactants, temperature, and boundary-layer thickness along the orifice need to be modeled to predict local deposition rates.

Efforts in FY 2008 will continue to evaluate the properties of NVD-coated orifices. These efforts will focus on evaluating coating adhesion, hardness, and composition.

A third process, drilling of micro-orifices using lasers, is also being investigated. Recent advances in laser processing, by means of percussion or trepanning, show an ability to fabricate small (<50 µm) holes. Argonne is working with two firms (Lasag and Sparkle-Optics) to characterize the properties of orifices produced in flat steel coupons. Figure 6 shows low- magnification scanning electron images of nominal 30-µm Ø orifices percussion drilled through a 1-mm-thick steel coupon by Sparkle-Optics. The "30-µm Ø" refers to the diameter on the exit side of the coupon. The inset in fig. 6 (top, right) shows a higher magnification of the middle orifice and illustrates the appearance of the re-melt material that is deposited around the periphery of the orifice on the entrance side.

Figures 7a and b show optical images of the entrance and exit surfaces of the '30-µm Ø orifices after lightly polishing both surfaces with 2400 grit paper. On the entrance side, the orifice is approximately 60-µm Ø, while on the exit side, the orifice is 30-µm Ø – thus indicating that the percussion drilling process produces a tapered orifice. Efforts in FY 2008 will continue to examine the potential of laser processing to produce micro-orifices on fuel injectors. Emphasis will be placed on evaluating the properties of the HAZ formed adjacent to the orifice by utilizing the APS.

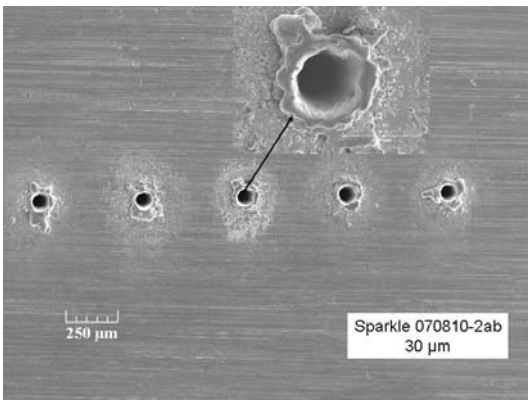

Figure 6: Scanning electron image of the entrance surface of percussion drilled orifices.

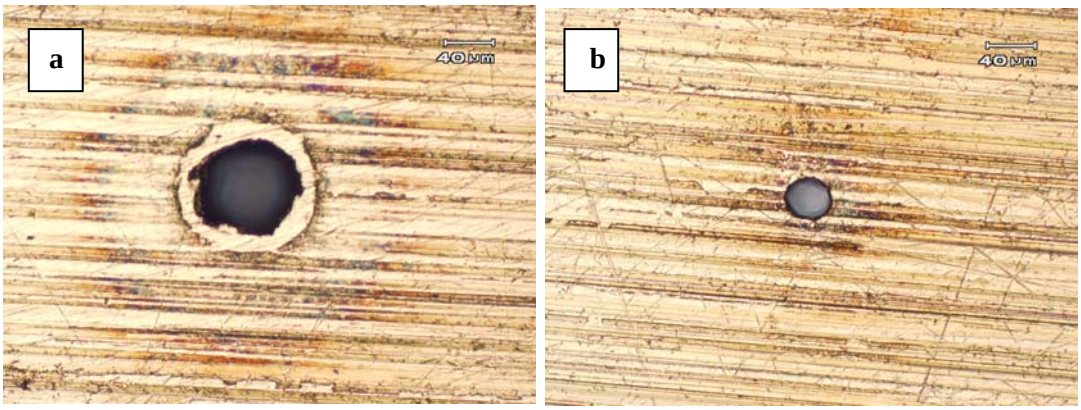

Figure 7: Optical images of the entrance (a) and exit (b) surfaces of percussion drilled orifices.

Conclusions

Several candidate methods are being evaluated and developed for fabricating nozzles with small (50-µm Ø) micro-orifices. Development of the EN aqueous-based plating process has been advanced to the stage where commercial nozzles were treated and characterized with an advanced phase-contrast x-ray imaging technique that confirmed uniform coating deposition along the orifice. Fuel-spray visualization studies performed at injection pressures up to 33,000 psi revealed uniform spray distributions. Two alternative processes for fabricating micro-orifices were examined: nickel vapor deposition and laser micro-drilling. Preliminary tests demonstrated the feasibility to produce small orifices, and these processes will undergo further evaluation.

References

1. Lyle M. Pickett and Dennis L. Siebers, Paper No. 2001-ICE-399, ICE Vol. 37-1, ed. V. W. Wong, *2001 Fall Technical Conference*, American Society of Mechanical Engineers, 2001.
2. L. M. Pickett, D. L. Siebers, A. F. Morales, J. Hachman, and A. K. Sinensky, "An Investigation of Diesel Soot Formation Processes Using High Aspect Ratio Micro-Orifices," presented at HARMST 2003 High-Aspect Ratio Micro-Structure Technology Workshop, Monterey, CA, 2003.
3. John B. Heywood, *Internal Combustion Engine Fundamentals*, McGraw-Hill, New York, 1988.
4. John B. Woodford and George R. Fenske, "Fabrication of Small Fuel Injector Orifices," *2005 Annual Progress Report, Automotive Propulsion Materials*, U.S. Department of Energy, Washington, D.C., 2005.
5. John B. Woodford and George Fenske, "Fabrication of Micro-Orifices for Diesel Fuel Injectors," *2006 Annual Progress Report, Automotive Propulsion Materials*, U.S. Department of Energy, Washington, D.C., 2006.
6. Kamel Fezzaa, Wah-Keat Lee, Seong-Kyun Cheong, Christopher F. Powell, Jin Wang, and Ming-Chia Lai, "Ultrafast X-ray Phase-Enhanced Microimaging for Visualizing Fuel Injection Process," SAE 2005-24-093, Society of Automotive Engineers, 2005.
7. R. Schaefer, US EPA-NVFEL, private communication, July, 2007.
8. G. Fenske and J. Woodford, "Nickel Vapor Deposition Orifice Coatings," Argonne National Laboratory Invention Disclosure, ANL-IN-06-030.
9. Rob Sheppard, "Nickel Vapor Deposition (NVD) Shell Tooling & Product Applications,"

http://www.weberman.on.ca/Resources/presentations/NVD_Shells_091107.pdf, September, 2007.

Publications and Presentations

J. Woodford and G. Fenske, "Fabrication of Small Orifice Fuel Injectors," DEER (Diesel Engine Emissions Reduction) Conference, August 2005.

J. B. Woodford and G. R. Fenske, *Fabrication of Small-Orifice Fuel Injectors for Diesel Engines*, Argonne National Laboratory Report, ANL-05/06, March 2005.

J. B. Woodford, G. R. Fenske, and J. M. Perez, "Deposit Formation on Electroless Nickel," submitted to *Energy & Fuels*.

G. Fenske, J. Woodford, J. Wang, and R Schaefer, "Fabrication and Characterization of Micro-Orifices for Diesel Fuel Injectors," submitted for presentation at the 2008 SAE International Powertrains, Fuels and Lubricants Congress, June 23-25, 2008, Shanghai, China.

Inventions and Patents

G. Fenske and J. Woodford, "Nickel Vapor Deposition Orifice Coatings," ANL-IN-06-030, patent application.

A Strong Energy Portfolio for a Strong America

Energy efficiency and clean, renewable energy will mean a stronger economy, a cleaner environment, and greater energy independence for America. Working with a wide array of state, community, industry, and university partners, the U.S. Department of Energy's Office of Energy Efficiency and Renewable Energy invests in a diverse portfolio of energy technologies.

For more information contact:
EERE Information Center
1-877-EERE-INF (1-877-337-3463)
www.eere.energy.gov